THE USE OF GOLD NANOSTRUCTURES IN THE IMAGING AND THERAPY OF CANCER

KAH CHEN YONG JAMES

NATIONAL UNVERSITY OF SINGAPORE

2009

THE USE OF GOLD NANOSTRUCTURES IN THE IMAGING AND THERAPY OF CANCER

KAH CHEN YONG JAMES

(*B.Eng.(Hons), NUS*)

A THESIS SUBMITTED

FOR THE DEGREE OF DOCTOR OF PHILOSOPHY

GRADUATE PROGRAMME IN BIOENGINEERING

NATIONAL UNVERSITY OF SINGAPORE

2009

DEDICATION

This thesis is dedicated to my beloved parents and wife, Amy. Without your love and prayer support, I would not have been able to do all these.

ACKNOWLEDGEMENTS

This work would not have been possible if not for the guidance and support of many, whom I would like to take this opportunity to express my sincere appreciation to. First and foremost, I would like to thank my two PhD supervisors Prof. Colin Sheppard and Prof. Malini Olivo for their invaluable guidance and advice. Through the many discussions in the course of this work, Prof. Colin has shown me that a true scientist is not just one who has a passion for science, but one who also ignites this passion in others around him. He is indeed one such role model who inspires me to go further and deeper in science. I also thank Prof. Malini for making the many resources including the laboratory facilities and funding possible for this project, as well as her support when the going gets tough. Her commitment in helping me to overcome whatever logistical or technical difficulties faced along the way was admirable and her commitment in prayers for all her students, including myself encouraged me.

I would also like to acknowledge the various collaborators of this project for their advice and resources rendered. This includes Prof. Subodh Mhaisalkar and Prof. Tim White as well as the staff members from the School of Materials Science and Engineering, Nanyang Technological University (NTU), in particular Dr. Nopphawan Phonthammachai and Dr. Anup Lohani for providing the research facilities and technical assistance in developing the nanomaterials in this project. In addition, both Prof. Subodh and Prof. Tim provided valuable intellectural contribution towards the initial synthesis of the gold nanoshells.

My sincere appreciation also goes out to Mr. Chow Tzu Hao, Mr. Song Kin San and Dr. Ng Beng Koon from the photonics group in the School of Electrical and Electronics Engineering, NTU for making their benchtop OCT system available for the phantom studies in this project. In addition, Tzu Hao also provided valuable advice in developing the OCT theoretical curve fitting for extraction of gold nanoshells concentration in tissue. I also wish to thank Kin San for his assistance in performing the small animal imaging.

The study of gold nanoshells pegylation and its uptake *in vitro* would not have been included in this thesis if not for the advice of my thesis committee member, Prof. Neoh Khoon Gee from the Department of Chemical and Biomolecular Engineering, National University of Singapore (NUS). She provided valuable suggestion towards the pegylation studies and her group members, in particular, Ms. Wuang Shy Chyi shared valuable suggestions on performing the antibody conjugation of gold nanoshells. I also wish to thank Dr. Lanry Yung from the same department in NUS for sharing his expertise and resources in the early studies of this project on gold nanoparticles, which laid the preliminary groundwork for further studies to build on.

Apart from these various collaborators, there are also many wonderful individuals who have contributed in various ways to make life more enjoyable to work in a laboratory. I shall attempt to mention them individually, although I do admit that the list is really non-exhaustive. These include my fellow colleagues in the Laboratory of Photodynamic Therapy and Diagnosis, National Cancer Centre: Bhuvana, William Chin, Vanaja, Karen Yee, Lucky, Patricia, Kho, Ali, and of course not forgetting Gerald who helped to make confocal imaging a more pleasant experience. I also want

to acknowledge the help by colleagues from the Singapore Bioimaging Consortium (SBIC) A*STAR, especially Chit Yaw who helped with some tissue characterization, as well as Dr. Praveen Thoniyot who helped to proof-read my manuscripts. Of course, the list would not be complete without all the wonderful final year undergraduates from NUS and NTU: Song Jing, Rachel, Iman, Keryi, Karen, Jie Han, Jason, and Theng Hong, who rendered practical help in one way or another. They provided me with valuable learning experience in my capacity as a mentor. The process of guiding these groups of students in their projects has helped me to cultivate the virtue of patience. This list of students also includes internship students from Temasek Polytechnic: Anne and Hazel, who were so kind to help with the daily cell culture routine when my schedule did not permit.

There are also people from the NUS Graduate Programme in Bioengineering (GPBE) whom I wish to make special mention, since they are the ones who truly put me on a stable platform to launch me well into the 5 years of my graduate studies. These include my two lab rotation supervisors, Dr. Caroline Lee from Department of Biochemistry, NUS and Prof. Stephen Hsu from Faculty of Dentistry, NUS who are so approachable whenever I needed directions, not just in research, but also in life. I also thank our GPBE chairmen Prof. Michael Ragunath, Prof. Hanry Yu and Prof. Teoh Swee Hin who gave me the opportunity to pursue graduate research work. The GPBE family also includes the group of dedicated administrative staff: Hui Min, Judy, Soo Hoon, Jannie, Irene and Marcus who have been so helpful in resolving whatever administrative issues I faced during my graduate coursework and research.

I also do greatly acknowledge the support of NUS in providing me with a research scholarship and the National Cancer Centre, Singapore for all the technical and research support that made this work possible. I am also grateful to my family members and church friends, many of whom have ceaselessly provided tremendous prayer support and encouragement during those tough times in the project when things did not seem to go anywhere. Of course, God truly answers the prayers of His persistent children and I thank God too, not just for His grace and faithfulness in carrying me through this project, but also for all of the above mentioned people whom He has brought into my life, many of whom have been my exemplary life mentors.

"For great is His love towards us, and the faithfulness of the Lord endures forever. Praise the Lord!" Psalm 117:2.

TABLE OF CONTENTS

SUMMARY

Conventional clinical diagnosis of epithelial cancer involving excisional biopsies followed by histopathological examination of suspicious lesions is often associated with a low detection sensitivity as well as psychological trauma and risk of infection to patients. Recent advances in reflectance-based optical imaging such as reflectance confocal endomicroscopy and Optical Coherence Tomography (OCT) are developed to perform minimally invasive "optical biopsies" to diagnose diseases *in vivo*. Although these imaging technologies provide cellular resolution, their optical contrast between normal and cancerous tissue is often too modest to be of any significant clinical value. Furthermore, they are unable to image the molecular changes associated with early stage carcinogenesis which is critical for early pre-cancerous detection and rational therapeutic intervention.

This thesis examines the use of gold nanostructures as an exogenous cancer-specific optical contrast agents for reflectance-based imaging to supplement the weak inherent contrast signal associated with disease pathology and improve the contrast between different tissue types involved in early-stage epithelial carcinogenesis. Here, the focus is on the development and application of gold nanoshells in cancer detection based on the expression of the Epidermal Growth Factor Receptor (EGFR) as a clinically relevant prognostic marker. The hypothesis is that the use of gold nanoshells could increase the optical contrast between normal and suspicious lesions and simultaneously provide useful molecular specific information for the diagnosis of these lesions *in vivo* when used with confocal reflectance microscopy and OCT.

The approach adopted includes developing and characterizing gold nanostructure probes, conducting *in vitro* assessment of their optical contrast, examing their optical properties in phantom models and evaluating their efficacy in animal models. Gold nanoshells that are optically tuned to the imaging source wavelength are designed based on theoretical prediction of their optimum dimensions prior to synthesis and chacterization of their optical properties. The gold nanoshells are then surface functionalized with anti-EGFR through covalent conjugation with the antibody and its ability to improve the optical contrast to discriminate cancer from normal cells and provide molecular mapping of EGFR on cellular surface are assessed *in vitro*.

The optical properties of gold nanoshells in non-biological tissue phantom models are examined under the OCT to investigate the different factors affecting the optical contrast in tissue phantoms. The results of *in vitro* and phantom studies provide the impetus for further *in vivo* studies which demonstrates the control of optical contrast by gold nanoshells in a mouse xenograft tumor model. This is achieved through different delivery modes, concentration variations of gold nanoshells and antibody targeting. The antibody targeting *in vivo* also allows gold nanoshells to image changes in molecular markers expression for real-time early diagnosis. Successful development of contrast enhancing gold nanostructure probes allows *in vivo* diagnostic imaging with increased sensitivity and specificity, resulting in early detection and management of pre-cancers through the combination of phenotypic markers and expression profiling of molecular markers using the gold nanostructure probes.

LIST OF TABLES

LIST OF FIGURES

LIST OF PUBLICATIONS

Journal articles

1. **Kah JCY**, Kho KW, Lee CGL, Sheppard CJR, Shen ZX, Soo KC, Olivo MC. Early diagnosis of oral cancer based on the surface plasmon resonance of gold nanoparticles. **Int J Nanomedicine** 2007; 2: 785–798.
2. Kho KW, **Kah JCY**, Lee CGL, Sheppard CJR, Shen ZX, Soo KC, Olivo MC. Applications of gold nanoparticles in the early detection of cancer. **J Mech Med Biol** 2007; 7: 19–35.
3. **Kah JCY**, Olivo MC, Lee CGL, Sheppard CJR. Molecular contrast of EGFR expression using gold nanoparticles as a reflectance-based imaging probe. **Mol Cell Probes** 2008; 22: 14–23.
4. **Kah JCY**, Phonthammachai N, Wan RCY, Song J, White T, Mhaisalkar S, Ahmad I, Sheppard C, Olivo M. Synthesis of gold nanoshells based on the deposition-precipitation process. **Gold Bull** 2008; 41: 23–36.
5. Phonthammachai N, **Kah JCY**, Guo J, Sheppard CJR, Olivo MC, Mhaisalkar SG, White TJ. Synthesis of contiguous silica-gold core-shell structures: Critical parameters and processes. **Langmuir** 2008; 24: 5109–5112.
6. **Kah JCY**, Lau WKO, Tan PH, Sheppard CJR, Olivo M. Endoscopic Image Analysis of Photosensitizer Fluorescence as a Promising Noninvasive Approach for Pathological Grading of Bladder Cancer *In Situ*. **J Biomed Opt** 2008; 13: 054022.

7. **Kah JCY**, Wan RCY, Wong KY, Mhaisalkar S, Sheppard CJR, Olivo M. Combinatorial treatment of photothermal therapy using gold nanoshells with conventional photodynamic therapy to improve treatment efficacy: an *in vitro* study. **Lasers Surg Med** 2008; 40: 584–589.
8. **Kah JCY**, Wong KY, Olivo M, Song JH, Fu WP, Mhaisalkar S, Neoh KG, Sheppard CJR. Critical parameters in the pegylation of gold nanoshells for biomedical applications: an in vitro macrophage study. **J Drug Targeting** 2009; 17: 181–193.
9. **Kah JCY**, Chow TH, Ng BK, Razul SG, Olivo M, Sheppard CJR. Concentration dependence of gold nanoshells on the enhancement of OCT images: a quantitative study. **Appl Opt** 2009; 48: D96–D108.
10. **Kah JCY**, Olivo M, Chow TH, Song KS, Koh KZY, Mhaisalkar S, Sheppard CJR. Control of optical contrast using gold nanoshells for OCT imaging of mouse xenograft tumor model *in vivo*. **J Biomed Opt** (in press, 2009).

Conference presentations

1. **Kah JCY**, Olivo MC, Lau WKO, Sheppard CJR. Pathological Diagnosis of Bladder Cancer by Image Analysis of Hypericin Induced Fluorescence Cystoscopic Images. In **2005 European Conferences on Biomedical Optics, Munich, Germany, 12 – 16 June 2005**.
2. **Kah JCY**, Lau WKO, Olivo MC. Image Analysis of Hypericin Induced Fluorescence Used in Pathological Diagnosis of Bladder Cancer. In **10th World Congress of the International Photodynamic Association, Munich, Germany, 2005**.

3. **Kah JCY**, Sheppard CJR, Lee CGL, Olivo MC. Antibody-conjugated Gold Nanoparticles and its Interactions with Epithelial Carcinoma Cells for Optical Molecular Imaging. In **Proceedings of NTU-SGH Symposium 2005**, pp 29.
4. **Kah JCY**, Olivo MC, Lee CGL, Sheppard CJR. Antibody-conjugated Gold Nanoparticles and Its Interaction with Epithelial Carcinoma Cells for Optical Molecular Imaging. In **Combined Scientific Meeting 2005, Singapore, 4 – 6 November 2005**.
5. **Kah JCY**, Sheppard CJR, Lee CGL, Olivo MC. Application of Antibody-Conjugated Gold Nanoparticles for Optical Molecular Imaging of Epithelial Carcinoma Cells. In **Photonics West BIOS 2006 Symposium on Biomedical Optics, San Jose, 21 – 26 January 2006**.
6. **Kah JCY**, Kho KW, Lee CGL, Sheppard CJR, Shen ZX, Soo KC, Olivo MC. Surface plasmon resonance of gold nanoparticles in the photodetection of early oral cancers. In **11th World Congress of the International Photodynamic Association, Shanghai, P. R. China, 28 – 31 March 2007.** (Awarded Young Investigators' Fellowship).
7. Olivo M, **Kah JCY**, Tan PH, Lau WKO. A Study of Hypericin as a Potential Fluorescence Marker for Detection and Pathological Grading of Transitional Cell Bladder Carcinoma. In **11th World Congress of the International Photodynamic Association, Shanghai, P. R. China, 28 – 31 March 2007.**
8. **Kah JCY**, Wan RCY, Chow TH, Phonthammachai N, Olivo MC, Mhaisalkar S, White TJ, Sheppard CJR. Exploiting the Optical Response of Metallodielectric core-shell particles for imaging and therapy of cancer. In **4th Scientific Meeting of the Biomedical Engineering Society (Singapore), Singapore, 19 May 2007.**

9. Chow TH, Tan KM, **Kah JCY**, Ng BK, Sheppard CJR. Ultrahigh resolution fourier domain optical coherence tomography for biomedical imaging. In **4th Scientific Meeting of the Biomedical Engineering Society (Singapore), Singapore, 19 May 2007.**
10. Ng XY, Asgarova R, Zhuang CBR, **Kah JCY**, Olivo MC. Development of protein assay based on gold nanoparticles. In **4th Scientific Meeting of the Biomedical Engineering Society (Singapore), Singapore, 19 May 2007.**
11. **Kah JCY**, Chow T, Olivo MC, Ng B, Gulam RS, Sheppard CJR. Improving the optical contrast of backscattering signal in reflectance-based imaging with gold nanoshells. In **2007 European Conferences on Biomedical Optics, Munich, Germany, 17 – 21 June 2007**.
12. Chow T, **Kah JCY**, Tan KM, Ng BK, Gulam RS, Sheppard CJR. Absorption effects in optical coherence tomography modeling. In **2007 European Conferences on Biomedical Optics, Munich, Germany, 17 – 21 June 2007**.
13. **Kah JCY**, Phonthammachai N, Song J, Chow TH, White TJ, Mhaisalkar SG, Olivo MC, Sheppard CJR. Synthesis of gold nanoshells from a precursor seed prepared using deposition-precipitation process: Applications in cancer imaging. In **International Conference on Materials for Advanced Technologies 2007, Singapore, 1 – 6 July 2007**.
14. **Kah JCY**, Ng XY, Asgarova R, Zhuang CB, Olivo MC. Development of protein assay based on the optical properties of gold nanoparticles. In **International Conference on Materials for Advanced Technologies 2007, Singapore, 1 – 6 July 2007**.
15. Wan RCY, **Kah JCY**, Olivo MC, Mhaisalkar SG. Combinational treatment of photothermal therapy using gold nanoshells with conventional photodynamic

therapy to enhance cellular destruction: An in vitro study. In **International Conference on Materials for Advanced Technologies 2007, Singapore, 1 – 6 July 2007**.

16. **Kah JCY**, Wan RCY, Chow TH, Olivo MC, Mhaisalkar SG, Sheppard CJR. The Use of Gold Nanoshells in Cancer Imaging and Therapy. In **Spring 2008 Optics and Photonics Congress BIOMED 2008, St. Petersburg, USA, 16 – 20 March 2008**.
17. **Kah JCY**, Chow TH, Shu TH, Koh KZY, Mhaisalkar SG, Olivo M, Sheppard CJR. Gold nanoshells as Contrast Agents for Optical Coherence Tomography. In **Optics within Life Sciences–10 Biophotonics Asia 2008, Singapore, 2 – 4 July 2008**.
18. Wong KY, **Kah JCY**, Sheppard CJR, Olivo M. Optimization of gold nanoshell surface characteristics using poly(ethylene glycol) for cancer diagnostics and therapies. In **Optics within Life Sciences–10 Biophotonics Asia 2008, Singapore, 2 – 4 July 2008**.
19. Chow TH, Tan KM, Tay CM, Ng BK, Razul SG, Chia TF, Poh WT, **Kah JCY**, Sheppard CJR. Plant diagnosis with optical coherence tomography. In **Optics within Life Sciences–10 Biophotonics Asia 2008, Singapore, 2 – 4 July 2008**.

CHAPTER ONE

INTRODUCTION

1.1 Conventional cancer diagnosis

The survival of cancer patients is related to different stages of malignancy detected. Early detection of malignant lesions is not only crucial to the clinical outcome of treatment, but also exerts a significant impact on reducing the recurrence rate in most cancers. This is true for many epithelial type cancers which originate in the epithelium of hollow organs in the body e.g. oral, lungs, GIT and bladder. The current clinical detection of most epithelial type cancers typically involve visual examination followed by invasive excisional needle biopsies on suspicious lesions and histological examination on the excised tissue as illustrated in Figure 1.1 below.

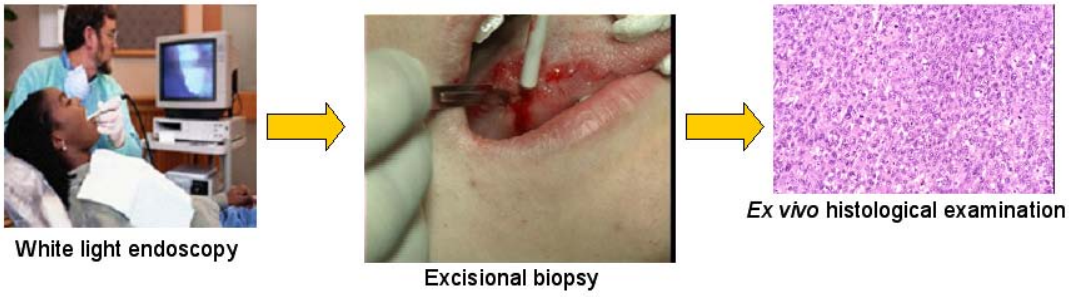

Figure 1.1. Conventional approach to clinical detection of epithelial type cancer such as oral cancer using white light endoscopy for visual examination followed by needle biopsies and histological examination of the biopsied tissue.

The biopsy process may introduce risks associated with tissue removal, along with delay, expense and psychological trauma to patients [1]. Biopsy is usually performed only under the condition that the lesions are spotted and appear abnormal [2]. Yet, pre-cancerous lesions can appear innocuous or occur in hidden sites and can therefore easily go undetected even with white light endoscopy [3]. Also, tissue sampling may not adequately represent the actual pathological condition of the entire tissue because of tissue heterogeneity, which is especially characteristic of tumors [4]. Furthermore, conventional histopathological diagnosis of these biopsies is largely based on phenotypic assessment of differences in cellular features which may not be discernable in early stage lesions that appear similar to surrounding normal tissue [5].

1.2 Optical imaging in biopsy

Amongst the various imaging tools available for use in laboratory research or clinical imaging of pathological conditions such as cancer, optical imaging finds its niche in providing subcellular resolution which is a pre-requisite for imaging at the cellular and molecular levels. To overcome the shortcomings associated with excisional biopsies, recent advances in optical imaging are geared towards performing the concept of optical biopsy. Amongst the wide range of optical imaging modalities available to clinicians today, fluorescence imaging remains the most widely used. Despite their known limitations in photobleaching which may result in a bias during quantitative signal analysis, practically all of the current optical molecular imaging efforts involve the use of fluorescence, due partly to its high signal-to-noise ratio and a large variety of dyes available for multilabeling. It has been widely investigated in both the laboratory and clinical settings to detect and diagnose suspicious conditions or lesions in various tissue and organs of the body.

These fluorescence techniques are based on direct visualization of changes in optical properties such as fluorescence in tissue. The changes in fluorescence can arise from fluorescent dyes selectively accumulated in lesions e.g. tumors as in the case of photodynamic diagnosis [6, 7] or it can also involve detection of changes in the intrinsic autofluorescence of tissue in the presence of tissue abnormalities [8]. These fluorescence are often used to detect pre-cancerous or flat lesions of epithelial carcinomas under a fluorescence endoscopy system which would otherwise easily go undetected under the naked eye as shown in Figure 1.2. Fluorescence imaging has recently demonstrated its potential in grading bladder cancer *in situ* [9].

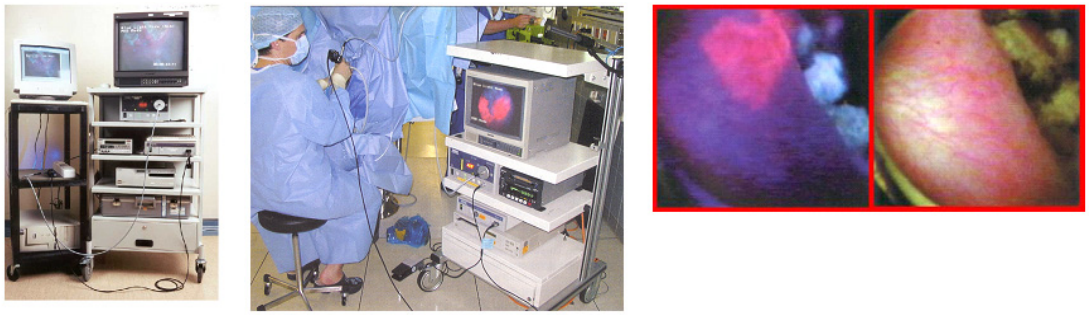

Figure 1.2. A fluorescence endoscopic system used in the clinical setting (left and middle) to detect flat lesions such as carcinoma *in situ* which would otherwise be missed under the naked eye (right). In this case, the flat lesion shows up in red fluorescence under the blue excitation light.

Other less widely used, but nonetheless emerging non-fluorescent based advanced optical imaging systems such as diffuse optical tomography, confocal reflectance endomicroscopy [10-12] and optical coherence tomography (OCT) [13, 14] etc. are increasingly gaining attention in the early detection of diseased conditions. These non-fluorescent imaging techniques form their image based on other types of optical changes such as optical absorption or scattering and offer promising clinical application especially in the area of cancer imaging by increasingly proving

themselves to offer alternative angles in examining the same biological problems or diseased conditions, thereby potentially yielding greater diagnostic values.

In areas where fluorescence imaging remains inaccessible such as imaging tissue histology *in situ*, these non-fluorescent techniques allow tissue structures such as stromal morphology to be imaged *in situ* without the need for any staining [14, 15]. These optical imaging systems, in particular the reflectance-based optical imaging such as reflectance confocal endomicroscopy and OCT, have been developed for *in situ* imaging of superficial tissue to perform minimally invasive optical biopsies to diagnose diseases *in vivo* due to the high resolution they afford [13, 16-19].

1.3 Reflectance-based optical imaging

Reflectance-based optical imaging technique is a class of non-fluorescent imaging that examines tissue and forms images based on incident light that are backscattered from tissue samples without the use of fluorescence. They collect the backscattered light from tissue to provide a detailed two-dimensional image of it with a high spatial resolution of 1–25 μm and penetration depth ranging from 200 μm to 2 mm without the need for physical sectioning [13, 20]. Unlike the fluorescence imaging which primarily examines molecular changes and are unable to image structures in tissue without the aid of multiple staining processes, these reflectance-based imaging techniques allow tissue structures such as stromal morphology to be imaged without any prior staining [14, 15].

These high-resolution optical imaging systems are emerging clinical imaging modalities that allow real-time, non-invasive imaging of epithelial tissue *in situ* at the

cellular resolution and have proven themselves to offer alternative angles to fluorescence imaging in examining the same diseased conditions. They also offer as alternatives to conventional histopathology by non-invasively imaging stromal morphology at high resolution in real-time to significantly improve our ability to visualize and evaluate the epithelial tissue *in vivo* at the microscopic level. These optical imaging systems are typically simple, portable and inexpensive and they provide resolution much higher compared to other existing clinical imaging modalities such as CT, MRI or PET.

Both the confocal reflectance and OCT image tissue based on such backscattered light and are able to detect tissue structural abnormalities by picking up changes in their light scattering behavior through refractive index mismatches in tissue. As such, they are well suited for examining superficial intraepithelial lesions. Several studies involving these imaging systems have reported promising applications in oncology such as the imaging of structural changes oral mucosa associated with carcinogenesis under a confocal endomicroscope [21], the detection of bladder cancer in small animal models [14] and the detection of oral cancer in animal models where OCT has shown to differentiate between tissues at different stages of malignancies [15].

Despite their advantages of doing away with biopsies and their ability to provide cellular resolution for imaging, the issues associated with phenotypic assessment of cellular features remains. As these optical systems rely on scattering processes in tissue to form images, they can be rather indiscriminate in highlighting diseased states [5]. Their modest optical contrast and specificity between normal and cancerous tissue especially those of early malignancies are often too low to be of any significant

clinical value [22-26]. Therefore, these imaging modalities may miss early stage carcinogenesis as the visual phenotypic cues for discrimination between non-malignant, pre-cancerous dysplastic and early carcinoma lesions are small. Changes associated with early stage carcinogenesis can be detected through molecular changes in tissue and these optical imaging modalities are unable to probe and image these early molecular abnormalities [27] which can provide crucial information for earlier and more accurate diagnosis of suspicious pre-cancerous lesions due to the detection limitations in their optics.

1.4 *In vivo* clinical molecular imaging

Molecular imaging sets forth to probe the molecular abnormalities in cancer biomarkers associated with carcinogenesis. These molecular changes usually precede any phenotypic changes which are a late manifestation of these molecular changes. Hence, while the phenotypic features of cancer may be absent in early stage pre-cancers, molecular changes such as genetic disturbances and receptor expression abnormalities are already present in these populations. They result in excess or reduced production of enzymatic or structural components of cells, or of factors regulating their production.

These early molecular signatures such as receptor expression abnormalities, which may remain present in small tumor populations, can provide critical information for earlier diagnosis of suspicious epithelial lesions compared to the later phenotypic changes [28]. Since these cancer-associated molecular markers precede phenotypic manifestations of disease, molecular imaging have the potential to base disease

detection on early molecular abnormalities before diseases become obvious with traditional anatomical-based imaging techniques.

While these molecular changes can be detected *in vitro* using immunohistochemical staining, they have yet to impact *in vivo* imaging mainly because the high-resolution optical imaging modalities are designed for imaging tissue structures rather than their intrinsic molecular events. However, with the current growing research interest in clinical molecular imaging, it is likely that in the near future, contrast agents targeted to molecular markers of disease will routinely provide molecular information that enables characterization of disease susceptibility long before pathologic changes occur at the anatomic level.

Molecular imaging requires a target cancer biomarker highly relevant to the pathology being examined. Amongst the wide range of cancer biomarkers investigated, the expression of Epidermal Growth Factor Receptor (EGFR) is a clinically relevant cancer biomarker often associated with epithelial type cancers. EGFR is encoded by the gene *c-erb*B-1, which is a prototype membrane of the type I transmembrane receptor tyrosine kinase found in cellular surface. The EGFR is a 170 kDa plasma membrane glycoprotein containing an extracellular ligand-binding domain, a single transmembrane region, a cytoplasmic domain which is composed of a tyrosine kinase domain and a C-terminal tail.

Since EGFR directs the initiation of processes such as growth, proliferation, apoptosis, adhesion, migration, and differentiation, it is related to the uncoupling of the growth program of cells from environmental signals. EGFR realize its function in

the initiation of cell growth processes when it is activated by the binding of the ligands EGF or TGFα to its external domain [29, 30]. Upon binding of a specific ligand to its extracellular ligand-binding domain, the EGFR receptor dimerizes or pair with another ErbB family member (see Figure 1.3 for the EGFR signaling pathway). This dimerization may be homodimerization (i.e. EGFR dimerizes with another EGFR) or heterodimerization (e.g. EGFR dimerizes with ErbB-2, ErbB-3, or ErbB-4) determined by the levels of each receptor, and the particular ligand bound to the receptor. This activation then results in phosphorylation of tyrosine amino acid residues in both receptors by the receptors' intrinsic tyrosine kinase activity, and subsequent cellular proliferation, transformation and division [31].

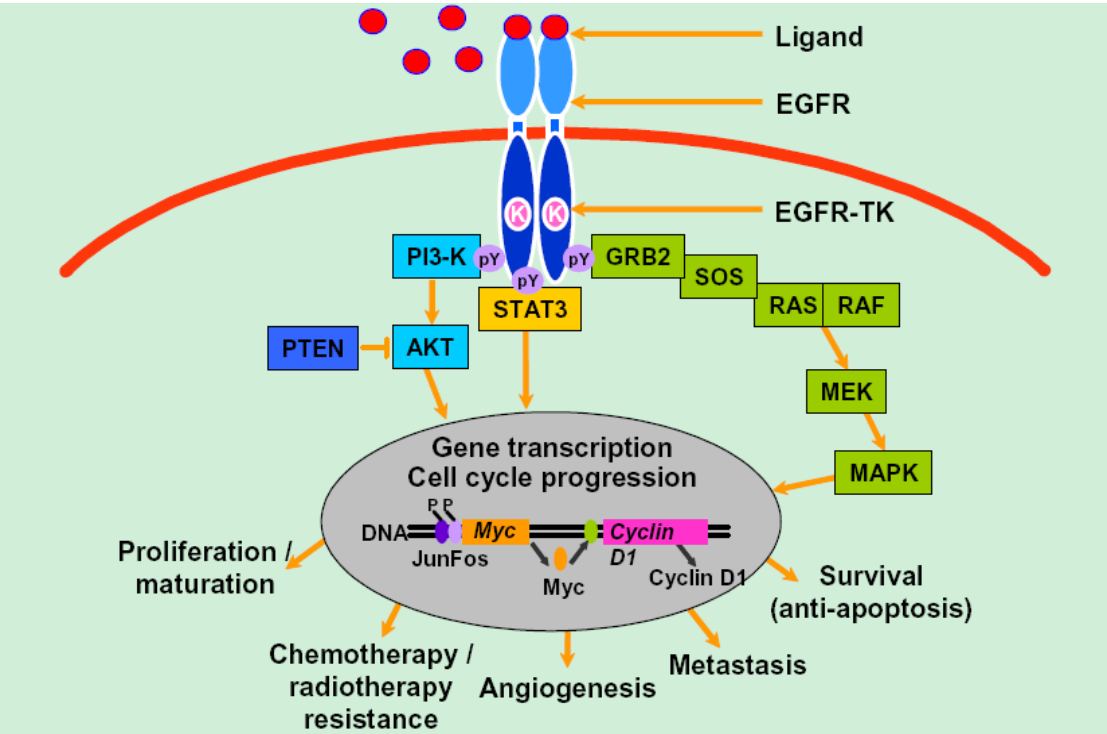

Figure 1.3. EGFR signaling transduction pathway in cancer cells.

Various 'adaptor' proteins, such as Shc and Grb2, are then recruited to the phosphorylated tyrosines, and transduce signals via major cell signaling pathways that

are comprised of signaling molecules such as the nitrogen-activated protein kinase (MAPK), and the p70 S6α kinase, and also multiple phosphoinositide 3-kinases (PI3K), protein kinase C (PKC), and the p70 S6β kinase. The sequential activation of these and other molecules transmit signals from the receptor dimers at the cell surface through particular pathways to, ultimately, the transcription machinery in the nucleus. The final aspect of the EGFR signaling process occurs with the receptor undergoing a conformational change (concomitant with ligand binding) that results in the exposure of motifs for endocytosis and degradation. The endocytosis of the receptor is the mechanism for down-regulation of signaling from the activated EGFR.

Overexpression, or increased abundance, of EGFR in cancers was first identified by investigators from LICR (Ludwig Institute for Cancer Research) who also have done dominant research in the EGFR area. EGFR is overexpressed in vast majority of epithelial cancers [32, 33]. EGFR expression in normal cells ranges from 40,000 to 100,000 receptors per cell [34]. In many cases, the number of EGFRs expressed in malignant cells is greater than that expressed in normal cells; up to 2×10^6 EGFRs per cell were reported in the human epidermoid carcinoma cells A-431 [35]. An ELISA analysis of the amount of EGFR in cell lysate of a few cancer cell lines belonging to two types of cancer i.e. nasopharyngeal carcinoma (NPC) and bladder carcinoma that are conducted by the author is also compared to normal human bronchial epithelium cells is shown in Figure 1.4. Compared to normal cells, the cancer cell lines all show higher EGFR expression in cell lysate.

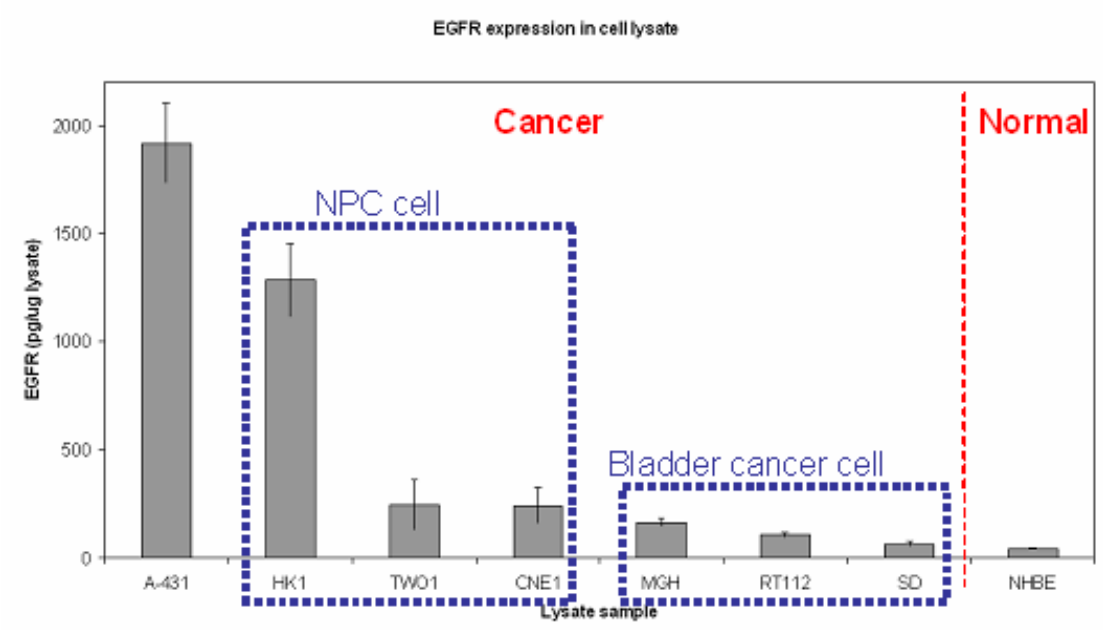

Figure 1.4. ELISA analysis of EGFR expression in cell lysate of a few cancer cell lines belonging to either the nasopharyngeal or bladder carcinoma family. The expression is compared to normal human bronchial epithelium (NHBE) cells which show much lesser EGFR expression. The EGFR expression for A-431 cells is shown as a positive control since A-431 is well known to have a high expression of EGFR.

EGFR overexpression is detected at all stages of carcinogenesis ranging from the premalignant early hyperplastic lesions to dysplasia and invasive carcinoma [36, 37]. In addition, EGFR expression is also known to be progressively elevated during the progression from hyperplasia to dysplasia to invasive carcinoma [38, 39]. Furthermore, EGFR expression is also elevated in normal epithelium that is adjacent to tumor [38].

Therefore, the ability to noninvasively image and assess the changes in EGFR expression in real time *in vivo* under high resolution reflectance-based optical imaging potentially holds several clinical implications for early cancer diagnosis that is based on molecular specific changes. It could translate into improved ability to detect early dysplastic changes leading to early detection of premalignant lesions and improved

diagnosis of cancer and reducing incidence of cancer in high-risk individuals. It could also potentially serve to monitor the progression of cancer. Also, with an image map of the expression level of relevant biomarker in early stage pre-cancerous lesions, rational treatment can be better prescribed, resulting in better patient management.

1.5 Optical coherence tomography

Amongst the different modalities in reflectance-based imaging, OCT is an emerging imaging modality that is gaining widespread attention in recent years [13]. It is a high resolution optical imaging system that can potentially be used to noninvasively image and assess molecular changes in real time *in vivo* with the aid of an appropriate contrast agent. It is based on the principle of low coherence interferometry [13, 40] using a low coherence NIR light source that produces cross-sectional images by measuring the time delays and magnitude of optical echoes of coherent light backscattered from tissue. OCT is analogous to acoustic ultrasonography except that instead of using reflected acoustic waves, it detects tissue abnormalities by picking up reflections of low coherence NIR light waves due to changes in backscattering of light arising from mismatches in refractive indices within the tissue sample [13, 41]. The basic OCT scheme is shown in Figure 1.5 below.

The key advantage of OCT in imaging is that it allows for high resolution cross-sectional tomographic imaging across a mucosal surface *in vivo* with a typical axial and lateral resolution of ≈ 10 and 25 μm respectively, although the resolution tends to decrease with depth. The OCT light source typically operates in the NIR region (800–1500 μm) where the scattering and absorption in tissue is minimal and the light

penetration in tissue is maximized to sufficiently pass through the mucosa to image tissue from the epithelium down to the serosa with depths of 2 to 3 mm *in situ*.

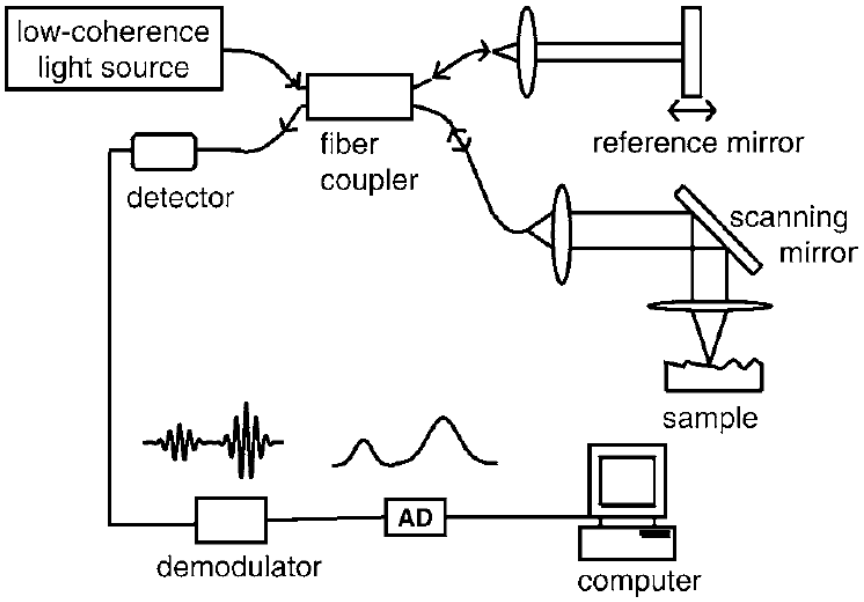

Figure 1.5. Typical setup of a basic time domain OCT system [27].

OCT is becoming a standard imaging modality in ophthalmology to image the retina and recent studies have shown promising applications for *in situ* oncological imaging specifically in bladder and gastroenterological applications to examine superficial epithelial-based tumors. Given its high resolution, OCT is able to perform an optical biopsy to image tissue microstructures *in vivo* with image quality comparable to conventional histopathology [14, 15, 40, 42, 43]. In fact, studies have shown that the structural features observed under the OCT correspond well to the stained morphological features in histology [44] as shown in Figure 1.6.

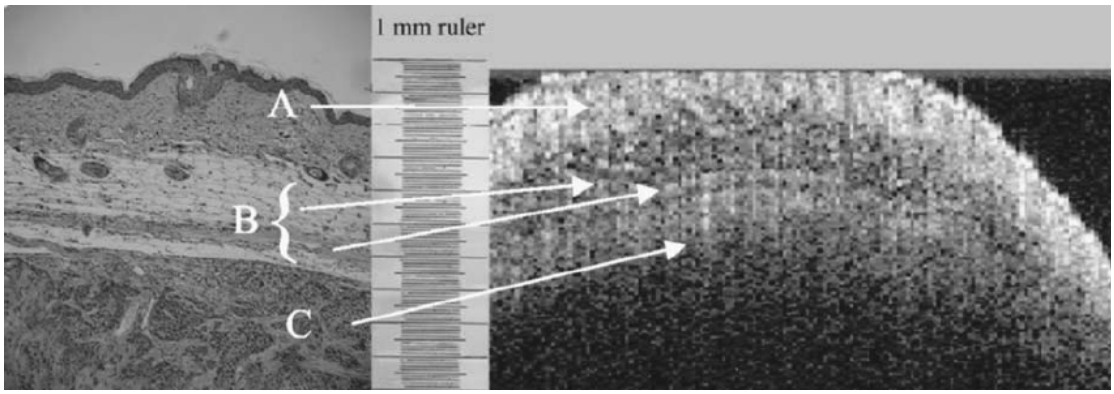

Figure 1.6. Histology image of untreated mouse skin with a subcutaneous tumor (left image), a ruler with a total length of 1 mm, and a representative OCT image (different location) is shown on the right image. Three different tissue layers in depth are indicated on the histology image: (A) skin, (B) connective tissue, and (C) tumor periphery consisting of the capsule and the upper part of the tumor, with arrows pointing to the same tissue layers in the OCT image to show the comparable correspondence between histology and OCT [45].

The ability to obtain high resolution images has led to several promising clinical applications in the diagnosis of cancers in real time [40, 42, 46-50] where OCT can be used to identify epithelial thickening and changes in stratification and structure of the mucosa during carcinogenesis [15, 51] without the need for tissue removal and sectioning. The use of OCT to image cancer in the hamster cheek pouch for different types of malignancy is shown in Figure 1.7 as an example. These tissue abnormalities that are observable under the OCT are usually associated with later stage carcinoma where the gross phenotypic changes are obvious compared to the subtle changes that are hardly observable in early stage carcinoma.

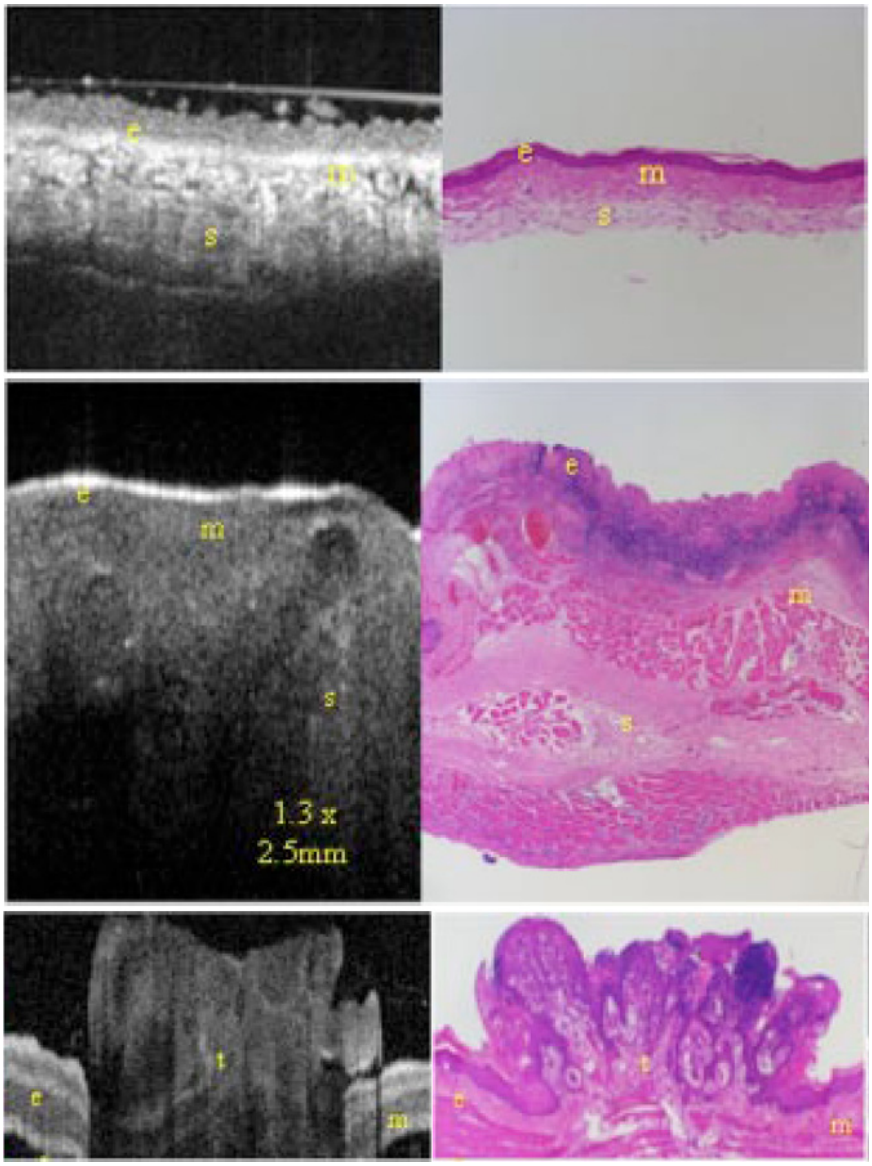

Figure 1.7. OCT image of a normal hamster cheek pouch versus H&E stained histological section (top). *In vivo* OCT image of cheek pouch with dysplasia versus the histological section (middle) where epithelial thickening, inflammation and increased cellular proliferation are evident. OCT image of hamster cheek pouch containing squamous cell carcinoma tumor versus histology (bottom). The labeling in the images are given by: e, squamous epithelium; m, mucosa; s, submucosa; t, fungiform malignant tissue; b, basement membrane [51].

The reason for the difficulty in picking up the changes is due to the OCT operating in reflectance mode. Optical contrast in reflectance is attributed to refractive index mismatches within the sample [40]. The image signal from tissue thus arises from spatial fluctuations in tissue refractive index, which are dependent on extracellular

matrix architecture and intracellular composition such as the density of organelles [52, 53]. Whilst the intrinsic OCT optical contrast in diseased state may arise from subcellular changes that alter light scattering such as increase in nuclear size, these optical change are usually similar amongst different tissue. Most pathological changes especially those associated with early stage carcinoma are usually not accompanied by an inherently strong endogenous contrast signal which can be imaged [23, 25]. Even though there are reports that demonstrate the use of OCT to identify phenotypic differences between normal and dysplastic tissue, the image contrast is often too modest to be of any significant clinical value.

Furthermore, many other valuable molecular indicators of tissue abnormalities do not generate obvious intrinsic optical contrast under the OCT and the coherence gating process underlying the formation of OCT images renders its detection of incoherent fluorescence processes impossible. This makes the OCT insensitive towards imaging molecular changes labeled with a fluorescence probe [27]. Their use for imaging of early molecular changes would thus require an alternative class of labelers that rely on elastic coherent light scattering and are compatible with the reflectance-based regime.

As with other optical imaging tools, the effectiveness of OCT in clinical imaging can be improved with appropriate contrast enhancement. Since OCT detects changes in optical scattering, image contrast enhancement can be achieved by delivery of contrast agents with good light scattering properties into the tissue and allowing them to localize in and change the light scattering property of specific region of interest. This image contrast enhancement can also be made specific to a relevant cancer biomarker i.e. EGFR for performing molecular imaging by using a target-specific

contrast agent which can target EGFR and elicit an image contrast to enhance the conspicuity of subtle pathologies for early detection of premalignant lesions.

1.6 Performing molecular contrast in OCT

Reflectance-based imaging of tissue is sensitive only to variations in refractive index within the tissue and molecular changes associated with pathophysiology do not result in these variations. Therefore, the ability of reflectance-based imaging to image cancer biomarkers is limited. Furthermore, the methods to elicit molecular contrast under an OCT are constrained by its coherent detection boundary of interferometry. The coherence gating process underlying the formation of OCT images renders their detection of incoherent fluorescence processes impossible. Therefore, fluorescent based contrast agents that are commonly used for molecular imaging in many optical imaging modalities cannot be detected in any OCT detection scheme since fluorescence is an incoherent optical process with no optical phase relationship with its excitation light field. This makes OCT insensitive towards imaging molecular changes labeled with a fluorescent contrast agent.

The use of OCT for *in situ* imaging of early molecular changes would therefore require alternative contrast agents that are compatible. Fortunately, various modified OCT schemes that show promise in imaging molecular changes with the aid of contrast agents have been reported to date and can be broadly categorized into three major groups. The first group of molecular contrast OCT schemes involves introducing contrast agents with a specific optically excitable absorption transition such as the pump-probe [54] and pump-suppression [55] molecular contrast OCT or a well-identified absorption spectrum in the target sample such as spectroscopic OCT

[56] and spectral triangulation MCOCT [57]. They rely on the changes in absorption spectrum of backscattered light to provide the contrast and are limited in their range of contrast agents and complex in instrumentation requirements.

The second group exploits coherent, nonlinear optical methods to identify endogenous molecular properties [58, 59] using contrast agents that can efficiently and coherently convert the incoming OCT illumination light field into an emission light field that is amendable to interferometry detection such as second harmonic OCT [60-62] and coherent anti-Stokes Raman scattering (CARS)-based contrast OCT [59]. These techniques are limited both in sensitivity and specificity [27].

The third group makes use of exogenous contrast agents that are able to alter the light scattering property of tissue to profile its distribution in the sample. The traditional way of improving the contrast in OCT images employs the use of osmotically active immersion liquids such as glycerol, propylene glycol, dextranes and concentrated glucose solution to cause a change in the tissue refractive index [63, 64]. This is improved with a new generation of contrast agents based on particle technologies due to their improved optical properties and ease of performing surface modifications. There are a few scattering-based particulate contrast agents reported to date such as the engineered oil-filled microspheres [65], air-filled microbubbles [66, 67], magnetic nanoparticles [68] and metallic nanostructures [26, 69-72]. These contrast agents have been developed to improve the OCT image by enhancing the intensity of backscattered light from the tissue. The improvement in optical contrast as demonstrated by these contrast agents is shown in Figure 1.8 below.

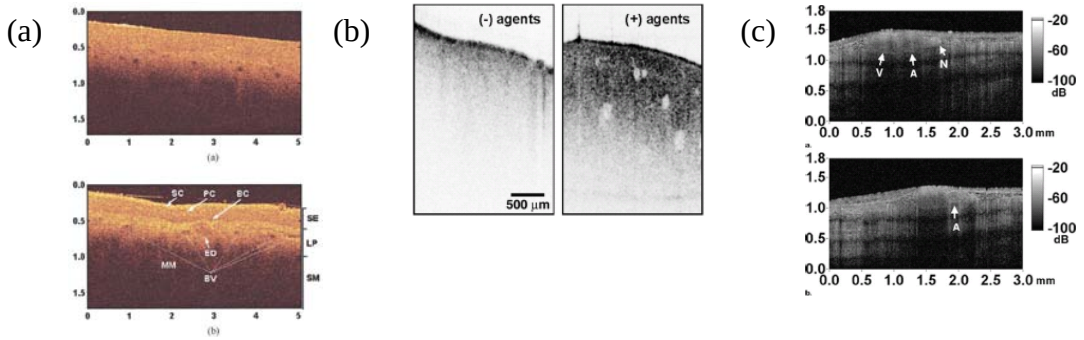

Figure 1.8. (a) OCT images of a normal human esophageal tissue without (top) and with (bottom) topical application of propylene glycol solution [64]. (b) OCT image enhancement with engineered microsphere contrast agents showing images of mouse liver (left) without and (right) with gold-shelled oil-filled microsphere contrast agents [65]. (c) OCT images obtained before (top) and after (bottom) injection of microbubbles [67].

These exogenous contrast agents are, in themselves, are nonspecific, but can be tagged to the relevant molecular markers with appropriate surface functionalization to perform molecular imaging. The advantage of using these scattering-based contrast agents is that their presence in tissue can create a sizable change in OCT signal without any complex modification to the existing OCT implementation.

Among these scattering-based contrast agents, metallic nanostructures have been the most widely investigated. Different types of metallic nanostructures with different shapes and metal composition having peak optical response over a broad range of wavelengths have recently been developed and investigated by several groups as promising contrast agents for reflectance-based imaging techniques due to their favorable optical properties. The peak optical response of some of these metallic nanostructures is shown in Figure 1.9.

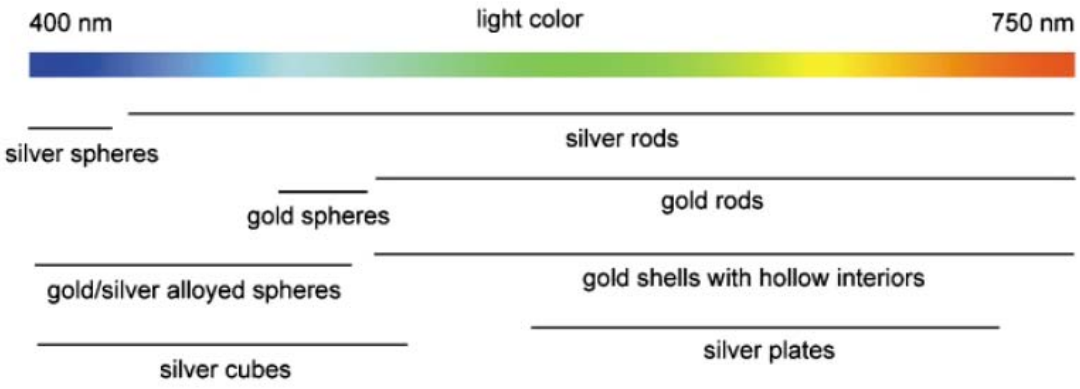

Figure 1.9. A list of silver and gold nanostructures having various morphologies, compositions, and structures, together with their typical locations of peak optical response in the visible regime [73].

Among these, gold nanostructures have been the most commonly used. The use of gold nanostructures as an OCT contrast agent with the potential to perform target-specific molecular contrast of EGFR expression for early cancer detection is examined in this thesis. For these contrast agents to be effective, three main considerations need to be addressed. Firstly, the contrast agent must be optically tuned and matched to the source wavelength of the OCT to provide an optimum scattering response to the system. Secondly, they must be functionalized with appropriate surface moieties not just to target and bind to the molecular target of interest to elicit the molecular contrast, but also to avoid immuno recognition and clearance from living systems. Thirdly, they must be sufficiently small to be efficiently delivered to the target tissue via the bloodstream.

1.7 Gold nanostructures as optical contrast agent in OCT

The use of several types of gold nanostructures such as solid gold nanoparticles [26], nanoshells [69, 72], nanocages [70] and nanorods [71] to address the limitations of reflectance-based imaging in biological imaging has been demonstrated [74, 75].

These nanostructures exhibit surface plasmon resonance (SPR) which allow them to resonantly scatter light when excited at their SPR frequency to create strong optical scattering signals for imaging [76, 77]. This optical scattering signal is much stronger compared to other non-metallic nanoparticles of similar size as shown in Figure 1.10.

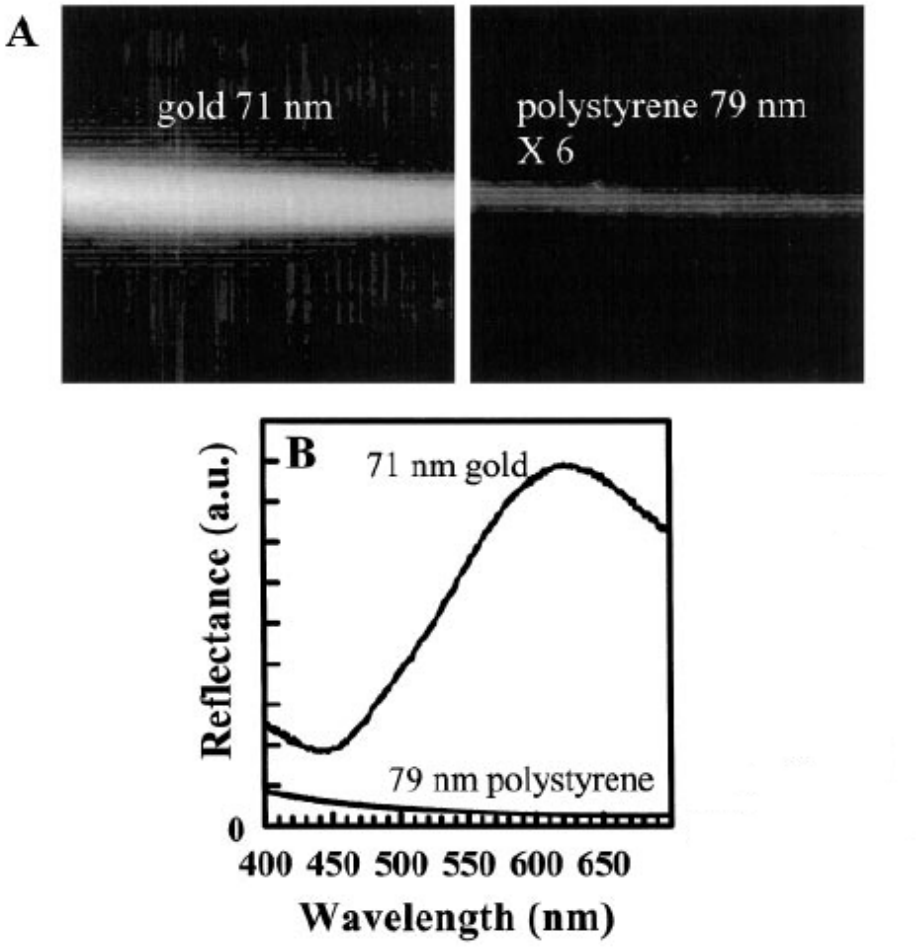

Figure 1.10. (A) and (B) compare scattering properties of gold particles and polystyrene beads of approximately the same diameter. In (A), suspensions of gold nanoparticles (left) and polymeric spheres (right) were illuminated by a laser pointer that provides light in the 630 – 680 nm region. The images were obtained using a regular web camera at a 90° angle relative to illumination. To acquire the images of both suspensions under the same conditions, the concentration of the polymeric beads (in particles/ml) was increased 6-fold relative to the concentration of the metal nanoparticles. (B) shows the wavelength dependence of visible light scattering by the polystyrene spheres and the gold nanoparticles. The spectra were obtained from suspensions with the same concentration of metal and polymeric nanospheres [26].

Gold nanostructures have been routinely used as optical labelers for electron microscopy and more recently, their use in reflectance-based molecular imaging has also been investigated. These gold nanostructures differ in their shape, size, composition and structure to give peak optical response at different spectral wavelength (Figure 1.9). Amongst the different types of gold nanostructures, gold nanoshells have been an emerging subject of recent research as their efficiency as an exogenous contrast agent for optical imaging of cells [72] and tissue phantoms [78] as well as a therapeutic agent for cancer [79] is well documented in recent years.

Gold nanoshells are a novel class of optically active metallodielectric concentric sphere nanostructure consisting of a spherical dielectric core, usually made of silica or polystyrene, surrounded by a thin gold shell of nanometer thickness [80-82]. They are generally easier to prepare compared to nanorods or nanocages and their synthesis is highly controlled. Their optical response is plasmonic in origin where the layer of gold allows these nanoparticles to exhibit surface plasmon resonance (SPR) in which the oscillating electron cloud in the gold shell interact with light to produce an optical response that resonantly scatters the light as illustrated in Figure 1.11 to produce a scattering cross section several times the particle geometric cross section in the NIR [83]. The scattering cross section is also much higher compared to other nanospheres of the same size but having different composition. Besides scattering, these particles can also absorb and convert light into thermal energy with excited at their SPR [84].

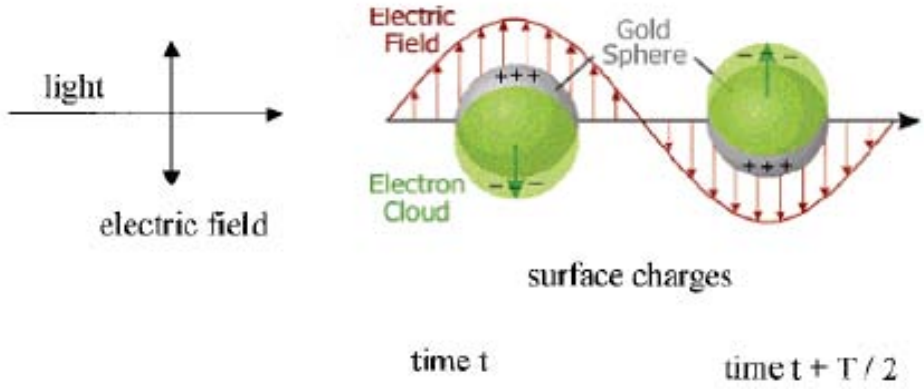

Figure 1.11. A scheme of surface plasmon absorption of spherical nanoparticles illustrating the excitation of the dipole surface plasmon oscillation to produce surface plasmon resonance when the excitation frequency matches the frequency of oscillation.

However, the main reason for the popularity of gold nanoshells in imaging lies in their unique core-shell nanostructure which allows a tunable optical response to match the excitation wavelength of many optical imaging systems. Unlike solid gold nanoparticles which possess a relatively invariable plasmon resonance peak at ≈ 520 nm, the peak optical response of gold nanoshells can be systematically tuned over a broad range of the optical spectrum from the visible right up to the near infrared (NIR) wavelengths [76]. This is done simply by changing the relative dimensions of the core size to shell thickness as well as the dielectric properties of the core and surrounding medium [85] as shown in Figure 1.12.

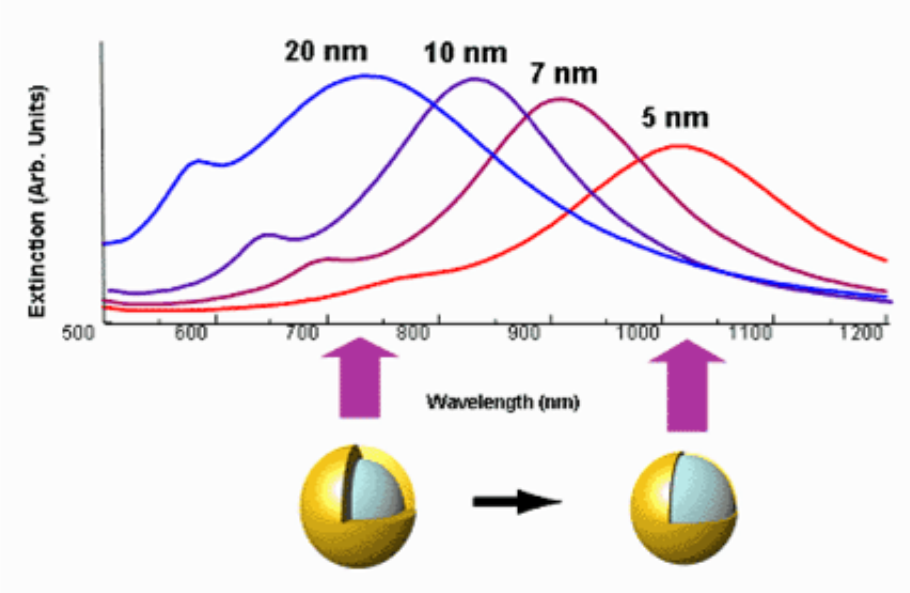

Figure 1.12. A Mie scattering plot of the plasmon resonance wavelength shift as a function of nanoshell composition. In this figure, the core and shell of the nanoparticles are depicted to relative scale directly beneath their corresponding optical resonances. For a core of a given size, forming thinner shells pushes the optical resonance to longer wavelengths [86].

The optical scattering properties of such structures coupled with their optical tunability have spur the use of gold nanoshells as a promising optical contrast agent where their optical response can be tuned to interact with light of a wide range of wavelengths, which includes the 750 – 800 nm optical window for biomedical imaging where tissue absorption of light is minimal to give rise to optimal light penetration as shown in Figure 1.13. This optical window includes the NIR region where the NIR scattering in tissue is also known to be weak. Gold nanoshells can thus be used to improve the SNR when used in the NIR region thus making them attractive as contrast agent in this wavelength range.

The wide range of light interaction also facilities the matching of gold nanoshells optical response to a range of light sources of different wavelengths used in different

promising clinical imaging modalities, especially those that operate in the NIR. These include the scatter-based darkfield imaging [72], optical coherence tomography (OCT) [81, 82, 87] and photoacoustic tomography (PAT) [88] for deep tissue imaging where the contrast between normal and pathological tissue is usually poor.

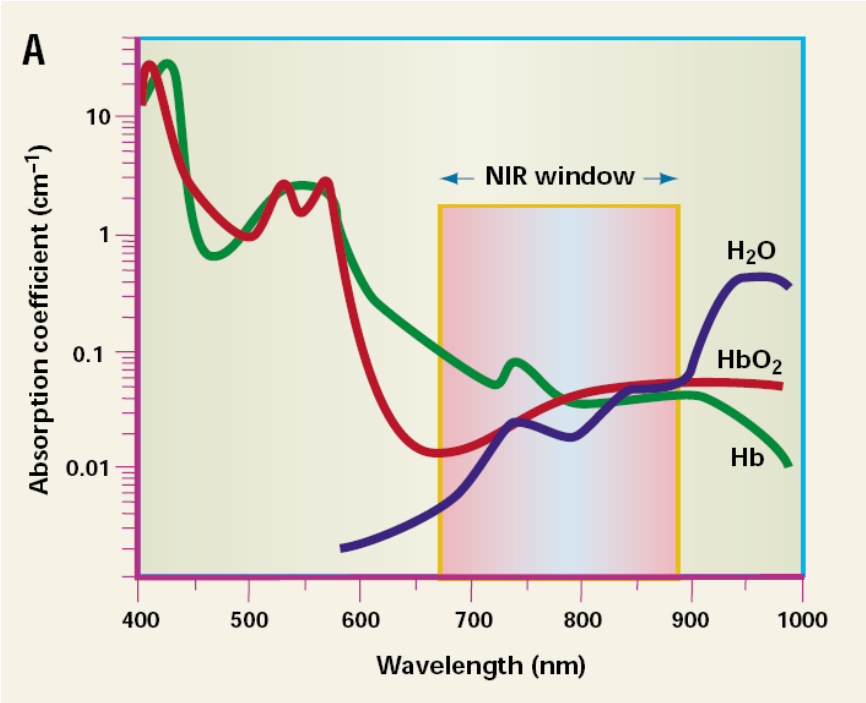

Figure 1.13. The NIR window is ideally suited for *in vivo* imaging because of minimal light absorption by hemoglobin (<650 nm) and water (>900 nm) [89].

Besides its spectral tunability, the relative contribution of the gold nanoshells optical extinction between scattering and absorption at a given wavelength can also be controlled by varying the absolute particle size [90]. Therefore, it is possible to engineer gold nanoshells to either primarily scatter light for imaging, or absorb and convert light into thermal energy to render them useful for photothermal therapy (PTT) applications such as the photothermal ablation of cancer cells. Such photothermal therapy offers a minimally invasive procedure to remove tumors providing an attractive option in situations where surgery is not possible. Several

studies using gold nanoshells immunotargeted to cancer cells have demonstrated effective destruction of the cancer cells upon exposure to NIR light, with cell damage limited to the laser treatment spot [79, 91-93] (See Figure 1.14).

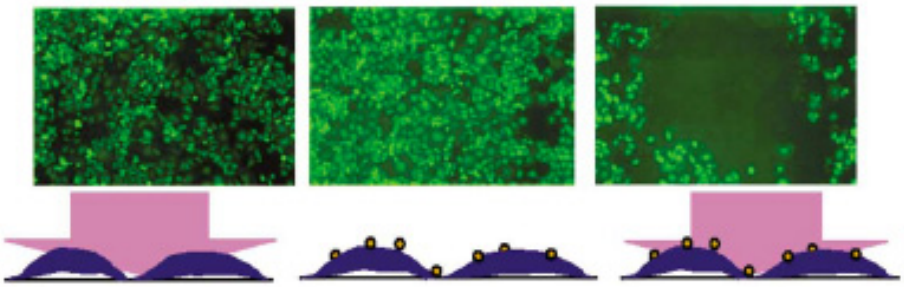

Figure 1.14. Calcein AM staining of cells (green fluorescence indicates cellular viability). Left: cells after exposure to laser only (no nanoshells). Middle: cells incubated with nanoshells but not exposed to laser light. Right: cell incubated with nanoshells after laser exposure. The dark circle seen in the image on the right corresponds to the region of cell death caused by exposure to laser light after incubation with nanoshells [81].

Apart from their optical properties, gold nanoshells also possess other favorable physicochemical properties for biomedical applications. Their rigid metallic structure makes them photostable and far less susceptible to chemical or thermal denaturation compared to many conventional fluorescent dyes. The surface of gold nanoshells can be readily functionalized with targeting moieties such as antibodies or peptides of interest for selective targeting to specific diseased sites to probe for specific proteins of clinical interest with high specificity and affinity [72, 81, 92, 94]. This is because the same conjugation protocols widely used to bind these biomolecules to colloidal gold can easily be modified for nanoshells.

Gold nanoshells can be designed to target to cancer biomarkers by conjugating them directly to antibodies using the simple non-covalent passive absorption or via linkers

with more robust coordinate bonds. Because of the ability of gold to form strong thiol and disulphide bonds, they can be attached to one end of the linkers bearing a thiol or disulphide group while the other end of the linker connect to the antibodies using amide bonds. Their coupling to appropriate biomarkers leads to the development of targeted contrast agents that provide useful optical signal to enable the competent imaging of cancer markers in tissue. Such molecular specific information may potentially assist clinicians by facilitating early molecular detection and diagnosis of pre-cancers [26, 71, 72].

The potential of gold nanoshells in biological applications have recently been demonstrated in several studies, including their use in molecular imaging, as contrast agents for OCT and also in photothermal therapeutic applications [72, 91, 92, 95]. Gold nanoshells with core made of microparticulate polymer beads or nanoparticulate silica have shown promise to enhance the optical contrast in OCT. Lee *et al.* reported the first demonstration of using gold nanoshells to improve the optical contrast in OCT by injecting oil-filled microspheres of diameter 0.2 to 2 μm surrounded by an approximate 50 nm thick gold shell into mice and imaging their liver to show an enhanced OCT signal compared to controls [65]. Gold nanoshells using silica as the core have also shown promise as non specific contrast agent in OCT [69]. The unique optical properties of gold nanoshells encourage further studies on their role as optically active agents in OCT.

1.8 Toxicity and clearance of gold nanostructures

Another reason for the popularity of gold in biological applications in that gold is also known to be biologically inert with excellent inherent biocompatibility [96, 97] in

living systems which renders them appropriate for biomedical applications. The use of gold in human subjects poses minimal toxicity as it has been approved by FDA for its medicinal uses as a dietary supplement as well as applied for long term clinical treatment of certain disease conditions such as rheumatoid arthritis [96, 98]. Despite their inert nature, it would still be worthwhile to mention some of the issues concerning the use of gold nanoparticles. Although the reported *in vitro* results on the use of gold nanoparticles seem promising, their use in the same manner *in vivo* would warrant attention to the challenges in the way these nanoparticles could potentially elicit any body response and subsequently be eliminated from the body system with minimal side effects after their diagnostic use.

Previous studies by other groups have shown that these gold nanoparticles tend to be taken up by the cells through endocytosis as fast as 1 h into the incubation with gold nanoparticles [97]. In most cases with antibody targeting, the antibody binding to cell surface receptor could potentially provide a receptor-mediated endocytosis route for the gold nanoparticles. Connor and colleagues examined a series of gold nanoparticles for cellular uptake and acute cytotoxicity in human leukemia cells and found that despite being taken up into the cells, spherical gold nanoparticles with a variety of surface modifiers were not inherently toxic to human cells [97]. Mukherjee et al have also shown that gold nanoparticles have no effect on gene expression or other global transcriptional pattern of human umbilical vein endothelial cells (HUVEC) [99].

Although tests on other forms of body response in terms of cellular adhesion effects, local biological effects or other systemic and remote effects have not been widely reported, previous literatures have shown that gold nanoparticles are sufficiently inert

to be injected to living animals without major complications. The small size of these particles enables them to extravasate out of the microcirculation easily and diffuse through the interstitial compartments of tissue efficiently. Without proper surface functionalization, most of the circulating nanoparticles will be trapped by reticuloendothelial system in liver, kidney, spleen and lungs and may remain there and in other tissue for a long time without interfering with metabolism of cells, although a small amount may be secreted to the bile or urine [100, 101].

Whilst metal poisoning is often associated with renal and hepatic toxicities, Mukherjee et al. have determined the effect of gold nanoparticles administration on liver and renal function on mice and found that there were no significant differences between serum levels of creatinine, blood urea nitrogen, bilirubin alkaline phosphatase, alanine aminotransferase, and aspartate aminotransferase between gold nanoparticles treated and untreated control animals after 7 days of administration, thus concluding minimal effect of gold nanoparticles in renal and hepatic functioning [102]. Despite the fact that gold nanoparticles have been injected to many patients in the past to treat rheumatoid arthritis or to study the function of reticuloendothelial system based on the past three decades of literature, there are only a few, if any, reports on complications of intravenous gold injection [103].

1.9 Hypothesis

The hypothesis behind this thesis is that the unique physico-optical properties of gold nanostructures can be optimized to enhance the optical contrast between normal and suspicious lesions as well as to perform molecular-specific contrast imaging of EGFR expression in these lesions for early cancer detection *in vivo* under reflectance-based

OCT. The hypothesis is based on the following observations. First, gold nanostructures can be engineered to strongly scatter or absorb light at frequencies coinciding with their surface plasmon resonances for imaging or photothermal conversion. Second, their surface plasmon resonance can be optically tuned and matched to the source wavelength of the optical imaging system to provide an optimum optical response. Third, gold nanostructures can easily be surface functionalized with a wide range of surface moieties such as antibodies to target and localize in cancerous tissue while avoiding the surrounding normal tissue as well as to avoid immuno recognition. Fourth, a rational selection of appropriate targeting moiety allows these nanoparticulates to probe and map the molecular expression of specific cancer biomarkers up to the cellular level. Lastly, gold nanostructures can be made sufficiently small to be efficiently delivered to the target tissue via the bloodstream.

1.10 Objective and organization of thesis

The main objective of the work presented in this thesis is to develop surface functionalized gold nanostructures with optimized optical properties and further investigate on three main aspects of their applications as cancer-specific optical contrast agents in reflectance-based imaging: 1. Their ability to enhance the optical signal under this form of imaging, 2. Their effectiveness in improving the optical contrast for discrimination between normal and suspicious pathological conditions, and 3. their potential in performing molecular specific imaging of EGFR expression in these pathological conditions for early cancer detection *in vivo*.

This thesis adopts a broad multidisciplinary approach towards the development of an appropriate optical agent and the understanding of their applications in imaging over a

wide range of biological models. The scope of this thesis includes a theoretical understanding of the optical properties of spherical gold nanoparticles and nanoshells that leads to a prediction of an appropriate particle dimension to achieve an optimized optical response based on the theoretical framework as discussed in Chapter 2. The preliminary study on the use of gold nanoparticles to improve optical contrast is then demonstrated in Chapter 3. Chapter 4 then follows with a detailed description on the synthesis of gold nanoshells based on the predicted dimensions provided in Chapter 2 and Chapter 5 gives an account of the characterization studies on their surface functionalization in the form of pegylation to reduce their immunogenicity *in vivo* and anti-EGFR conjugation to confer specific targeting on the particles.

The three main aspects of their applications as optical contrast agents as described earlier are also examined in three different models, namely, an *in vitro* cellular model, a phantom model and an *in vivo* small animal tumor model under two different types of reflectance-based imaging i.e. the confocal reflectance microscopy and OCT. The ability of gold nanostructures to elicit an optical contrast to discriminate cancer from normal cells under the confocal reflectance microscope *in vitro* is demonstrated in Chapter 6. Chapter 7 examines the changes in OCT signal against theoretical OCT models with different concentration of gold nanoshells in a tissue phantom while Chapter 8 describes the investigation on the control of optical contrast provided by gold nanoshells in a mouse xenograft tumor model. In addition to the main thrust of this thesis in imaging, a small scope of this thesis is also set aside to assess the potential photothermal therapeutic efficacy of gold nanoshells in combination with conventional photodynamic therapy (PDT) *in vitro* in Chapter 9. The last Chapter 10 gives the conclusion and future direction of this work documented in this thesis.

1.11 References

1. Crow P, Stone N, Kendall CA, Persad RA, Wright MP. Optical diagnostics in urology: current applications and future prospects. *BJU Int* 2003; 92(4): 400-407.

2. Lumerman H, Freedman P, Kerpel S. Oral epithelial dysplasia and the development of invasive squamous cell carcinoma. *Oral Surg Oral Med Oral Pathol Oral Radiol Endod* 1995; 79(3): 321-329.

3. Spafford MF, Koch WM, Reed AL, Califano JA, Xu LH, Eisenberger CF, Yip L, Leong PL, Wu L, Liu SX, Jeronimo C, Westra WH, Sidransky D. Detection of head and neck squamous cell carcinoma among exfoliated oral mucosal cells by microsatellite analysis. *Clin Cancer Res* 2001; 7(3): 607-612.

4. Blasberg RG. Molecular imaging and cancer. *Mol Cancer Ther* 2003; 2(3): 335-343.

5. Wickline SA, Lanza GM. Molecular imaging, targeted therapeutics, and nanoscience. *J Cell Biochem Suppl* 2002; 39: 90-97.

6. Olivo M, Lau W, Manivasager V, Bhuvaneswari R, Wei Z, Soo KC, Cheng C, Tan PH. Novel photodynamic diagnosis of bladder cancer: ex vivo fluorescence cytology using hypericin. *Int J Oncol* 2003; 23(6): 1501-1504.

7. Sim HG, Lau WK, Olivo M, Tan PH, Cheng CW. Is photodynamic diagnosis using hypericin better than white-light cystoscopy for detecting superficial bladder carcinoma? *BJU Int* 2005; 95(9): 1215-1218.

8. Zheng W, Lau W, Cheng C, Soo KC, Olivo M. Optimal excitation-emission wavelengths for autofluorescence diagnosis of bladder tumors. *Int J Cancer* 2003; 104(4): 477-481.

9. Kah JCY, Lau WKO, Tan PH, Sheppard CJR, Olivo M. Endoscopic Image Analysis of Photosensitizer Fluorescence as a Promising Noninvasive Approach for Pathological Grading of Bladder Cancer In Situ. *J Biomed Opt* 2008; 14(5).

10. Collier T, Guillaud M, Follen M, Malpica A, Richards-Kortum R. Real-time reflectance confocal microscopy: comparison of two-dimensional images and three-dimensional image stacks for detection of cervical precancer. *J Biomed Opt* 2007; 12(2): 024021.

11. Scope A, Gill M, Benveuto-Andrade C, Halpern AC, Gonzalez S, Marghoob AA. Correlation of dermoscopy with in vivo reflectance confocal microscopy of streaks in melanocytic lesions. *Arch Dermatol* 2007; 143(6): 727-734.

12. Yoshida S, Tanaka S, Hirata M, Mouri R, Kaneko I, Oka S, Yoshihara M, Chayama K. Optical biopsy of GI lesions by reflectance-type laser-scanning confocal microscopy. *Gastrointest Endosc* 2007; 66(1): 144-149.

13. Huang D, Swanson EA, Lin CP, Schuman JS, Stinson WG, Chang W, Hee MR, Flotte T, Gregory K, Puliafito CA, et al. Optical coherence tomography. *Science* 1991; 254(5035): 1178-1181.

14. Xie T, Zeidel M, Pan Y. Detection of tumorigenesis in urinary bladder with optical coherence tomography: optical characterization of morphological changes. *Opt. Express* 2002; 10(24): 1431-1443.

15. Wilder-Smith P, Jung WG, Brenner M, Osann K, Beydoun H, Messadi D, Chen Z. In vivo optical coherence tomography for the diagnosis of oral malignancy. *Lasers Surg Med* 2004; 35(4): 269-275.

16. Fujimoto JG, Brezinski ME, Tearney GJ, Boppart SA, Bouma B, Hee MR, Southern JF, Swanson EA. Optical biopsy and imaging using optical coherence tomography. *Nat Med* 1995; 1(9): 970-972.

17. Hoffman A, Goetz M, Vieth M, Galle PR, Neurath MF, Kiesslich R. Confocal laser endomicroscopy: technical status and current indications. *Endoscopy* 2006; 38(12): 1275-1283.

18. Gibson AP, Hebden JC, Arridge SR. Recent advances in diffuse optical imaging. *Phys Med Biol* 2005; 50(4): R1-43.

19. White WM, Baldassano M, Rajadhyaksha M, Gonzalez S, Tearney GJ, Anderson RR, Fabian RL. Confocal reflectance imaging of head and neck surgical specimens. A comparison with histologic analysis. *Arch Otolaryngol Head Neck Surg* 2004; 130(8): 923-928.

20. Rajadhyaksha M, Grossman M, Esterowitz D, Webb RH, Anderson RR. In vivo confocal scanning laser microscopy of human skin: melanin provides strong contrast. *J Invest Dermatol* 1995; 104(6): 946-952.

21. Zheng W, Harris M, Kho KW, Thong PS, Hibbs A, Olivo M, Soo KC. Confocal endomicroscopic imaging of normal and neoplastic human tongue tissue using ALA-induced-PPIX fluorescence: a preliminary study. *Oncol Rep* 2004; 12(2): 397-401.

22. Manfrini O, Mont E, Leone O, Arbustini E, Eusebi V, Virmani R, Bugiardini R. Sources of error and interpretation of plaque morphology by optical coherence tomography. *Am J Cardiol* 2006; 98(2): 156-159.

23. Ebert B, Sukowski U, Grosenick D, Wabnitz H, Moesta KT, Licha K, Becker A, Semmler W, Schlag PM, Rinneberg H. Near-infrared fluorescent dyes for enhanced contrast in optical mammography: phantom experiments. *J Biomed Opt* 2001; 6(2): 134-140.

24. Koenig F, Knittel J, Stepp H. Diagnosing cancer in vivo. *Science* 2001; 292(5520): 1401-1403.

25. Troy TL, Page DL, Sevick-Muraca EM. Optical properties of normal and diseased breast tissues: prognosis for optical mammography. *Journal of Biomedical Optics* 1996; 1(3): 342-355.

26. Sokolov K, Follen M, Aaron J, Pavlova I, Malpica A, Lotan R, Richards-Kortum R. Real-time vital optical imaging of precancer using anti-epidermal growth factor receptor antibodies conjugated to gold nanoparticles. *Cancer Res* 2003; 63(9): 1999-2004.

27. Yang C. Molecular contrast optical coherence tomography: a review. *Photochem Photobiol* 2005; 81(2): 215-237.

28. Sokolov K, Aaron J, Hsu B, Nida D, Gillenwater A, Follen M, MacAulay C, Adler-Storthz K, Korgel B, Descour M, Pasqualini R, Arap W, Lam W, Richards-Kortum R. Optical systems for in vivo molecular imaging of cancer. *Technol Cancer Res Treat* 2003; 2(6): 491-504.

29. Adamson ED, Rees AR. Epidermal growth factor receptors. *Mol Cell Biochem* 1981; 34(3): 129-152.

30. Massague J. Epidermal growth factor-like transforming growth factor. II. Interaction with epidermal growth factor receptors in human placenta membranes and A431 cells. *J Biol Chem* 1983; 258(22): 13614-13620.

31. Partanen AM. Epidermal growth factor and transforming growth factor-alpha in the development of epithelial-mesenchymal organs of the mouse. *Curr Top Dev Biol* 1990; 24: 31-55.

32. Eisbruch A, Blick M, Lee JS, Sacks PG, Gutterman J. Analysis of the epidermal growth factor receptor gene in fresh human head and neck tumors. *Cancer Res* 1987; 47(13): 3603-3605.

33. Ke LD, Adler-Storthz K, Clayman GL, Yung AW, Chen Z. Differential expression of epidermal growth factor receptor in human head and neck cancers. *Head Neck* 1998; 20(4): 320-327.

34. Walker F, Orchard SG, Jorissen RN, Hall NE, Zhang HH, Hoyne PA, Adams TE, Johns TG, Ward C, Garrett TP, Zhu HJ, Nerrie M, Scott AM, Nice EC, Burgess AW. CR1/CR2 interactions modulate the functions of the cell surface epidermal growth factor receptor. *J Biol Chem* 2004; 279(21): 22387-22398.

35. Fabricant RN, De Larco JE, Todaro GJ. Nerve growth factor receptors on human melanoma cells in culture. *Proc Natl Acad Sci U S A* 1977; 74(2): 565-569.

36. Kannan S, Balaram P, Chandran GJ, Pillai MR, Mathew B, Nair MK. Co-expression of ras p21 and epidermal growth factor receptor during various stages of tumour progression in oral mucosa. *Tumour Biol* 1994; 15(2): 73-81.

37. Nouri AM, Thompson C, Cannell H, Symes M, Purkiss S, Amirghofran Z. Profile of epidermal growth factor receptor (EGFr) expression in human malignancies: effects of exposure to EGF and its biological influence on established human tumour cell lines. *Int J Mol Med* 2000; 6(4): 495-500.

38. Shin DM, Ro JY, Hong WK, Hittelman WN. Dysregulation of epidermal growth factor receptor expression in premalignant lesions during head and neck tumorigenesis. *Cancer Res* 1994; 54(12): 3153-3159.

39. Todd R, Wong DT. Epidermal growth factor receptor (EGFR) biology and human oral cancer. *Histol Histopathol* 1999; 14(2): 491-500.

40. Tearney GJ, Brezinski ME, Bouma BE, Boppart SA, Pitris C, Southern JF, Fujimoto JG. In vivo endoscopic optical biopsy with optical coherence tomography. *Science* 1997; 276(5321): 2037-2039.

41. Boppart SA, Bouma BE, Pitris C, Tearney GJ, Southern JF, Brezinski ME, Fujimoto JG. Intraoperative assessment of microsurgery with three-dimensional optical coherence tomography. *Radiology* 1998; 208(1): 81-86.

42. Sergeev A, Gelikonov V, Gelikonov G, Feldchtein F, Kuranov R, Gladkova N, Shakhova N, Snopova L, Shakhov A, Kuznetzova I, Denisenko A, Pochinko V, Chumakov Y, Streltzova O. In vivo endoscopic OCT imaging of precancer and cancer states of human mucosa. *Opt. Express* 1997; 1(13): 432-440.

43. Boppart SA, Brezinski ME, Pitris C, Fujimoto JG. Optical coherence tomography for neurosurgical imaging of human intracortical melanoma. *Neurosurgery* 1998; 43(4): 834-841.

44. Boppart SA, Luo W, Marks DL, Singletary KW. Optical coherence tomography: feasibility for basic research and image-guided surgery of breast cancer. *Breast Cancer Res Treat* 2004; 84(2): 85-97.

45. Aalders MC, Triesscheijn M, Ruevekamp M, de Bruin M, Baas P, Faber DJ, Stewart FA. Doppler optical coherence tomography to monitor the effect of photodynamic therapy on tissue morphology and perfusion. *J Biomed Opt* 2006; 11(4): 044011.

46. Pitris C, Goodman A, Boppart SA, Libus JJ, Fujimoto JG, Brezinski ME. High-resolution imaging of gynecologic neoplasms using optical coherence tomography. *Obstet Gynecol* 1999; 93(1): 135-139.

47. Jesser CA, Boppart SA, Pitris C, Stamper DL, Nielsen GP, Brezinski ME, Fujimoto JG. High resolution imaging of transitional cell carcinoma with optical coherence tomography: feasibility for the evaluation of bladder pathology. *Br J Radiol* 1999; 72(864): 1170-1176.

48. Pan Y, Lavelle JP, Bastacky SI, Meyers S, Pirtskhalaishvili G, Zeidel ML, Farkas DL. Detection of tumorigenesis in rat bladders with optical coherence tomography. *Med Phys* 2001; 28(12): 2432-2440.

49. Tearney GJ, Brezinski ME, Southern JF, Bouma BE, Boppart SA, Fujimoto JG. Optical biopsy in human urologic tissue using optical coherence tomography. *J Urol* 1997; 157(5): 1915-1919.

50. Brezinski ME, Tearney GJ, Bouma BE, Izatt JA, Hee MR, Swanson EA, Southern JF, Fujimoto JG. Optical coherence tomography for optical biopsy. Properties and demonstration of vascular pathology. *Circulation* 1996; 93(6): 1206-1213.

51. Matheny ES, Hanna NM, Jung WG, Chen Z, Wilder-Smith P, Mina-Araghi R, Brenner M. Optical coherence tomography of malignancy in hamster cheek pouches. *J Biomed Opt* 2004; 9(5): 978-981.

52. Beauvoit B, Chance B. Time-resolved spectroscopy of mitochondria, cells and tissues under normal and pathological conditions. *Mol Cell Biochem* 1998; 184(1-2): 445-455.

53. Beauvoit B, Kitai T, Chance B. Contribution of the mitochondrial compartment to the optical properties of the rat liver: a theoretical and practical approach. *Biophys J* 1994; 67(6): 2501-2510.

54. Rao KD, Choma MA, Yazdanfar S, Rollins AM, Izatt JA. Molecular contrast in optical coherence tomography by use of a pump probe technique. *Opt. Lett.* 2003; 28(5): 340-342.

55. Yang C, Choma MA, Lamb LE, Simon JD, Izatt JA. Protein-based molecular contrast optical coherence tomography with phytochrome as the contrast agent. *Opt. Lett.* 2004; 29(12): 1396-1398.

56. Xu C, Ye J, Marks DL, Boppart SA. Near-infrared dyes as contrast-enhancing agents for spectroscopic optical coherence tomography. *Opt. Lett.* 2004; 29(14): 1647-1649.

57. Yang C, McGuckin LEL, Simon JD, Choma MA, Applegate B, Izatt JA. Spectral triangulation molecular contrast optical coherence tomography with indocyanine green as the contrast agent. *Opt. Lett.* 2004; 29(17): 2016-2018.

58. Marks DL, Boppart SA. Nonlinear interferometric vibrational imaging. *Phys Rev Lett* 2004; 92(12): 123905.

59. Vinegoni C, Bredfeldt J, Marks D, Boppart S. Nonlinear optical contrast enhancement for optical coherence tomography. *Opt. Express* 2004; 12(2): 331-341.

60. Jiang Y, Tomov I, Wang Y, Chen Z. Second-harmonic optical coherence tomography. *Opt. Lett.* 2004; 29(10): 1090-1092.

61. Yazdanfar S, Laiho L, So P. Interferometric second harmonic generation microscopy. *Opt. Express* 2004; 12(12): 2739-2745.

62. Applegate BE, Yang C, Rollins AM, Izatt JA. Polarization-resolved second-harmonic-generation optical coherence tomography in collagen. *Opt. Lett.* 2004; 29(19): 2252-2254.

63. Bashkatov AN, Genina EA, Sinichkin YP, Tuchin VV: The influence of glycerol on the transport of light in the skin *Proceedings of SPIE - The International Society for Optical Engineering* 2002; 4623:144-152.

64. Wang RK, Elder JB. Propylene glycol as a contrasting agent for optical coherence tomography to image gastrointestinal tissues. *Lasers in Surgery and Medicine* 2002; 30(3): 201-208.

65. Lee TM, Oldenburg AL, Sitafalwalla S, Marks DL, Luo W, Toublan FJ, Suslick KS, Boppart SA. Engineered microsphere contrast agents for optical coherence tomography. *Opt Lett* 2003; 28(17): 1546-1548.

66. Christiansen C, Kryvi H, Sontum PC, Skotland T. Physical and biochemical characterization of Albunex, a new ultrasound contrast agent consisting of air-filled albumin microspheres suspended in a solution of human albumin. *Biotechnol Appl Biochem* 1994; 19 (Pt 3): 307-320.

67. Barton JK, Hoying JB, Sullivan CJ. Use of microbubbles as an optical coherence tomography contrast agent. *Acad Radiol* 2002; 9 Suppl 1: S52-55.

68. Oldenburg AL, Gunther JR, Boppart SA. Imaging magnetically labeled cells with magnetomotive optical coherence tomography. *Opt. Lett.* 2005; 30(7): 747-749.

69. Barton JK, Halas NJ, West JL, Drezek RA: Nanoshells as an optical coherence tomography contrast agent *Proceedings of SPIE - The International Society for Optical Engineering* 2004; 5316:99-106.

70. Chen J, Saeki F, Wiley BJ, Cang H, Cobb MJ, Li ZY, Au L, Zhang H, Kimmey MB, Li X, Xia Y. Gold nanocages: bioconjugation and their potential use as optical imaging contrast agents. *Nano Lett* 2005; 5(3): 473-477.

71. Huang X, El-Sayed IH, Qian W, El-Sayed MA. Cancer cell imaging and photothermal therapy in the near-infrared region by using gold nanorods. *J Am Chem Soc* 2006; 128(6): 2115-2120.

72. Loo C, Hirsch L, Lee MH, Chang E, West J, Halas N, Drezek R. Gold nanoshell bioconjugates for molecular imaging in living cells. *Opt Lett* 2005; 30(9): 1012-1014.

73. Sun Y, Xia Y. Gold and silver nanoparticles: a class of chromophores with colors tunable in the range from 400 to 750 nm. *Analyst* 2003; 128(6): 686-691.

74. Akerman ME, Chan WC, Laakkonen P, Bhatia SN, Ruoslahti E. Nanocrystal targeting in vivo. *Proc Natl Acad Sci U S A* 2002; 99(20): 12617-12621.

75. Gao X, Cui Y, Levenson RM, Chung LW, Nie S. In vivo cancer targeting and imaging with semiconductor quantum dots. *Nat Biotechnol* 2004; 22(8): 969-976.

76. Oldenburg SJ, Jackson JB, Westcott SL, Halas NJ. Infrared extinction properties of gold nanoshells. *Applied Physics Letters* 1999; 75(19): 2897-2899.

77. Hao E, Li S, Bailey RC, Zou S, Schatz GC, Hupp JT. Optical Properties of Metal Nanoshells. *J. Phys. Chem. B* 2004; 108(4): 1224-1229.

78. Zagaynova EV, Shirmanova MV, Orlova AG, Balalaeva IV, Kirillin MY, Kamensky VA, Bugrova ML, Sirotkina MA: Gold nanoshells for OCT imaging contrast: From model to in vivo study *Progress in Biomedical Optics and Imaging - Proceedings of SPIE* 2008; 6865.

79. Stern JM, Stanfield J, Kabbani W, Hsieh JT, Cadeddu JA. Selective prostate cancer thermal ablation with laser activated gold nanoshells. *J Urol* 2008; 179(2): 748-753.

80. Averitt RD, Sarkar D, Halas NJ. Plasmon Resonance Shifts of Au-Coated Au2S Nanoshells: Insight into Multicomponent Nanoparticle Growth. *Physical Review Letters* 1997; 78(22): 4217 LP - 4220.

81. Loo C, Lin A, Hirsch L, Lee MH, Barton J, Halas N, West J, Drezek R. Nanoshell-enabled photonics-based imaging and therapy of cancer. *Technol Cancer Res Treat* 2004; 3(1): 33-40.

82. Hirsch LR, Gobin AM, Lowery AR, Tam F, Drezek RA, Halas NJ, West JL. Metal nanoshells. *Ann Biomed Eng* 2006; 34(1): 15-22.

83. Averitt RD, Westcott SL, Halas NJ. Linear optical properties of gold nanoshells. *J. Opt. Soc. Am. B* 1999; 16(10): 1824-1832.

84. Mulvaney P. Surface Plasmon Spectroscopy of Nanosized Metal Particles. *Langmuir* 1996; 12(3): 788-800.

85. Oldenburg SJ, Averitt RD, Westcott SL, Halas NJ. Nanoengineering of optical resonances. *Chemical Physics Letters* 1998; 288(2-4): 243-247.

86. West JL, Halas NJ. Engineered nanomaterials for biophotonics applications: improving sensing, imaging, and therapeutics. *Annu Rev Biomed Eng* 2003; 5: 285-292.

87. Gobin AM, Lee MH, Halas NJ, James WD, Drezek RA, West JL. Near-infrared resonant nanoshells for combined optical imaging and photothermal cancer therapy. *Nano Lett* 2007; 7(7): 1929-1934.

88. Wang Y, Xie X, Wang X, Ku G, Gill KL, O'Neal DP, Stoica G, Wang LV. Photoacoustic Tomography of a Nanoshell Contrast Agent in the in Vivo Rat Brain. *Nano Lett.* 2004; 4(9): 1689-1692.

89. Weissleder R. A clearer vision for in vivo imaging. *Nat Biotechnol* 2001; 19(4): 316-317.

90. Oldenburg SJ, Hale GD, Jackson JB, Halas NJ. Light scattering from dipole and quadrupole nanoshell antennas. *Applied Physics Letters* 1999; 75(8): 1063-1065.

91. Hirsch LR, Stafford RJ, Bankson JA, Sershen SR, Rivera B, Price RE, Hazle JD, Halas NJ, West JL. Nanoshell-mediated near-infrared thermal therapy of tumors under magnetic resonance guidance. *Proc Natl Acad Sci U S A* 2003; 100(23): 13549-13554.

92. Loo C, Lowery A, Halas N, West J, Drezek R. Immunotargeted nanoshells for integrated cancer imaging and therapy. *Nano Lett* 2005; 5(4): 709-711.

93. Stern JM, Stanfield J, Lotan Y, Park S, Hsieh JT, Cadeddu JA. Efficacy of laser-activated gold nanoshells in ablating prostate cancer cells in vitro. *J Endourol* 2007; 21(8): 939-943.

94. Paciotti GF, Myer L, Weinreich D, Goia D, Pavel N, McLaughlin RE, Tamarkin L. Colloidal gold: a novel nanoparticle vector for tumor directed drug delivery. *Drug Deliv* 2004; 11(3): 169-183.

95. Agrawal A, Huang S, Wei Haw Lin A, Lee MH, Barton JK, Drezek RA, Pfefer TJ. Quantitative evaluation of optical coherence tomography signal enhancement with gold nanoshells. *J Biomed Opt* 2006; 11(4): 041121.

96. West JL, Halas NJ. Applications of nanotechnology to biotechnology commentary. *Curr Opin Biotechnol* 2000; 11(2): 215-217.

97. Connor EE, Mwamuka J, Gole A, Murphy CJ, Wyatt MD. Gold nanoparticles are taken up by human cells but do not cause acute cytotoxicity. *Small* 2005; 1(3): 325-327.

98. Abrams MJ, Murrer BA. Metal compounds in therapy and diagnosis. *Science* 1993; 261(5122): 725-730.

99. Mukherjee P, Bhattacharya R, Patra CR. Nanogold in Cancer Therapy and Diagnosis. In: Kumar CSSR, ed. Nanomaterials for Cancer Diagnosis, ed. 1st, vol. 7 Weinheim: WILEY-VCH Verlag GmbH & Co. KGaA, 2006:86-120.

100. Eghtedari M, Oraevsky A, Copland JA, Kotov NA, Conjusteau A, Motamedi M. High sensitivity of in vivo detection of gold nanorods using a laser optoacoustic imaging system. *Nano Lett* 2007; 7(7): 1914-1918.

101. Copland JA, Eghtedari M, Popov VL, Kotov N, Mamedova N, Motamedi M, Oraevsky AA. Bioconjugated gold nanoparticles as a molecular based contrast agent: implications for imaging of deep tumors using optoacoustic tomography. *Mol Imaging Biol* 2004; 6(5): 341-349.

102. Mukherjee P, Bhattacharya R, Wang P, Wang L, Basu S, Nagy JA, Atala A, Mukhopadhyay D, Soker S. Antiangiogenic properties of gold nanoparticles. *Clin Cancer Res* 2005; 11(9): 3530-3534.

103. Gumpel JM. The role of radiocolloids in the treatment of arthritis. *Rheumatol Rehabil* 1974; 13(1): 1-9.

CHAPTER TWO

OPTICAL PROPERTIES OF GOLD NANOSTRUCTURES

Abstract

The theoretical approach based on Mie theory to describe the optical properties of two types of gold nanostructures: homogenous spherical gold nanoparticles and gold nanoshells with a core-shell structure is discussed in this chapter. These optical properties include their optical scattering ability, optical tunability and optical extinction modes. Based on this theoretical examination, various optical parameters of gold nanoshells i.e. their optical extinction, scattering, absorption, backscattering efficiencies and cross-sections are also calculated and subsequently used to provide a theoretical plot of their optical spectra for different sizes and to select an optimized size for imaging. The backscattering cross section is selected as an appropriate metric for which the design of gold nanoshells is optimized against. The theoretical results demonstrate that gold nanostructures inherently possess stronger optical scattering compared to dielectric nanoparticles of same size and that their peak optical resonance and optical extinction mode can be tuned by their physical dimensions. The extinction peak shifts to longer wavelengths as the size of the gold nanoparticle is increased while the shell thickness to core radius ratio of gold nanoshells is decreased. The theoretical prediction also suggests that the gold nanoshells synthesized with a silica core radius of 81 nm and gold shell thickness of 23 nm would provide an optimum backscattering response under OCT with source wavelength of 840 nm. This work has been submitted for publication in *Optics Communications*.

2.1 Introduction

Nanoparticles composing of coinage metals such as copper, silver and gold present unique optical properties. When excited with an electromagnetic field, these nanoparticles produce an intense interaction with light in the form of scattering or absorption attributed to the collective oscillation of electrons on the particle surface, termed as surface plasmon resonance. The resonant frequency is highly dependent on particle size, shape, material, and environment. By altering these characteristics, the frequency can be shifted over a wide range of wavelengths, making them attractive as functional materials for many applications including electronic and optical devices [1], chemical and biological sensors [2-5], optical energy transport [6-8], thermal ablation [9] and contrast agents in optical imaging which is the subject of interest in this thesis.

The synthesis of uniform colloidal gold nanoparticles has been widely reported for some time. New experimental techniques have recently produced core-shell nanoparticles with a consistent size and shape [10-13]. A strong surface plasmon resonance is observed when the layered nanoparticle is composed of silica and gold, which can be shifted in wavelength by adjusting the relative thickness of the shell and core material. The concentric sphere geometry of the nanoparticles also allows for control of their optical properties in a highly predictive manner, making them a new class of materials that are capable of tailoring radiation throughout the visible and infrared wavelength regimes [12, 13].

The nanoparticle optical extinction is typically measured. Extinction is the sum of absorption and scattering. Classical electrodynamics accurately describes the

scattering and absorption of electromagnetic waves by particles in this nanometer-size regime. Scattering arises when charged particles are accelerated by a field and reradiate. Hence, light scattering is the secondary radiation scattered by the induced oscillatory motion of protons/electrons within an obstacle when illuminated by a light source. Absorption occurs when the particle takes energy out of the beam and converts it to other forms. The equations that govern macroscopic electromagnetic fields that give rise to scattering and absorption are known as Maxwell's Equations. These laws of electromagnetic theory express the behavior of the electric and magnetic portions of a field, as well as the relationship between the two. Maxwell's Equations for a field varying harmonically in time are

$$\nabla \cdot E = 0$$

$$\nabla \cdot H = 0$$

$$\nabla \times E = i\omega\mu H$$

$$\nabla \times H = -i\omega\varepsilon E\,, \qquad (2.1)$$

where E is the electric field, H is the magnetic field, ω is the angular frequency, μ is the permeability, and ε is the permittivity (dielectric constant).

The optical properties of a nanosphere of arbitrary radius and dielectric constant can be defined within Maxwell's Equations. In that sense, Mie was the first to provide the solutions to the scattering and absorption by homogeneous spheres which are commonly referred to as Mie Theory [14]. Excellent descriptions of Mie Scattering are also given by van de Hulst [15] and by Bohren and Huffman [16]. Since then several papers have appeared that refine and extent the theory for non-symmetrical

particles, sphere with inclusions[16-18] and particles with radially variable refractive indices, commonly called the n-layer problem [18-22], of which gold nanoshells can be classified under. However, for the solutions provided in these literatures, some of the expressions therein are not explicit.

The problem which Mie solutions attempt to solve lies in finding the electromagnetic field at all points in the particle and medium given the particle radius and dielectric constant. The solutions are subject to the boundary condition that the fields must be continuous when crossing between the particle and the medium. All fields are expanded in vector spherical harmonics. The polarization of the incident field, boundary conditions, and orthogonality of the basis dictate the expansions. Once the fields are known, the optical properties of the particle can be calculated from the scattered field in the far field regime.

The applications of the Mie functions in this thesis are directed toward the study of the optical properties of two types of spherical gold nanostructures: homogenous spherical gold nanoparticles and gold nanoshells with a core-shell structure. While there have been numerous papers published on the optical properties of spherical gold nanoparticles (both experimental and theoretical), the number of theoretical studies on dielectric materials coated with gold is relatively much fewer. This chapter attempts to fill the void by providing a detail discussion on the optical properties of these two types of gold nanostructures based on the theoretical approach.

In this chapter, the theoretical description of their optical properties based on Mie theory is discussed. This theoretical description is used to compute their optical

response in terms of different optical parameters such as the extinction, scattering and backscattering efficiencies and their corresponding cross-sections. From the computed efficiencies, the theoretical optical spectrum for each of the parameter can be predicted and characterized for changes in the particle sizes. Amongst these optical parameters, the backscattering cross section is selected as an appropriate parameter to be used to design and optimize the dimensions of gold nanoshells as suitable reflectance-based optical probe that would provide the best optical response for confocal reflectance microscopy and OCT imaging. Based on the theoretical prediction, the backscattering cross sectional response of gold nanoshells is also computed for different size configurations to select an optimized size appropriate for OCT imaging.

The Mie theoretical framework for the scattering and absorption of gold nanostructures described in this chapter is implemented as programs written in the numeric computation and visualization software, MATLAB (Math Works, 1992). Functions have been developed to compute their Mie coefficients as well as optical parameters which include the extinction, scattering and backscattering efficiencies and their corresponding cross-sections. The present programs are largely related to the formalism of Bohren and Huffman [16] which is described in more details in the following sections.

2.2 Mie solution for spherical gold nanostructures

2.2.1 Mie coefficients for homogenous gold nanoparticles

The key parameters for Mie calculations of the scattered field are the Mie coefficients a_n and b_n of the nanoparticle which are used to compute the optical efficiencies and cross sections of the nanoparticle. The coefficients of the scattered electrical field for a spherically homogeneous nanoparticle are given below.

$$a_n = \frac{m^2 j_n(mx)[xj_n(x)]' - \mu_1 j_n(x)[mxj_n(mx)]'}{m^2 j_n(mx)[xh_n^{(1)}(x)]' - \mu_1 h_n^{(1)}(x)[mxj_n(mx)]'}; \quad (2.2)$$

$$b_n = \frac{\mu_1 j_n(mx)[xj_n(x)]' - j_n(x)[mxj_n(mx)]'}{\mu_1 j_n(mx)[xh_n^{(1)}(x)]' - h_n^{(1)}(x)[mxj_n(mx)]'} \quad (2.3)$$

where m is the refractive index of the nanoparticle relative to the ambient medium. In the subsequent calculations, the ambient medium refers to water, so m takes on the refractive index of gold relative to water. The size parameter is given by $x = kr$, r is the radius of the sphere, $k = 2\pi/\lambda$ is the wave number and λ the wavelength of the incident light source in the ambient medium. μ_1 is the ratio of the magnetic permeability of the sphere to the magnetic permeability of the ambient medium. The Index n runs from 1 to ∞, but the infinite series occurring in Mie formulas can be truncated at a maximum, n_{max} given by $n_{max} = x + 4x^{1/3} + 2$.

The functions $j_n(z)$ and $h_n^{(1)}(z) = j_n(z) + iy_n(z)$ are spherical Bessel functions and spherical Hankel functions of order n (n = 1, 2,…) respectively and of the given arguments, $z = x$ or mx. As observed from its definition, the spherical Hankel functions are linear combinations of j_n and y_n and in the case of Mie calculations, the

first type is required. The superscript primes mean derivatives with respect to the argument and they follow from the spherical Bessel functions themselves, namely

$$[zj_n(z)]' = zj_{n-1}(z) - nj_n(z);\ [zh_n^{(1)}(z)]' = zh_{n-1}^{(1)}(z) - nh_n^{(1)}(z) \tag{2.4}$$

The computation of the two Mie coefficients is the most challenging in Mie computations due to the involvement of these spherical Bessel functions up to high order. The computation has so far worked well up to $x = 10^4$ using the built-in double-precision Bessel functions in MATLAB. However, there is a maximum x value for stable and correct computation of Mie scattering. For a small or moderate imaginary refractive index m'', the maximum size parameter ranges somewhere between 10^4 and 10^5, but for $m'' >> 1$, the maximum size parameter is strongly diminished.

For completeness, the following relationships between ordinary Bessel and spherical Bessel functions are given:

$$j_n(z) = \sqrt{\frac{\pi}{2z}} J_{n+0.5}(z);\ y_n(z) = \sqrt{\frac{\pi}{2z}} Y_{n+0.5}(z) \tag{2.5}$$

Here, $J_v(z)$ and $Y_v(z)$ are ordinary Bessel functions of the first and second kind and are standard functions which can be found in MATLAB. For $n = 0$ and 1, the spherical Bessel functions are simply given by

$$j_0(z) = \frac{\sin z}{z};\ j_1(z) = \frac{\sin z}{z^2} - \frac{\cos z}{z};\ y_0(z) = -\frac{\cos z}{z};\ y_1(z) = -\frac{\cos z}{z^2} - \frac{\sin z}{z} \tag{2.6}$$

The recurrence formula can be used to obtain higher orders

$$f_{n-1}(z) + f_{n+1}(z) = \frac{2n+1}{z} f_n(z);\ (2n+1)[f_n(z)]' = nf_{n-1}(z) - (n+1) f_{n+1}(z) \qquad (2.7)$$

where f_n denotes either of the Bessel functions j_n or y_n.

As the gold nanoparticles is non-magnetic i.e. $\mu_1 = 1$, this means that the permittivity of the nanoparticle relative to the ambient medium is given by $\varepsilon = m^2$. In this case, equations 2.2 and 2.3 simplify to the expressions below which can be computed from the programs written in MATLAB.

$$a_n = \frac{m^2 j_n(mx)[xj_n(x)]' - j_n(x)[mxj_n(mx)]'}{m^2 j_n(mx)[xh_n^{(1)}(x)]' - h_n^{(1)}(x)[mxj_n(mx)]'}; \qquad (2.8)$$

$$b_n = \frac{j_n(mx)[xj_n(x)]' - j_n(x)[mxj_n(mx)]'}{j_n(mx)[xh_n^{(1)}(x)]' - h_n^{(1)}(x)[mxj_n(mx)]'} \qquad (2.9)$$

2.2.2 Mie coefficients for core-shell gold nanoshells

Similar equations can also be used to calculate the Mie coefficients of core-shell nanoparticles. The approach is the same, except the system is now slightly more complex. There are two radii and two refractive indices that must be included. This corresponds to one set for the core material and one set for the shell material. In addition, there are two boundary conditions imposed to account for the core, shell, and medium. The expressions for the Mie coefficients are more difficult to compute; once known, however, they can be inserted into Equation 2.18 - 2.20 to yield the optical efficiencies. The Mie Coefficients a_n and b_n of inhomogeneous core-shell structures are used in the same way as the ones for homogeneous nanoparticles to

compute their optical efficiencies and cross sections. The problem for core-shell nanostructures is adequately described in Figure 2.1.

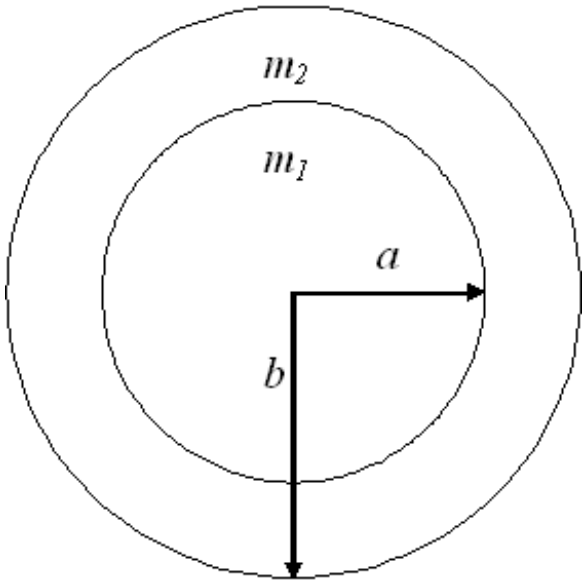

Figure 2.1. A core-shell nanostructure with two compartments placed radially symmetric around the core showing the geometry used in Mie calculations. The core has radius a and relative refractive index m_1 and a total nanoparticle radius b with the shell layer having a relative refractive index m_2.

In general, there are two compartments placed radially symmetric around the core. The core-shell structure has an inner core radius a with size parameter $x = ka$ ($k = 2\pi/\lambda$ is the wave number, with λ being the wavelength of the incident light source in the ambient medium as before) and m_1 is the refractive index of the core relative to the ambient medium. The outer shell has an outer radius b with relative refractive index m_2 and size parameter $y = kb$. In computing the Mie coefficients, the assumption is that the core and the shell material of gold nanoshells are non-magnetic and as such, the magnetization of the particle is governed by the magnetization of the ambient medium and the magnetic permeability between the particle and the medium is unchanged i.e. $\mu_{medium} = \mu_{core} = \mu_{shell}$. The explicit expressions used to compute the Mie coefficients are as follow:

$$a_n = \frac{(\tilde{D}_n / m_2 + n/y)\psi_n(y) - \psi_{n-1}(y)}{(\tilde{D}_n / m_2 + n/y)\xi_n(y) - \xi_{n-1}(y)}; \tag{2.10}$$

$$b_n = \frac{(m_2\tilde{G}_n + n/y)\psi_n(y) - \psi_{n-1}(y)}{(m_2\tilde{G}_n + n/y)\xi_n(y) - \xi_{n-1}(y)} \tag{2.11}$$

where the functions $\tilde{D}_n$ and $\tilde{G}_n$ are defined as below.

$$\tilde{D}_n = \frac{D_n(m_2 y) - A_n\chi_n'(m_2 y)/\psi_n(m_2 y)}{1 - A_n\chi_n(m_2 y)/\psi_n(m_2 y)}; \tag{2.12}$$

$$\tilde{G}_n = \frac{D_n(m_2 y) - B_n\chi_n'(m_2 y)/\psi_n(m_2 y)}{1 - B_n\chi_n(m_2 y)/\psi_n(m_2 y)} \tag{2.13}$$

$$A_n = \psi_n(m_2 x)\frac{mD_n(m_1 x) - D_n(m_2 x)}{mD_n(m_1 x)\chi_n(m_2 x) - \chi_n'(m_2 x)}; \tag{2.14}$$

$$B_n = \psi_n(m_2 x)\frac{D_n(m_1 x)/m - D_n(m_2 x)}{D_n(m_1 x)\chi_n(m_2 x)/m - \chi_n'(m_2 x)} \tag{2.15}$$

Now $m = \frac{m_2}{m_1}$ and the functions $\psi_n(z) = zj_n(z)$ and $\chi_n(z) = -zy_n(z)$ follow the Riccati-Bessel function of the first and second kind respectively, while the function $\xi_n(z) = zh_n^{(1)}(z)$ follows the Hankel function [23]. The derivatives χ_n' is given by the recurrence relations $\chi_n'(z) = \chi_{n-1}(z) - \frac{n\chi_n(z)}{z}$. Also, D_n is the logarithmic derivative of $\psi_n(z)$ given by $D_n(z) = \frac{d}{dz}\ln\psi_n(z) = \frac{\psi_n'(mx)}{\psi_n(mx)} = \frac{[mx \cdot j_n(mx)]'}{mx \cdot j_n(mx)}$. The function $D_n(z)$ is computed by downward recurrence relation:

$$D_{n-1}(z) = \frac{n}{z} - \frac{1}{D_n(z) + n/z} \tag{2.16}$$

An important consideration to be made is the number of terms a_n and b_n required for convergence. The convergence criterion derived for the homogenous gold nanoparticles as described earlier is used [16] as there is no evidence in the literature that this criterion is flawed for inhomogeneous core-shell structures. In effect, the maximum number of terms n_{max} to be calculated follows the schema

$$n_{\max} = \begin{cases} y + 4y^{1/3} + 1, & x \in [0.02,8] \\ y + 4.05y^{1/3} + 2, & x \in (8,4200] \\ y + 4y^{1/3} + 2, & x \in (4200,20000] \end{cases} \tag{2.17}$$

However, it has been indicated in many publications that even if only the criterion $y + 4.05y^{1/3} + 2$ is used, the difference in the results is negligible [24].

2.2.3. Mie efficiencies and cross sections

The optical efficiencies Q_i for the interaction of light with a scattering particle of radius r are given by their optical cross sections σ_i normalized to the particle geometrical cross section, $\sigma_g = \pi r^2$, where i stands for extinction ($i = ext$), absorption ($i = abs$), scattering ($i = sca$) and backscattering ($i = b$), thus $Q_i = \frac{\sigma_i}{\pi r^2}$. These efficiencies are dimensionless cross sections in their true meaning. For example, the extinction efficiency denoted by Q_{ext} may be interpreted as defined measurable

quantity of the 'shadow' of area σ_{ext} that may be casted on a detector by a particle. This is to say a particle will reduce detector area by σ_{ext} with an efficiency Q_{ext}.

Equations 2.2 and 2.3 in conjunction with Equation 2.17, can be used to determine the extinction (Q_{ext}), scattering (Q_{sca}), and backscattering (Q_b) efficiencies and as such their corresponding cross sections. The scattering efficiency Q_{sca} follows from the integration of the scattered power over all directions, and the extinction efficiency Q_{ext} follows from the Extinction Theorem [15, 25], also called Forward-Scattering Theorem. These two, together with the backscattering efficiency Q_b are given by

$$Q_{ext} = \frac{2}{x^2}\sum_{n=1}^{\infty}(2n+1)\,\mathrm{Re}(a_n + b_n) \tag{2.18}$$

$$Q_{sca} = \frac{2}{x^2}\sum_{n=1}^{\infty}(2n+1)(|a_n|^2 + |b_n|^2) \tag{2.19}$$

$$Q_b = \frac{1}{x^2}\left|\sum_{n=1}^{\infty}(2n+1)(-1)^n(a_n - b_n)\right|^2 \tag{2.20}$$

where x is the overall size parameter and Re denotes the real part of the resulting complex number ($a_n + b_n$). Note that the expressions above are applicable for both the homogeneous gold nanoparticles and inhomogeneous gold nanoshells with core-shell structure. As before in the case of Mie coefficients, the index n runs from 1 to ∞, but the infinite series occurring in Mie formulas can be truncated after n_{max} terms as given by $n_{max} = x + 4x^{1/3} + 2$ as discussed earlier in Equation 2.17.

Energy conservation requires that $Q_{ext} = Q_{sca} + Q_{abs}$, or $\sigma_{ext} = \sigma_{sca} + \sigma_{abs}$. Thus the absorption efficiency Q_{abs} can be approximated as $Q_{abs} \approx Q_{ext} - Q_{sca}$. Note that the condition $C_{abs} \leq C_{ext}$ must always be satisfied.

2.3 Materials and methods

2.3.1 Theoretical prediction of optical spectrum

Based on the Mie theoretical framework discussed earlier in the previous section, a set of Mie functions has been developed in MATLAB that computes the Mie coefficients a_n and b_n, anisotropy factor, g, efficiencies of extinction, scattering and backscattering and their corresponding cross-sections for homogeneous gold nanoparticles as well as the core-shell gold nanoshells. The theoretically predicted optical spectrum is then plotted by another program written in MATLAB using the optical efficiencies computed for each quantum increment in wavelength over a range of wavelength from visible to NIR.

The required input parameters to these functions include the size parameters, $x = ka$ and $y=kb$ where a and b are the sphere inner and outer radius as described earlier in Figure 2.1. Another input is the complex refractive indices, $m = m' + im''$ of the core and shell relative to the ambient medium. In this case, the refractive index of the silica core is assumed to be a constant at m_{silica} = 1.43 [13, 26] and the embedding medium is taken to be water with m_{water} = 1.33 [12, 27]. The frequency-dependent complex refractive index of gold is obtained from previously published experimental data [28, 29] which have been smoothed and interpolated as shown in Figure 2.2. The last input is the information about the incident light source; namely the wavelength.

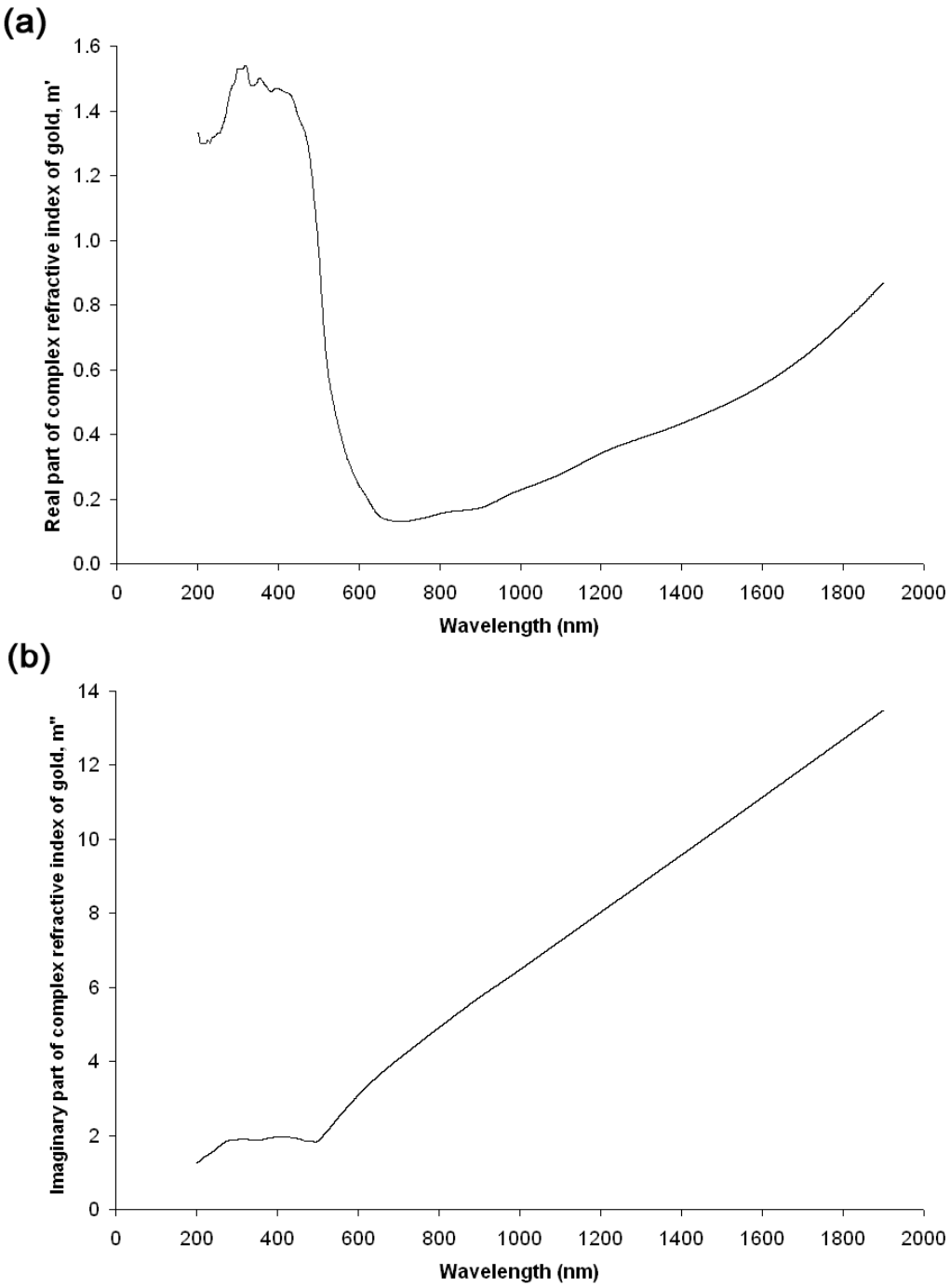

Figure 2.2. (a) Real part and (b) imaginary part of the frequency-dependent complex refractive index of gold as a function of wavelength.

2.3.2 Determination of optimum gold nanoshells dimension

To select gold nanoshells with optical properties that provide the best signal enhancement in OCT, various optical parameters of gold nanoshells over a range of physical dimensions are calculated using the computed solutions to Mie theory as described earlier for an excitation wavelength of 840 nm. This is the source wavelength of the OCT system used in this study. The calculations are based on a single gold nanoshell for simplification. The bulk effects due to particle heterogeneities are not considered as the heterogeneity in a population of gold nanoshells is assumed to be low. For each optical parameter such as extinction, scattering, absorption and backscattering of gold nanoshells, the optical cross section which is the product of the optical efficiency and geometrical cross section is computed as a function of core radius and shell thickness over a size range which can be readily synthesized with current laboratory methods.

The calculated optical parameters over a range of core radii and shell thicknesses are then converted to a color-coded core radius-to-shell thickness space-maps of optical cross sections used to aid in the selection of gold nanoshells with suitable optical response. The backscattering cross section parameter is selected as an appropriate metric for predicting the OCT signal and thereby using it as a criterion for selecting the gold nanoshells to be used in this study since the backscattering of light is the basis in which the OCT images are generated. Based on the backscattering cross section space map, the dimension of gold nanoshells that produced the largest backscattering cross section is selected for further experimental investigations to be discussed in more details in subsequent chapters.

2.4 Results and discussion

2.4.1 Optical tunability of gold nanoparticles

The extinction spectrum of a solid gold nanoparticle has been calculated using Mie Theory as described in section 2.2.1 and 2.2.3. This consists of calculating the extinction efficiency from Equation 2.18 at many different wavelengths. The extinction spectrum for several nanoparticle radii can be seen in Figure 2.3.

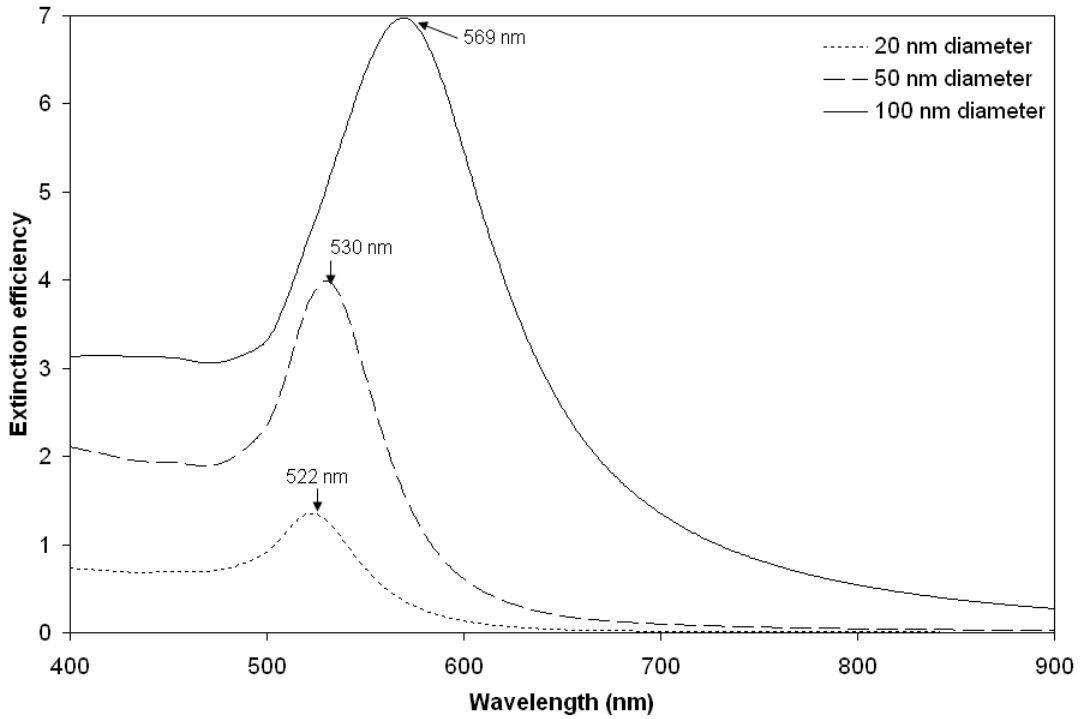

Figure 2.3. Extinction efficiency of spherical gold nanoparticles of varying radii. The values indicated are the wavelengths corresponding to the peak extinction.

The wavelength corresponding to maximum extinction shifts to longer wavelengths (red shift) as the size of the nanoparticle increases. The peak seen at 522 nm corresponds to the resonance condition for small gold nanoparticles, specifically, when $\mathrm{Re}\{\varepsilon\} = -2\varepsilon_{med}$, where the dielectric constant of medium water

is $\varepsilon_{med} = m_{water}^2 = 1.769$. This in turn corresponds to a gold nanoparticle size of 20 nm. As the size increases to 50 nm and 100 nm, the extinction peak red shifts to 530 nm and 569 nm respectively. Although this extinction peak varies with size, its sensitivity towards size variations remains poor within this size range commonly used in biological applications as the peak hardly red shifts by more than 50 nm even as the size of the nanoparticle increases fivefold.

A large red shift of the dipole peak and a much more complex spectrum occur when the particle radius is increased further, as seen in Figure 2.4. A 200 nm gold nanoparticle displays a broadened dipole peak at 765 nm. Also evident is the appearance of a quadrupole peak at 561 nm. The higher-order modes in the field expansion become important as the nanoparticle becomes larger. This results in the appearance of quadrupole resonances and possibly octopole peaks for very large particles.

Hence, the influence of higher-order multipoles is evident for large nanoparticles, making the spectra more complex. Although the dipole peak appearing in the NIR wavelength for 200 nm gold nanoparticles seems encouraging towards their use in NIR imaging, its intensity is much reduced compared to the dipole peak intensity of smaller nanoparticles. Furthermore, the synthesis of spherical gold nanoparticles of this size remains a challenge in practice as large gold nanoparticles are known to deviate from spherical form during synthesis.

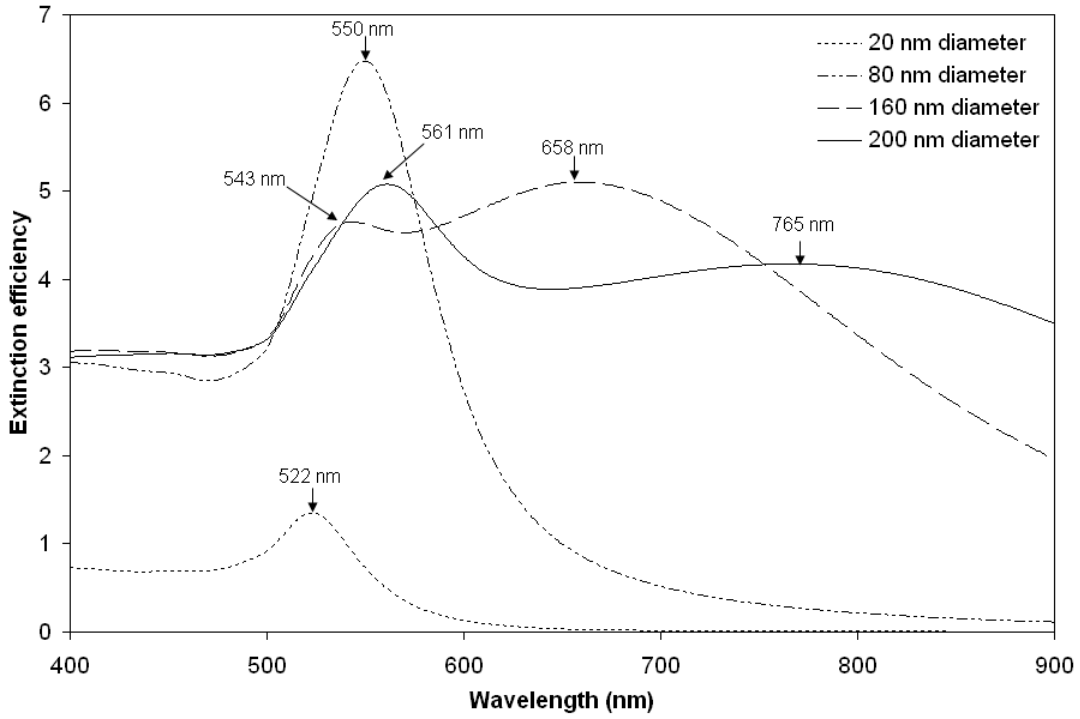

Figure 2.4. Extinction efficiency of larger spherical gold nanoparticles of varying radii showing the higher order multipole peaks. The values indicated are the wavelengths corresponding to the peak extinction.

2.4.2 Optical tunability of gold nanoshells

The optical properties of gold nanoshells with a silica core surrounded by a gold shell are examined in this section. Figure 2.5 shows the extinction spectrum for several nanoparticles with different ratios of core to shell size. The total nanoparticle diameter is kept constant at 100 nm. The spectrum with a peak at 569 nm is the extinction from a solid gold nanoparticle having a diameter of 100 nm with no silica core (Figure 2.3). As the shell thickness is decreased, the peaks red shift and at the same time become more intense. It is also noted that the extinction efficiency of gold nanoshells as given by the peak intensity is also higher compared to solid gold nanoparticles. Hence, increasing the ratio of core radius to total radius causes the peak to shift red. Thinning

the shell layer also produces a large increase in polarization at the sphere boundary, which yields the more intense extinction peaks.

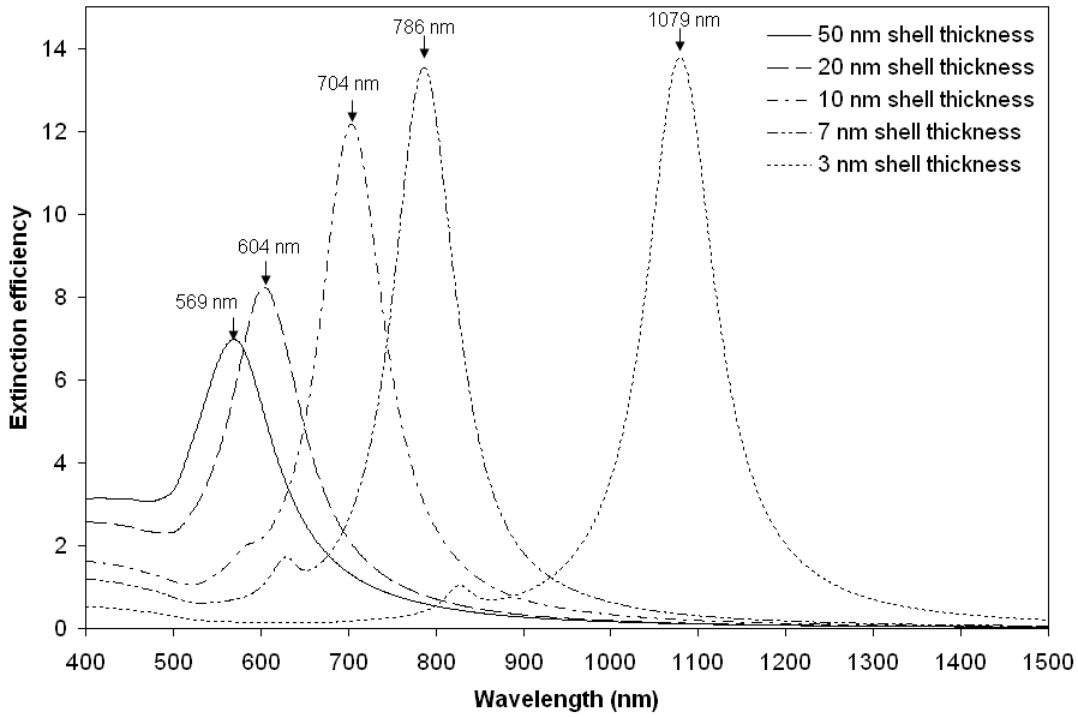

Figure 2.5. Extinction efficiency of gold nanoshells with different ratios of core to shell size. The core is silica and the shell is gold. The total nanoparticle diameter is 100 nm.

The same general trends are observed when the gold nanoshell size is increased. Figure 2.6 shows the equivalent plot for a gold nanoshell with diameter of 200 nm having different ratios of core to shell size. Again, as the shell thickness of the gold nanoshell is decreased, the dipole plasmon resonance red shifts toward longer wavelengths. This red shift is accompanied by an increase in the peak intensity. Higher-order poles begin to show up in the spectrum for larger particles. Quadrupole peaks can be seen at approximately 565, 621, 731, 819 and 921 nm.

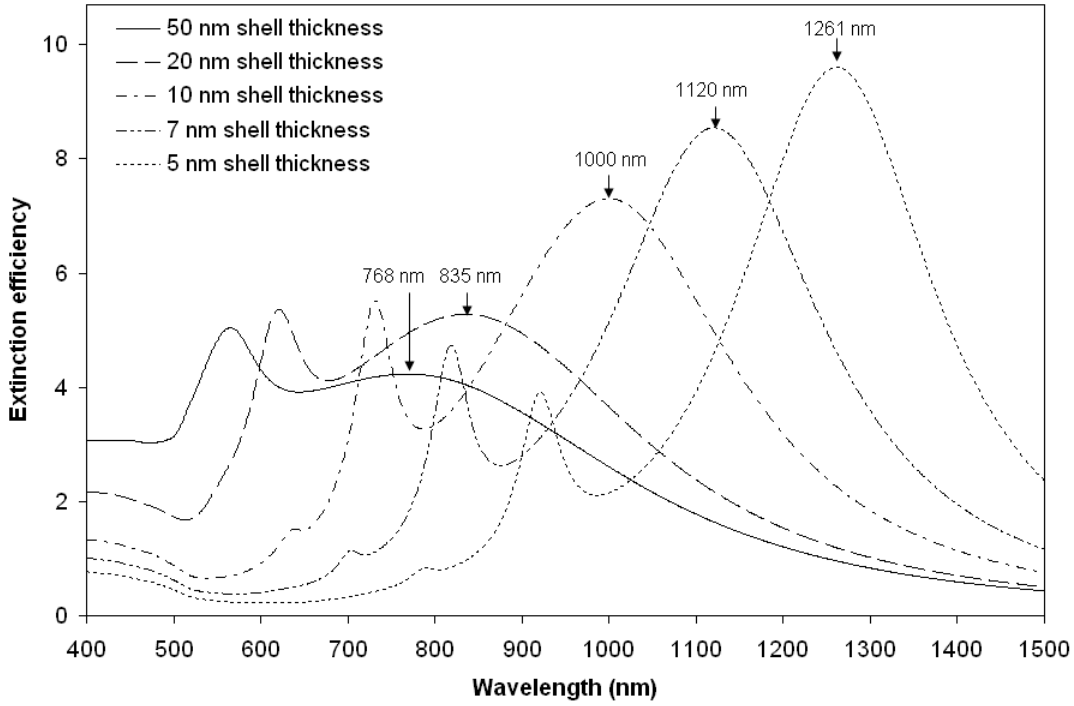

Figure 2.6. Extinction efficiency of gold nanoshells with different ratios of core to shell size. The core is silica and the shell is gold. The total nanoparticle diameter is 200 nm.

2.4.3 Adjustment of optical extinction mode

In addition to its optical tunability, it is also possible to engineer gold nanoshells to either predominantly scatter or absorb light by tailoring the core and shell fabrication materials or by varying the overall size of the gold nanoshells relative to the wavelength of the light at their optical resonance. Light scattering would be desired for reflectance-based imaging applications (see Chapters 6 to 8) while light absorbance permits photothermal-based therapy applications (see Chapter 9). The adjustment of scattering and absorption efficiency is demonstrated in Figure 2.7 which shows the predicted extinction, scattering and absorption spectra calculated based on Mie theory for two nanoshell configurations, one designed to scatter light and the other to preferentially absorb light with the peak at the same wavelength.

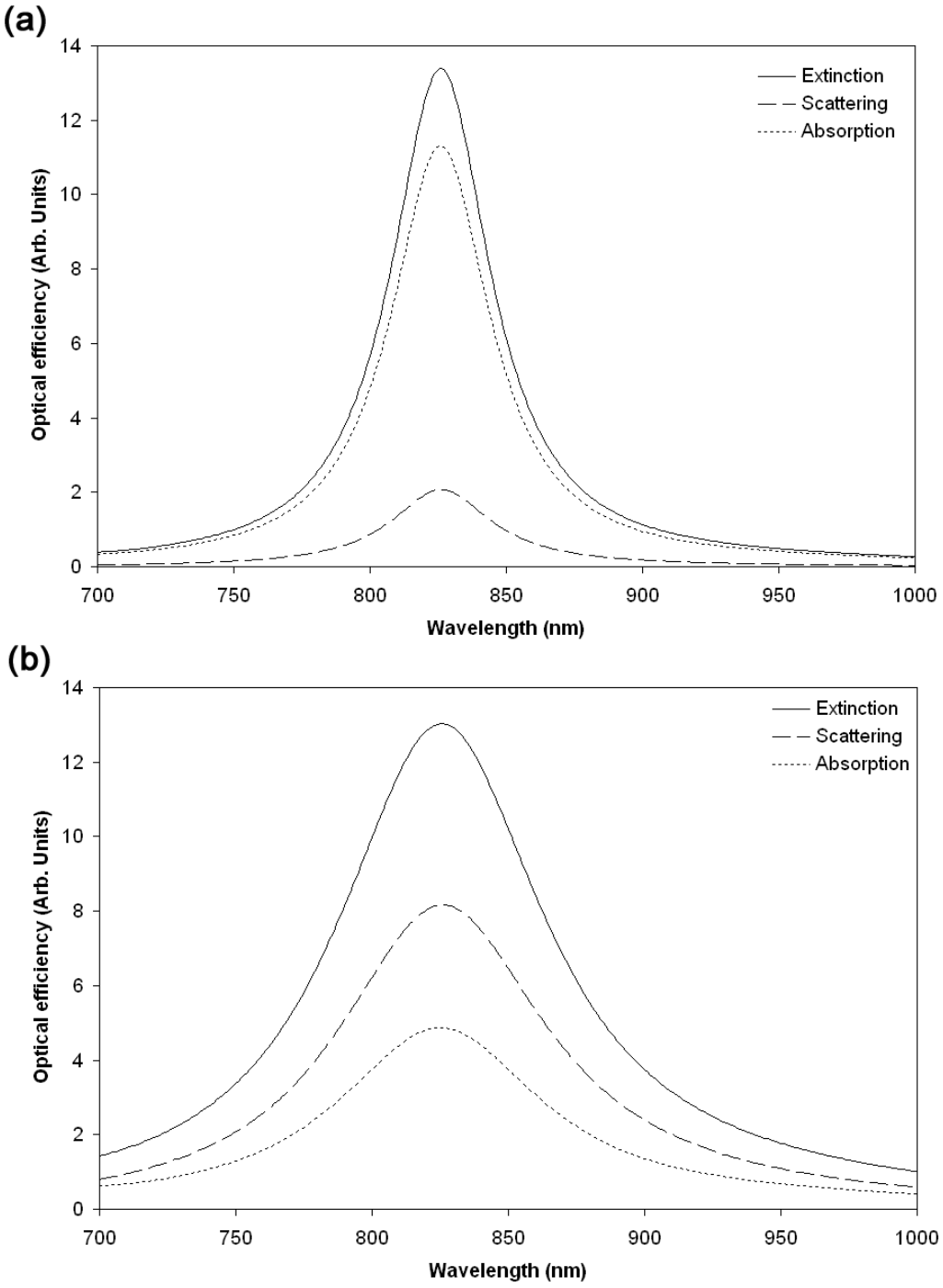

Figure 2.7. The predicted extinction efficiency, scattering efficiency and absorption efficiency are shown for two nanoshells with (a) an absorbing configuration (core radius = 23 nm; shell thickness = 3 nm) and (b) a scattering configuration (core radius = 46 nm; shell thickness = 7 nm).

With the core radius-to-shell thickness ratio kept constant, a smaller nanoshell (core radius = 23 nm; shell thickness = 3 nm) result in an absorbing configuration with the absorption efficiency higher than the scattering efficiency. As the overall size of the nanoshell double while maintaining the core-to-shell ratio constant (core radius = 46 nm; shell thickness = 7 nm), the extinction peak remains at 826 nm, but the scattering efficiency becomes higher than the absorption efficiency to result in a scattering configuration. In general, light absorption dominates the extinction spectrum for particles of relatively smaller radius and light scattering becomes the dominant process for larger nanoparticles.

2.4.4 Comparison of scattering properties

The scattering efficiency of solid gold nanoparticles and gold nanoshells is compared to two other common dielectric nanoparticle of the same size but having different dielectric constant. The results in Figure 2.8 show that the theoretical scattering efficiency of 100 nm gold nanostructures is much higher across all wavelengths compared to the common dielectric nanoparticles of the same size. Here, the scattering spectrum of gold nanoparticles shows a peak at 578 nm with a scattering efficiency of 4.73 and the gold nanoshells show a peak at 786 nm with a scattering efficiency of 8.63. These peaks are attributed to the surface plasmon resonance of gold as discussed earlier and are absent in the scattering spectrum of both silica and polystyrene nanoparticles.

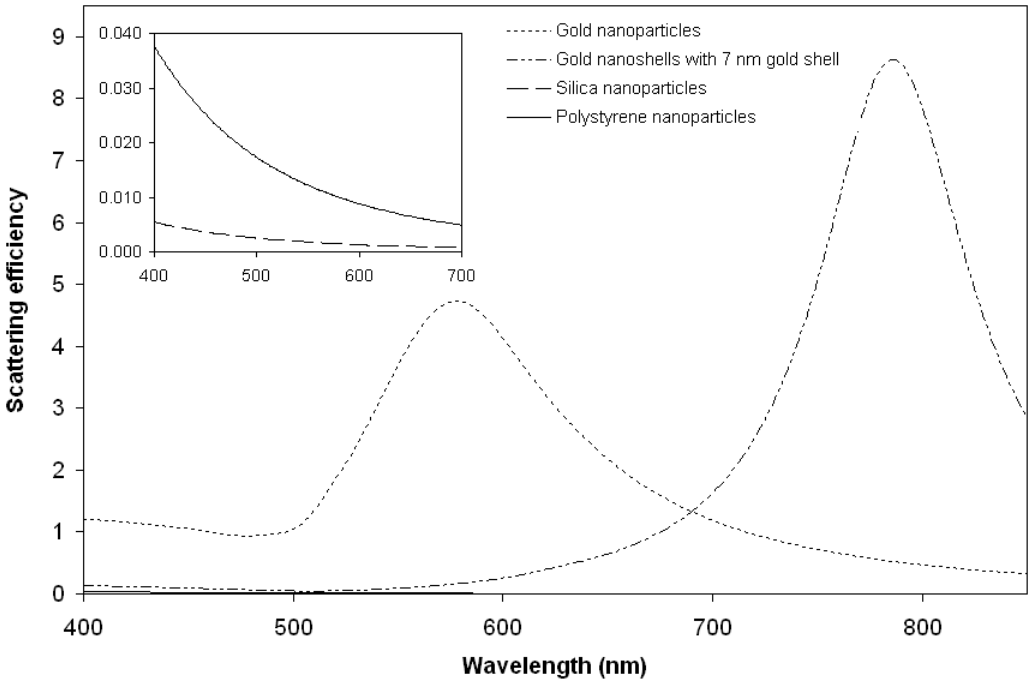

Figure 2.8. Scattering spectrum of plasmonic gold nanoparticles and gold nanoshells compared to dielectric silica and polystyrene nanoparticles with the same size of 100 nm diameter. The insert shows a scale up of the scattering spectrum of both dielectric nanoparticles.

In contrast, the scattering efficiency of these two dielectric nanoparticles without the plasmon resonance effect of gold is much lower with a maximum of < 0.04 (Figure 2.8 insert). Furthermore, it is also observed that the larger dielectric constant of polystyrene ($m_{polystyrene}$ = 1.59) [30] over that of silica (m_{silica} = 1.43) produces a scattering efficiency that is approximately four times higher across all wavelengths. The plasmonic optical response of gold nanostructures thus allow them to resonantly scatter light especially at their surface plasmon resonance where the large scattering efficiency gives rise to a correspondingly large scattering cross section compared to non-plasmonic nanoparticles of the same size. Also, when compared to molecular species such as organic chromophores, the absorption and scattering cross sections of gold nanoparticles are typically 5 – 6 orders in magnitude higher.

2.4.5 Computation of optimum gold nanoshells dimension

The various optical parameters of gold nanoshells in water are computed over a range of core radii and shell thicknesses at 840 nm excitation to select an appropriate size of gold nanoshells that gives the best signal enhancement in OCT applications. Figure 2.9 shows the contour plots of the extinction, absorption, scattering and backscattering cross section as well as anisotropy factor, g of gold nanoshells as a function of both core radius and shell thickness up to an overall diameter of 280 nm. Overall, the gold nanoshells have extinction cross section that increases with size with the largest extinction cross section occurring at core radius larger than 90 nm and shell thickness of more than 15 nm. Both the extinction and scattering cross section appear to be more sensitive to changes in the shell thickness compared to the core radius.

The similarity between the extinction and scattering contour plot (Figure 2.9a and b) implies that the predominant extinction cross section is attributed to light scattering rather than absorption except in cases where the core radius is larger than 90 nm and the shell thickness is about 7 to 8 nm (Figure 2.9c). The contour plot of the anisotropy factor (Figure 2.9e) shows that most of the size configurations produce gold nanoshells that tend to scatter light isotropically, except in cases of large core radii of > 90 nm coupled with gold shell of < 10 nm thickness where the gold nanoshells tend to be slightly more forward scattering with $g \approx 0.4$. The backscattering cross section contour plot (Figure 2.9d) also shows a region around 80 nm radius and 20 nm shell thickness where a large backscattering cross section in the order of 2×10^{-9} cm^2 occurs. Gold nanoshells with this size are expected to strongly enhance the OCT signal because of their strong backscattering response.

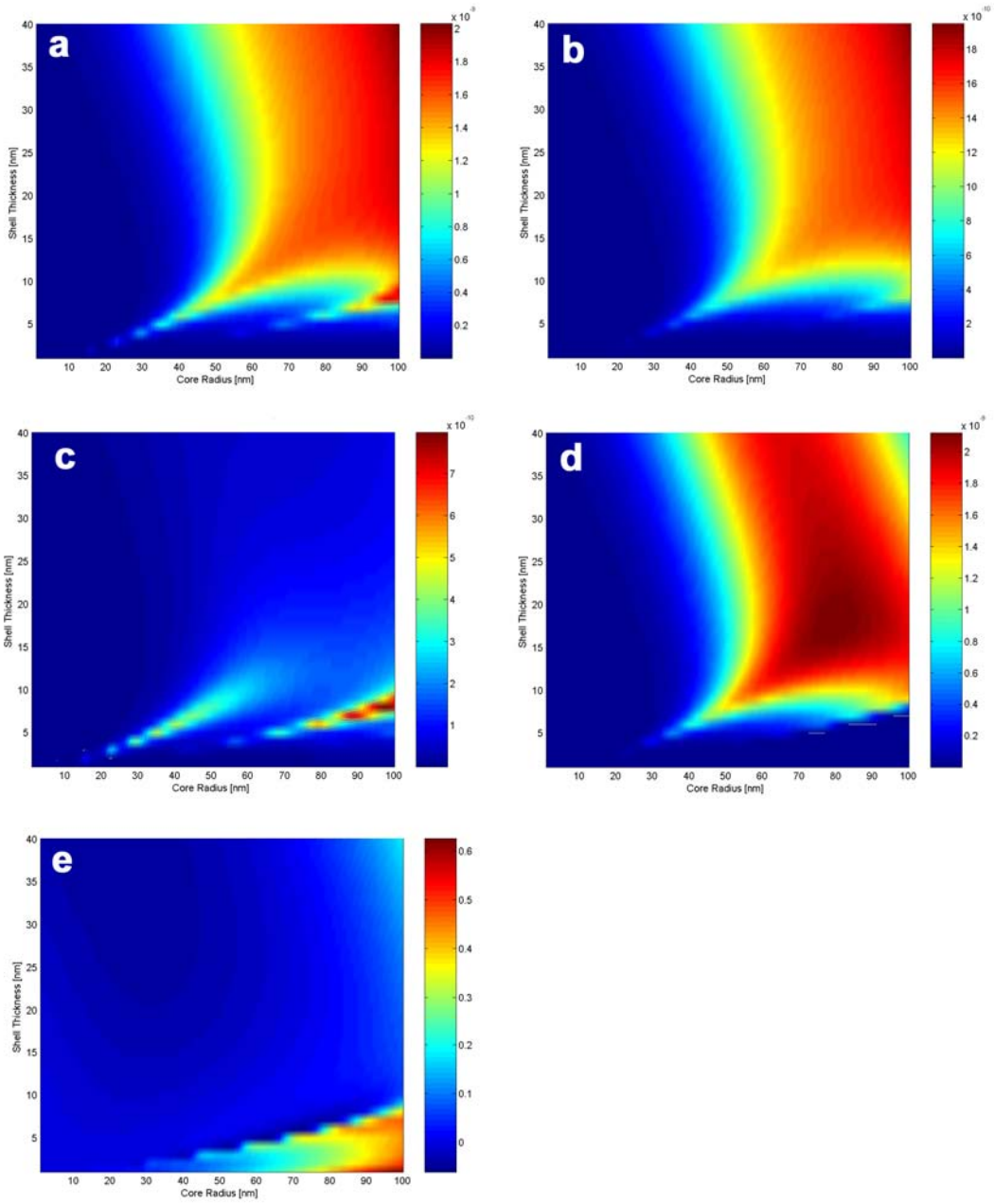

Figure 2.9. Computed optical cross section for each of the four optical parameters: (a) extinction, (b) scattering, (c) absorption and (d) backscattering of gold nanoshells as well as (e) anisotropy factor as a function of core radius (0 nm – 100 nm) and shell thickness (0 nm – 40 nm) at an excitation of 840 nm, a wavelength used in OCT imaging application. These contour plots aid in specifying the dimensions of gold nanoshells with desirable optical properties to be used in subsequent study where their effect on imaging signal is investigated. Except for the anisotropy factor, the cross section values associated with the color coded scale bar is given in cm^2.

An understanding of how various optical parameters affect the OCT signal would facilitate the selection of a relevant parameter as the criterion of choice for which the design of gold nanoshells can be optimized against to make them appropriate as optical probes for OCT. In general, optical characterization of OCT has been studied by several groups and a few theoretical models have been established to relate these optical parameters of the sample being imaged to its corresponding A-scan signal profile [31-33]. Most of these numerical models have been developed with an aim to extract out the optical parameters from the average A-scan profile of the OCT image for diagnostic purposes or applications such as glucose sensing in diabetes [34].

With these numerical models, the reverse can also be performed i.e. to predict how the OCT signal would change with certain optical parameters and hence design gold nanoshells based on these parameters. It is known from other studies that the OCT depth-dependent A-scan signal profile is affected by at least three optical parameters: the extinction coefficient, μ_t affects the slope of the signal [35, 36], the backscattering coefficient, μ_b affects the offset of the signal intensity [37] and the anisotropy factor, g affects the linearity of the A-scan signal profile with depth [38, 39].

The extinction and backscattering coefficients are related to their respective cross sections by the following simple relationship: optical coefficient, $\mu = \rho \times \sigma$ where ρ is the volume density i.e. number of particles per unit volume and σ is the optical cross section. Based on this relationship, the results in Figure 2.9 suggest several inferences linking the physical dimension of gold nanoshells to the possible changes in OCT signal, assuming the concentration of particles maintains a constant. Firstly, as the overall size of the gold nanoshells increases, the larger extinction cross section

would imply that the depth dependent OCT signal would attenuate faster with depth. Since the extinction cross section is more sensitive to changes in shell thickness, this implies that small increases in the shell thickness can greatly increase the OCT signal attenuation with depth compared to small increases in the core radius.

Since the predominant optical extinction is attributed to light scattering for the size range of gold nanoshells shown in Figure 2.9, this means that the attenuation observed in the depth-dependent OCT signal is attributed mainly to the light scattering of gold nanoshells which makes them well-suited as optical agents for scattering-based imaging technique. This OCT signal can be increased by having a positive offset to the overall signal. Previous studies by Oldenburg et al. have suggested that a large backscattering coefficient is able to produce a positive offset to increase the overall OCT signal and hence the image brightness [37]. This is expectedly so since OCT is a reflectance-based imaging technique that detects backscattered light from sample.

Because of its relation to the OCT signal offset, the backscattering cross section is used as the criterion of choice for which the design of the gold nanoshells is optimized again for OCT signal enhancement. With a large backscattering cross section at the OCT source wavelength, gold nanoshells can potentially be useful in enhancing OCT signal from the tissue. Based on the results in Figure 2.9d, gold nanoshells with a core radius and shell thickness of ≈ 80 nm and 20 nm respectively are predicted to produce an optimum backscattering cross section and hence backscattering coefficient to increase the overall OCT image brightness.

It is of worth to note that the optical cross section is used in the contour plot simulation instead of the optical efficiency. Since the optical cross section is the product of the optical efficiency and geometrical cross section, the cross section takes into account an additional factor due to the geometrical size of the gold nanoshells that may also affect the OCT signal. While the optical efficiency itself can provide the gold nanoshells with a good measure of its optical merit, it would be insufficient to predict the final OCT signal based solely on its optical efficiency since gold nanoshells with a high backscattering efficiency may still, for example, produce a small backscattering coefficient if their geometrical size is small [40].

2.5 Conclusion

In this chapter, the theoretical basis for the calculation of various optical parameters of spherical gold nanostructures are presented. The Mie theory of scattering and absorption of small particles as formalized by Bohren and Huffman [16] is used. These optical parameters are used to predict their various optical spectrum e.g. extinction, scattering and absorption spectrum which is in turn used to demonstrate their optical properties such as optical tunability, strong scattering and versatility in tailoring the extinction between scattering and absorption. The optical properties of spherical gold nanostructures can be tuned by adjusting their physical dimensions. The dielectric properties of the material are also important in playing a large role in the intensity and placement of the plasmon resonances.

The optical parameters obtained from theoretical calculation are also used to generate the contour plot of intensity of various parameters over a wide range of gold nanoshells core size and shell thickness to facilitate the selection of appropriate size

configurations of gold nanoshells for imaging. The design of an appropriate optical probe for any optical imaging modality requires a good understanding of how various optical parameters affect the generation of the image signal. For OCT, the backscattering cross section is used as a parameter of choice for which the design of gold nanoshells can be optimized for signal enhancement. The contour plots have shown that gold nanoshells with a silica core radius of 81 nm and gold shell thickness of 23 nm would provide an optimum backscattering response under OCT with source wavelength of 840 nm. The synthesis process of gold nanoshells based on this size configuration is described in the following chapter.

2.6 References

1. Yvo Dirix CB, Walter Caseri, Paul Smith. Oriented Pearl-Necklace Arrays of Metallic Nanoparticles in Polymers: A New Route Toward Polarization-Dependent Color Filters. *Advanced Materials* 1999; 11(3): 223-227.

2. Elghanian R, Storhoff JJ, Mucic RC, Letsinger RL, Mirkin CA. Selective colorimetric detection of polynucleotides based on the distance-dependent optical properties of gold nanoparticles. *Science* 1997; 277(5329): 1078-1081.

3. Taton TA, Mirkin CA, Letsinger RL. Scanometric DNA array detection with nanoparticle probes. *Science* 2000; 289(5485): 1757-1760.

4. Cao YC, Jin R, Mirkin CA. Nanoparticles with Raman spectroscopic fingerprints for DNA and RNA detection. *Science* 2002; 297(5586): 1536-1540.

5. Loo C, Lin A, Hirsch L, Lee MH, Barton J, Halas N, West J, Drezek R. Nanoshell-enabled photonics-based imaging and therapy of cancer. *Technol Cancer Res Treat* 2004; 3(1): 33-40.

6. Quinten M, Leitner A, Krenn JR, Aussenegg FR. Electromagnetic energy transport via linear chains of silver nanoparticles. *Opt Lett* 1998; 23(17): 1331-1333.

7. Lezec HJ, Degiron A, Devaux E, Linke RA, Martin-Moreno L, Garcia-Vidal FJ, Ebbesen TW. Beaming light from a subwavelength aperture. *Science* 2002; 297(5582): 820-822.

8. Thio T, Ghaemi HF, Lezec HJ, Wolff PA, Ebbesen TW. Surface-plasmon-enhanced transmission through hole arrays in Cr films. *J. Opt. Soc. Am. B* 1999; 16(10): 1743-1748.

9. Hirsch LR, Stafford RJ, Bankson JA, Sershen SR, Rivera B, Price RE, Hazle JD, Halas NJ, West JL. Nanoshell-mediated near-infrared thermal therapy of tumors under magnetic resonance guidance. *Proc Natl Acad Sci U S A* 2003; 100(23): 13549-13554.

10. Gittins DI, Caruso F. Tailoring the Polyelectrolyte Coating of Metal Nanoparticles. *J. Phys. Chem. B* 2001; 105(29): 6846-6852.

11. Gittins DI, Susha AS, Schoeler B, Caruso F. Dense Nanoparticulate Thin Films via Gold Nanoparticle Self-Assembly. *Advanced Materials* 2002; 14(7): 508-512.

12. Oldenburg SJ, Averitt RD, Westcott SL, Halas NJ. Nanoengineering of optical resonances. *Chemical Physics Letters* 1998; 288(2-4): 243-247.

13. Oldenburg SJ, Westcott SL, Averitt RD, Halas NJ. Surface enhanced Raman scattering in the near infrared using metal nanoshell substrates. *The Journal of Chemical Physics* 1999; 111(10): 4729-4735.

14. Mie G. Beitrage zur Optic Truber Madien, speziell kolloidaler Metallosungen. *Ann Phys* 1908; 25: 337-388.

15. van de Hulst HC. Light Scattering by Small Particles. New York, NY: Dover Publication, 1981.

16. Bohren CF, Huffman DR. Absorption and Scattering of Light by Small Particles. New York, NY: Wiley-Interscience, 1998.

17. Wiscombe WJ. Improved Mie Scattering Algorithms. *Appl Opt* 1980; 19(9): 1505-1509.

18. Volkov NG, Kovach VY. Scattering of Light by Inhomogeneous Spherically Symmetrical Aerosol Particles. *Izvestiya Atmospheric and Oceanic Physics* 1990; 26(5): 381-385.

19. Perelman AY. Scattering by particles with radially variable refractive indices. *Appl. Opt.* 1996; 35(27): 5452-5460.

20. Bhandari R. Analytic Expressions, calculational forms for scattering by a multilayered sphere. *Proceedings of SPIE - The International Society for Optical Engineering* 1985; 540: 500-511.

21. Aden AL, Kerker M. Scattering of Electromagnetic Waves from Two Concentric Spheres. *Journal of Applied Physics* 1951; 22(10): 1242-1246.

22. Averitt RD, Westcott SL, Halas NJ. Linear optical properties of gold nanoshells. *J. Opt. Soc. Am. B* 1999; 16(10): 1824-1832.

23. Spiegel RS, Liu J. Mathematical Handbook. New York: McGraw-Hill, 1998.

24. Ludlow IK. Systematic behavior of the Mie scattering coefficients of spheres as a function of order. *Phys Rev* 1996; 55(3): 2909-2924.

25. Ishimaru A. Wave propagation and scattering in random media, vol. 1. Orlando, FL: Academic Press, 1978.

26. Graf C, van Blaaderen A. Metallodielectric Colloidal Core-Shell Particles for Photonic Applications. *Langmuir* 2002; 18(2): 524-534.

27. Oldenburg SJ, Jackson JB, Westcott SL, Halas NJ. Infrared extinction properties of gold nanoshells. *Applied Physics Letters* 1999; 75(19): 2897-2899.

28. Johnson PB, Christy RW. Optical Constants of the Noble Metals. *Physical Review B* 1972; 6(12): 4370 LP - 4379.

29. Lynch DW, Hunter WR. Comments on the Optical Constants of Metals and an Introduction to the Data for Several Metals. In: E. P, ed. Handbook of Optical Constants of Solids Orlando, FL: Academic Press, 1985:286-295.

30. Shi W, Sahoo Y, Swihart MT, Prasad PN. Gold Nanoshells on Polystyrene Cores for Control of Surface Plasmon Resonance. *Langmuir* 2005; 21(4): 1610-1617.

31. Thrane L, Yura HT, Andersen PE. Analysis of optical coherence tomography systems based on the extended Huygens-Fresnel principle. *J. Opt. Soc. Am. A* 2000; 17(3): 484-490.

32. Kholodnykh AI, Petrova IY, Larin KV, Motamedi M, Esenaliev RO. Precision of Measurement of Tissue Optical Properties with Optical Coherence Tomography. *Appl. Opt.* 2003; 42(16): 3027-3037.

33. van Leeuwen TG, Faber DJ, Aalders MC. Measurement of the axial point spread function in scattering media using single-mode fiber-based optical coherence tomography. *Selected Topics in Quantum Electronics, IEEE Journal of* 2003; 9(2): 227-233.

34. Esenaliev RO, Larin KV, Larina IV, Motamedi M. Noninvasive monitoring of glucose concentration with optical coherence tomography. *Opt Lett* 2001; 26(13): 992-994.

35. Izatt JA, Hee MR, Owen GM, Swanson EA, Fujimoto JG. Optical coherence microscopy in scattering media. *Opt. Lett.* 1994; 19(8): 590-592.

36. Faber D, van der Meer F, Aalders M, van Leeuwen T. Quantitative measurement of attenuation coefficients of weakly scattering media using optical coherence tomography. *Opt. Express* 2004; 12(19): 4353-4365.

37. Oldenburg AL, Hansen MN, Zweifel DA, Wei A, Boppart SA. Plasmon-resonant gold nanorods as low backscattering albedo contrast agents for optical coherence tomography. *Opt. Express* 2006; 14(15): 6724-6738.

38. Schmitt JM, Knüttel A, Bonner RF. Measurement of optical properties of biological tissues by low-coherence reflectometry. *Appl. Opt.* 1993; 32(30): 6032-6042.

39. Schmitt JM, Knuettel AR, Gandjbakhche AH, Bonner RF: Optical characterization of dense tissues using low-coherence interferometry, Podbielska H, ed. *Holography, Interferometry, and Optical Pattern Recognition in Biomedicine III* 1993; 1889:197-211.

40. Lin AW, Lewinski NA, West JL, Halas NJ, Drezek RA. Optically tunable nanoparticle contrast agents for early cancer detection: model-based analysis of gold nanoshells. *J Biomed Opt* 2005; 10(6): 064035.

CHAPTER THREE

PRELIMINARY STUDY ON GOLD NANOPARTICLES *IN VITRO*

Abstract

Following the theoretical discussion in Chapter 2, the resonance light scattering property of gold nanoparticles under reflectance-based imaging is demonstrated in this chapter as a preliminary *in vitro* study on their potential use as molecular contrast probes for imaging molecular changes associated with carcinoma. Gold nanoparticles were synthesized and conjugated to anti-epidermal growth factor receptor (EGFR) for imaging. Their localization on nasopharyngeal carcinoma CNE2 cells and normal human lung fibroblast NHLF cells were imaged and compared under confocal microscopy *in vitro*. The localization of gold bioconjugates on EGFR increases the reflectance properties of CNE2 cells and the regions of increased reflectance correspond to regions of high EGFR expression in the cells. The optical properties of normal fibroblast cells are not greatly affected. These gold bioconjugates are thus able to map the expression of relevant biomarkers and elicit an optical contrast to discriminate cancer from normal cells under confocal reflectance microscopy. The results as described in this chapter demonstrates the potential of gold nanoparticles to target and probe cancer cells and illuminates them for cancer detection under reflectance-based imaging systems based on biomolecular changes. The work presented in this chapter has been published in *International Journal of Nanomedicine 2007; 2: 785-798* and *Molecular and Cellular Probes 2008; 22: 14-23.*

3.1 Introduction

Gold nanoparticles show potential as contrast agents for reflectance-based optical imaging systems to address the limitation of these systems in providing contrast for early molecular signatures present in cells and tissue based on their optical properties [1-3]. The reflectance confocal endomicroscope is an example of a reflectance-based imaging system. It is essentially an endoscope that performs confocal microscopy in the reflectance mode and is able to able to achieve subcellular resolution. It has a typical system setup as shown in Figure 3.1 below. The use of confocal endomicroscopy to image cellular structures and other morphological features associated with carcinoma within living tissue to a depth of about 100 to 200 μm has been demonstrated [4].

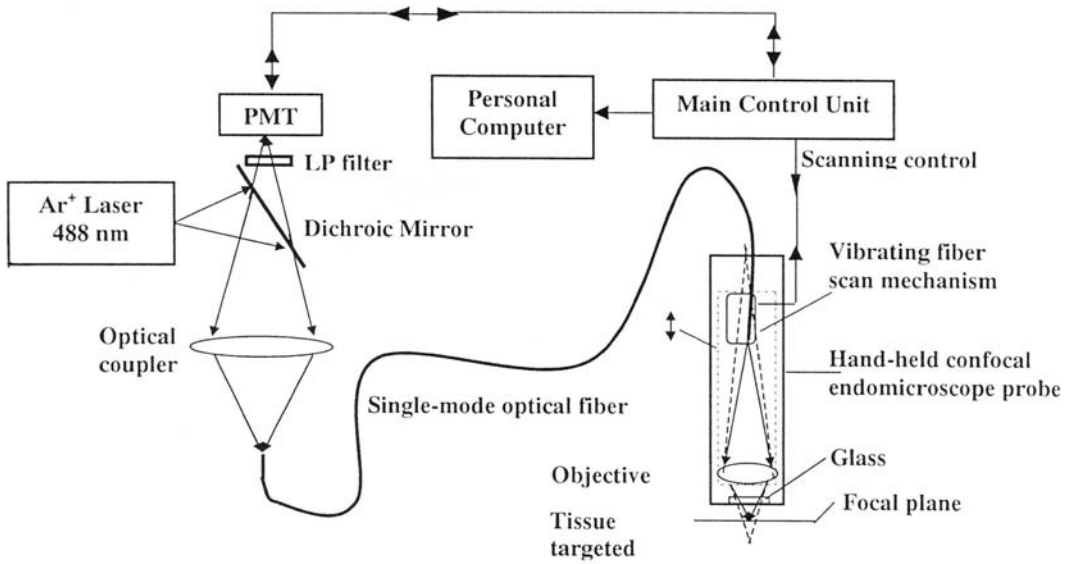

Figure 3.1. Typical schematic diagram of a laser confocal endomicroscope system with a handheld rigid probe that was used for imaging [4].

However, such system operating in the visible light range can image no further than ≈ 200 μm below the mucosal surface [4], and hence would be insufficient to image the entire epithelium and its underlying mucosa stromal. Furthermore, molecular abnormalities in cells do not present changes in cellular light scattering behavior that can be picked up by the microscope, hence requiring the need of a mediating agent to transduce these changes into optical signals.

The potential of gold nanoparticles to function as contrast agents arises from their unique optical response to light which allow them to resonantly scatter light when excited at their surface plasmon resonance frequency [5]. Such property has also been theoretically demonstrated earlier in Chapter 2. Besides a strong scattering response from individual particles, the scattering cross section per particle is also known to increase when gold nanoparticles aggregate and their surface plasmon interact to produce an even larger optical signal [2]. This mode of enhanced scattering from coupled surface plasmon resonances of aggregated gold nanoparticles can be exploited to further enhance the optical scattering signal when the gold nanoparticles are brought close together under the influence of biochemical processes associated with disease pathology in cellular environment.

Apart from their optical properties, gold nanoparticles also possess other favorable physicochemical properties for use as cancer targeting optical probes. They can be easily conjugated to antibodies or peptides through electrostatic charge interaction or coordinate bonding to probe for specific cellular biomarkers with high specificity and affinity [6]. When coupled with appropriate biomarkers which is known to be overexpressed in most epithelial cancer, these gold nanoparticles bioconjugates may

provide useful optical signal for molecular specific information to assist clinicians in diagnosis of precancers. As discussed in Chapter 1, the epidermal growth factor receptor (EGFR) is one such clinically relevant cell surface receptor biomarker that is overexpressed in vast majority of epithelial cancer but not in normal cells [7-10]. Its expression is known to correlate with cancer progression in the epithelial origin [11, 12]. Gold nanoparticles are also generally biocompatible and benign in biological tissues and have been applied for clinical treatment of other disease conditions such as rheumatoid arthritis [13].

The first demonstration of gold nanoparticles in optical imaging by Sokolov et al. uses these solid gold nanoparticles to create an optical contrast to image precancer [2]. In this chapter, the preparation of antibody conjugated gold nanoparticles and their use as an optical probe to increase the molecular contrast of a clinically relevant biomarker of epithelial cancer is demonstrated *in vitro* under confocal reflectance microscopy. The focus in this case is on the imaging of changes in molecular expression of EGFR. The optical signal intensity of cells in the presence and absence of gold nanoparticles and between normal and cancer cells incubated with gold nanoparticles are compared. The reflectance signal from the gold nanoparticles does not just increase the optical contrast, but also allows a molecular mapping of the EGFR biomarker expression. The results shown in this chapter serve as a preliminary demonstration of the potential of gold nanostructures to perform molecular contrast imaging of cancerous signatures of tissues for early detection of epithelial carcinoma under reflectance-based imaging systems.

3.2 Materials and methods

3.2.1 Synthesis and characterization of gold nanoparticles

Gold nanoparticles of 20 nm in diameter were synthesized based on established protocols [14]. Briefly, a 200 ml solution of 0.259mM tetrachloroauric acid ($HAuCl_4$, Sigma-Aldrich) was brought to 90 °C before a 3 ml solution of 34mM trisodium citrate (Sigma-Aldrich) was added rapidly to the $HAuCl_4$ solution, while maintaining vigorous stirring throughout the process. The mixture was heated continuously at 90 °C for the next 10 minutes under stirring before a color change from gray to ruby red was observed, indicating the formation of the gold nanoparticles. The particle size was determined by transmission electron microscopy (TEM) (Jeol JEM-1010), operating at 100 kV and their UV–Vis extinction spectrum was characterized using a UV–Vis spectrophotometer (Shimadzu UV-2401 PC). The concentration of gold nanoparticles in the colloid was measured against known standards from British Biocell International Ltd. (EMGC.15, particle concentration = 1.4×10^{12} particles per ml), using the absorption spectroscopy and was stored at 4°C when not used.

3.2.2 Conjugation of gold nanoparticles with anti-EGFR

The mouse monoclonal anti-EGFR (Santa Cruz Biotechnology, Inc.) was used as the molecular marker of interest for imaging its expression in cells. Gold nanoparticles have been conjugated to various antibodies for biological applications such as staining studies since 1950s' [14]. Therefore, the 20 nm gold nanoparticles were conjugated to anti-EGFR via established protocols for passive absorption of anti-EGFR on the surface of gold nanoparticles. The conjugates are simply formed by noncovalant interactions between the citrate capping molecules on the surface of the gold

nanoparticles and the antibodies (see Figure 3.2). The binding is in such a way that the bioactivity of the antibodies are preserved and thus the conjugates can be used for further biofunctional studies such as imaging cancer biomarker in this case.

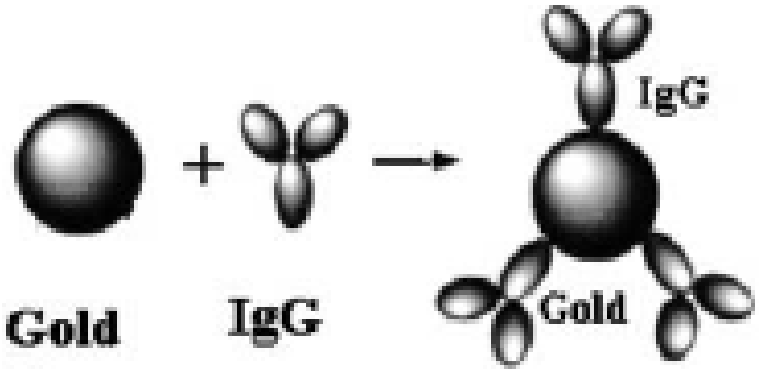

Figure 3.2. Graphical scheme of gold nanoparticles-IgG conjugation [15].

Briefly, the conjugation was performed by incubating the colloidal gold nanoparticles with anti-EGFR for about 10 minutes at room temperature according to the procedure modified from Geoghegan and Ackerman [6]. The minimal amount of anti-EGFR required to tag the surface of gold nanoparticles and stabilize them against salt-induced aggregation was determined using titration with varying amounts of anti-EGFR [14]. The optimal pH of conjugation was also determined by titration with various amount of potassium carbonate. The pH of the gold nanoparticles colloid was adjusted to the isoelectric point of the antibody to give the optimum pH for conjugation where the non-covalent binding of anti-EGFR form very stable complex with gold nanoparticles.

The successful conjugation of antibodies on gold nanoparticles was ascertained by addition of 10% common salt solution and observing any visible color change in the colloidal solution. The stability of the conjugated particle against salt-induced

aggregation can be assessed by the value of OD580/OD520 in the absorption spectrum. The presence of salt will cause unconjugated gold nanoparticles to aggregate and result in a visible color change from red to purple or gray in the colloidal solution while conjugated gold nanoparticles will remain stable in red as shown in Figure 3.3.

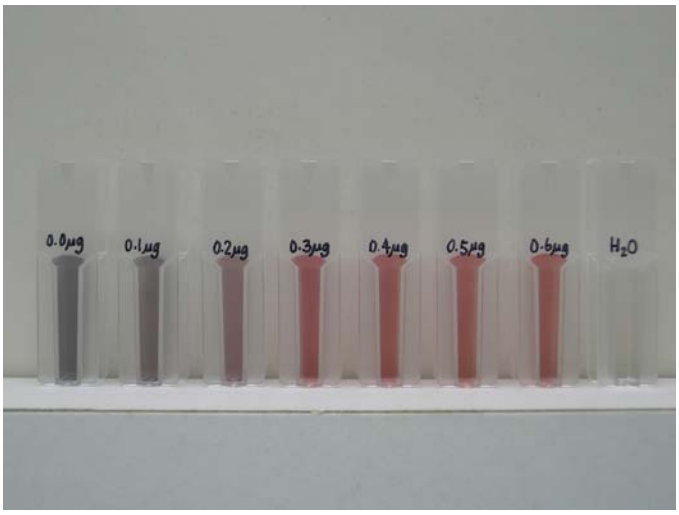

Figure 3.3. Gold nanoparticles with a range of different amount of anti-EGFR conjugated aggregate to different degree to give a range of color in the colloid upon salt-induced aggregation. Those that are sufficiently conjugated to give stable nanoparticles in the presence of salt remain red (towards the right) while those that are insufficiently conjugated will aggregate in the presence of salt to give a purple or grey colloid (towards the left).

After the 10 minutes of incubation time, the anti-EGFR conjugated gold nanoparticles were then washed and resuspended in 1 X PBS buffer (pH 7.4) containing 5% bovine serum albumin (BSA) (Sigma Aldrich, Inc.) and stored at 4 °C. Spectrophotometry was used to confirm conjugation of anti-EGFR to gold nanoparticles. The gold nanoparticles were also conjugated to BSA, a non-cellular binding protein, as negative control probes using the same procedures as above. BSA was coated on the gold nanoparticles to stabilize them against aggregation in salt-containing physiological medium such as PBS and RPMI through steric exclusion.

3.2.3 Cell culture and EGFR expression analysis

Both the poorly differentiated nasopharyngeal epithelium carcinoma CNE2 cell line (kindly provided by Professor K. M. Hui, National Cancer Centre Singapore) and the normal human lung fibroblast (NHLF) cell line (Clonetics, Cambrex Walkersville, MD) were used in this study. The CNE2 cells were grown in RPMI 1640 supplemented with 10% fetal bovine serum, 2mM glutamine, sodium pyruvate, non-essential amino acids and 100 unit/ml penicillin/streptomycin while the normal cells were grown in fibroblast growth medium (Cambrex Corp.). Both cell lines were grown to about 1 x 10^6 cells in petri dish and maintained at 37 °C in humidified 5% CO_2 and 95% air atmosphere. To verify the differential expression of EGFR between the normal and cancer cells, fluorescence-activated cell sorting (FACS) analysis on both cell lines was performed using a primary mouse anti-EGFR (Santa Cruz Biotechnology, Inc.) staining followed by secondary staining using FITC conjugated chicken anti mouse IgG (Molecular Probes). The cells were ran through a flow cytometer and sorted based on the fluorescence intensity of the FITC staining which corresponded to the EGFR expression on the cells.

3.2.4 Cellular imaging *in vitro*

Prior to imaging, both cell lines (1 x 10^6 cells) were trypsinized and fixed in 2% paraformaldehyde before incubating them with the anti-EGFR conjugated gold nanoparticles for 2 h at 37 °C. The cells were also incubated with BSA conjugated gold nanoparticles as a negative control for the antibody binding. Following the incubation, the cells were rinsed thrice with PBS to wash away the excess and unbounded gold bioconjugates and were then placed on a microscope slide for

imaging. Imaging was performed using a confocal microscopy (Carl Zeiss LSM510 Meta) in the reflectance mode with 20 X and 40 X objectives under 543 nm excitation with a helium neon laser. To compare the EGFR mapping on cells between labeling with gold nanoparticles and labeling with conventional immunofluorescence dye, the CNE2 cells were also incubated with anti-EGFR in the absence of gold nanoparticles and then further stained with secondary FITC conjugated chicken anti-mouse (CAM-FITC) IgG for another 1 h at 37 °C and examined for anti-EGFR immunofluorescence staining under confocal fluorescence microscopy at 488 nm excitation with an argon laser. The experiments were performed in triplicates to ascertain reproducibility.

3.3 Results and discussion

3.3.1 Synthesis and characterization of the gold bioconjugates

The TEM image of the synthesized gold nanoparticles is shown in Figure 3.4. The TEM image shows that the particles are uniformly spherical and monodisperse with an average diameter of 20 ± 1.8 nm.

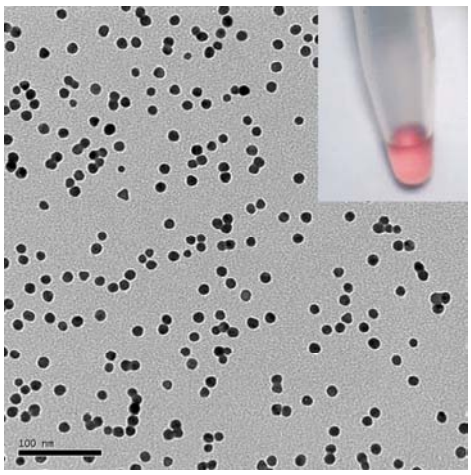

Figure 3.4. TEM image of the synthesized gold nanoparticles with inset showing the red gold nanoparticles colloid.

The extinction spectrum of the gold nanoparticles in Figure 3.5 shows a sharp peak at 520 nm which corresponds to the surface plasmon resonance typical of gold nanoparticles of that size [14, 16] and matches the excitation wavelength of the confocal reflectance system at 543 nm well to allow good optical response when the gold nanoparticles are excited for imaging. The measured spectrum also agrees well with the theoretical spectrum as shown in Figure 2.3. Since the light scattering of biological tissue in this wavelength range is small compared to the light scattering afforded by gold nanoparticles [17], the presence of gold nanoparticles in tissue may be distinguishable from its scattering intensity. From the intensity of the extinction spectrum, the particle concentration was determined to be approximately 1.23 x 10^{12} particles per ml when measured against standards.

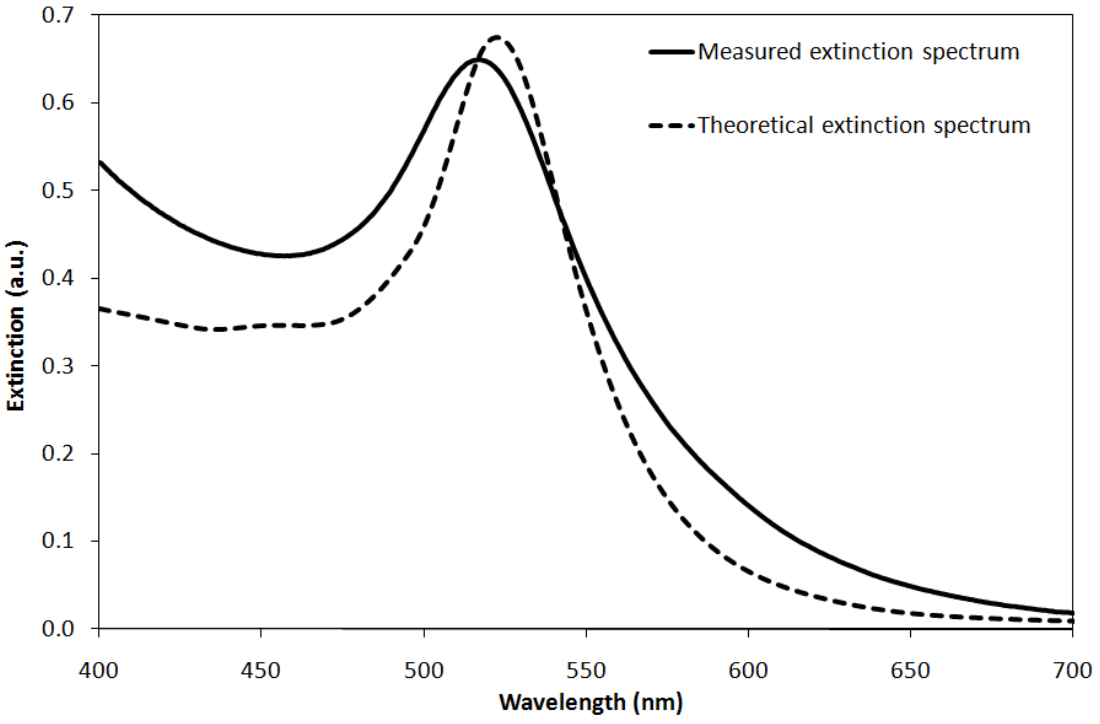

Figure 3.5. Measured extinction spectrum of the 20nm gold nanoparticles synthesized by reduction with sodium citrate. The theoretical extinction spectrum is also shown as comparison.

The gold nanoparticles were conjugated to monoclonal anti-EGFR via passive absorption of the antibodies onto its surface. Both the antibody titration and pH titration suggested that about 0.4 mg of anti-EGFR was needed to conjugate and stabilize 1 ml of gold nanoparticles colloid (1.23×10^{12} particles) at an optimum pH of 8 to give the optimal stability of gold nanoparticles against salt-induced aggregation. Spectrophotometry was used to confirm the successful conjugation of anti-EGFR to gold nanoparticles. The extinction spectrum of the gold nanoparticles both before and after conjugation with anti-EGFR was measured and is shown in Figure 3.6. The UV-Visible extinction spectrum shows a characteristic red-shift (≈ 6 nm) of the peak of the surface plasmon resonance which is typical of protein binding on the surface of the gold nanoparticles. The 6 nm red-shift in the peak surface plasmon resonance of the gold nanoparticles after conjugation with the antibody is associated with alterations in the local refractive index and hence dielectric constant around the surface of the gold nanoparticles due to the presence of a layer of antibodies around its surface. The change in dielectric constant affects the light scattering properties of gold nanoparticles according to the Mie theory [18]. This red-shift is typical of protein binding on the surface of the gold nanoparticles and serves as an indication of the successful conjugation of the anti-EGFR on surface of the gold nanoparticles. An additional verification of anti-EGFR binding to the surface of the nanoparticles is their stability in 10% common salt solution where the gold bioconjugates did not aggregate to result in a color change after the addition of salt solution. The reduction in the intensity of the peak after conjugation could be due to the loss in some gold nanoparticles during the washing steps after conjugation.

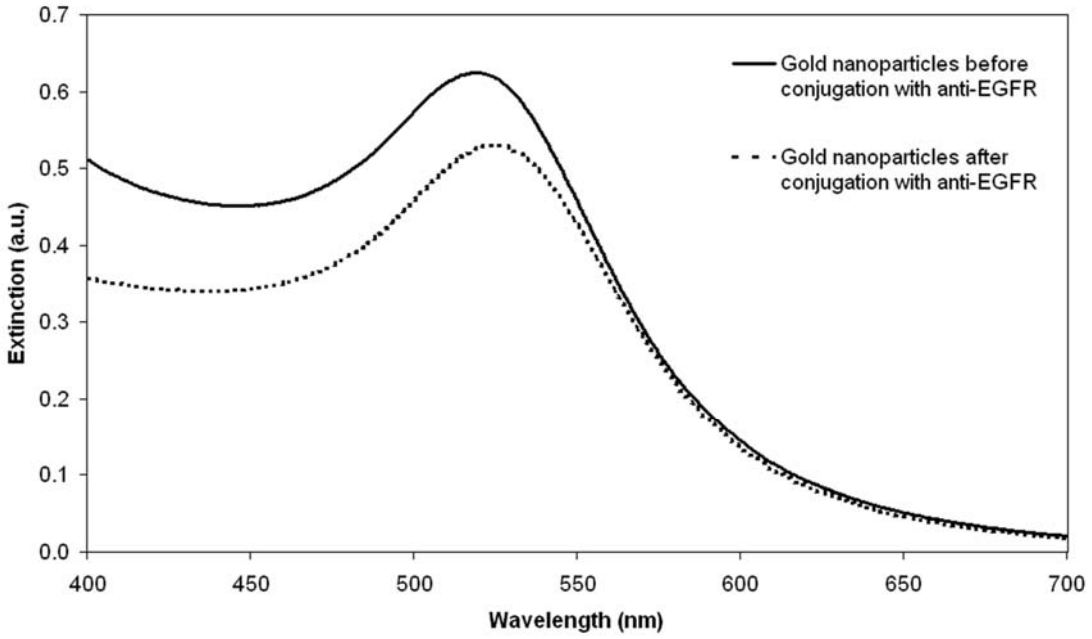

Figure 3.6. Changes in extinction spectrum of gold nanoparticles after conjugation with anti-EGFR to demonstrate the binding of anti-EGFR on gold nanoparticles. Spectrum after conjugation is shown in dashed line.

3.3.2 FACS analysis of EGFR expression

The expression of EGFR in the two cell lines used was analyzed by FACS. The result of the FACS analysis as shown in Figure 3.7, shows two distinct fluorescence populations of CNE2 cells not observed in NHLF cells. The lower fluorescence population corresponds to the reference fluorescence of cells from secondary FITC conjugated IgG staining only, in the absence of primary anti-EGFR, while the higher fluorescence population corresponds to fluorescence of cells population after both the primary and secondary staining of EGFR on the cells. The higher fluorescence population in CNE2 cells shows strong EGFR staining on the cells and hence indicates a high level of EGFR expression on the CNE2 cells. On the other hand, such higher fluorescence population is not observable in NHLF cells, indicating minimal EGFR staining due to the nominal expression level of EGFR in NHLF cells. This

result verifies an overexpression of EGFR in the cancerous CNE2 cells compared to the nominal expression level in normal NHLF cells.

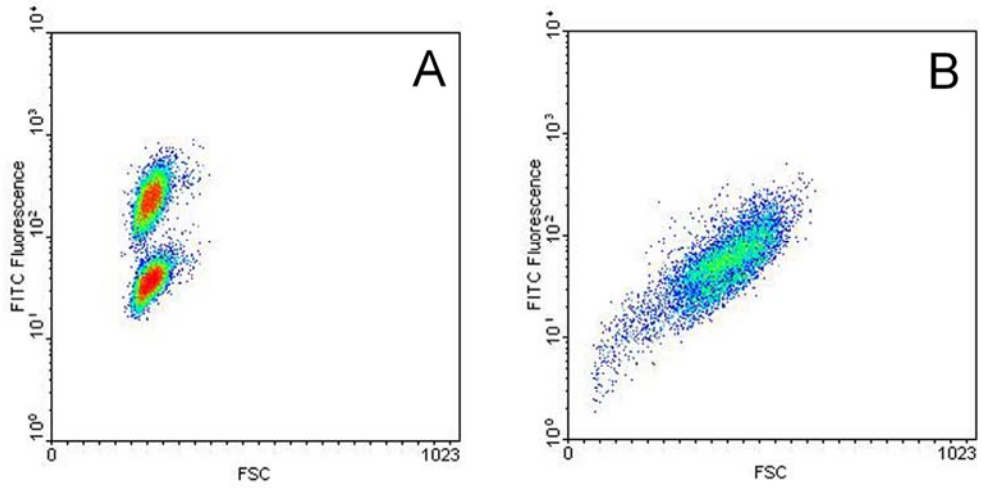

Figure 3.7. FACS analysis of EGFR expression in (a) CNE2 cells and (b) NHLF cells.

3.3.3 Increase in optical contrast of cancer cells

The ability of gold nanoparticles to increase the optical scattering of cells when attached to their surface was investigated by labeling the cells with these particles and observing them under confocal reflectance microscopy. Figure 3.8 shows the confocal reflectance images of CNE2 cells before and after labeling with anti-EGFR conjugated gold nanoparticles, as well as CNE2 cells labeled with the control BSA conjugated gold nanoparticles which are not known to exhibit high binding affinity to the cells. A significant increase in the reflectance signal was observed in the cells labeled with the antibody conjugated gold nanoparticles compared to the other two negative controls where the reflectance signal seems to be non-specific and at random and could barely be resolved from the dark background. The increase in reflectance

signal can be attributed to the localization of gold nanoparticles on the cell membrane as it was not observed in the unlabeled cells.

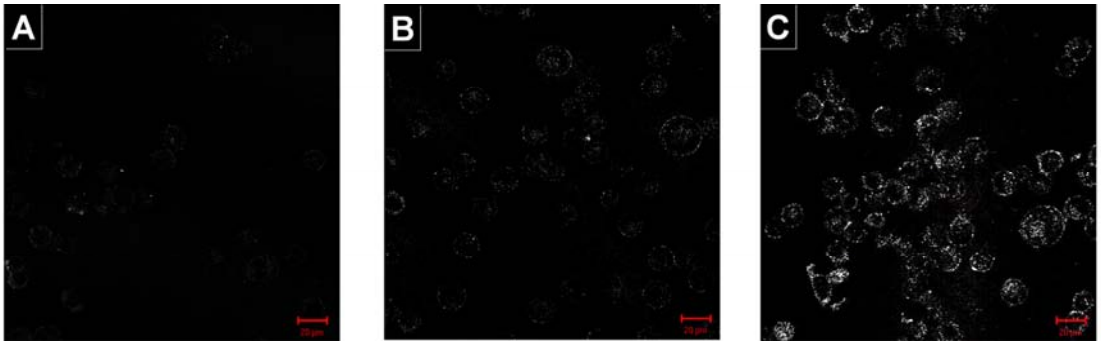

Figure 3.8. Confocal reflectance images of CNE2 cells (a) before labeling; (b) after labeling with the control BSA conjugated gold nanoparticles; and (c) after labeling with anti-EGFR conjugated gold nanoparticles. Images are cross-sectional slices of cells taken at the mid-focal plane at 20 x magnification. False-color reflectance images obtained at excitation 543 nm. Scale bar in all images is 20 μm.

The results have shown that the anti-EGFR were able to target and bind to the extracellular domain of EGFR on the cellular membrane even after conjugation to the gold nanoparticles. This means that the anti-EGFR still retains its antigen-binding sites and activity after conjugation. The localization of the anti-EGFR gold nanoparticles forms highly reflective beacons due to the strong resonant light scattering response of gold nanoparticles on the cell surface to the excitation light. This resonant scattering condition is further enhanced when the gold nanoparticles cluster close together on the cell membrane as they attach to their receptor and their surface plasmon interacts with each other. This result in bright reflectance rings being formed around the cytoplasmic membrane as their optical reflectance properties were increased significantly under confocal reflectance microscopy.

In contrast, the strong reflectance signal from the bright scattering rings was not observed in the control labeling with a non-binding BSA conjugated gold nanoparticles as BSA was unable to target and bind to the cells and were therefore removed during the washing steps. These results clearly demonstrate that the anti-EGFR gold nanoparticles can serve as a potential optical contrast agent to increase the detection visibility of cells under reflectance-based imaging systems.

In addition to increasing the optical scattering on cells, the anti-EGFR conjugated gold nanoparticles also exhibited specific targeting and binding to cancer cells overexpressing EGFR compared to normal cells. The labeling of anti-EGFR gold nanoparticles on both CNE2 and NHLF cells under confocal reflectance microscopy is shown in Figure 3.9 together with their corresponding autofluorescence image. The autofluorescence images of the two cell lines show similar autofluorescence level.

However, as EGFR is differentially expressed in the two cell lines used in this study, this differential expression of EGFR can be exploited to regulate the amount of gold nanoparticles attached to the cells and thus eliciting an optical contrast to ‘‘illuminate’’ the cancer over normal cells and discriminating them based on such differential expression rather than consequential phenotypic changes. The overexpression of transmembrane EGFR in CNE2 cells caused more anti-EGFR gold nanoparticles to be selectively bounded to the cytoplasmic membrane of the CNE2 cell compared to the nominal EGFR expression in normal NHLF cells. This results in significantly higher reflectance intensity, sufficient to elicit an optical contrast between them for discriminating the cancerous against from normal cells.

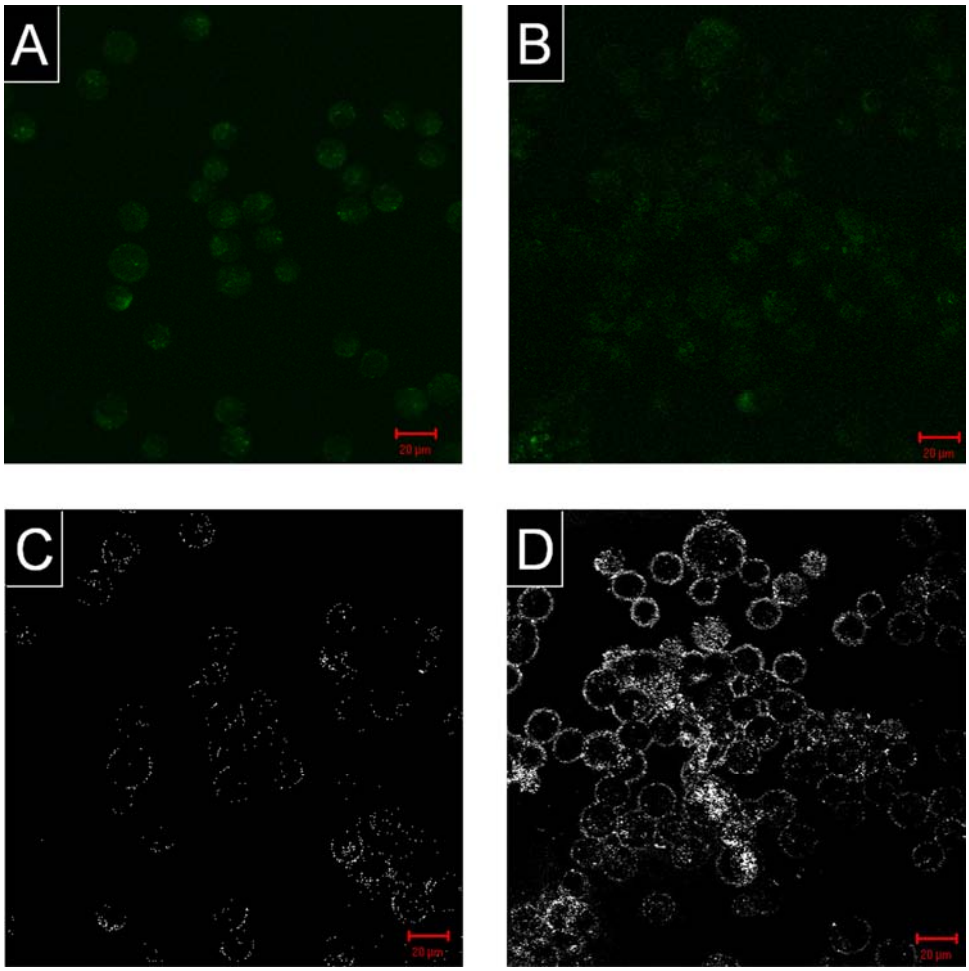

Figure 3.9. Autofluorescence image of (a) NHLF and (b) CNE2 cells. Their corresponding confocal reflectance images after labeling the (c) NHLF and (d) CNE2 cells with anti-EGFR gold nanoparticles is shown below the autofluorescence image. Images are cross-sectional slices of cells taken at the mid-focal plane at 20x magnification. False-color fluorescence images obtained at excitation 488nm and reflectance images obtained at excitation 543 nm. Scale bar in all images is 20 µm.

In practice, the EGFR expression is detected at all stages of carcinogenesis, from normal-early hyperplasia, dysplasia to invasive carcinoma [19] and it is elevated during the progression from hyperplasia to dysplasia and increases during progression from dysplasia to invasive carcinoma [7], thus giving a spectrum of expression levels with disease progression. As the reflectance signal depends on the level of EGFR expression, its intensity may provide indications of the progression of diseases at the molecular level. However, heterogeneous labeling with the anti-EGFR gold

nanoparticles on CNE2 cells was also observed (Figures 3.8c and 3.9d). This heterogeneity of protein expression in cell lines is common and has been described previously in the case of EGFR [20].

3.3.4 Molecular mapping of EGFR expression

Besides increasing the optical contrast to discriminate cancer from normal cells, the strong optical response of gold nanoparticles can also be exploited to transduce molecular signals into observable optical signals to generate molecular contrast to image the expression of EGFR in cancer cells. The potential of anti-EGFR conjugated gold nanoparticles as a probe to perform molecular imaging was investigated by first identifying the regions of high level of EGFR expression and subsequently mapping the reflectance signal from the gold nanoparticles to these regions. The confocal immunofluorescence image of a representative CNE2 cell stained with anti-EGFR is shown in Figure 3.10b together with a corresponding confocal reflectance image of CNE2 cell labeled with anti-EGFR conjugated gold nanoparticles as shown in Figure 3.10d. The intrinsic autofluorescence and reflectance images of unlabeled cells are also shown as negative control in Figure 3.10a and c respectively.

In the immunofluorescence labeling shown in Figure 3.10b, a ring of higher fluorescence intensity was observed around the cytoplasmic membrane of the CNE2 cell and not within the cell. As the image was a confocal image showing the cross-sectional slice of cells taken at the mid-focal plane, this ring of strong fluorescence intensity shows that the anti-EGFR labeling is specific and predominantly localize on the cell membrane where a high level of their transmembrane EGFR expression is

found instead of within the cell. The uniform anti-EGFR staining also implies a relatively homogenous distribution of the anti-EGFR antibody on the cell surface.

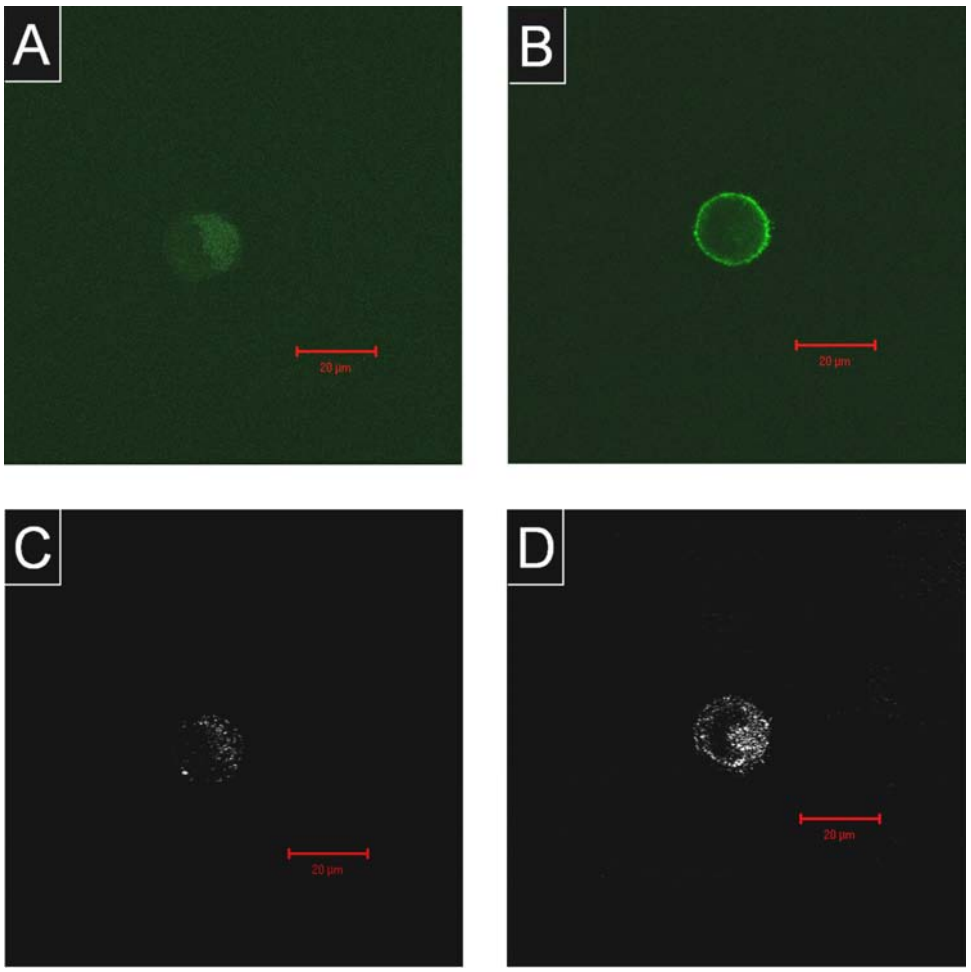

Figure 3.10. The (a) autofluorescence and (c) reflectance image of a representative unlabeled CNE2 cell is shown as control to the (b) anti-EGFR immunofluorescence labeling and (d) labeling with anti-EGFR conjugated gold nanoparticles on another representative CNE2 cell to demonstrate EGFR mapping. Images are cross-sectional slices of cells taken at the mid-focal plane at 40 x magnification. False-color fluorescence images obtained at excitation 488 nm and reflectance images obtained at excitation 543 nm. Scale bar in all images is 20 µm.

A comparison of this labeling pattern with the confocal reflectance image in Figure 3.10d shows that the strong reflectance signal that forms a bright scattering ring around the cytoplasmic membrane is consistent with the regions of high fluorescence intensity on the cell membrane. As discussed previously, this bright scattering ring is

associated with the localization of anti-EGFR gold nanoparticles on the cell membrane as it was not observed in the unlabeled cells. Since the gold labeling pattern corresponded well to the typical fluorescent labeling pattern of high EGFR expression, this strong reflectance signal was thus able to provide a map of EGFR expression under confocal reflectance microscopy. This reflectance-based optical approach to *in vitro* molecular imaging thus shows that the anti-EGFR-conjugated gold nanoparticles can serve as an effective molecular probe to target specific cancer biomarkers in cancer cells.

However, the high reflectance observed was not be found exclusively on the membrane as other cellular components could also produce such reflective signals. Apart from this ring of bright scattering, a region of higher reflectance signal within the cell was also observed as seen from the intrinsic reflectance image of the unlabeled cell in Figure 3.10c. As this region was present in the cell without the gold nanoparticles staining (Figure 3.10c), it could not be due to the presence of gold nanoparticles in the cytoplasm.

It is widely known that cells have their own region of intrinsic reflectance as the cell nucleus and other various organelles in the cells are also known to be generally reflective due to the changes in their refractive index from the cytoplasm. This was observed in Figure 3.10c where the region of visible reflectance at the top right of the cell could possibly be due to the reflectance from the nucleus and not from the cell membrane since this region occupied a sizeable portion of the cell and was not continuous around the cell perimeter. The reflectance from the membrane, on the other hand, appeared weak as it was not evident especially at the bottom left of the

cell. Similarly, the region of higher reflectance signal inside the cell in Figure 3.10d may also be attributed to the cell nucleus. Therefore, the signal-to-noise ratio achieved using such reflective probe to image biomarker expression is generally lower than that achieved with fluorescent probes.

Despite such reflectance noise from other cellular components, the results have still shown the ability of gold nanoparticles probe to discriminate between cancer and normal cells based on the reflectance images and that the reflectance signal from the gold nanoparticles probes should provide sufficiently high contrast against intrinsic reflectance signals in cells and tissue to map the biomarker expression under certain imaging modalities where the use of fluorescence regime is not possible e.g. in OCT.

3.4 Conclusion

As cancer-associated molecular markers precede phenotypic manifestations of disease, there is a growing research interest in clinical molecular diagnostics for early cancer detection. Combining advances in biomedical optics and nanotechnology offers the opportunity to significantly impact future strategies towards the detection of cancer. This preliminary study demonstrates the potential of antibody conjugated gold nanoparticles to target and provide an optical contrast to discriminate cancer from normal cells based on their differential expression of EGFR as well as their potential to map the EGFR expression for molecular imaging under reflectance-based imaging.

The results of this preliminary *in vitro* study can be extended to noninvasive *in vivo* imaging using other reflectance-based high resolution optical imaging systems such as OCT or fiber based reflectance confocal endomicroscopy imaging systems, where the

use of gold nanostructures as optical contrast agents can widen the functionality of these imaging systems to include molecular imaging of cancerous signatures of the tissue, in addition to their ability to perform anatomical imaging.

This combination of detailed anatomical resolution coupled with molecular information from suspicious epithelial lesions can greatly enhance the sensitivity and specificity of optical imaging *in vivo* to provide more information about the diseased site for early cancer detection. The current results encourage further work in developing and assessing other types of gold nanostructures as potential *in vivo* contrast agents with a red-shifted surface plasmon resonance appropriate for use with the NIR illumination wavelength of OCT. One such promising gold nanostructure is the gold nanoshells and its synthesis is described in the following Chapter 4.

3.5 References

1. Schultz S, Smith DR, Mock JJ, Schultz DA. Single-target molecule detection with nonbleaching multicolor optical immunolabels. *Proc Natl Acad Sci U S A* 2000; 97(3): 996-1001.

2. Sokolov K, Follen M, Aaron J, Pavlova I, Malpica A, Lotan R, Richards-Kortum R. Real-time vital optical imaging of precancer using anti-epidermal growth factor receptor antibodies conjugated to gold nanoparticles. *Cancer Res* 2003; 63(9): 1999-2004.

3. El-Sayed IH, Huang X, El-Sayed MA. Surface plasmon resonance scattering and absorption of anti-EGFR antibody conjugated gold nanoparticles in cancer diagnostics: applications in oral cancer. *Nano Lett* 2005; 5(5): 829-834.

4. Zheng W, Harris M, Kho KW, Thong PS, Hibbs A, Olivo M, Soo KC. Confocal endomicroscopic imaging of normal and neoplastic human tongue tissue using ALA-induced-PPIX fluorescence: a preliminary study. *Oncol Rep* 2004; 12(2): 397-401.

5. Mulvaney P. Surface Plasmon Spectroscopy of Nanosized Metal Particles. *Langmuir* 1996; 12(3): 788-800.

6. Geoghegan WD, Ackerman GA. Adsorption of horseradish peroxidase, ovomucoid and anti-immunoglobulin to colloidal gold for the indirect detection of concanavalin A, wheat germ agglutinin and goat anti-human immunoglobulin G on cell surfaces at the electron microscopic level: a new method, theory and application. *J Histochem Cytochem* 1977; 25(11): 1187-1200.

7. Shin DM, Ro JY, Hong WK, Hittelman WN. Dysregulation of epidermal growth factor receptor expression in premalignant lesions during head and neck tumorigenesis. *Cancer Res* 1994; 54(12): 3153-3159.

8. Eisbruch A, Blick M, Lee JS, Sacks PG, Gutterman J. Analysis of the epidermal growth factor receptor gene in fresh human head and neck tumors. *Cancer Res* 1987; 47(13): 3603-3605.

9. Ke LD, Adler-Storthz K, Clayman GL, Yung AW, Chen Z. Differential expression of epidermal growth factor receptor in human head and neck cancers. *Head Neck* 1998; 20(4): 320-327.

10. Nouri AM, Thompson C, Cannell H, Symes M, Purkiss S, Amirghofran Z. Profile of epidermal growth factor receptor (EGFr) expression in human malignancies: effects of exposure to EGF and its biological influence on established human tumour cell lines. *Int J Mol Med* 2000; 6(4): 495-500.

11. Shin DM, Gimenez IB, Lee JS, Nishioka K, Wargovich MJ, Thacher S, Lotan R, Slaga TJ, Hong WK. Expression of epidermal growth factor receptor, polyamine levels, ornithine decarboxylase activity, micronuclei, and transglutaminase I in a 7,12-dimethylbenz(a)anthracene-induced hamster buccal pouch carcinogenesis model. *Cancer Res* 1990; 50(8): 2505-2510.

12. Todd R, Wong DT. Epidermal growth factor receptor (EGFR) biology and human oral cancer. *Histol Histopathol* 1999; 14(2): 491-500.

13. Abrams MJ, Murrer BA. Metal compounds in therapy and diagnosis. *Science* 1993; 261(5122): 725-730.

14. Hayat M. Colloidal gold: principles, methods and applications. San Diego, CA: Academic, 1989.

15. Zhang CX, Zhang Y, Wang X, Tang ZM, Lu ZH. Hyper-Rayleigh scattering of protein-modified gold nanoparticles. *Analytical Biochemistry* 2003; 320(1): 136-140.

16. Murillo LE, Viera O, Vicuna E. Growth kinetics of gold nanoparticles. *Comput Nanosci Nanotechnol* 2002: 435-438.

17. Taroni P, Pifferi A, Torricelli A, Comelli D, Cubeddu R. In vivo absorption and scattering spectroscopy of biological tissues. *Photochem Photobiol Sci* 2003; 2(2): 124-129.

18. Bohren CF, Huffman DR. Absorption and Scattering of Light by Small Particles. New York, NY: Wiley-Interscience, 1998.

19. Kannan S, Balaram P, Chandran GJ, Pillai MR, Mathew B, Nair MK. Co-expression of ras p21 and epidermal growth factor receptor during various stages of tumour progression in oral mucosa. *Tumour Biol* 1994; 15(2): 73-81.

20. Monaghan P, Ormerod MG, O'Hare MJ. Epidermal growth factor receptors and EGF-responsiveness of the human breast-carcinoma cell line PMC42. *Int J Cancer* 1990; 46(5): 935-943.

CHAPTER FOUR

SYNTHESIS OF GOLD NANOSHELLS

Abstract

The promising results from the gold nanoparticles provide impetus for further studies on the use of gold nanoshells for NIR imaging. This chapter provides a description of the synthesis of gold nanoshells which involves the preparation of precursor seed particles consisting of nanoparticulate gold loaded on a dielectric core as scaffolds on which the layer of contiguous gold shell is grown. The conventional route in preparing these seed particles involves a two-step process of synthesizing colloidal gold nanoparticles followed by attaching them to amine functionalized dielectric core. In this chapter, the use of a single step direct deposition-precipitation (DP) process to replace the two-step process is described. The various factors such as pH (4-11), temperature (65-86 °C) and time (3-60 minutes) of reaction, as well as the effect of amine functionalization of silica on the deposition of gold onto amorphous silica spheres were investigated. Amine functionalization of the silica surface is able to alter its isoelectric point to facilitate the deposition of gold hydroxide nanoparticles ($Au(OH)_3$). By varying the pH and time of reaction, it is also possible to control the size of $Au(OH)_3$ nanoparticles and density of seeding. The progressive growth of the $Au(OH)_3$ seeds to eventually form a complete layer of gold shell was monitored by TEM and the bathochromic shift of the UV-Vis extinction was correlated with the evolution of shell growth. The work presented in this chapter has been published in *Gold Bulletin 2008; 41: 23-36* and *Langmuir 2008; 24: 5109-5112*.

4.1 Introduction

The common synthesis route of gold nanoshells involves the synthesis of the dielectric core material e.g. silica or polystyrene spheres and the attachment of small nanoparticulate gold such as colloidal gold nanoparticles, usually formed from a separate process, onto their surface to form the precursor seed particle for subsequent growth of the polycrystalline gold shell in a controlled manner (Figure 4.1a) [1-4]. However, it has proved challenging to attain high dispersions of gold nanoparticles over silica surfaces [2, 5] and has led Halas et al. to devise a procedure where an amine-terminated coupling agent was grafted to the core surface to functionalize the surface with terminal amine groups that facilitate the capture and attachment of colloidal gold [6] (Figure 4.1a). As there is usually a weak interaction between the core material and gold, the grafting of an amine terminated coupling agent to the core grants it a nucleophilic surface for coordinate bonding with the gold nanoparticles.

This approach has proved suitable for several core materials (e.g., silica, polystyrene, ferrous oxide) [1, 4, 7], although the process is costly and tedious. In this common synthesis route, the colloidal gold particles function as nucleation sites for the additional gold to be added on to eventually form a shell. These small colloidal gold are typically formed from the reduction of gold salt by strong reducing agents [8, 9] and may require several days of aging [3], up to 2 weeks for their size to stabilize before they are seeded onto the surface functionalized silica core. Whilst this common two-step process of seeding i.e. formation of small colloidal gold followed by attachment to the core is effective, it is also laborious and costly.

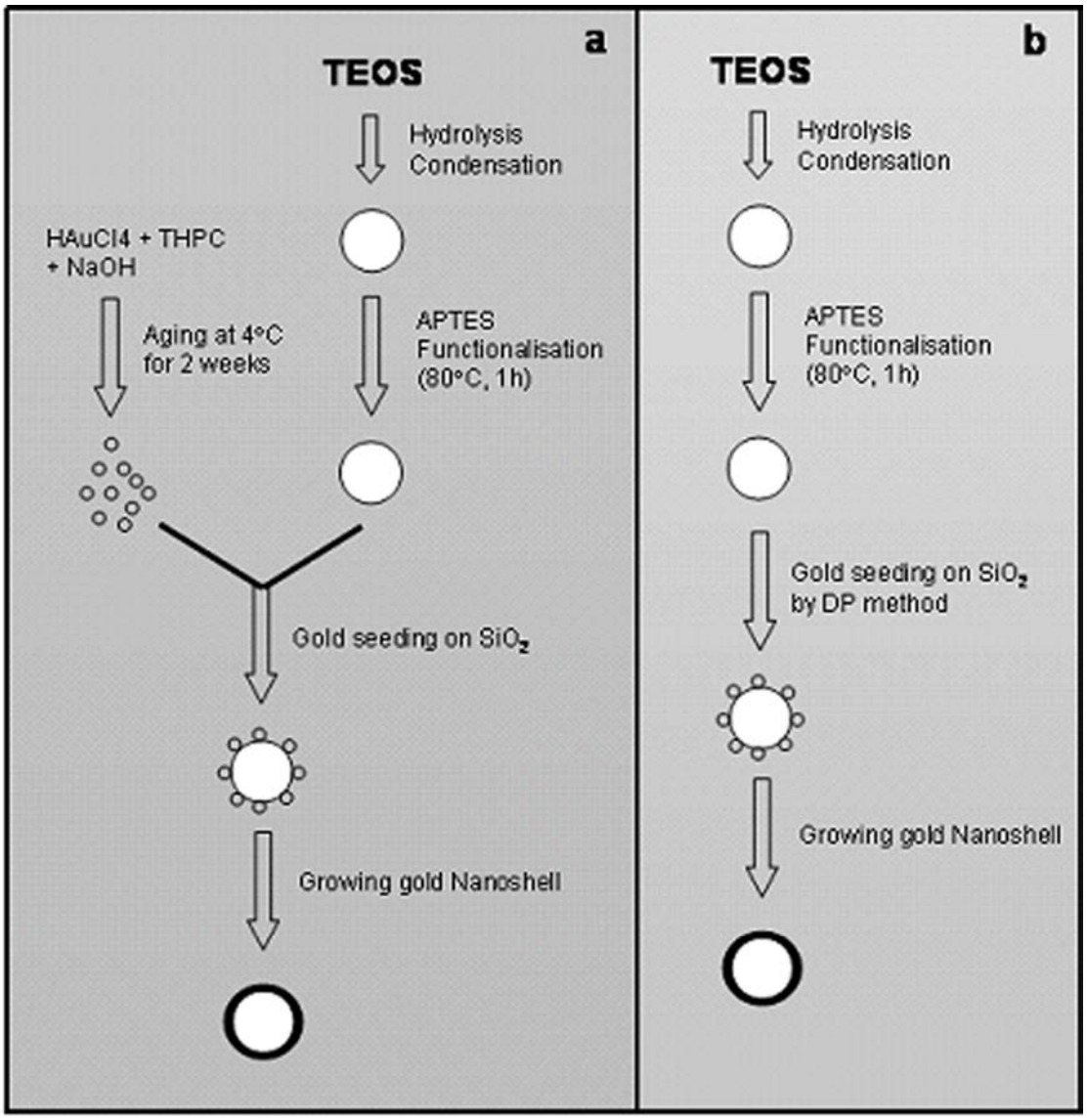

Figure 4.1. The approach for synthesis of gold nanoshells using the (a) common two-step process of seeding gold nanoparticulate on silica and (b) the single step DP process of gold seeding on silica prior to subsequent shell growth.

Different surface seeding strategies were also reported by other groups to prepare the precursor seed particles. Examples of these strategies include the use of electrostatic attraction to attach preformed anionic colloidal particles onto a polycationic polyethyleneimine functionalized polystyrene microspheres, as demonstrated by Ji et. al [10]. Besides using preformed colloidal particles, the electroless plating approach is another strategy where the metal ions or complex cations were absorbed onto the

silica surface by the negatively charged Si-OH groups on the surface through electrostatic attraction and were subsequently reduced in situ to form the seed particles [11, 12]. Another possible approach employed the use of the solvent-assisted route where the polystyrene core was immersed in a mixed solvent of ethanol and acetone containing the gold salt, causing the surface layer of the polystyrene colloid to swell by the mixed solvent and permeated by the gold ions. The gold ions were subsequently reduced such that the swollen layer of the polystyrene colloids was uniformly loaded with gold nanoparticles [12]. Apart from seeding using colloidal gold or silver, Lim et al. seeded tin (Sn) particles on the surface of silica, which in this case, the Sn particles formed on the silica surface acted as a linker site between the silica core and the gold shell as well as an efficient catalytic surface for the reduction of gold ions on the silica surface [13].

The deposition-precipitation (DP) process of loading small gold particles on a metal oxide support base developed by Haruta's group is an attractive alternative that can directly crystallize gold on silica [14]. It has been widely investigated in the catalytic field to form supported nanoparticulate gold catalysts for low temperature oxidation of carbon monoxide [15-19]. The DP method, in essence, entails placing the support in contact with an aqueous solution of gold (III) chloride ($HAuCl_4$), the pH of which has been raised by the addition of a base, so that upon heating, oxidic precursor particles are formed on the support. The size and density of the nanoparticulate gold on the substrate is easily controlled by key parameters, including the concentration of $HAuCl_4$ and its mass ratio to the support, type of support base, reaction temperature and time, and the pH of reaction [18].

This DP method is the easiest to handle and is used now for producing commercial gold catalysts in a highly controlled manner. However, stringent control of these variables is required to avoid diversiform gold crystals as the isoelectric point (IEP) of silica is close to pH 2 [20, 21], above which the surface is negatively charged and unsuitable for the fine deposition of anionic gold species (e.g. $[Au(OH)_xCl_{4-x}]^-$). Alternatively, basic conditions may be used, but cationic complexes such as $[Au(en)_2]^{3+}$ are difficult to prepare [22].

In the synthesis of gold nanoshells described in this chapter, the DP method is demonstrated as a simple and direct alternative route to loading nanoparticulate gold onto the silica core that serve as nucleation sites in a single-step process to form the precursor seed particle without the need for prior synthesis of colloidal gold (Scheme 1b). Compared to the widely-used two-step technique of synthesizing small colloidal gold particles from reducing $HAuCl_4$ by alkaline tetrakis(hydroxymethyl) phosphonium chloride (THPC) followed by attaching them to the surface functionalized silica core [1-4], this method results in a single-step process to form the precursor seed particles. This precursor seed particle was then used for further growth of a layer of gold shell to form the gold nanoshells. The various factors such as the pH, temperature and time of reaction, as well as the presence of surface functionalization on the deposition of gold were investigated and optimized. The gradual growth of the homogenous gold shell on the precursor seed particle prepared from this DP method is also demonstrated. The effects of other reactants on the growth of the shell will also be briefly discussed.

4.2 Materials and methods

4.2.1 Reagents for synthesis

The reagents used for the synthesis of silica nanoparticles include tetraethyl orthosilicate (TEOS, 99%, Merck), ammonia (NH_3, 27%, Merck), ammonia hydroxide (NH_4OH, 14.2 M, ISPL), absolute ethanol (C_2H_5OH, 99.9%, Merck) and milliQ water. 3-aminopropyltriethoxysilane (APTES, Sigma-Aldrich) dissolved in 1 part water and 3 parts absolute ethanol to form a 12 mM APTES stock solution was used as an amine terminated silanizing agent to functionalize the surface of the silica nanoparticles with an amine terminal group. Hydrogen tetrachloroaurate (III), also known as gold (III) chloride ($HAuCl_4.3H_2O$, 99.99%, Alfa Aesar) was prepared in 6.35 mM and 25 mM aqueous solution for the DP process of seeding gold hydroxide ($Au(OH)_3$) nanoparticles and for growing of the gold shell respectively. A solution of 0.1M sodium hydroxide (NaOH, Merck) was used to adjust the pH during the DP process of seeding. Potassium carbonate (K_2CO_3, 99%, Sigma-Aldrich) was used to raise the pH of HAuCl4 for its hydrolysis to form gold hydroxide solution for growing the gold shell. Both the sodium borohydride ($NaBH_4$, 98%, Sigma-Aldrich) and sodium citrate dihydrate ($HOC(COONa)(CH_2COO\ Na)_2.2H_2O$, 99%, Aldrich) were used in the reduction process of the gold hydroxide solution to grow the gold shell.

4.2.2 Synthesis of silica core and surface functionalization

The dielectric monodisperse silica nanoparticles were synthesized using the common Stöber procedure [23], which involved the hydrolysis and condensation of TEOS in a sol-gel process. The volume of individual reagents in the reaction mixture used for producing the different sizes of silica nanoparticles were summarized in Table 4.1.

The mixtures were allowed to stir vigorously overnight for the reaction to complete. The white turbid suspension was subsequently centrifuged and washed in ethanol and distilled water for at least 5 times at 10,000 rpm for 30 minutes each before resuspending them in 80% by mass of absolute ethanol prior to surface functionalization. Using this protocol, spherical and monodispersed silica nanoparticles from a size range of 50 nm to 440 nm in diameter were synthesized.

Table 4.1. Reaction volumes of various reactants used to synthesize the silica nanoparticles core of different diameter sizes.

Size (nm)	Ethanol (ml)	H_2O (ml)	NH_3 (ml)	NH_4OH (ml)	TEOS (ml)
78.9 ± 10.5	138.0	10.8	-	2.4	6.6
120.6 ± 8.4	92.0	3.1	-	4.45	6.0
210.9 ± 8.0	138.0	4.65	0.675	6.0	9.0
248.8 ± 16.7	138.0	4.65	3.75	6.0	9.0
298.9 ± 11.2	138.0	4.65	6.0	6.0	9.0
377.0 ± 14.7	138.0	10.8	15.0	6.0	9.0
439.7 ± 14.7	138.0	10.8	30.0	6.0	9.0

The silica nanoparticles were then surface functionalized with a terminal amine group by grafting them with 12 mM APTES in volume ratio of 3:7 under constant heating and vigorous stirring at 80 °C for 1 h to make the surface amenable for deposition of small gold particles. Under this condition, the APTES used was in molar excess to achieve a complete surface functionalization. The amine grafted silica particles were then cooled to room temperature and washed with at least 7 cycles of centrifugation and redispersion in absolute ethanol and distilled water at 8,000 rpm for 30 minutes

each to remove residual reactants before resuspending them in 1 ml of water for every 0.3 g of silica used for surface functionalization.

4.2.3 DP process of seeding gold hydroxide nanoparticles

The amine grafted silica nanoparticles were then seeded with $Au(OH)_3$ nanoparticles on its surface using the DP process. Briefly, 4.5 ml of 0.1M NaOH was added to 20 ml of 6.35 mM solution of $HAuCl_4$ and allowed to stir for about 15 minutes before the solution became mild yellowish. The addition of NaOH raised the pH of the $HAuCl_4$ and allowed hydrolysis of $HAuCl_4$ to take place to form gold hydroxide solution at pH 8 as shown in the reaction schematic in Figure 4.2.

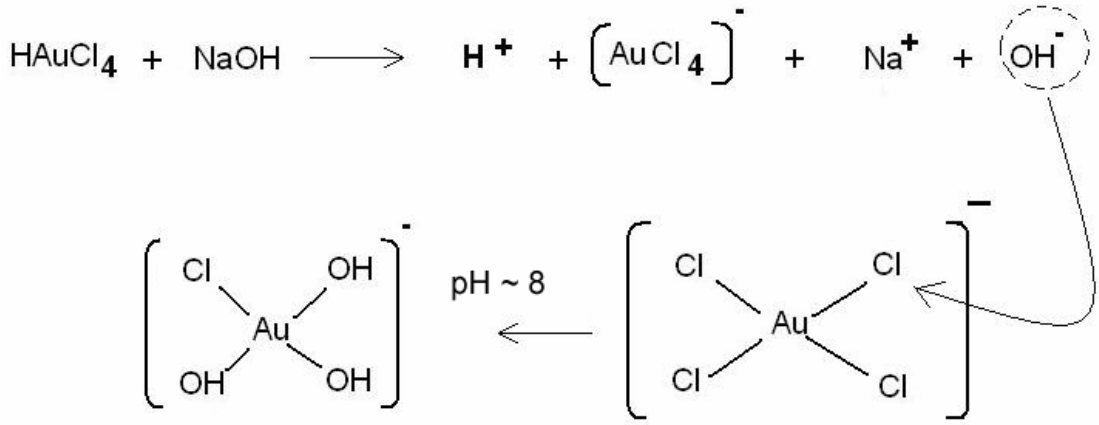

Figure 4.2. Hydrolysis of $HAuCl_4$ by addition of NaOH to form gold hydroxide $HAuCl(OH)_3$ (or $Au(OH)_3$) solution for subsequent seeding onto the silica nanoparticles.

The amine grafted silica particles in 1 ml was then added to this gold hydroxide solution and the solution was heated at 70 °C for 30 minutes under vigorous stirring where the color of the mixture turned from milky white to orange-brown as shown in Figure 4.3 as an indication of successful loading of $Au(OH)_3$ nanoparticles on the

amine grafted silica. The product was then centrifuged and washed with distilled water for at least 5 times at 800 rpm for 1 h each and the final brown pellet was ultrasonically redispersed in distilled water to give a final volume of 40 ml of precursor seed solution.

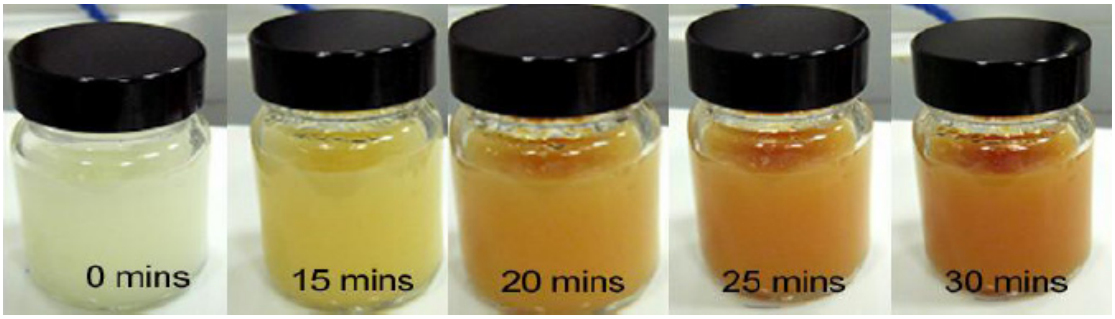

Figure 4.3. Gradual color change during the DP process indicates the loading of $Au(OH)_3$ nanoparticles on the amine grafted silica. It was later found from the TEM images that the darker the solution, the higher the density of seeding.

Based on mass calculation, the concentration of the 300 nm diameter precursor seed particles in the seed solution was of the order of 2.3×10^{11} particles per ml. In this study, the pH, temperature and heating time of reaction were varied to investigate the effects of these factors on the size and seeding density of the $Au(OH)_3$ nanoparticle seeds. The pH was varied by changing the volume of 0.1M NaOH added to the $HAuCl_4$. The $Au(OH)_3$ nanoparticles were deposited on a range of different sizes of silica cores as shown in Table 4.1. The direct seeding of $Au(OH)_3$ nanoparticles on silica surface without the terminal amine group was also investigated. In this case, the synthesized silica nanoparticles were added directly to the gold hydroxide solution and the mixture heated to proceed with the DP process.

4.2.4 Growth of gold shell

The $Au(OH)_3$ nanoparticles deposited on the surface of the silica acted as nucleation sites and were allowed to grow in size by further addition of more gold reduced from $HAuC1_4$ onto these small gold hydroxide nanoparticles until they eventually coalesce together to form a continuous complete layer of gold shell around the silica core. In growing the shell, the pH of $HAuCl_4$ was adjusted to around 10.1 by addition of 60 mg of K_2CO_3 to 1.5 ml of 25 mM $HAuCl_4$ diluted in 100 ml of water and allowing the solution to stir in the dark overnight at room temperature for the $HAuCl_4$ to hydrolyze and age to give a colorless gold hydroxide solution. This solution is subsequently referred to as K-gold. The 40 ml of precursor seed particles were ultrasonically redispersed and 0.5 ml of the seed solution was added to different volumes of K-gold before a freshly prepared 6.6 mM $NaBH_4$ was added at 1 ml for every 10 ml of K-gold to reduce the complex gold hydroxide anions in the K-gold onto the $Au(OH)_3$ seeds. This reduction resulted in an almost immediate color change: red, purple, blue or green depending on the shell thickness and degree of completeness.

The ratio of seed solution to K-gold solution controls the amount of gold available for deposition on the silica surface, hence the growth of the shell depended on the amount of K-gold used. Different volume ratios of K-gold to precursor seed particles from 5:1 to 300:1 were varied to demonstrate the progressive growth of the shell. In this reduction step, 1 ml of 10 mM sodium citrate dihydrate per 20 ml of K-gold was also added to slow the reaction and stabilize the gold nanoshells by acting as a capping agent. Using this approach of synthesis, the core size and shell thickness of the gold nanoshells could be varied by changing the size of the silica core nanoparticles and the amount of $HAuCl_4$ for reduction respectively. The gold nanoshells were prepared

to a final concentration of 5 x 10^9 particles per ml as determined using absorption spectroscopy and were stored at 4 °C when not in use.

4.2.5 Characterization of gold nanoshells

The synthesized silica, precursor seed particles and gold nanoshells at different stages of shell growth was imaged using the transmission electron microscopy (TEM) (Jeol JEM-2100F) in brightfield mode using an objective aperture of 20 µm operating at 200 kV. The particle size was also characterized by TEM. Samples were prepared by placing a drop of solution on a carbon coated copper grid and allowing the grid to dry on filter paper. The average size and size distribution of the silica nanoparticles were determined from the TEM images using the ImageJ software (National Institutes of Health, USA). The optical extinction spectrum of gold nanoshells at different stages of shell growth was measured in water using a UV-Vis spectrophotometer (Shimadzu UV-2401 PC) in the wavelength range from 400 nm to 900 nm with the sample placed in a cell with a pathlength of 10 mm.

To compare the experimentally measured spectrum with theoretically predicted spectrum, a program for the calculation of theoretical optical spectrum of core-shell structures based on Mie theory was written in MATLAB (see Chapter 2). This program is similar to that used to compute the optical cross section space maps as described earlier in Chapter 2. The calculations require the following as input: the refractive indices of the silica core (assumed to be constant at η = 1.43) and the water medium (η = 1.33), the frequency-dependent dielectric constant of gold [24], the size of the core, and the thickness of the shell. The theoretical extinction spectrum was predicted using the data for the silica core radius obtained by TEM measurements and

the thickness of the gold shells was calculated by subtracting the silica core radius from the total particle radius also obtained by TEM. These spectra were then adjusted to the measured extinction spectra by a fitting procedure.

4.3 Results

4.3.1 Effect of amine terminated surface functionalization

The influence of surface functionalization of the silica cores with a terminal amine group on the deposition of $Au(OH)_3$ nanoparticles during the DP process of seeding was investigated. Both amine grafted and ungrafted silica cores were subjected to the same seeding conditions in DP and the results are shown in Figure 4.4 for a 30 minutes heating with 6.35 mM $HAuCl_4$ adjusted to pH 8 with 4.5 ml of 0.1 M NaOH.

The presence of the terminal amine group on the surface of amine functionalized silica results in $Au(OH)_3$ nanoparticles that were smaller and uniform in size and shape, although large gold clusters were occasionally observed (Figure 4.4c). The formation of these large clusters is discussed in more detail as the effect of heating duration is examined. The $Au(OH)_3$ seeds formed were homogenously distributed on the silica surface with high seeding density i.e. small inter-particle distances and high coverage on the silica core. The seed particles were typically about 4 nm in size.

In contrast, the $Au(OH)_3$ seeds on the bare surface of the ungrafted silica cores were generally larger and less uniform in size and shape. The seed particles in this case range from 4 to 15 nm. The distribution of these seed particles was also less homogenous with regions of different seeding density observable, although in general,

the seeding density and hence surface coverage is lower on the ungrafted silica compared to the amine grafted silica cores. This result clearly shows the influence of the amine terminated surface functionalization on the DP process of seeding $Au(OH)_3$ nanoparticles in terms of the seed size, uniformity and surface coverage.

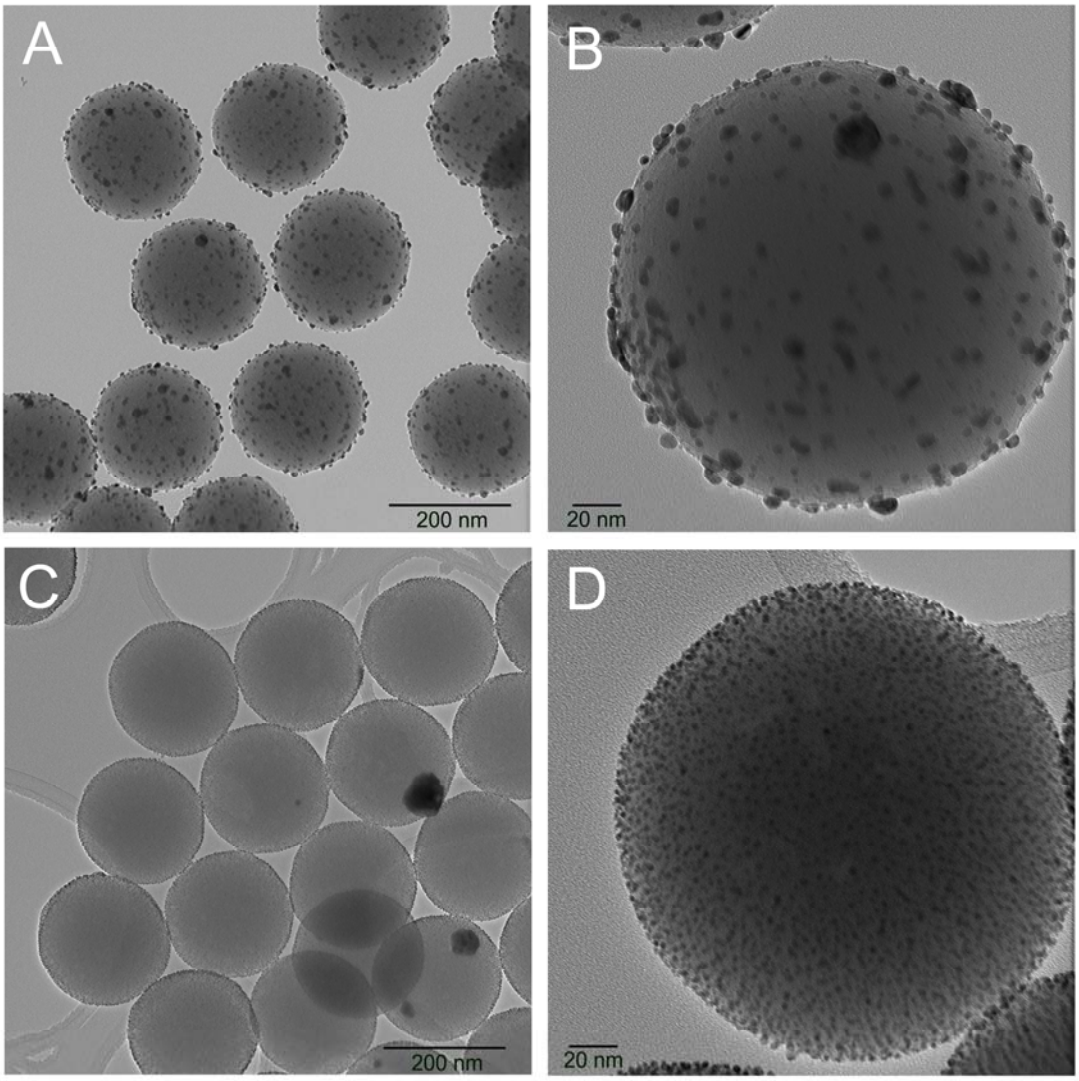

Figure 4.4. The DP process of seeding gold hydroxide nanoparticles on (a) ungrafted naked silica cores with (b) a higher magnification image of a single precursor seed particle. This seeding result is compared to (c) silica cores grafted with terminal amine groups and (d) its corresponding higher magnification image of a single precursor seed particle showing the details of the gold hydroxide nanoparticles.

4.3.2 Effect of pH

The pH in which the DP process occurs was varied by adding different amounts of 0.1 M NaOH to the 6.35 mM $HAuCl_4$ to investigate how the pH and hence the degree of hydrolysis of $HAuCl_4$ affects the loading of $Au(OH)_3$ nanoparticles on the amine grafted silica. Four different amounts of NaOH was used: 1.6 ml, 3.3 ml, 4.5 ml and 6 ml, and these results in approximate pH of 4, 6, 8 and 11 respectively after 15 minutes of stirring the hydrolyzed $HAuCl_4$ solution prior to adding the amine grafted silica. The DP process of loading $Au(OH)_3$ nanoparticles under these four pHs with 30 minutes heating is shown in Figure 4.5.

At low pH of around 4, the solution was pale yellow after the DP reaction and the TEM image revealed that the density of the seed was low and was not very homogenously distributed with regions showing higher density of $Au(OH)_3$ nanoparticles compared to others (Figure 4.5a). The seed particles were generally small, typically < 5 nm, although the variation in size distribution is large with seed particles as big as 10 nm.

As the pH increases to 6, the solution turned orange. One dominant observation under the TEM was the presence of two populations of seed particles with different sizes formed on the amine grafted silica core (Figure 4.5b). The smaller seed particles with sizes of < 2 nm were seeded with high density on the surface. These small particles were as fine as 1 nm and they achieved an almost complete coverage on the surface. The large seed particles with mean size of about 7 nm were scattered amongst the smaller seeds in a non-homogenous manner and with much lower seeding density.

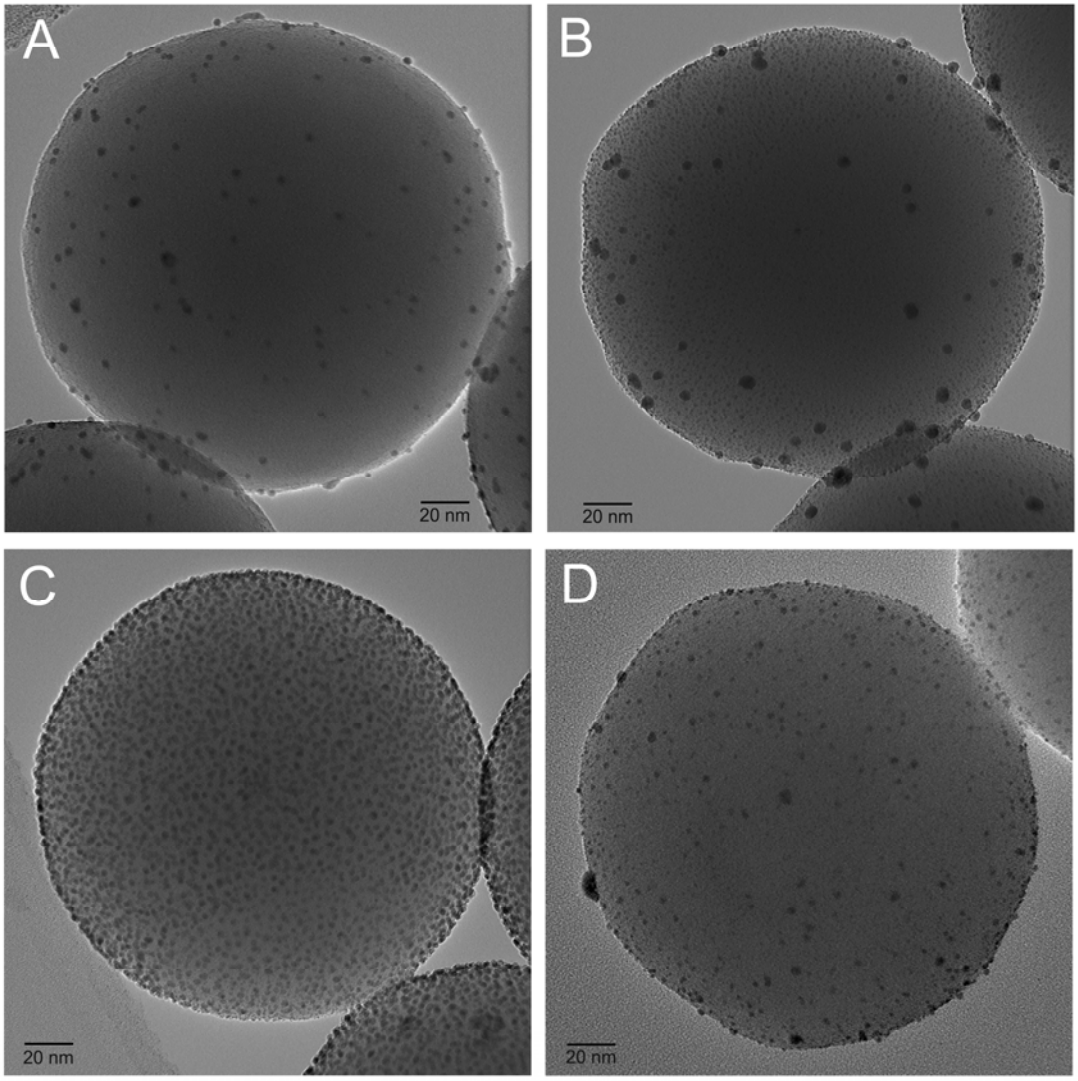

Figure 4.5. The DP process of seeding gold hydroxide nanoparticles at (a) pH of 4, (b) pH of 6, (c) pH of 8 and (d) pH of 11 on the surface of amine functionalized silica cores to illustrate the influence of pH on the seeding efficiency using the DP method.

These two populations were not observed when the pH was raised further to pH 8 where similar observations were made as that shown in Figure 4.4d. At this pH, the solution after the DP reaction was dark orange and the density of $Au(OH)_3$ nanoparticle seeds on the silica core remains high and homogenously distributed with a narrow size distribution centered at around 4 nm (Figure 4.5c).

Further increase in the pH to 11 reduced the density of the $Au(OH)_3$ nanoparticle seeds although the particles remained rather homogeneously distributed on the silica core (Figure 4.5d). The lower density of seeds results in a pale yellow solution similar to that observed at pH 4, but in this case, the density of the seeding is slightly higher than pH 4. The $Au(OH)_3$ seed particles had a large variation in size distribution, ranging from 4 nm to as big as 20 nm. These results thus suggest a general pH dependence of the size and seeding density of the $Au(OH)_3$ seeds on the silica core and that to achieve a high density of $Au(OH)_3$ loading for subsequent effective shell growth, a rather narrow optimal working range of pH at around 8 needs to be effected.

4.3.3 Effect of temperature and duration of reaction

The DP reaction for the formation and deposition of $Au(OH)_3$ nanoparticles on the amine functionalized silica cores was observed to occur only at temperature over 65 °C. The mixture containing the hydrolyzed $HAuCl_4$ solution at pH 8 and amine grafted silica remained milky white at < 65 °C, but started to turn pale yellow at around 65 °C before eventually turning dark orange as heating continued. It was found that the temperature of reaction had little influence on the size and seeding density of the seeds. The DP reaction heated at 68 °C and 86 °C for the same duration of less than 20 minutes showed no observable differences in the size of the $Au(OH)_3$ seeds or their density of seeding (results not shown).

However, the duration of heating at temperature > 67 °C affected the size of the deposited $Au(OH)_3$ nanoparticle seeds. This influence of heating duration was investigated by heating the mixture (with pH 8) at 70 °C for 3, 30, and 60 minutes and the results were shown in Figure 4.6. Generally, the mean $Au(OH)_3$ nanoparticles

seed size increased with the duration of heating from 2 nm for a 3 minutes reaction time to 4 nm for a 30 minutes reaction time and 7 nm for a 60 minutes reaction time.

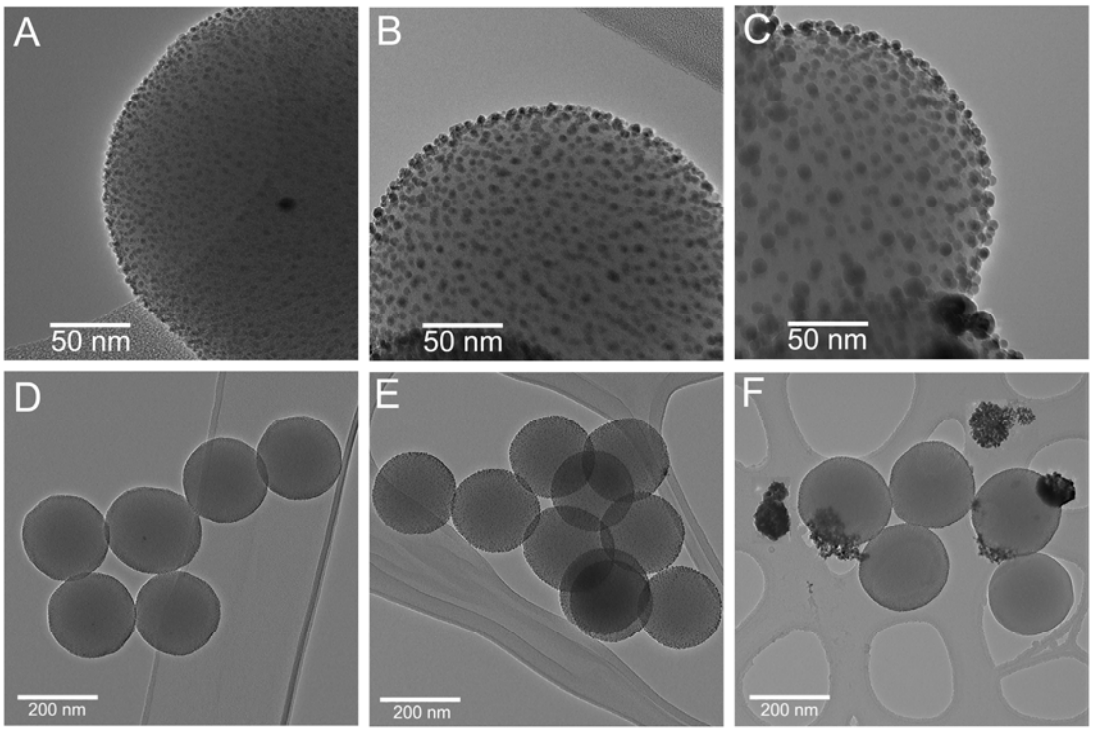

Figure 4.6. Comparison of DP process of seeding small gold nanoparticles on amine functionalized silica cores for different heating duration of 3, 30 and 60 minutes at temperature > 67 °C. Images on the top row were taken with the same magnification of 150,000X while images on the bottom row were taken with the same magnification of 20,000X.

Beyond an hour of heating, the size of the $Au(OH)_3$ seeds was observed to remain unchanged at 7 nm. However, the more prominent observation with prolonged heating was the higher tendency for formation of large gold clusters, typically larger than 20 nm as the heating proceeded beyond 30 minutes (Figure 4.6c). The formation of these large gold clusters would subsequently affect the growth of gold shell on the precursor seed particles as these gold clusters could also serve as catalytic sites that compete with the $Au(OH)_3$ nanoparticles seeds for the reduction of additional gold during the shell growth process.

4.3.4 Growth of gold shell

The versatility of using the DP process to seed $Au(OH)_3$ nanoparticles on a range of silica core sizes functionalized with a terminal amine group: 50, 130, 220, 300 and 440 nm in diameter is demonstrated. The precursor seed particles formed from different sizes of silica core at pH 8 with reaction duration of 30 min are shown in Figure 4.7. For the range of silica sizes investigated, the size and size distribution of the $Au(OH)_3$ nanoparticle seeds remained uniformly centered at 4 nm and the $Au(OH)_3$ nanoparticles were also homogenously distributed on the surface.

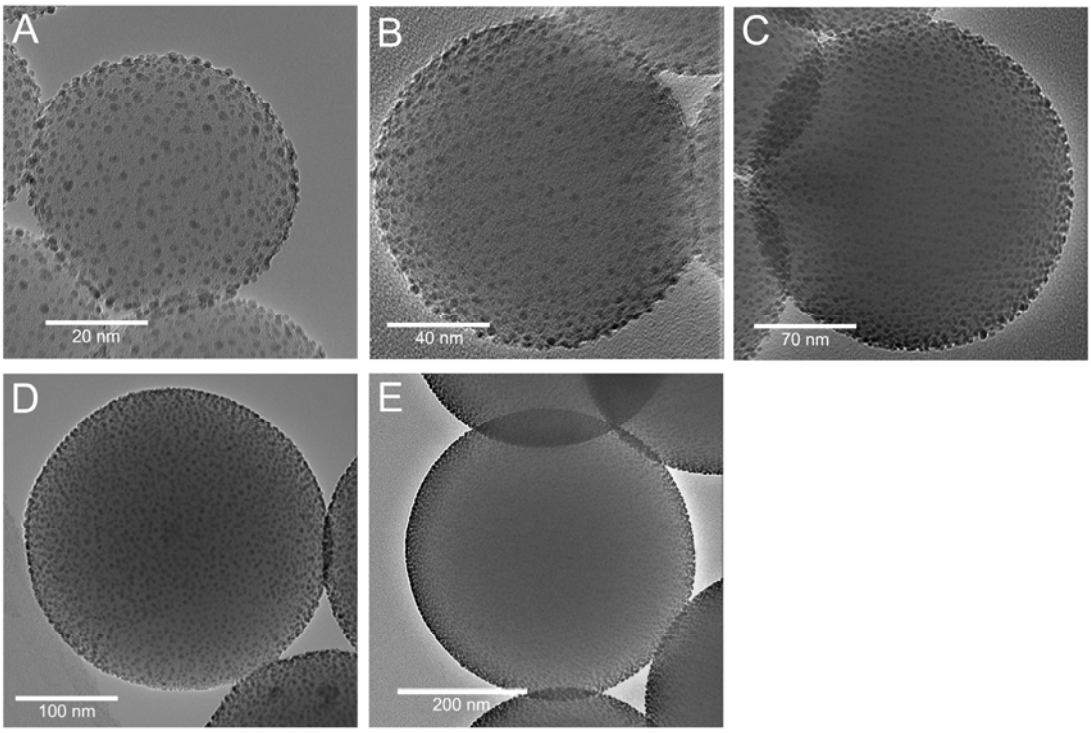

Figure 4.7. Precursor seed particles formed from a range of five different silica cores sizes: 50, 130, 220, 300, and 440 nm, as shown from (a) to (e) respectively, using the DP process of seeding small gold hydroxide nanoparticles on silica cores at pH 8 and with a reaction duration of 30 min.

The precursor $Au(OH)_3$ seeded silica formed from seeding at pH 8 under a seeding temperature of 70 °C for 30 min (Figure 4.8a) were then used for the further growth of a layer of gold shell around the silica by reducing more hydrolyzed $HAuCl_4$ i.e. gold hydroxide solution from the aged K-gold on them. Different K-gold-to-seed ratios from 5:1 to 300: 1 were used to progressively grow the $Au(OH)_3$ seed nanoparticles until they coalesce together with their increase in size and eventually form a complete layer of gold shell. The typical growth of the seed particles on a silica core size of 300 nm diameter is illustrated in Figure 4.8 as an example. The results for increasing K-gold-to-seed ratios of 5:1, 20:1, 40:1, 70:1, 100:1, 160:1, 200:1 and 300:1 for growing a shell around the 300 nm core are shown in Figure 4.8b to i respectively.

The results show a progressive growth in the seed size at lower ratios up to around 70:1, beyond which they started to coalesce together at 100:1. At a ratio of 200:1, the amount of gold ions was barely sufficient to form a complete layer of gold shell around the silica core with a thickness of about 10 nm. Based on calculation of the core size and concentration of the precursor seed particles as well as the dimension and density of the gold shell, a ratio of 190:1 was required to form a 10 nm thick uniform shell around the 300 nm diameter silica. The experimental amount is thus consistent with that obtained from mass calculation of the same dimension. Beyond this ratio of 200:1, the shell thickened to about 30 nm at a ratio of 300:1. Thicker gold shell can be grown at even higher K-gold-to-seed ratios using this same technique and the same technique could be applied to grow the shell on other silica core sizes.

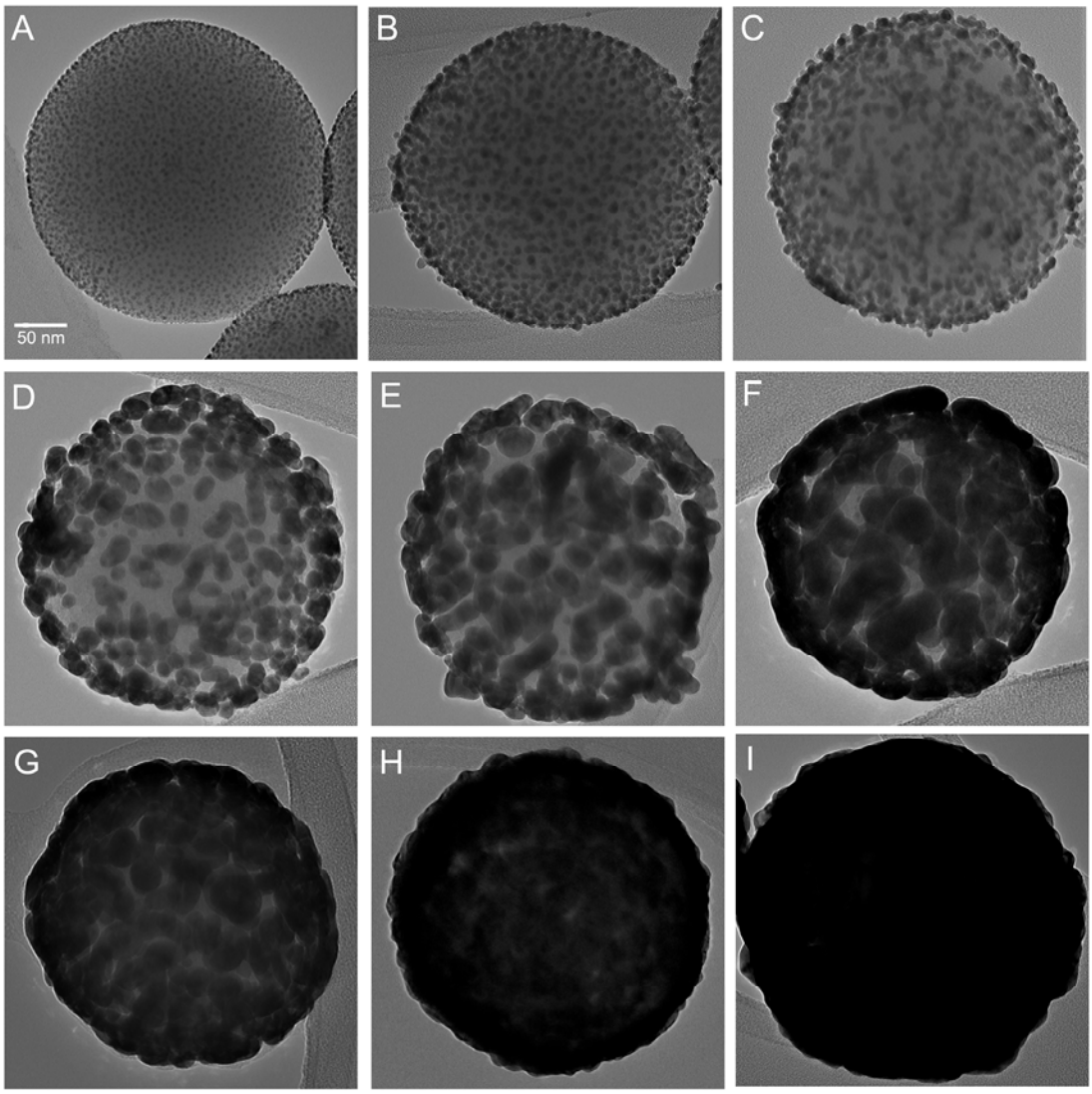

Figure 4.8. Growth of the gold hydroxide nanoparticle seeds by reducing the aged gold hydroxide (K-gold) solution on the (a) precursor seed particles to progressively form a complete layer of gold shell i.e. Au(0) with increasing K-gold-to-seed ratios of (b) 5:1, (c) 20:1, (d) 40:1, (e) 70:1, (f) 100:1, (g) 160:1, (h) 200:1 and (i) 300:1 for a silica core size of 300 nm in diameter. All images in figures taken with the same magnification with the scale bar shown in (a).

As the $Au(OH)_3$ nanoparticle seeds were in the order of 4 nm and they need to grow and coalesce together before forming a complete shell covering, this technique of shell growth imposed a minimum shell thickness of around 10 nm (Figure 4.8g). As the shell grows to different thickness, the color of the resulting colloid also exhibit a

gradual change to give a spectrum of color corresponding to different stages of growth and thickness of the gold shell as shown in Figure 4.9 below.

Figure 4.9. Colloidal solution of gold nanoshells showing a spectrum of color corresponding to different stages of shell growth and thickness of gold shell. Generally, as the shell grows on the silica core, the color changes gradually as shown in the direction from left to right.

The changes in UV-Vis extinction spectra of the gold nanoshells at different stages of seed growth for the 300 nm diameter core corresponding to the same K-gold-to-seed ratios as in Figure 4.8 were measured and shown in Figure 4.10. The theoretically predicted extinction spectrum based on Mie theory for a single gold nanoshell with a silica core of 300 nm and shell thickness of 28 nm is also shown for comparison.

Since the $Au(OH)_3$ nanoparticles do not exhibit any surface plasmon resonance, the extinction spectrum of the initial precursor seed particles loaded with $Au(OH)_3$ nanoparticles shows a typical optical response of a Mie particle scatterer with the absence of any extinction peak. As the $Au(OH)_3$ seeds were initially reduced by $NaBH_4$ to gold, i.e. Au^0 nanoparticles and began to grow slightly in size at low K-gold ratios, the formation of an extinction peak of 560 nm, typical of the surface plasmon resonance of large gold nanoparticles, was observed to indicate the formation and initial growth of the gold seeds.

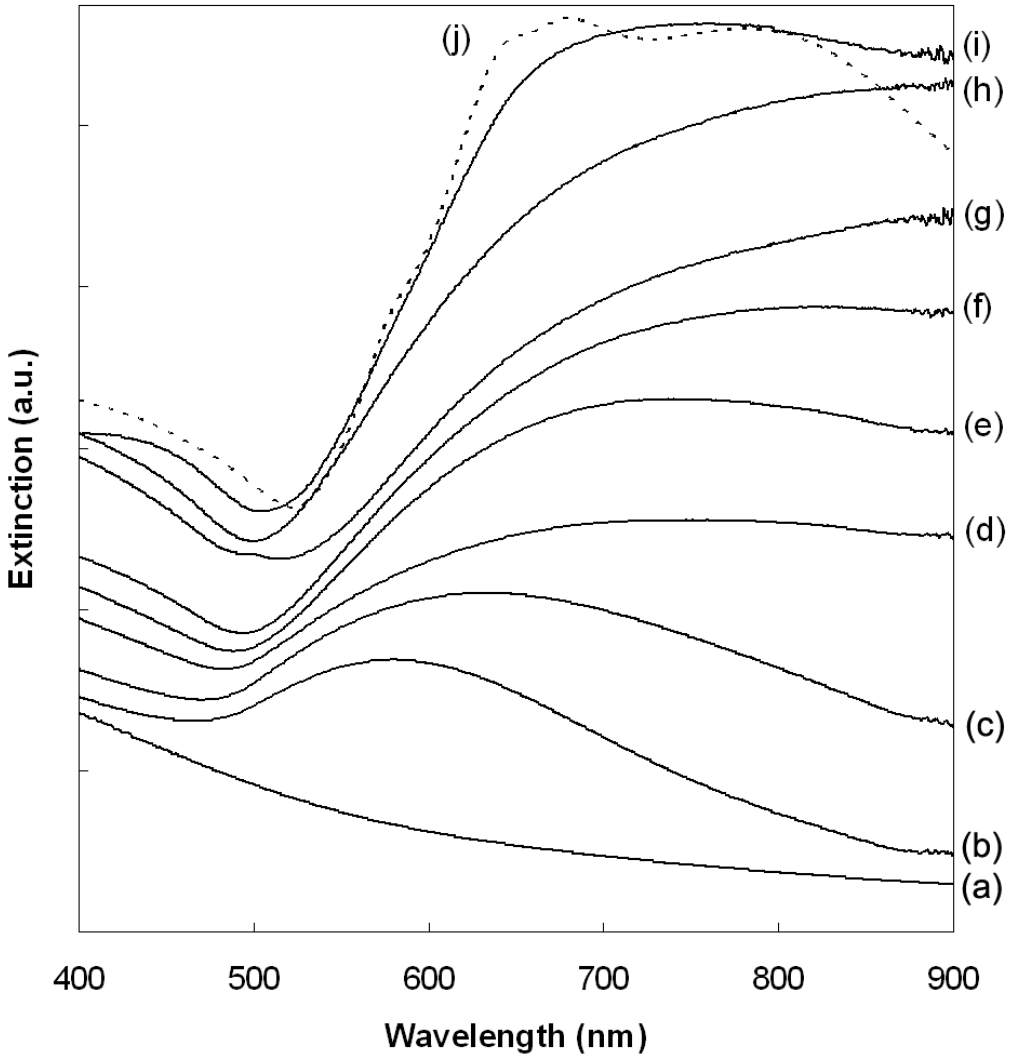

Figure 4.10. Measured UV-Vis extinction spectrum of the gold nanoshells at different stages of seed growth on the (a) precursor seed particles arising from a range of different K-gold-to-seed ratio of (b) 5:1, (c) 20:1, (d) 40:1, (e) 70:1, (f) 100:1, (g) 160:1, (h) 200:1 and (i) 300:1 for a silica core size of 300 nm. The theoretically predicted spectrum (j), shown in dashed line based on the Mie theory for a 300 nm diameter silica core with a 28 nm gold shell is also shown together for comparison.

The UV-Vis spectra at higher K-gold:silica ratios show a gradual red shift in the plasmon resonance peak towards higher wavelength from 630 nm at 20:1 to about 900 nm at 160:1, indicating the growth of the seed and increasing plasmon interactions between the neighboring seed particles as they grow closer together. Apart from peak shifts, the extinction spectra also increase in intensity with the growth of the gold seed

particles due to the increasing surface plasmon response and optical cross sections from the larger gold particles. The seeds continue to grow further in size until a complete shell was obtained (Figure 4.10g). In this case, the peak plasmon resonance for this configuration was determined to be around 800 nm. Further thickening of the gold shell caused a blue shift back in the wavelength of the peak optical response as observed in Figure 4.10i.

When compared to theoretically predicted spectrum based on Mie theory for the same dimensions, the measured extinction spectrum of the gold nanoshells having a 300 nm diameter core and 28 nm shell generally agreed well with the theoretical spectrum with small differences that can be attributed to the heterogeneity within the population of gold nanoshells formed. Such heterogeneity is inevitable due to the size variations in the silica core as well as the small differences in the thickness of the shell formed. The agreement of the experimentally measure spectrum with the theoretically calculated spectrum using Mie theory implies that the constituent scattering, absorption and backscattering spectrum as well as anisotropy of the gold nanoshells can also be predicted with good accuracy from Mie theory. These constituent spectra are useful in examining the optical response of gold nanoshells for bioimaging or therapeutic applications based on the absorption or backscattering metric.

4.4 Discussion

4.4.1 Deposition-precipitation of $Au(OH)_3$ on oxide support

The process of deposition-precipitation of $Au(OH)_3$ on oxide support starting from a gold precursor in the form of an aqueous solution of $HAuCl_4$ has been widely used in

the catalytic field involving seeding such gold particles on metal oxide substrate to form nanoparticulate gold catalyst [15-19]. It is clear from recent work on the characterization of gold on alumina that addition of base to $HAuCl_4$ hydrolyzes the chloroauric anion i.e. $[AuCl_4]^-$ in solution to form a few major species of negatively charged gold complex anions of the general form $[Au(OH)_xCl_{4-x}]^-$ with the composition depending on the extent of hydrolysis [25] as given below.

$$AuCl_4^- + (OH)^- <=> AuCl_3(OH)^- + Cl^-$$

$$AuCl_3(OH)^- + (OH)^- <=> AuCl_2(OH)_2^- + Cl^-$$

$$AuCl_2(OH)_2^- + (OH)^- <=> AuCl(OH)_3^- + Cl^-$$

$$AuCl(OH)_3^- + (OH)^- <=> Au(OH)_4^- + Cl^-$$

The extent of hydrolysis in turn depends on the pH which gives an indication of the amount of OH^- available for hydrolysis. To promote the exchange of chloride in $[AuCl_4]^-$ with OH^- during hydrolysis, the aqueous solutions should be warmed to a temperature in the range of 60 – 80 °C [17].

Out of these six species, only $Au(OH)_3$ precipitates [25]. As a result, the gold available in solution is only partially deposited on the support as the remaining species remain dissolved in the solution. It is the control of hydrolysis to tune the speciation of $[Au(OH)_xCl_{4-x}]^-$ that subsequently influence the amount of nanoparticulate $Au(OH)_3$ seeds formed on the substrate as well as their size and density on the silica. Therefore, this method has to be strictly controlled in terms of the pH value, the resulting dimension and seeding density of the $Au(OH)_3$ nanoparticles being dependent on it.

For typical $HAuCl_4$ concentration of the millimolar range used in most DP process, careful control of the pH in the range of 6 to 10, and temperature in the range of 60 to 80 °C enable selective crystallization and deposition of $Au(OH)_3$ nanoparticles only on the surfaces of metal oxide support without precipitation and crystallization in the liquid phase. It was found that the $Au(OH)_3$ nanoparticles loaded onto the silica nanoparticles using this controlled hydrolysis and DP method were stable towards magnetic stirring and ultrasonication.

4.4.2 Nature of support substrate surface

The nature of the support substrate surface also exerts a tandem effect on the extent of hydrolysis of $HAuCl_4$ on the deposition of the $Au(OH)_3$, as demonstrated in the results (see section 4.3.1). The unfortunate drawback of DP method is that it is not effective in the presence of metal oxides supports whose isoelectric point (IEP) is below 5 [17].

Although the direct deposition of $Au(OH)_3$ on bare silica surface (IEP ≈ 2) without any surface functionalization is possible with the reaction schematic as shown in Figure 4.11, the deposition has shown to be poor as demonstrated by the seeding results on bare silica nanoparticles in Figure 4.4b. The reason for this is that above this pH i.e. pH > 2, its surface is negatively charged which hinders the attraction of $[Au(OH)_xCl_{4-x}]^-$ to its surface for subsequent deposition.

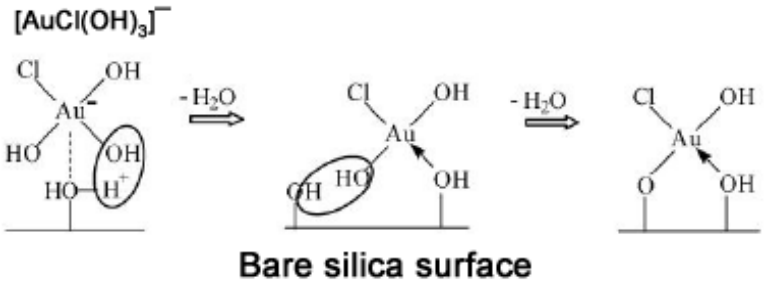

Figure 4.11. Reaction schematic of depositing $Au(OH)_3$ on bare silica surface without any surface functionalization [18].

As demonstrated in section 4.3.1, the problem associated with the low IEP of silica nanoparticles is addressed by functionalizing their surface with a terminal amine group prior to seeding the $Au(OH)_3$ nanoparticles. The reaction schematics for the grafting of APTES onto the silica nanoparticles are shown in Figure 4.12 below.

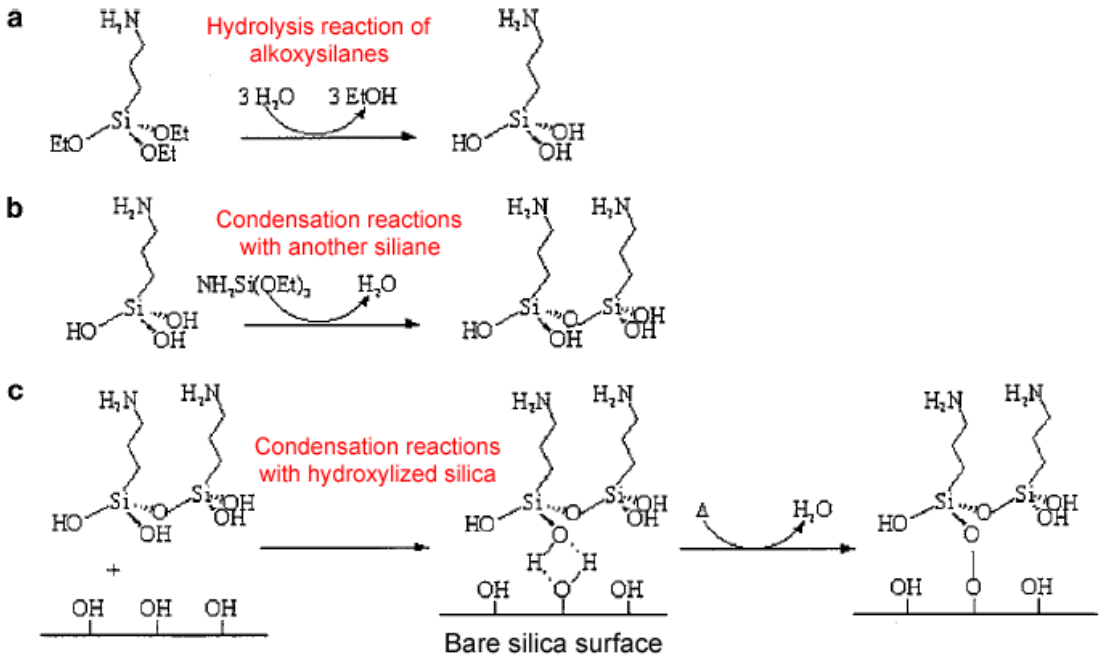

Figure 4.12. Equations of (a) hydrolysis reaction from alkoxysilanes, and (b) of condensation reactions with another silane or (c) with the hydroxylized silica [26].

Use of APTES is a typical example of obtaining cationic amine groups on nanosize particles [27]. Direct silanation of silica nanoparticles using a silane-coupling agent such as APTES is attractive for the control of surface properties. The amine groups on the silica surface effectively modify the IEP of silica nanoparticle since the grafting of APTES on the silica nanoparticles caused a drastic change in the IEP of silica particles from 2 to 9. At a pH of 8, the surface of amine grafted silica becomes positively charged, making the surface favorable for attraction of $[Au(OH)_xCl_{4-x}]^-$ and subsequent deposition of $Au(OH)_3$ as shown in Figure 4.13.

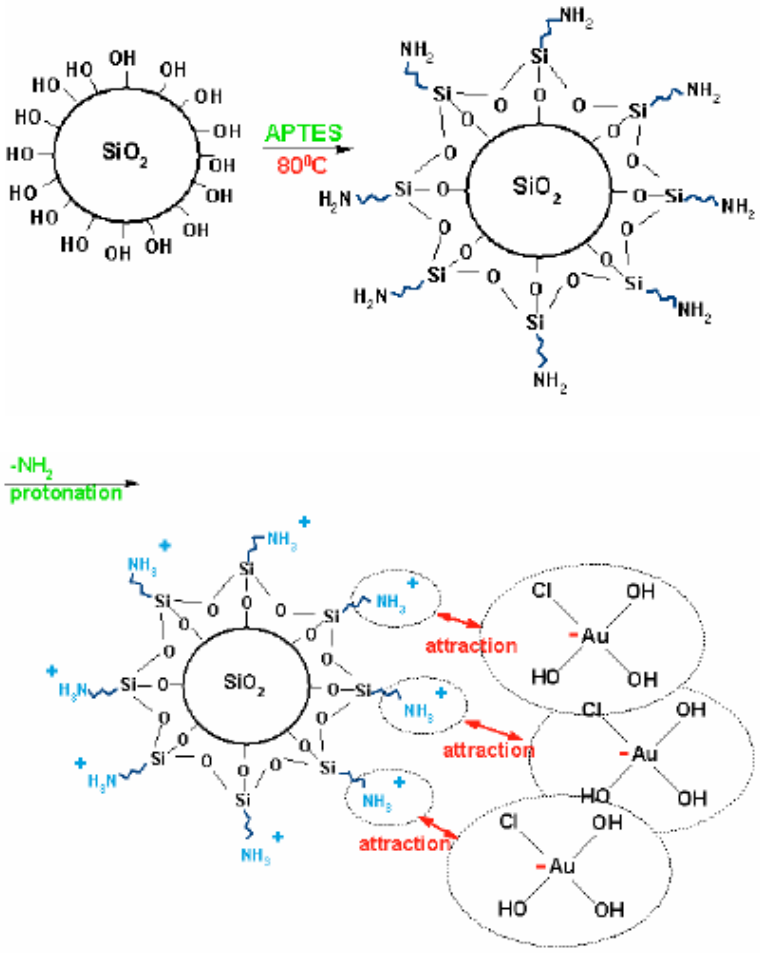

Figure 4.13. The surface functionalization of silica nanoparticles with a terminal amine group using APTES confers the surface a positive charge that favors the electrostatic attraction of the gold complex anion species for deposition.

Therefore, surface functionalization of silica nanoparticles with APTES results in favorable electrostatics and this favorable electrostatics coupled with dominant formation of $[Au(OH)_3Cl]^-$ from the hydrolysis of $HAuCl_4$ at around pH 8 [28] (to be discussed in more detail below) results in much high density of smaller $Au(OH)_3$ nanoparticles deposited on the silica. Furthermore, it is also known that the introduction of a support with polar surface groups i.e. silica with surface-functionalized $-NH_2$ groups leads to the acceleration of the hydrolysis reaction near the functionalized surface [29]. The formed nanoparticles of hydrated metal oxides are immediately adsorbed onto the surface of the silica.

4.4.3 Influence of pH on seeding density

Besides the influence of surface functionalization, the effect of other factors such as pH and time of reaction on the seeding process is also demonstrated. Perhaps one of the key factors controlling the seeding density of $Au(OH)_3$ nanoparticles on the silica core is pH. In this case, two conditions in the DP process that are sensitive to the pH come into play: the hydrolysis of $HAuCl_4$ to give $[Au(OH)_3Cl]^-$ as the dominant species that would precipitate [25] and a surface with appropriate IEP to facilitate the adsorption of $[Au(OH)_xCl_{4-x}]^-$. These two conditions must both be satisfied to achieve good seeding on the silica. It has been found from previous studies that preparation at a mildly basic pH range of 7 to 9 is preferable for most oxide support [30] because at this pH, the value of x in $[Au(OH)_xCl_{4-x}]^-$ is close to 3 where precipitation is the most efficient as mentioned earlier. This pH range is also compatible with the IEP of most metal oxide [17] for electrostatic attraction and deposition as discussed previously.

As mentioned earlier, the amine grafted silica substrate surface has an IEP ≈ 9. At pH below this IEP, the surface is positively charged and is capable of adsorbing more of the negatively charged gold species as illustrated in Figure 4.14. However, at a much lower pH of 3 to 4, there is little hydrolysis of the Au–Cl bond to form $Au(OH)_3$, and many studies have shown that the soluble $AuCl_3.H_2O$ is the major species with traces of other $[Au(OH)_xCl_{4-x}]^-$ species at this pH [18, 28]. Therefore, there is a low precipitation of $Au(OH)_3$ species and its density of seeding remains poor and inhomogeneous despite the favorable electrostatic adsorption from the substrate.

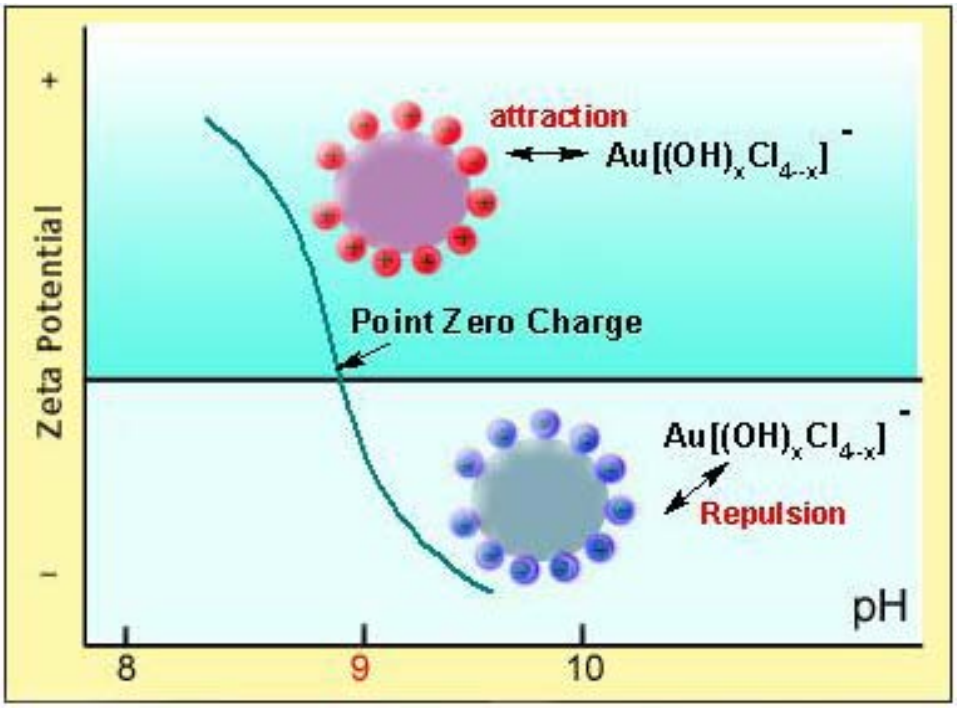

Figure 4.14. The deposition of $[AuCl(OH)_3]^-$ requires an attractive charge on the surface of the grafted silica nanoparticles which can be obtained at pH less than its IEP of 9. This attractive charge serves to attract the gold complex anion after its hydrolysis, which at pH of 9 gives the dominant species of $[AuCl(OH)_3]^-$. At pH higher than IEP, the surface gives a repulsive charge which reduces the efficiency of deposition.

As the pH increases to 6 while maintaining below the isoelectric point, the extent of hydrolysis increases due to increasing replacement of more Au–Cl with Au–OH in the

complex $[Au(OH)_xCl_{4-x}]^-$ anion. More of the precipitating $[Au(OH)_3Cl]^-$ species are formed and the density of the $Au(OH)_3$ nanoparticles increases correspondingly until a high seeding density is achieved at pH 8. At this pH, the hydrolysis forms $[Au(OH)_3Cl]^-$ as the dominant species and their electrostatic attraction to the positively charged amine grafted surface (IEP ≈ 9) facilitated their deposition.

Further increase in pH to 11 beyond the IEP of the amine grafted surface causes adsorption of the negatively charged $[Au(OH)_xCl_{4-x}]^-$ complex to reduce rapidly due to repulsive negative charge from the surface [15] (Figure 4.14). Furthermore, since $Au(OH)_3$ is amphoteric, its solubility increases due to the formation of $[Au(OH)_4]^-$ at higher pH, thus making the soluble $[Au(OH)_4]^-$ the most dominant species at high pH [18] instead of the precipitating $[Au(OH)_3Cl]^-$. This reduces the efficiency of precipitation and results in a lower density of $Au(OH)_3$ nanoparticles on the silica as the amount of $Au(OH)_3$ species available for deposition is decreased. Therefore, there is a narrow optimal working range of pH where the $[Au(OH)_xCl_{4-x}]^-$ can be attracted to the surface and with sufficient hydrolysis to form the precipitate for deposition.

4.4.4 Effect of temperature

The DP reaction for the formation of $Au(OH)_3$ nanoparticles on the amine grafted silica cores seem to take place at temperature above 65 °C. The role of temperature probably accounts for the rate of precipitation and deposition of the $Au(OH)_3$ nanoparticles which can take place as rapid as 3 min (see Figure 4.6a). Apart from affecting the rate of reaction, the size and seeding density of the $Au(OH)_3$ nanoparticles are not affected much by temperature if the duration of reaction is not a

limiting factor. Hence there were little or no observable differences in the seeding with temperature variation beyond 65 °C at longer heating time of 30 min.

The more dominant factor rather, is the duration of reaction at temperature > 65 °C where the size of $Au(OH)_3$ increases with the duration of heating and gold clusters larger than 20 nm were formed with prolonged heating time of beyond 30 min. The growth of the $Au(OH)_3$ nanoparticles and formation of large gold clusters can be accounted for by briefly considering the surface energetics of the nanoparticles. As the precipitation and deposition of $Au(OH)_3$ nanoparticles on amine grafted silica progresses with heating duration, the terminal amine groups on the silica available for attachment to $Au(OH)_3$ nanoparticles starts to saturate and crystal growth of the existing deposited $Au(OH)_3$ nanoparticles become a more dominant process compared to further deposition of new $Au(OH)_3$ nanoparticles on APTES.

This growth arises from the continuous precipitation of $Au(OH)_3$ in solution and aggregation of these new precipitates with existing deposited $Au(OH)_3$ particles. This yields increasingly larger $Au(OH)_3$ nanoparticles until their surface charge, which progressively becomes more negative due to the presence of chloride [15] as more $Au(OH)_3$ aggregates, render them energetically unfavorable for further growth. In this case, prolonged heating causes the $[Au(OH)_3Cl]^-$ in the solution to precipitate and aggregate with each other instead to form larger gold clusters of $Au(OH)_3$ in the solution. Such nanoparticles formed in solution compete with the deposited $Au(OH)_3$ as reduction sites for K-gold, thus reducing the efficiency of shell growth.

4.4.5 Growth of gold shell

The $Au(OH)_3$ nanoparticles are seeded on silica to function as nucleation sites where they will be reduced to Au^0 nanoparticles while the K-gold is also simultaneously reduced to deposit more Au^0 on them in the process of growing the gold shell. In the growth of the gold shell, the pH of K-gold solution is important to nanoshell formation on the precursor seed particles as it controls the speciation of $[Au(OH)_xCl_{4-x}]^-$ which in turn affect its reduction on the $Au(OH)_3$ nanoparticles. In this case, the gold to be reduced on the seeds was prepared by adjusting the pH of $HAuCl_4$ solution through the addition of K_2CO_3 to around 10.1, where hydrolysis of most of the Au–Cl bond occurs after an overnight aging in the dark to form the soluble gold hydroxide complex $[Au(OH)_4]^-$ as the dominant species [18] as shown in Figure 4.15 below.

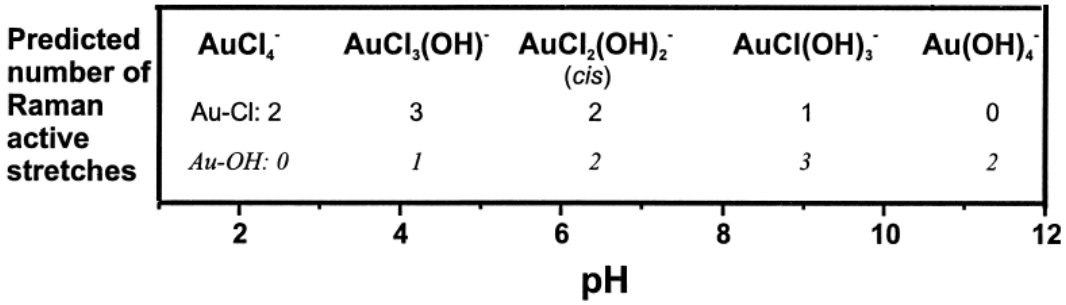

Figure 4.15. Predicted number of Raman active stretches for both Au-Cl and Au-OH over a range of different pH by Murphy *et. al.* which indicates the predominant $[Au(OH)_xCl_{4-x}]^-$ species formed at different pH. The pH of HAuCl4 solution can be adjusted by addition of a base such as NaOH (see section 4.4.1 and 4.4.3) or K_2CO_3 to different complex gold anionic species of the form $[Au(OH)_xCl_{4-x}]^-$. Whilst the pH is raised to 8 by NaOH to form the dominant specie $AuCl(OH)_3^-$ for DP process of seeding, the pH is raised to 10.1 by K_2CO_3 to form the dominant specie $Au(OH)_4^-$ for the growth of gold shell [28].

Amongst the six species of $[Au(OH)_xCl_{4-x}]^-$ discussed earlier, $[Au(OH)_4]^-$ seems to have the lower tendency to be reduced in solution to form colloidal gold even with a strong reducing agent as evident from its slow and gradual color change when

reduced. This is in contrast to the reduction of other $[Au(OH)_xCl_{4-x}]^-$ species formed at lower pH where that the addition of $NaBH_4$ causes an instantaneous color change to form colloidal gold. This observation may possibly be attributed to a weaker reduction potential of $[Au(OH)_4]^-$ compared to other species although the electrochemistry of different species of $[Au(OH)_xCl_{4-x}]^-$ is not well characterized.

During the reduction of K-gold, the $Au(OH)_3$ nanoparticles also serve as catalytic sites to facilitate preferential reduction of $[Au(OH)_4]^-$ on the seed particles for shell growth. It was found that adjustment to other pH < 10 by adding smaller amount of K_2CO_3 results in the formation of other dominant species that have greater tendency to be reduced in solution to form colloidal gold thus diminishing their preferential reduction on the seed particles and effectiveness in growing the gold shell.

In reducing the K-gold solution of $[Au(OH)_4]^-$ onto the precursor seed particles, the freshly prepared $NaBH_4$ was used as the reducing agent. It was noted that increasing the amount of $NaBH_4$ used for reduction also resulted in a corresponding increase in the tendency of gold nanoshells to aggregate. Furthermore, the formation of a brown scattering solution was also observed when a large amount of $NaBH_4$ was added. The formation of such brown scattering solution has also been reported by others [1] and on closer examination under the TEM, this observation is due to the presence of large bulk gold particles (data not shown). However, if the amount of $NaBH_4$ used is too little, the solution will contain unreacted K-gold in solution. The amount described represents a good compromise based on the molar ratio of reagents used for the redox reaction. In addition to $NaBH_4$, sodium citrate dihydrate was also added during the

reduction for shell growth. The use of sodium citrate to slow the reaction and stabilize the gold nanoshells during the reduction process has been reported by others [12, 29].

4.5 Conclusion

The use of a DP process of seeding nanoparticulate gold onto amine functionalized silica core particles to form the precursor seed particles has shown to be a feasible alternative route for the growth of a gold shell in the synthesis of gold nanoshells. Compared to the widely-used two-step strategy of synthesizing small colloidal gold nanoparticles from reduction of $HAuCl_4$ by THPC followed by their attachment onto the silica core, the DP method of seeding is time and cost effective since it condenses the process into a single-step that requires just 10 minutes of heating reaction to form the precursor seed particles without the need for prior synthesis of colloidal gold. The DP process requires amine functionalization on the silica surface to alter the isoelectric point of silica from 2 to 9 to facilitate the deposition of $Au(OH)_3$ nanoparticles and hence improving the uniformity and density of seeding. The seeding density and size of the $Au(OH)_3$ nanoparticle seeds can also be controlled by varying the pH of $HAuCl_4$ solution, as well as the time of reaction. The DP technique has been used to seed $Au(OH)_3$ nanoparticles on different sizes of silica cores to form the precursor seed particles which are then used to form the gold nanoshells of different sizes for subsequent *in vitro* and *in vivo* studies described in the remaining chapters. However, before these gold nanoshells can be used effectively in biological studies, their surface has to be functionalized appropriately in terms of pegylation and antibody conjugation which is discussed in more detail in the next Chapter 5.

4.6 References

1. Graf C, van Blaaderen A. Metallodielectric Colloidal Core-Shell Particles for Photonic Applications. *Langmuir* 2002; 18(2): 524-534.

2. Shi W, Sahoo Y, Swihart MT, Prasad PN. Gold nanoshells on polystyrene cores for control of surface plasmon resonance. *Langmuir* 2005; 21(4): 1610-1617.

3. Oldenburg SJ, Westcott SL, Averitt RD, Halas NJ. Surface enhanced Raman scattering in the near infrared using metal nanoshell substrates. *The Journal of Chemical Physics* 1999; 111(10): 4729-4735.

4. Pham T, Jackson JB, Halas NJ, Lee TR. Preparation and Characterization of Gold Nanoshells Coated with Self-Assembled Monolayers. *Langmuir* 2002; 18(12): 4915-4920.

5. Guczi L, Peto G, Beck A, Frey K, Geszti O, Molnar G, Daroczi C. Gold nanoparticles deposited on SiO2/Si100: correlation between size, electron structure, and activity in CO oxidation. *J Am Chem Soc* 2003; 125(14): 4332-4337.

6. Averitt RD, Sarkar D, Halas NJ. Plasmon Resonance Shifts of Au-Coated Au2S Nanoshells: Insight into Multicomponent Nanoparticle Growth. *Physical Review Letters* 1997; 78(22): 4217 LP - 4220.

7. Oldenburg SJ, Averitt RD, Westcott SL, Halas NJ. Nanoengineering of optical resonances. *Chemical Physics Letters* 1998; 288(2-4): 243-247.

8. Duff DG, Baiker A, Edwards PP. A new hydrosol of gold clusters. 1. Formation and particle size variation. *Langmuir* 1993; 9(9): 2301-2309.

9. Duff DG, Baiker A, Gameson I, Edwards PP. A new hydrosol of gold clusters. 2. A comparison of some different measurement techniques. *Langmuir* 1993; 9(9): 2310-2317.

10. Ji T, Lirtsman VG, Avny Y, Davidov D. Preparation, Characterization, and Application of Au-Shell/Polystyrene Beads and Au-Shell/Magnetic Beads. *Advanced Materials* 2001; 13(16): 1253-1256.

11. Kobayashi Y, Salgueirino-Maceira V, Liz-Marzan LM. Deposition of Silver Nanoparticles on Silica Spheres by Pretreatment Steps in Electroless Plating. *Chem. Mater.* 2001; 13(5): 1630-1633.

12. Zhang J, Liu J, Wang S, Zhan P, Wang Z, Ming N. Facile Methods to Coat Polystyrene and Silica Colloids with Metal. *Advanced Functional Materials* 2004; 14(11): 1089-1096.

13. Lim YT, Park OO, Jung H-T. Gold nanolayer-encapsulated silica particles synthesized by surface seeding and shell growing method: near infrared responsive materials. *Journal of Colloid and Interface Science* 2003; 263(2): 449-453.

14. Haruta M, Kobayashi T, Sano H, Yamada N. Novel Gold Catalysts for the Oxidation of Carbon Monoxide at a Temperature far Below 0 °C. *Chem. Lett.* 1987; 16(2): 405-408.

15. Kung HH, Kung MC, Costello CK. Supported Au catalysts for low temperature CO oxidation. *Journal of Catalysis* 2003; 216(1-2): 425-432.

16. Prati L, Martra G. New gold catalysts for liquid phase oxidation. *Gold Bull* 1999; 32(3): 96-101.

17. Haruta M. Nanoparticulate gold catalysts for low-temperature CO oxidation. *Journal of New Materials for Electrochemical Systems* 2004; 7(3): 163-172.

18. Moreau F, Bond GC, Taylor AO. Gold on titania catalysts for the oxidation of carbon monoxide: control of pH during preparation with various gold contents. *Journal of Catalysis* 2005; 231(1): 105-114.

19. Ivanova S, Pitchon V, Petit C, Herschbach H, Dorsselaer AV, Leize E. Preparation of alumina supported gold catalysts: Gold complexes genesis, identification and speciation by mass spectrometry. *Applied Catalysis A: General* 2006; 298: 203-210.

20. Cheng X, Chen M, Zhou S, Wu L. Preparation of SiO2/PMMA composite particles via conventional emulsion polymerization. *Journal of Polymer Science Part A: Polymer Chemistry* 2006; 44(12): 3807-3816.

21. Yin D, Qin L, Liu J, Li C, Jin Y. Gold nanoparticles deposited on mesoporous alumina for epoxidation of styrene: Effects of the surface basicity of the supports. *Journal of Molecular Catalysis A: Chemical* 2005; 240(1-2): 40-48.

22. Zanella R, Sandoval A, Santiago P, Basiuk VA, Saniger JM. New preparation method of gold nanoparticles on SiO2. *J Phys Chem B* 2006; 110(17): 8559-8565.

23. Stöber W, Fink A, Bohn E. Controlled growth of monodisperse silica spheres in the micron size range. *Journal of Colloid and Interface Science* 1968; 26(1): 62-69.

24. Johnson PB, Christy RW. Optical Constants of the Noble Metals. *Physical Review B* 1972; 6(12): 4370 LP - 4379.

25. Chang C-K, Chen Y-J, Yeh C-t. Characterizations of alumina-supported gold with temperature-programmed reduction. *Applied Catalysis A: General* 1998; 174(1-2): 13-23.

26. Simon A, Cohen-Bouhacina T, Porte MC, Aime JP, Baquey C. Study of two grafting methods for obtaining a 3-aminopropyltriethoxysilane monolayer on silica surface. *J Colloid Interface Sci* 2002; 251(2): 278-283.

27. Xu Z, Liu Q, Finch JA. Silanation and stability of 3-aminopropyl triethoxy silane on nanosized superparamagnetic particles: I. Direct silanation. *Applied Surface Science* 1997; 120(3-4): 269-278.

28. Murphy PJ, LaGrange MS. Raman spectroscopy of gold chloro-hydroxy speciation in fluids at ambient temperature and pressure: a re-evaluation of the effects of pH and chloride concentration. *Geochimica et Cosmochimica Acta* 1998; 62(21-22): 3515-3526.

29. Dokoutchaev A, James JT, Koene SC, Pathak S, Prakash GKS, Thompson ME. Colloidal Metal Deposition onto Functionalized Polystyrene Microspheres. *Chem. Mater*. 1999; 11(9): 2389-2399.

30. Wolf A, Schüth F. A systematic study of the synthesis conditions for the preparation of highly active gold catalysts. *Applied Catalysis A: General* 2002; 226(1-2): 1-13.

CHAPTER FIVE

SURFACE FUNCTIONALIZATION OF GOLD NANOSHELLS

Abstract

The effective use of gold nanoshells in biological studies would require appropriate surface functionalization in terms of pegylation and antibody conjugation. While antibody conjugation confers specific targeting capability, pegylation of gold nanoshells provides an effective means to reduce their reticulo-endothelial system (RES) clearance in body. In this chapter, a parametric investigation on the pegylation factors that affect the macrophage uptake of gold nanoshells is described, with the aim to optimize their pegylation and minimize their macrophage uptake. Gold nanoshells were synthesized and pegylated using methoxy-poly(ethylene glycol)-thiol and an *in vitro* macrophage assay was employed to examine the effect of surface density of PEG, chain length of the PEG and size of the gold nanoshells on their macrophage uptake. The results have shown that a saturated surface density would minimize macrophage uptake which could be obtained by experimental titration based on the Ellman's reagent. The surface density of PEG is influenced by the chain length of PEG and size of gold nanoshells. PEG with molecular weight of around 2000 Da and a size range larger than 186 nm would be appropriate for facilitating a high surface density. The *in vitro* macrophage system described in this chapter thus provides a good model to accurately predict the RES response to different pegylation parameters. This work has been published in *Journal of Drug Targeting 2009; 17(3): 181–193.*

5.1 Introduction

The effective delivery of gold nanoshells to the intended site of interest is crucial for any imaging or therapeutic applications. Most of the available data to date on the *in vivo* delivery of gold nanoshells for biomedical applications are based on intratumoral administration into the site of interest. With the exception of superficial tumors, the direct injection of gold nanoshells into deep seeded tumor sites may not be clinically feasible. Several *in vivo* studies involving systemic intravenous administration of gold nanoshells are emerging [1-3] and because of their ability to reach deep seeded tumors, such means of delivery are desirable for widespread clinical application.

Intravenous administration of gold nanoshells allows these nanoparticles to target and accumulate in the tumor sites either through passive targeting based on the enhanced permeation and retention (EPR) mechanism or active targeting with the aid of a targeting moiety. Unfortunately, an efficient intravenous delivery of nanoparticles to the tumor site is not straightforward and is often hampered by complications arising from their rapid elimination from the systemic blood circulation. This elimination is due to the presence of the reticulo-endothelial system (RES), also known as the mononuclear phagocytic system (MPS) in the body [4].

The RES comprises macrophages and monocytes found in the liver (Kupffer cells), spleen and bone marrow. Despite the biocompatibility of gold and their inert biological activities in the body, these gold nanoshells may still be recognized by the RES through the opsonin proteins that adsorb on their surface [5]. The most common opsonins are complement proteins such as C3, C4, C5 and immunoglobulins found in the blood serum components that assist macrophages in recognizing foreign particles.

As the opsonins adsorb on the surface of nanoparticles, the macrophages attach themselves to the opsonins bound to the nanoparticles and phagocytosis takes place. For nanoparticles which cannot be degraded, they are accumulated in one of the RES organs, usually the liver or the spleen [6-8].

Various strategies have been developed to reduce the uptake and elimination of foreign nanoparticles from the bloodstream by the RES in order to prolong their systemic blood circulation time. This is to ensure more of these particles are delivered to the target site of interest. A commonly employed strategy to reduce opsonization and mask these nanoparticles from macrophage recognition is to block their electrostatic or hydrophobic interactions with opsonins using a polymer coating. Amongst the various polymers used for this purpose, poly(ethylene glycol) (PEG) is currently the most popular and the most effective in prolonging circulation time [4, 9].

The layer of PEG on the nanoparticles confers them a hydrophilic surface that serves to mask the gold nanoshells from RES recognition. It is widely known that hydrophilic particles stay longer in the bloodstream than hydrophobic particles. The surface of gold nanoshells is known to be hydrophobic in nature which makes them susceptible to a whole host of hydrophobic interactions with the milieu of proteins found in the biological environment. This is especially true for the common opsonin proteins that tend to be adsorbed on the surface of hydrophobic particles through hydrophobic interactions [5] which assist the macrophages in recognizing and attaching themselves to the opsonin-bound foreign particles for phagocytosis.

The ethylene glycol functional group in the PEG is known to interact well with water molecules and so when the PEG chain molecules are self-assembled close together on the surface of the gold nanoshells, the spaces between these PEG chains can attract water molecules and facilitate their “trapping” to create a hydrophilic layer of water cloud around the gold nanoshells. Besides the PEG polymers that sterically block the electrostatic or hydrophobic interactions of gold nanoshells with opsonins by themselves, this hydrophilic layer also serves as a barrier to prevent the adsorption of opsonins that mediate macrophage recognition and subsequent phagocytosis and thus masking the gold nanoshells from the RES. The flexibility of the PEG chains continuously squeezes out the water molecules, preventing proteins from diffusing into the barrier and contacting the bare surface of the gold nanoshell [10].

Besides masking the foreign nanoparticles from the RES, PEG can also confer the nanoparticles a hydrophilic surface to improve their stability in aqueous media. As with other types of nanoparticles, the small size of gold nanoshells renders them a high surface energy which makes these particles susceptible to aggregation. The van der Waals forces of attraction are known to exert its effect over a relatively long range, extending over a distance of a few nanometers [9]. Despite having a negatively charged surface arising from the cloud of loose electrons, gold nanoshells are subject to Brownian motion in the aqueous colloid due to its colloidal nature and can easily be brought together within the range of the van der Waals forces that destabilizes the colloidal suspension. This is especially true in a highly ionic environment where charge screening occurs, resulting in flocculation of the gold nanoshells. Such an absence of effective charge stabilization on their surface compromises their stability

in solution especially in biological environment with a high ionic content that reduces the charge screening on these nanoshell particles.

Aggregation of gold nanoshells can severely hamper the gold nanoshells from performing their intended imaging or therapeutic functions in biomedical applications. Their surface plasmon resonance will be altered in terms of shifted resonance wavelength and reduced resonance intensity upon aggregation which renders the gold nanoshells less efficient in eliciting optical contrast in imaging applications. The aggregated size of gold nanoshells may also compromise their ability to transverse through blood vessels and reach their target site for therapeutic applications.

The layer of PEG on the surface of gold nanoshells can help to stabilize the gold nanoshells in an aqueous environment by providing a steric barrier between interacting gold nanoshells particles i.e. steric stabilization. This steric repulsion can act to attenuate the attractive van der Waals forces. However, such repulsion among the gold nanoshells may also cause stress within the PEG layer, increasing the risk of PEG desorption from the gold nanoshell surface [9]. Therefore the mPEG-thiol used to bind to the gold nanoshells surface require a strong covalent Au-S thiol bond to provide a strong anchoring that minimizes the desorption of PEG. Steric stabilization has also been used to explain the reduction in the uptake of stabilized particles by macrophages in other colloidal suspension systems [9]. Besides steric stabilization, the presence of PEG layer on the gold nanoshells can also confer the nanoshells a hydrophilic surface to improve their interaction with the aqueous media hence improving their stability.

Therefore, the pegylation i.e. the binding of PEG chains onto the surface of gold nanoshells for any biological applications is crucial for at least two reasons: 1. To improve their aqueous stability in biological environment, hence improving their imaging and therapeutic efficacy, and 2. To mask them from being recognized and eliminated by the RES from the systemic blood circulation before reaching their targeted site of interest and performing their intended function. There have been extensive parametric studies to investigate and optimize the pegylation of other types of nanoparticles such as liposomes [11-13] and polystyrene [14-16] nanoparticles and all have demonstrated the efficacy of PEG in reducing phagocytosis. Although the pegylation of gold nanoshells has also been reported in several *in vivo* application studies [1-3], the process has not been optimized for minimizing macrophage uptake. A previous study by James et al. has shown that even with pegylation on gold nanoshells, the amount of gold nanoshells that are trapped in the RES organs is about 5 times that found in the target tumors [17].

This chapter describes a detailed analysis on the various parameters that would affect the macrophage uptake of gold nanoshells with the aim to optimize their pegylation conditions and minimize their macrophage uptake. In the study described in this chapter, an *in vitro* macrophage model system is employed to perform a parametric investigation on the various factors that would affect the macrophage uptake of gold nanoshells with the objective of using these in vitro results to optimize the gold nanoshells pegylation conditions for further *in vivo* studies. The macrophage model system represents an effective way to test the uptake of the nanoparticles since the cells behave in similar manner in terms of recognition and uptake as they would *in vivo* and have been used extensively by other previously reported studies [18-20].

Gold nanoshells were synthesized and pegylated and examined for the following three parameters on the macrophage uptake: the surface density of PEG, chain length of the PEG used and the size of the gold nanoshells. The effect of these parameters on the RES uptake will be extrapolated and briefly discussed in light of the *in vitro* macrophage model. Such a study would provide valuable insights to improve the current state of biodistribution in tumors.

5.2 Materials and Methods

5.2.1 Synthesis and pegylation of gold nanoshells

Gold nanoshells were synthesized in a four-step process as described earlier in Chapter 4. The process of shell growth on the gold hydroxide seeded silica was imaged by transmission electron microscopy (TEM) (Jeol JEM-1010) operating at 100 kV. The particle size was also characterized by TEM. The gold nanoshells were prepared to a final concentration of approximately 2×10^{13} particles/ml as determined by correlating its extinction spectroscopy data to the theoretical extinction cross section data of the gold nanoshell based on Mie theory as described in Chapter 2. The synthesized gold nanoshells were stored at 4°C when not in use.

The gold nanoshells were pegylated using the heterobifunctional methoxy-poly(ethylene glycol)-thiol (mPEG-thiol) of various molecular weights (MW): 750, 2000, 5000, 10000 and 20000 Da (≥ 92%, Celares GmbH). Here, the thiol end was attached to the gold surface of the nanoshells while the other end was capped with a methoxy terminal group. The reaction schematic for the synthesis and pegylation of gold nanoshells is shown in Figure 5.1 below. The mPEG-thiol was dissolved in water

to give a range of concentration from 0.05 to 20 µmol/ml before adding it to the gold nanoshells colloid. The mPEG-thiol was attached to the gold nanoshells in water by incubating 1 ml of the gold nanoshells colloid (2 x 10^{13} particles/ml) with 1 ml of the mPEG-thiol solution under sonication for 5 minutes at room temperature. The pegylated gold nanoshells were then rinsed 5 times with Milli-Q water to remove excess mPEG-thiol from the pegylated gold nanoshells, before redispersing them in phosphate buffer solution (1X PBS, pH 7.4) and stored in 4 °C until further use.

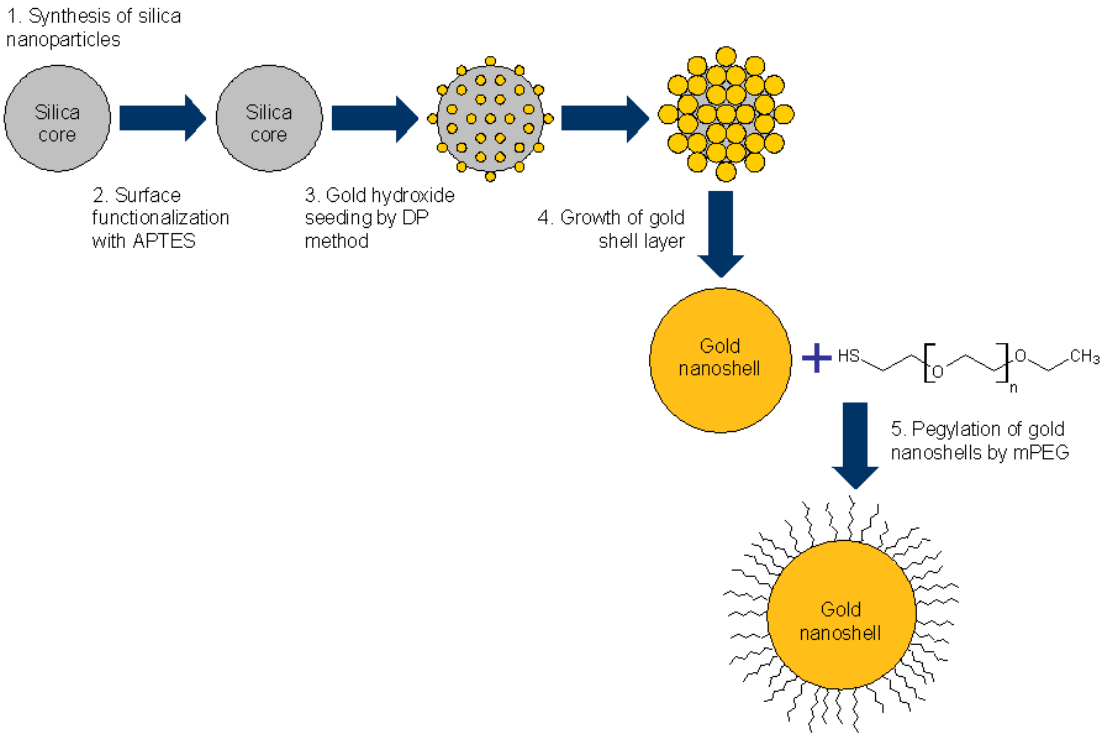

Figure 5.1. Reaction schematic of the synthesis and pegylation of gold nanoshells with core of 81 nm radius and gold shell thickness of 23 nm used in this study. The synthesis of the gold nanoshells is described in more detail in Chapter 4.

The successful pegylation of gold nanoshells was determined using X-ray photoelectron spectroscopy (XPS) by examining the changes in the sulphur (2p) spectra. The sulphur (2p) spectra would indicate the presence of thiol group on the surface of the gold nanoshells. The saturation amount of mPEG-thiol on the gold

nanoshells surface was also determined by quantitation of unbound thiol group from mPEG-thiol using Ellman's reagent. The Ellman's reagent (5, 5'-dithiobis-(2-nitrobenzoic acid) or DTNB) (Sigma-Aldrich) was used to detect the presence of unbound thiol group from the excess mPEG-thiol when the gold nanoshells surface was saturated [21]. It was added to the supernatant obtained after the first centrifuge that removes the excess mPEG-thiol immediately after pegylation. The presence of excess mPEG-thiol will cause a visible color change in the reagent which can be quantified at absorbance of 430 nm (TECAN Sunrise Absorbance Reader). The reaction of Ellman's reagent with a thiol and the color change in the reagent is shown in Figure 5.2 below.

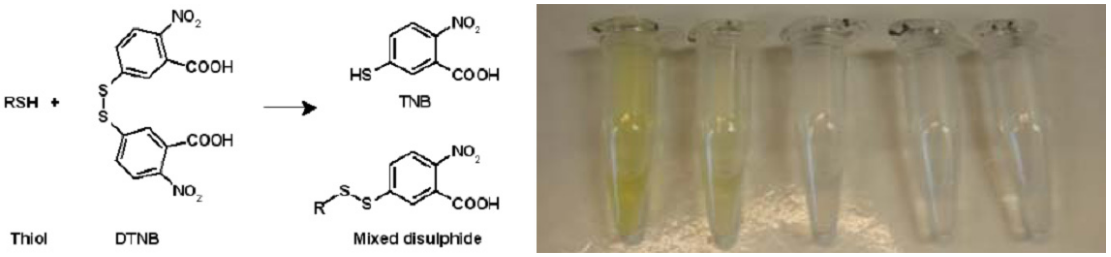

Figure 5.2. Reaction of DTNB (Ellman's reagent) with a thiol to release 2-nitro-5-mercaptobenzoic acid (TNB), which ionizes to the TNB^- anion in water at neutral and alkaline pH. This TNB^- ion has a strong yellow color. The image on the right shows the color change in Ellman's reagent on detection of different concentration of mPEG-thiol.

5.2.2 Imaging of macrophage uptake

The mouse leukaemic monocyte macrophage cell line RAW 264.7 was used in the *in vitro* uptake studies of gold nanoshells. The RAW 246.7 cells were grown in RPMI 1640 supplemented with 10% fetal bovine serum, 2 mM glutamine, sodium pyruvate, non-essential amino acids and 100 units/ml penicillin/streptomycin and maintained at 37 °C in humidified 5% CO_2 and 95% air atmosphere. Prior to the uptake studies, the

macrophages were harvested and seeded in the wells of a 6-well plate (Iwaki) at 5 x 10^5 macrophages in each well suspended in 2 ml of the culture medium. The plates were incubated overnight for cells to settle and adhere to the floor of the wells. The medium in the wells with macrophages was aspirated and replaced with a mixture of 100 µl of gold nanoshells (2 x 10^{13} particles/ml) in 1.9 ml of culture medium. The macrophages were incubated with the pegylated gold nanoshells for 1 h at 37 °C. The macrophage loaded with gold nanoshells were then rinsed thrice with 1X PBS to wash away the excess non-ingested gold nanoshells and fixed in 4% paraformaldehyde.

The uptake of gold nanoshells by the macrophages was imaged with both the brightfield and laser scanning confocal microscope (Carl Zeiss LSM510 Meta) under the fluorescence and reflectance mode. The autofluorescence of the macrophages and the reflectance of the gold nanoshells were imaging using an Olympus 63x oil immersion objective at 488 nm excitation with an argon laser and 633 nm excitation with a helium-neon laser respectively and superimposed together. The confocal images were taken at various optical sections of the cells and reconstructed to form a z-stack showing the transverse side profile of the cells. The brightfield microscopy was done using the Olympus CK40 microscope with a 20x objective.

5.2.3 Phagocytosis assay

A phagocytosis assay was developed to assess the amount of gold nanoshells uptake by the macrophages based on the UV-Vis absorption intensity of ingested gold nanoshells extracted from the macrophages. After incubating the macrophages with gold nanoshells, the existing medium in the wells was discarded and each well was gently rinsed five times with 1X PBS to remove the excess gold nanoshells that were

not ingested while keeping the macrophages intact in the wells. The macrophages were then lysed using the mammalian protein extraction reagent (M-Per®, Pierce) to release the ingested gold nanoshells out of the cells. The suspension of extracted gold nanoshells in each well was transferred to a centrifuge tube to be centrifuged and rinsed for at least three times with Milli-Q water to remove the cellular components which might otherwise interfere with the UV-Vis absorption measurement of the extracted gold nanoshells. After the last rinse, the extracted gold nanoshells were resuspended in 500 µl of Milli-Q water and assessed for their UV-Vis absorption (UV-2401 PC UV-Vis spectrophotometer, Shimadzu Corp) from 400 to 900 nm.

The amount of gold nanoshells phagocytosed by the macrophages seeded in the wells was expressed as a percentage of the original amount of gold nanoshells added to each well based on their absorption intensity. The calculation is as such: the UV-Vis spectra of the originally added gold nanoshells and the extracted phagocytosed gold nanoshells were obtained. The peak absorption value (A_o) and its associated peak wavelength, λ_o of the original gold nanoshells added was noted and the absorption value of the phagocytosed gold nanoshells (A_p) at λ_o was then measured. The percentage of gold nanoshells phagocytosed per 100 µl of gold nanoshells colloid (2 x 10^{13} particles/ml) incubated with 5 x 10^5 macrophage cells was then given by $(\frac{A_p}{A_o} \times 100)\%$. In the phagocytosis assay, each condition investigated was done in triplicates to reduce random experimental errors.

5.3 Results and discussion

5.3.1 Synthesis and characterization of gold nanoshells

Gold nanoshells with a range of silica core diameters were synthesized to investigate the effect of gold nanoshells sizes on the macrophage uptake. The sizes include 79, 100, 140, 162, 181 and 196 nm. In the shell growth process, the gold hydroxide to seed solution volume ratio controls the amount of gold ions available for reduction and deposition on the silica surface. To control the gold nanoshells sizes, the volume ratio has been adjusted to maintain a constant shell thickness of 23 nm for all the silica core sizes, thus giving an overall size of 125, 146, 186, 208, 227 and 242 nm respectively based on the core sizes described above. The TEM image in Figure 5.3 shows the typical progressive growth of the gold shell around a 162 nm silica core to give a final gold nanoshell size of 208 nm.

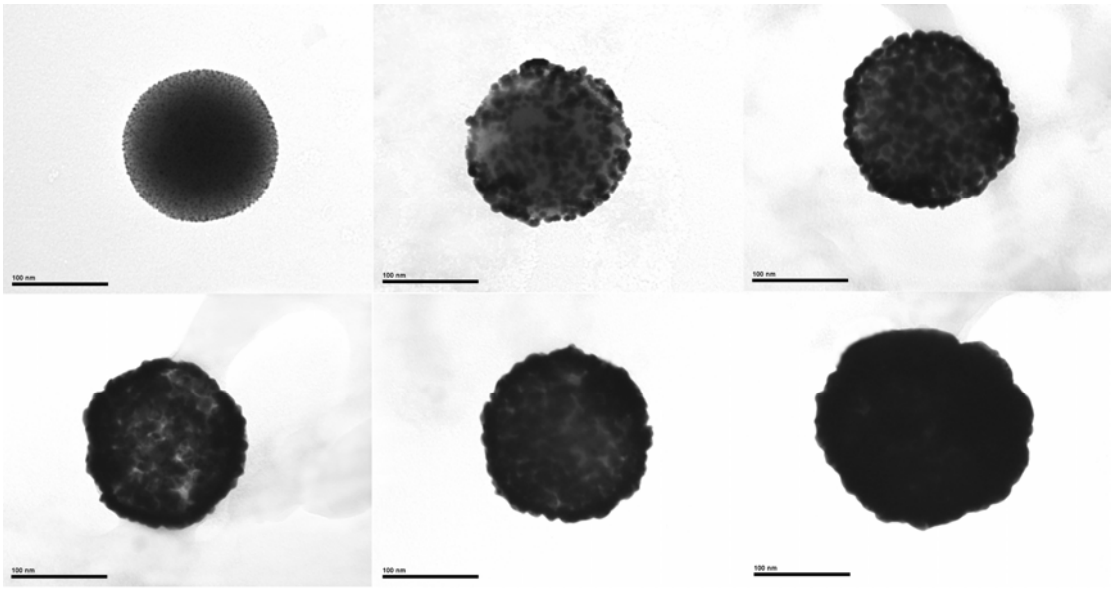

Figure 5.3. TEM images of nanoshell growth on a 162 nm silica nanoparticle core showing the initial gold hydroxide nanoparticles deposited on the silica and gradual growth and coalescence of these nanoparticles on the silica surface until a complete growth of 23 nm thick gold shell is obtained.

The gold nanoshells synthesized were spherical and generally monodispersed. The surfaces of the particles were also relatively smooth with an average surface roughness of 10 to 15 nm i.e. <10% of the particle radius from visual inspection. The gold nanoshells were then pegylated and the presence of mPEG-thiol on the gold nanoshells was assessed by XPS as shown in Figure 5.4. The XPS spectrum of the pegylated gold nanoshells shows a peak at binding energy of ≈ 163 eV which correspond to the binding energy for sulphur (2p). This peak indicates the presence of thiol group on the surface of gold nanoshells arising from the successful pegylation since such a peak is absent from the XPS spectrum of the naked gold nanoshells.

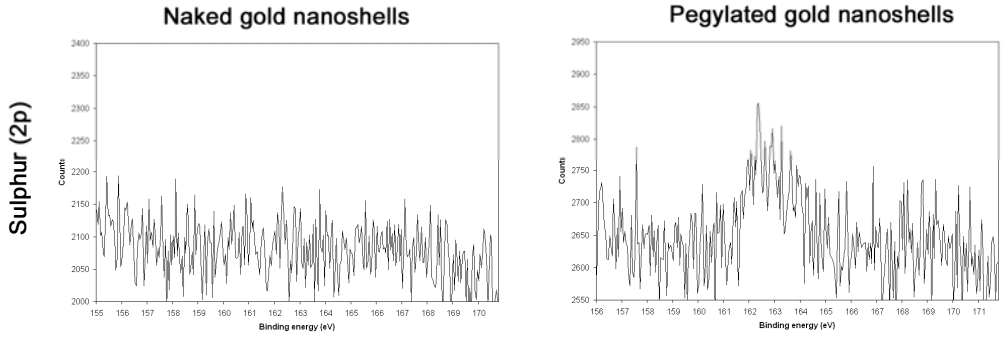

Figure 5.4. XPS of naked gold nanoshells (left) and pegylated gold nanoshells (right) to detect the presence of sulphur (2p) at binding energy of 163 eV. The peak observed indicates the successful thiol bonding on the surface of gold due to pegylation.

5.3.2 Reduction in macrophage uptake with pegylation

The effect of pegylation in reducing the macrophage uptake of gold nanoshells was demonstrated by imaging the accumulation of gold nanoshells in macrophages under the confocal microscope after 1 h of incubation. In this case, the 227 nm gold nanoshells are arbitrary selected for the imaging amongst the sizes synthesized. The

confocal images in Figure 5.5a show the green autofluorescence of the macrophages with the reflectance of the gold nanoshells superimposed in yellow.

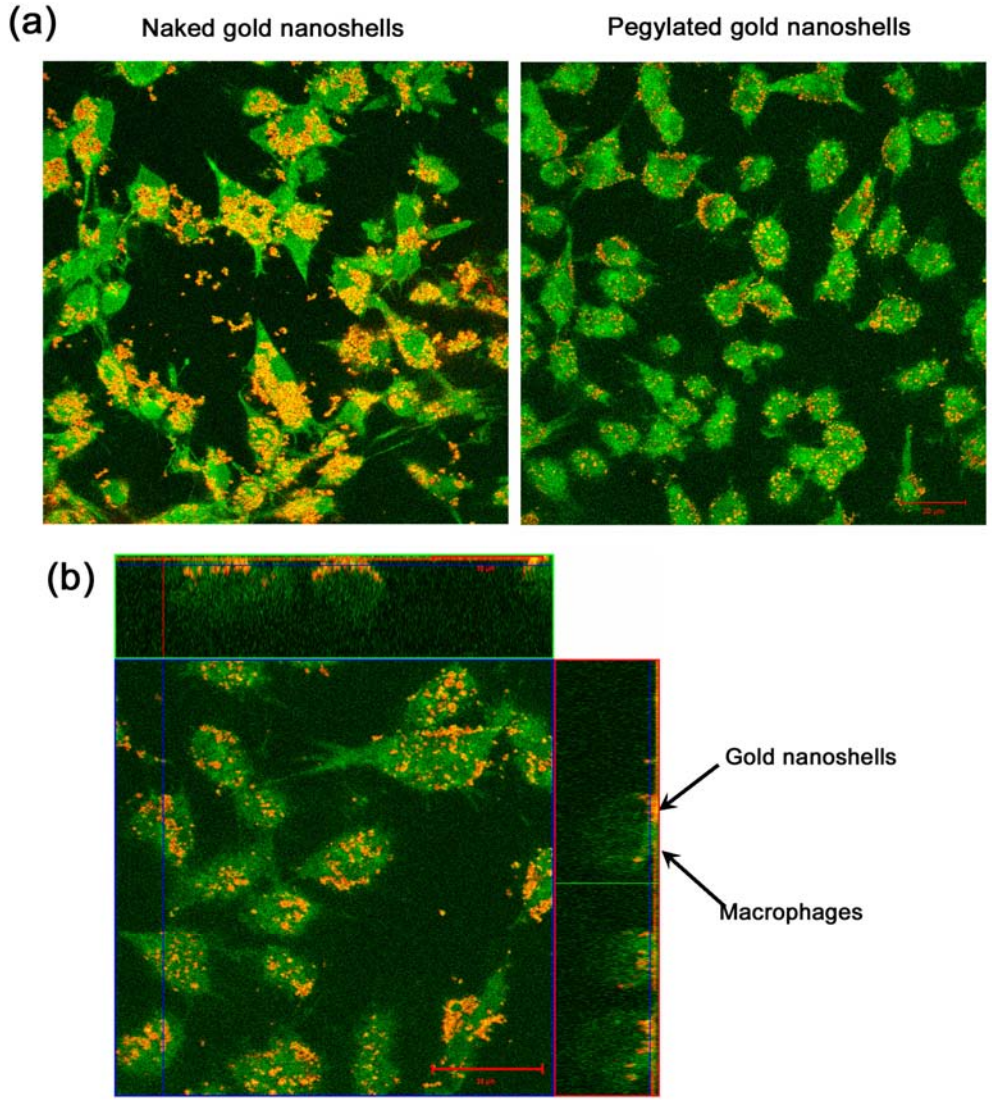

Figure 5.5. (a) Confocal images showing the accumulation of both naked and pegylated 227 nm gold nanoshells ingested in the macrophages. The macrophages are pseudo-colored green based on their autofluorescence and the reflectance from the gold nanoshells is pseudo-colored yellow. Images are taken at 63X magnification with an oil immersion lens. False-color autofluorescence and reflectance images are obtained at excitation of 488 nm and 633 nm respectively. Scale bar in both images is 20 μm. (b) The same confocal image with a z-stack reconstructed at the sides of the main image based on a series of optical sections to show the transverse side profile of the cells. The transverse section of the cells shows that the naked gold nanoshells are located inside the cells after being ingested by the macrophages.

A large amount of naked gold nanoshells is observed to co-localize together with the cells compare to the pegylated gold nanoshells where a much smaller amount is observed with the cells. The naked gold nanoshells appear aggregated possibly due to the high ionic content in the cell culture medium that reduces the charge stabilization in the nanoshells. The instability and aggregation of gold nanoshells may account for their increased macrophage uptake. Furthermore, the accumulation of the naked gold nanoshells appears to be randomized with no apparent pattern of distribution in the cells and the amount observed in each cell is also not homogeneously distributed.

To further ascertain that the gold nanoshells were ingested in the cells rather than being bound non-specifically on the cells surface, a z-stack showing the transverse side profile of the cells was reconstructed based on a series of optical sections to show the exact localization of gold nanoshells in the macrophages. The transverse cross section of the cells in Figure 5.5b shows that the naked gold nanoshells are located inside the cells after being ingested by the macrophages. Most of the gold nanoshells are found near the base of the cells with only a small amount being ingested further up into the cells. These gold nanoshells may have been freshly ingested given the short incubation time of 1 h.

5.3.3 Effect of surface density of PEG on macrophage uptake

Although the reduction in macrophage uptake due to pegylation is well known, the correlation between macrophage uptake and the extent of pegylation has not been systematically studied. Therefore, the surface density of PEG on the gold nanoshells was varied and the respective amount of gold nanoshells ingested was measured. This relationship would provide insight to the optimum amount of PEG needed to

functionalize the gold nanoshells to minimize macrophage uptake. In this case, the different surface density of PEG on gold nanoshells was implemented by incubating the nanoshells (227 nm, 2 x 10^{13} particles) with different amount of mPEG-thiol (MW = 2000 Da) from 0.05 to 20 µmol to control the amount of mPEG-thiol available to bind to the gold nanoshells surface. The results in Figure 5.6 shows the percentage of gold nanoshells phagocytosed for different amount of mPEG-thiol added to gold nanoshells. As the amount of mPEG-thiol increases from 0 to 2.5 µmol, the percentage of gold nanoshells phagocytosed decreases from 78.9% to 8.9%.

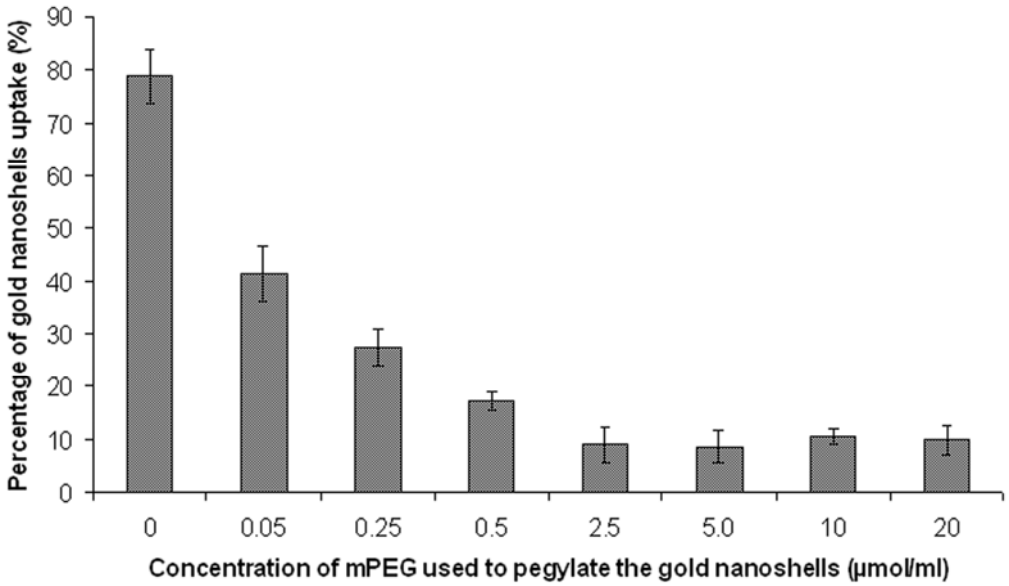

Figure 5.6. The percentage of gold nanoshells phagocytosed for different concentration of mPEG-thiol (MW = 2000 Da) added to pegylated the 227 nm gold nanoshells (2 x 10^{13} particles/ml) to give a range of surface density of PEG.

The corresponding brightfield images showing the macrophage uptake for each of the mPEG-thiol concentration is shown in Figure 5.7. Due to the plasmonic color of the colloidal gold nanoshells, the presence of ingested gold nanoshells in the macrophages gives the cells a greenish stain under the brightfield microscope to provide an indication on its loading in the cells. With the percentage of gold

nanoshells phagocytosed decreases from 78.9% to 8.9%, the brightfield images also show a reduction in the green staining by gold nanoshells in the macrophages. The density of PEG chains assembled on the gold nanoshells surface controls the amount of water molecules that could be “trapped” to form the hydrophilic layer. Based on the amount of mPEG-thiol used in the study, an attempt is made to estimate the number of PEG molecules bound on the gold nanoshells surface with the assumption that all mPEG-thiol added to the gold nanoshells are bound to the particles surface.

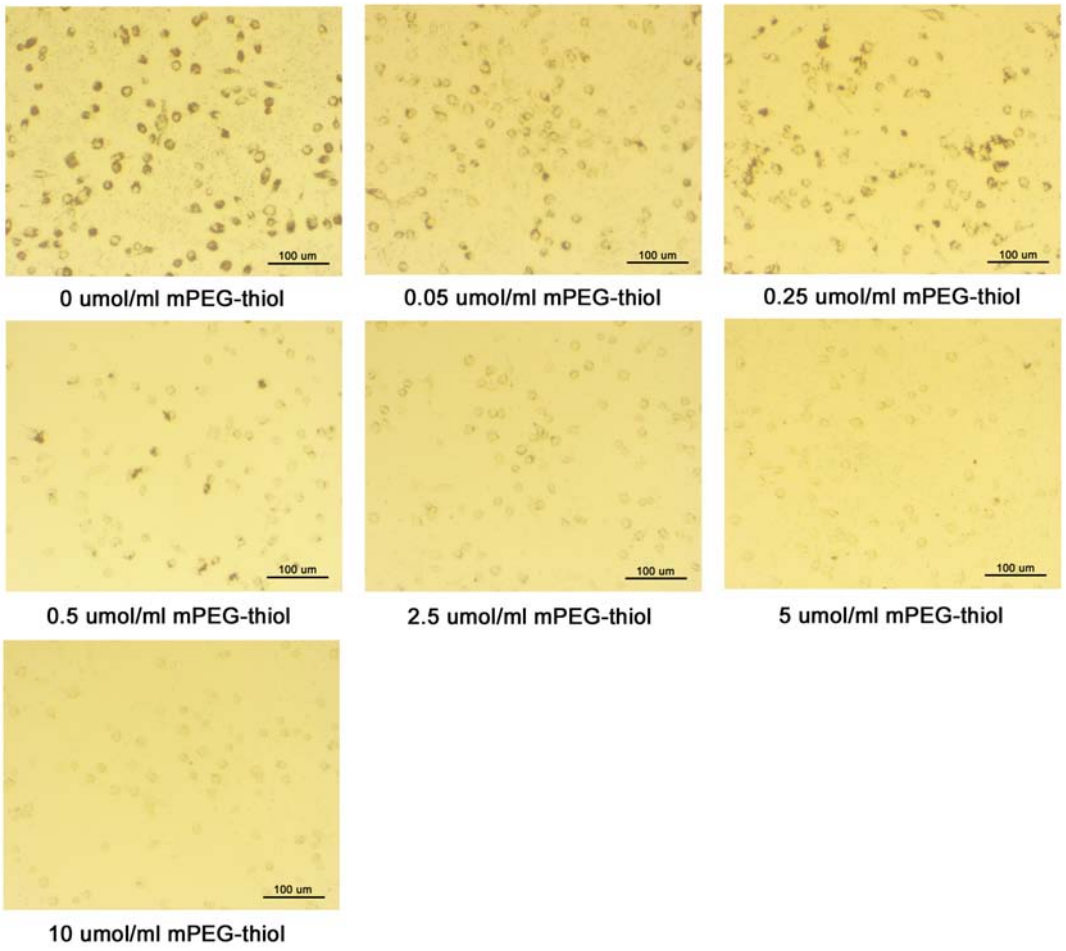

Figure 5.7. The brightfield images showing the gold nanoshells pegylated with the different amount of mPEG-thiol being taken up by the macrophages after 1 h of incubation. Due to the plasmonic color of the gold nanoshells, the presence of ingested gold nanoshells in the macrophages gives the cells a greenish stain under the brightfield microscope that provides an indication on its loading in the cells.

With an approximate 2 x 10^{13} gold nanoshells available for pegylation, the addition of 0.05 µmol mPEG-thiol (MW 2000 Da) would give about 1500 molecules per gold nanoshell particle (diameter of 227 nm) with each mPEG-thiol molecule having a calculated footprint of about 108 nm^2 on the particle surface (0.0093 PEG/nm^2). With such a sparse amount of mPEG-thiol chains, the water interaction level is low and much of the hydrophobic surface on the gold nanoshells remains available for hydrophobic binding to proteins. Furthermore, the vast footprint provides little steric hindrance to opsonins such as immunoglobulins with a typical size of about 15 nm. This encourages macrophage recognition and uptake.

As the amount of mPEG-thiol on the surface increases to 0.5 µmol, each gold nanoshell particle would be pegylated with about 15 000 molecules of mPEG-thiol with each molecule having a calculated footprint of only about 10.8 nm^2 (0.093 PEG/nm^2). This increased closeness of the PEG chains allows greater interaction with water molecules and thus the amount of hydrophobic surface available for hydrophobic interactions with macrophage recognition proteins reduces and the corresponding macrophage uptake reduces by more than 8 fold. Hence the correlation obtained from the experiments was expected.

5.3.4 Saturation of PEG on gold nanoshells surface

As the amount of mPEG-thiol added to the gold nanoshells increases beyond 2.5 µmol, there is no further reduction in the macrophage uptake which maintain at around 10% as shown in Figure 5.6. The corresponding brightfield images also show similar staining intensity with no observable change in gold nanoshells loading in the macrophages. This indicates that saturation of mPEG-thiol binding on the gold

nanoshells surface may have occurred at around 2.5 µmol and the excess mPEG-thiol were removed from the pegylated gold nanoshells during the rinsing steps.

This saturation amount in the binding of mPEG-thiol on the gold nanoshells was further verified by measuring the amount of excess mPEG-thiol that were left unbound using the Ellman's reagent test which detects the presence of unbound thiol group from the mPEG-thiol in the reaction mixture. In such a test, the amount of excess mPEG-thiol is determined by measuring the absorbance of Ellman's reagent at 430 nm. The extrapolated results as shown in Figure 5.8 suggest that excess mPEG-thiol in the supernatant appears only after adding more than 2.5 µmol of mPEG-thiol and thus confirm that a minimum of 2.5 µmol of mPEG-thiol is sufficient to saturate the PEG binding on the gold nanoshells surface to achieve an optimum surface density of PEG.

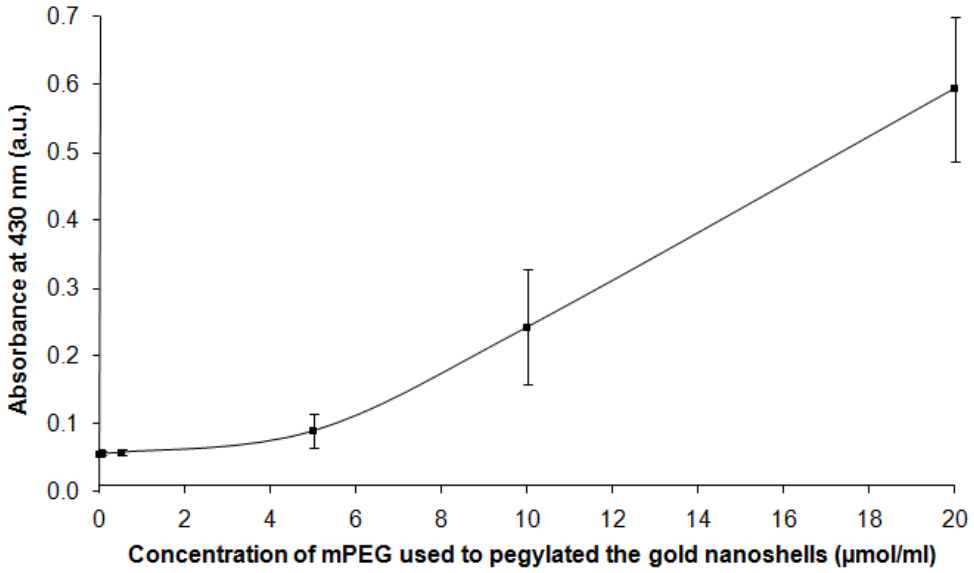

Figure 5.8. Quantitation of unbound thiol group from the excess mPEG-thiol in the supernatant using Ellman's reagent after the addition of different amount of mPEG-thiol to the 227 nm gold nanoshells. The extrapolated results further confirm that excess mPEG-thiol in the supernatant appears only after adding more than 2.5 µmol of mPEG-thiol to the 2 x 10^{13} gold nanoshells when the surface of the gold nanoshells is saturated with PEG binding.

Intuitively, for the PEG barrier to be the most effective, it has to saturate and cover the entire surface of a particle. A full PEG coverage denies small opsonins the opportunity to approach the nanoshells surface to minimize macrophage recognition. Because of the small size of mPEG-thiol molecule (published literature has shown that a 1000 Da PEG gives 1.8 nm hydrodynamic diameter [22]), the experimental results show that more mPEG-thiol molecules can be packed further onto the surface of the gold nanoshell particle until a saturation point in the PEG binding is reached at 2.5 µmol. This would correspond to about 75 000 molecules of mPEG-thiol on each gold nanoshell particle with each molecule having a footprint of just 2.2 nm^2 (0.46 PEG/nm^2). At this point, the footprint available per 2000 Da mPEG-thiol molecule is smaller than the cross sectional area based on the hydrodynamic diameter of a single 1000 Da mPEG-thiol molecule itself [22]. Thus the mPEG-thiol molecules are so tightly packed that no further binding of mPEG-thiol molecules can occur.

With a surface saturated with PEG, any further addition of mPEG-thiol will only form excesses in the supernatant as detected by the Ellman's reagent. The saturated surface characteristic also causes no further reduction in the macrophage uptake beyond the saturation amount of mPEG-thiol added since the hydrophilic surface layer is already optimized by the maximum number of mPEG-thiol molecules loaded. Such a parametric investigation to titrate out the saturation amount of PEG would be beneficial to determine the minimum amount of PEG that is sufficient to saturate the PEG binding on the gold nanoshells surface and achieve an optimum surface density of PEG chains without causing additional wastage of reagents since increasing the PEG concentration would not result in any further decrease in phagocytosis.

It would be of worth to note that the amount of mPEG-thiol as determined in the study i.e. 2.5 µmol is only appropriate for 227 nm gold nanoshells at 2 x 10^{13} particles/ml. But the present study provides an approximate indication to the saturation amount per particle in a generic manner since the PEG molecular footprint of 2.2 nm^2 (0.46 PEG/nm^2) for surface saturation may well be applied for nanoparticles of other sizes and concentration and the same technique can be applied to gold nanoshells of other sizes and concentration to determine their respective optimum PEG amount.

5.3.5 Effect of PEG chain length on macrophage uptake

Besides the surface density of PEG, the chain length of the PEG molecule also plays a role in mediating the macrophage uptake of gold nanoshells. The effect of different chain length of PEG on the macrophage uptake of the gold nanoshells was investigated by pegylating the 186 nm gold nanoshells with mPEG-thiol of five different molecular weights: MW = 750, 2000, 5000, 10 000 and 20 000 Da, all having the same concentration of 2.5 µmol/ml as determined earlier. Since the physical chain length is a parameter that is difficult to measure experimentally, a parametric investigation on the PEG chain length is examined on the basis of their molecular weight. As the mPEG-thiol is a linear chain polymer, its molecular weight is closely correlated to its chain length. For each molecular weight, their respective percentage of phagocytosis is obtained as shown in Figure 5.9.

Figure 5.9 shows that a relatively larger amount of phagocytosis takes place for gold nanoshells pegylated with both the shortest and longest chain used in our study. In this case, the percentage of phagocytosis for gold nanoshells pegylated with 750 Da mPEG-thiol is 10.2% while the gold nanoshells pegylated with the longest 20 000 Da

mPEG-thiol shows a phagocytosis percentage of 48.2%. In between these two molecular weights, the percentage of gold nanoshells uptake in the mid-range of PEG molecular weights is very much lower, averaging at around 1%. In fact, the percentage of phagocytosis is lowest at 0.6% for gold nanoshells pegylated with 2000 Da mPEG-thiol. Within this mid-range, there are also small increases in the macrophage uptake as the mPEG-thiol molecular weight is increased from 2000 Da to 5000 Da (0.9%) and 10 000 Da (2.1%). Our results thus suggest that there is an optimum range of molecular weight of PEG that can be used to pegylated the gold nanoshells to minimize their macrophage recognition and uptake.

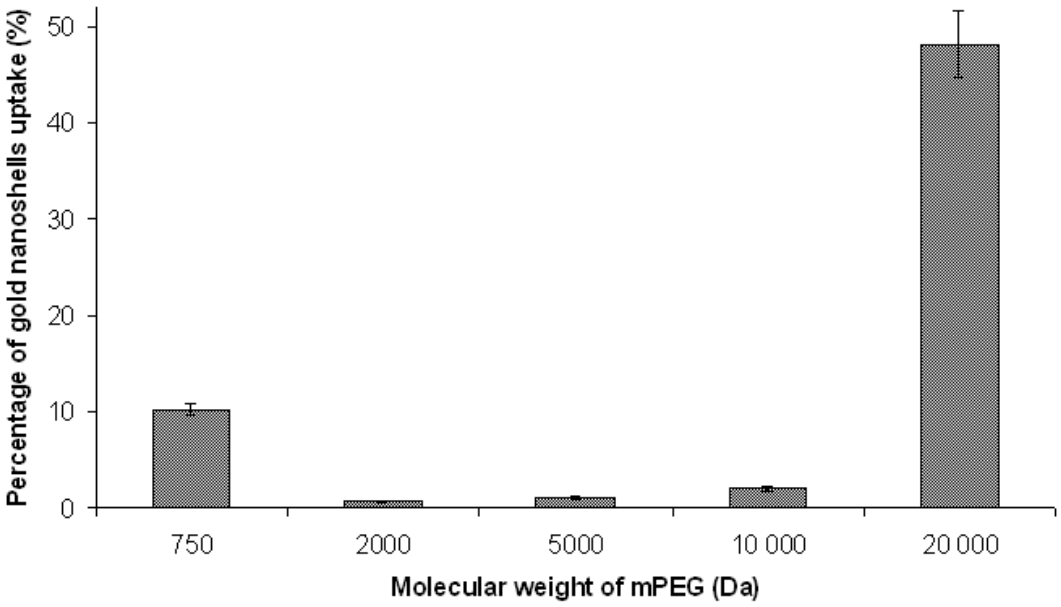

Figure 5.9. The percentage of gold nanoshells phagocytosed for 186 nm gold nanoshells (2 x 10^{13} particles/ml) pegylated with different chain length of mPEG-thiol as given by their molecular weight to show the effect of different chain length of mPEG-thiol on the macrophage uptake of gold nanoshells. All the pegylation are done using the same concentration of 2.5 µmol/ml for each molecular weight of mPEG-thiol added to the gold nanoshells.

The results above demonstrate the influence of the chain length in agreement with that reported by others [23]. PEG is known to exist in a wide range of molecular weights, but is also widely known that only a narrow range is appropriate for biological applications. The results in Figure 5.9 confirm this for gold nanoshells where gold nanoshells pegylated with either the smallest (750 Da) or the largest (20 000 Da) mPEG-thiol show higher percentages of phagocytosis than those pegylated with mPEG-thiol of molecular weights in between.

A minimum molecular weight of PEG is often required for pegylation to avoid macrophage recognition because PEG chains that are too short lose their flexibility. This flexibility of PEG chains is important because it facilitates transient and rapid changes in the structural formation of the PEG layer [12] around the gold nanoshells in the biological fluid environment to make it difficult for proteins or macrophages to tether to it. In another study by Bergström et al. [24], protein adsorption was found to be dramatically increased on polystyrene particles coated with poly(ethylene oxide) of 1000 Da and below, with PEG of 250 Da virtually offering no protein rejection ability at all. The short chain 750 Da mPEG-thiol used in this study could have such compromised flexibility that results in their higher macrophage uptake.

On the other hand, PEGs with too much flexibility that are often associated with long chain lengths may also not be effective in minimizing phagocytosis. Given their very high flexibility, these PEG chains that are too long have a high tendency to fold into coils or bend into a mushroom-like configuration on the surface of the gold nanoshell [18] as shown in Figure 5.10. Such foldings or mushroom configurations often lead to lower surface density of PEG since the folding of long chains occupies more space

and forms a steric barrier to the attachment of other neighboring PEGs on the gold nanoshells surface.

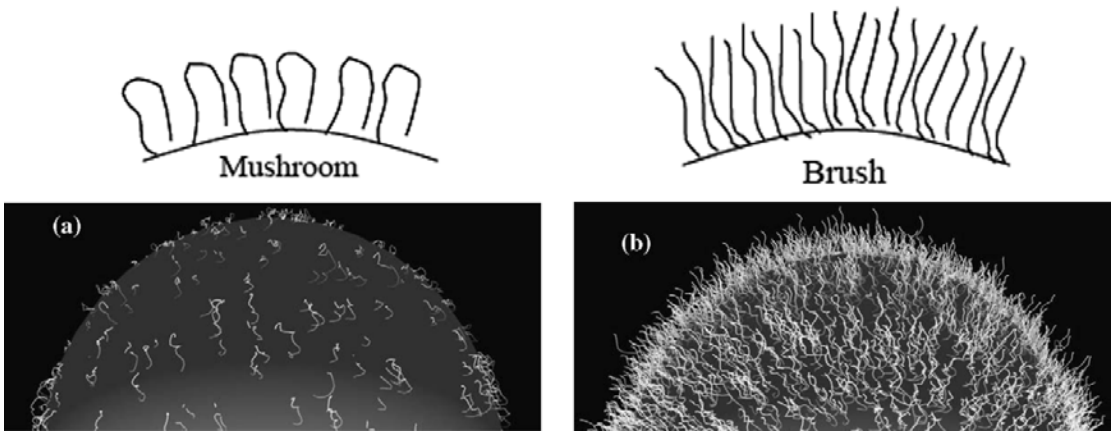

Figure 5.10. Schematic diagrams of brush and mushroom configurations of PEG chains on upper hemisphere of a nanoparticle. In (a), the low surface coverage of PEG chains is the result of a "mushroom" configuration where most of the chains are located closer to the particles surface. In (b), the "brush" configuration leads to a high surface coverage where most of the chains are extended away from the surface [4].

In a study on stealth niosomes which are a type of non-ionic surfactant vesicular drug carriers, often considered as the novel forms of liposomes, Shi et al. found that the grafting surface density was 0.53, 0.45 and 0.17 PEG/nm^2 for niosomes pegylated with 2000, 5000 and 10 000 Da PEG respectively [25] and so attributed the low density of high molecular weights PEG to the fact that the long hydrophilic chains were more likely to fold into coils in solution compared to shorter chains. This suggest a link between the PEG molecular weight and the PEG surface density and that the uptake is ultimately affected more by surface density than on PEG molecular weight.

The dependence of macrophage uptake on the surface density of PEG has been discussed earlier. An optimum range of molecular weight of PEG between the two

ends would allow them to tether to the gold nanoshell surface in a predominantly brush-like configuration with minimal folding. This brush configuration allows a higher density of PEG to be bound to the surface of gold nanoshells and hence provides a more robust barrier than a folded or mushroom configuration. The results in this study have shown that the moderate chain length between 2000 Da to 5000 Da gives the lowest macrophage uptake. This range of molecular weight represents a good compromise between flexibility of PEG and surface density of PEG to reduce opsonization and minimize macrophage recognition and uptake. Other similar studies that investigate the effect of molecular weights of stabilizing polymer chains in reducing the macrophage uptake of other colloidal drug delivery systems have also shown similar results, advocating the most effective molecular weight of PEG in the range of 1500 to 3500 Da [26-28].

5.3.6 Effect of gold nanoshell sizes on macrophage uptake

The size of the nanoparticles is known to influences their clearance rate and final biodistribution in the body [23]. The above parametric studies are done using gold nanoshells of 186 nm (silica core diameter of 140 nm with gold shell of 23 nm). Since the particle size is also known to be a major factor affecting the fate of pegylated particles when administered into the body, a similar macrophage study on a range of gold nanoshells sizes would provide valuable insights on the sensitivity of the macrophages to their sizes. Gold nanoshells were synthesized with six different sizes: 125, 146, 186, 208, 227 and 242 nm that are appropriate for intravenous delivery and pegylated with mPEG-thiol of 2000 Da. The results of their macrophage uptake are shown in Figure 5.11 below.

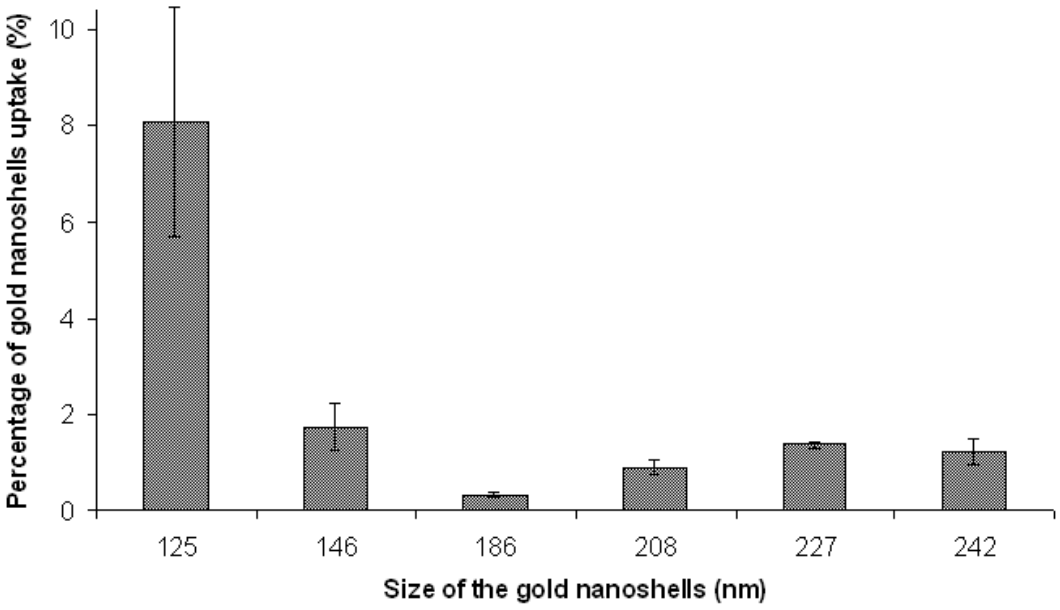

Figure 5.11. The percentage of gold nanoshells phagocytosed for different sizes of gold nanoshells (2 x 10^{13} particles/ml) pegylated with mPEG-thiol (MW = 2000 Da) at a concentration of 2.5 µmol/ml. The six different sizes are used to investigate the sensitivity of macrophages to gold nanoshells sizes and are appropriate for applications involving intravenous administration.

The results in Figure 5.11 show that the smallest size 125 nm gold nanoshells used in this study is the most susceptible to phagocytosis by macrophages with 8.1% of the gold nanoshells ingested. The macrophage uptake is reduced as the diameter of the gold nanoshells increases from 125 to 146 nm (1.7% of gold nanoshells phagocytosed) before the percentage of phagocytosis reaches the lowest at 0.54% when the gold nanoshells are 186 nm. As the diameter of the gold nanoshells increases beyond 186 nm, the amount of gold nanoshells ingested by the macrophages begins to increase again although the change is small and barely noticeable.

From Figure 5.11, a small positive correlation between the size of gold nanoshells and phagocytosis is observed when the gold nanoshells are larger than 186 nm. In this case, the macrophage uptake is increased gradually from 0.9% (208 nm) to 1.4% (227

nm) and remains rather constant at around 1.2% when the gold nanoshells size reaches 242 nm. From these results, gold nanoshells with a size of 186 nm seem to be the least sensitive to macrophage uptake, but increasing their size by another 60 nm beyond this size will not significantly increase their phagocytosis. These results on the sizes of gold nanoshells, together with that on the parametric investigation of the PEG chain length is summarized in Table 5.1 below which shows the results in terms of macrophage uptake versus size and PEG coating simultaneously.

Table 5.1. Summary table of the *in vitro* macrophage uptake results for two of the parameters investigated in this study: the chain length of the PEG used and the size of the gold nanoshells.

Sizes of gold nanoshells pegylated with 2000 Da PEG (nm)	**Macrophage uptake (%) with S.D.**	**PEG chain length on 186 nm gold nanoshells (Da)**	**Macrophage uptake (%) with S.D.**
125	8.08 ± 2.39	750	10.21 ± 0.54
146	1.74 ± 0.49	2000	0.59 ± 0.02
186	0.54 ± 0.05	5000	0.93 ± 0.15
208	0.90 ± 0.16	10 000	2.07 ± 0.28
227	1.37 ± 0.08	20 000	48.22 ± 3.43
242	1.22 ± 0.28		

Most *in vivo* studies on other types of polymeric nanoparticles uptake by macrophages have reported that smaller nanoparticles are removed more slowly from blood circulation than larger nanoparticles [4]. The ability of smaller nanoparticles to better escape recognition by macrophages is, however, not observed in this study. Instead, the smallest gold nanoshells used i.e. 125 nm causes the highest macrophage uptake. Furthermore, the percentage of phagocytosis actually increases as the diameters decreases from 186 nm to 146 nm and 125 nm. Unlike the case of polymeric nanoparticles that are often more stable in aqueous medium even in the absence of

any functional stabilizing agent on their surface, the surface of gold nanoparticles is highly susceptible to aggregation and is thus very much dependent on the presence of stabilizing agents such as PEG. Unfortunately, the surface density of PEG is also dependent on the particle surface curvatures. A study by Li et al. on poloxamer coated polystyrene nanoparticles of diameters 69 nm, 130 nm, 212 nm and 272 nm has shown that surface density of poloxamer adsorbed decreases with decreasing particle size i.e. higher particle surface curvature [29]. This could explain the observation that the smaller gold nanoshells show a higher macrophage uptake.

Since gold nanoshells possess the same spherical nature as polystyrene, similar inference can be made on gold nanoshells. As the smaller nanoshells possess a higher surface curvature than larger ones, this suggests that smaller nanoshells may prove less efficient for PEG chains to bind and form covalent bonds with the gold surface compared to the flatter surface of larger gold nanoshells with a smaller curvature. Consequently, smaller gold nanoshells will have lower surface density of PEG chains on their surfaces than their larger counterparts. The effect of having a lower surface density of PEG has been discussed previously in terms of a reduced aqueous stability and less effective masking from RES.

The higher risk of aggregation with a lower surface density of PEG is especially prominent in small gold nanoshells where their surface energy is high. Therefore, even though the smaller gold nanoshells sizes may better escape recognition by macrophages, the higher tendency of aggregation of these particles may still exert a more dominant effect in increasing the macrophage uptake. As the size of the gold nanoshells increases beyond 186 nm, the particle surface curvature becomes more

conducive for PEG binding and so this size dependence effect on the PEG surface density and hence the macrophage uptake becomes less pronounced since the macrophage uptake remains relatively constant at the larger sizes.

5.4 Conclusion

Pegylation of gold nanoshells with mPEG-thiol provides an effective means to reduce macrophage phagocytosis. The three factors that are examined in this chapter which can affect the ability of macrophage to ingest gold nanoshells include the PEG surface density, PEG molecular weight and size of gold nanoshells. The results suggest that the effect of molecular weight of PEG and size of gold nanoshells can also influence the surface density of PEG, thus implying the surface density of PEG as a critical end parameter that determines their macrophage uptake. A saturated surface density would minimize any macrophage uptake and this could be obtained by experimental titration based on the Ellman's reagent. The results have also shown that a suitable range of PEG molecular weight of around 2000 Da and a size range larger than 186 nm would be appropriate for facilitating a high surface density. Sizes that are too small would render a less effective coating of PEG to overcome aggregation.

Although the *in vitro* macrophage system provides a good model to accurately predict the RES response to different pegylation parameters, it would be of worth to note that the reduced phagocytosis *in vitro* may not necessary be translated to the same desired results *in vivo* since a whole host of other physiological factors may further complicate *in vivo* conditions. Nonetheless, the merits of this model allows results from this study to be used to synthesize long circulating gold nanoshells which can be injected intravenously into animal subjects for further *in vivo* studies.

Whilst the effective pegylation of gold nanoshells would be sufficient to prolong their circulation time for slow *in vivo* delivery to tumor site via the EPR effect, the delivery of these gold nanoshells to specific molecular markers in suspicious lesions would require specific targeting capability in the form of antibody conjugation. The conjugation of antibody to gold nanoshells and the application of the entire bioconjugate construct for specific molecular imaging are described in more detail in the following Chapter 6.

5.5 References

1. Gobin AM, Lee MH, Halas NJ, James WD, Drezek RA, West JL. Near-infrared resonant nanoshells for combined optical imaging and photothermal cancer therapy. *Nano Lett* 2007; 7(7): 1929-1934.

2. Wang Y, Xie X, Wang X, Ku G, Gill KL, O'Neal DP, Stoica G, Wang LV. Photoacoustic Tomography of a Nanoshell Contrast Agent in the in Vivo Rat Brain. *Nano Lett.* 2004; 4(9): 1689-1692.

3. O'Neal DP, Hirsch LR, Halas NJ, Payne JD, West JL. Photo-thermal tumor ablation in mice using near infrared-absorbing nanoparticles. *Cancer Lett* 2004; 209(2): 171-176.

4. Owens DE, 3rd, Peppas NA. Opsonization, biodistribution, and pharmacokinetics of polymeric nanoparticles. *Int J Pharm* 2006; 307(1): 93-102.

5. Frank MM, Fries LF. The role of complement in inflammation and phagocytosis. *Immunol Today* 1991; 12(9): 322-326.

6. Illum L, Davis SS, Muller RH, Mak E, West P. The organ distribution and circulation time of intravenously injected colloidal carriers sterically stabilized with a block copolymer--poloxamine 908. *Life Sci* 1987; 40(4): 367-374.

7. Panagi Z, Beletsi A, Evangelatos G, Livaniou E, Ithakissios DS, Avgoustakis K. Effect of dose on the biodistribution and pharmacokinetics of PLGA and PLGA-mPEG nanoparticles. *Int J Pharm* 2001; 221(1-2): 143-152.

8. Gref R, Domb A, Quellec P, Blunk T, Müller RH, Verbavatz JM, Langer R. The controlled intravenous delivery of drugs using PEG-coated sterically stabilized nanospheres. *Advanced Drug Delivery Reviews* 1995; 16(2-3): 215-233.

9. Storm G, Belliot SO, Daemen T, Lasic DD. Surface modification of nanoparticles to oppose uptake by the mononuclear phagocyte system. *Advanced Drug Delivery Reviews* 1995; 17(1): 31-48.

10. Torchilin VP. Polymer-coated long-circulating microparticulate pharmaceuticals. *J Microencapsul* 1998; 15(1): 1-19.

11. Allen TM. Long-circulating (sterically stabilized) liposomes for targeted drug delivery. *Trends Pharmacol Sci* 1994; 15(7): 215-220.

12. Woodle MC, Lasic DD. Sterically stabilized liposomes. *Biochim Biophys Acta* 1992; 1113(2): 171-199.

13. Woodle MC, Newman MS, Martin FJ. Liposome leakage and blood circulation: Comparison of adsorbed block copolymers with covalent attachment of PEG. *International Journal of Pharmaceutics* 1992; 88(1-3): 327-334.

14. Harper GR, Davies MC, Davis SS, Tadros TF, Taylor DC, Irving MP, Waters JA. Steric stabilization of microspheres with grafted polyethylene oxide reduces phagocytosis by rat Kupffer cells in vitro. *Biomaterials* 1991; 12(7): 695-700.

15. Tan JS, Butterfield DE, Voycheck CL, Caldwell KD, Li JT. Surface modification of nanoparticles by PEO/PPO block copolymers to minimize interactions with blood components and prolong blood circulation in rats. *Biomaterials* 1993; 14(11): 823-833.

16. Gref R, Minamitake Y, Peracchia MT, Trubetskoy V, Torchilin V, Langer R. Biodegradable long-circulating polymeric nanospheres. *Science* 1994; 263(5153): 1600-1603.

17. James WD, Hirsch LR, West JL, O'Neal PD, Payne JD. Application of INAA to the build-up and clearance of gold nanoshells in clinical studies in mice. *J Radioanal Nucl Ch* 2007; 271: 455-459.

18. Zahr AS, Davis CA, Pishko MV. Macrophage uptake of core-shell nanoparticles surface modified with poly(ethylene glycol). *Langmuir* 2006; 22(19): 8178-8185.

19. Illum L, Jacobsen LO, Muller RH, Mak E, Davis SS. Surface characteristics and the interaction of colloidal particles with mouse peritoneal macrophages. *Biomaterials* 1987; 8(2): 113-117.

20. Wuang SC, Neoh KG, Kang E-T, Pack DW, Leckband DE. Heparinized Magnetic Nanoparticles: In-Vitro Assessment for Biomedical Applications. *Advanced Functional Materials* 2006; 16(13): 1723-1730.

21. Ellman GL. Tissue sulfhydryl groups. *Arch Biochem Biophys* 1959; 82(1): 70-77.

22. Nagahama M, Hayashi S, Morimitsu S, Sakurai J. Biological activities and pore formation of Clostridium perfringens beta toxin in HL 60 cells. *J Biol Chem* 2003; 278(38): 36934-36941.

23. Vonarbourg A, Passirani C, Saulnier P, Benoit JP. Parameters influencing the stealthiness of colloidal drug delivery systems. *Biomaterials* 2006; 27(24): 4356-4373.

24. Bergstrom K, Osterberg E, Holmberg K, Hoffman AS, Schuman TP, Kozlowski A, Harris JH. Effects of branching and molecular weight of surface-bound poly(ethylene oxide) on protein rejection. *J Biomater Sci Polym Ed* 1994; 6(2): 123-132.

25. Shi B, Fang C, Pei Y. Stealth PEG-PHDCA niosomes: effects of chain length of PEG and particle size on niosomes surface properties, in vitro drug release, phagocytic uptake, in vivo pharmacokinetics and antitumor activity. *J Pharm Sci* 2006; 95(9): 1873-1887.

26. Moghimi SM, Hunter AC. Capture of stealth nanoparticles by the body's defences. *Crit Rev Ther Drug Carrier Syst* 2001; 18(6): 527-550.

27. Golander CG, Herron JN, Lim K, Claesson P, Stenius P, Andrade JD. Properties of immobilized PEG films and interaction with proteins, experiments and modeling. In: Harris JM, ed. Poly(ethylene glycol) chemistry: biotechnical and biomedical applications New York: Plenum Press, 1992:221-245.

28. Antonsen KP, Hoffman AS. Water structure of PEG solutions by differential calorimetry measurements. In: Harris JM, ed. Poly(ethylene glycol) chemistry: biotechnical and biomedical applications New York: Plenum Press, 1992:15-27.

29. Li J-T, Caldwell KD, Rapoport N. Surface Properties of Pluronic-Coated Polymeric Colloids. *Langmuir* 1994; 10(12): 4475-4482.

CHAPTER SIX

CELLULAR IMAGING WITH GOLD NANOSHELLS

Abstract

The use of gold nanoshells as a molecular contrast agent for performing molecular imaging under reflectance-based imaging systems requires appropriate antibody conjugation in addition to pegylation to facilitate the targeting and binding to these molecular targets. This chapter describes the antibody conjugation to gold nanoshells and the application of the entire gold bioconjugate construct for specific molecular imaging of the Epidermal Growth Factor Receptor (EGFR) *in vitro* under confocal reflectance microscopy. Gold nanoshells were synthesized and surface functionalized by conjugating them to anti-EGFR before introducing them to cells to examine for optical changes. The results show at least three areas where the imaging is improved upon with antibody functionalized gold nanoshells. Firstly, the optical response of gold nanoshells is able to provide a general contrast enhancement by increasing the reflectance signal. Secondly, this enhancement can be made specific to discriminate cancer from normal cells and lastly, molecular expression can be imaged when the gold nanoshells are conferred specificity to the molecular marker. These results suggest the potential of gold nanoshells in performing molecular contrast optical imaging under reflectance mode with appropriate surface functionalization. This work has been submitted for publication in *Molecular Imaging and Biology* and *Technology in Cancer Research and Treatment.*

6.1 Introduction

Gold nanoparticles are bioinert optical plasmonic materials under development for clinical imaging and drug delivery [1-3]. The first demonstration of such an application by Sokolov et al. uses the gold nanoparticles to create an optical contrast to image precancer [4]. Since then, similar observations have also been published recently to corroborate such findings [5, 6]. While the use of gold nanoparticles as optical labelers in reflectance-based optical imaging is well appreciated, it is limited to a narrow optical excitation range that is appropriate for use with only certain optical systems having a suitable matching wavelength. This is due to its rather invariable optical plasmon resonance, typically at 520 nm (see Chapter 2.4.1). Although its plasmon resonance is known to vary with size of the nanoparticles, in practice, the plasmon resonance of gold nanoparticles hardly red-shifts by more than 60 nm before their sizes become impractical for biological applications [7].

Hence, for most optical imaging systems that operate in the near infrared (NIR) wavelengths, which is within the region of optimum physiological transmissivity of light best suited for optical bioimaging, such as the OCT, the use of gold nanoparticles is restrictive since their peak optical response (≈ 520 nm) is not matched to the 700-1300 nm wavelength commonly for NIR imaging, resulting in their sub-optimum optical performance as contrast agents.

In principle, the optical limitations associated with gold nanoparticles can be addressed by the use of gold nanoshells. Gold nanoshells have emerged as a promising class of optical contrast agent with the potential to deliver the needed red-shifted plasmon resonance to NIR wavelength. These nanoparticles employ a core-

shell construction with a spherical dielectric core is surrounded by a thin gold layer [8-16]. Unlike solid gold nanoparticles, the optical response of gold nanoshells can be tuned from the visible right up to the NIR wavelength range by changing the relative dimension of the gold shell thickness to the core radius to match the excitation wavelength of the light source of interest in different applications [17]. Hence, they are versatile for use with both the confocal reflectance microscope and OCT.

Besides a strong scattering response from individual particles, gold nanoshells have the ability to undergo coupled SPR when closely-spaced to promote strong interaction with photons [18]. The scattering cross section per particle is known to increase when gold nanostructures aggregate and their surface plasmon interact to produce an even larger optical signal [4]. This mode of enhanced scattering from coupled SPR can be exploited to further enhance the optical scattering signal for better optical contrast when the gold nanoshells are brought close together under the influence of biochemical processes associated with disease pathology in cellular environment.

Apart from their optical properties, gold nanoshells also present inert biological activities in living systems which make them appropriate for biological applications [19-21]. They can be surface functionalized readily with targeting moieties such as antibodies or peptides to probe for specific cellular biomarkers with high specificity and affinity. When coupled with appropriate biomarkers, these gold nanoshells bioconjugates may potentially provide useful optical signal for molecular specific information in the diagnosis of early pathologies such as pre-cancers before phenotypic changes occur [22].

Since the optical resonance of the gold nanoshells can be easily tuned to the NIR, these gold nanostructures would therefore be preferred over solid gold nanoparticles as contrast agents for imaging applications involving longer optical wavelength. In this chapter, the antibody conjugation of gold nanoshells is described, together with their use as appropriate reflectance-based contrast agent for performing molecular specific contrast under confocal reflectance microscopy operating at 633 nm excitation. Their strong optical scattering response is exploited to improve the optical detectability of certain clinically relevant molecular markers which is subsequently used to discriminate abnormal from normal cells based on their differential expression in epithelial cell types *in vitro*. The EGFR is one such clinically relevant cell surface receptor biomarker used for imaging in this study that is overexpressed in vast majority of epithelial cancer but not in normal cells [23, 24]. Their ability to map the molecular expression of EGFR in these cells is also evaluated in comparison to conventional fluorescence staining.

6.2 Materials and methods

6.2.1 Synthesis and characterization of gold nanoshells

Gold nanoshells were synthesized in a four-step process as described earlier in Chapter 4. (Figure 6.1) [25]. The process of shell growth on the silica core was imaged under transmission electron microscopy (TEM) (Jeol JEM-1010) operating at 100 kV. The particle size was also characterized by TEM. Gold nanoshells with a 162 nm diameter silica core surrounded with a gold shell of 23 nm thickness were synthesized in this process based on the dimension as determined earlier in Chapter 2 for optimum backscattering response. Their extinction spectrum was characterized

using a UV-Vis spectrophotometer (Shimadzu UV-2401 PC) in the wavelength range from 400 nm to 900 nm. This experimentally measured spectrum was then compared to the theoretically predicted spectrum determined from a program written in MATLAB that calculates the theoretical optical spectra of core-shell structures based on Mie theory, which is described in more details in Chapter 2. The gold nanoshells were prepared to a final concentration of approximately 5 x 10^9 particles per ml as determined by correlating its measured extinction spectroscopy data to the theoretical extinction cross section data of the gold nanoshell based on Mie theory. The synthesized gold nanoshells were stored at 4°C when not in use.

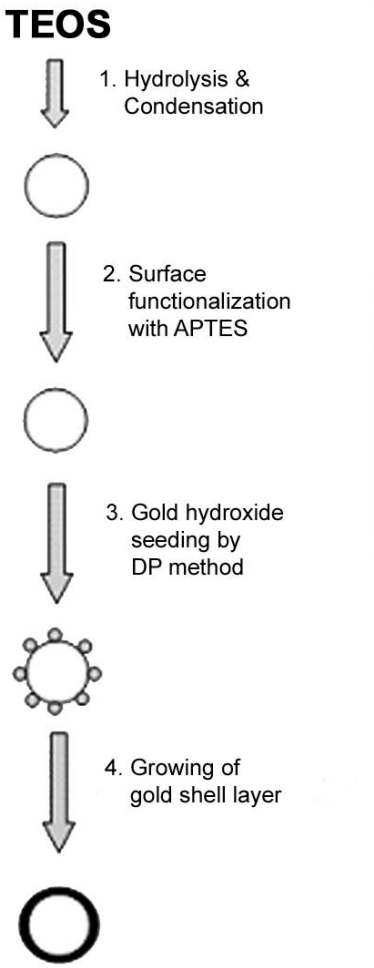

Figure 6.1. Schematic representation of the four-step process in the synthesis of gold nanoshells.

6.2.2 Conjugation of gold nanoshells with anti-EGFR

The monoclonal anti-EGFR (Santa Cruz Biotechnology Inc.) was conjugated to gold nanoshells using the heterobifunctional poly(ethylene)glycol SH-PEG-COOH (MW = 3000 g/mol) (Celares GmbH) as the linker where the thiol end was attached to the gold surface of the nanoshells and the carboxylic end reacted with amine groups on the anti-EGFR via carbodiimide chemistry to form amide bond as shown in Figure 6.2. In addition, another heterobifunctional methoxy-poly(ethylene glycol)-thiol MeO-PEG-SH (mPEG-thiol) (MW = 2000 g/mol) (Celares GmbH) was also attached to the gold surface that function as spacers in between the SH-PEG-COOH to "dilute" the functional groups on the gold surface to avoid too many conjugation sites while improving the stability of gold nanoshells in aqueous solution.

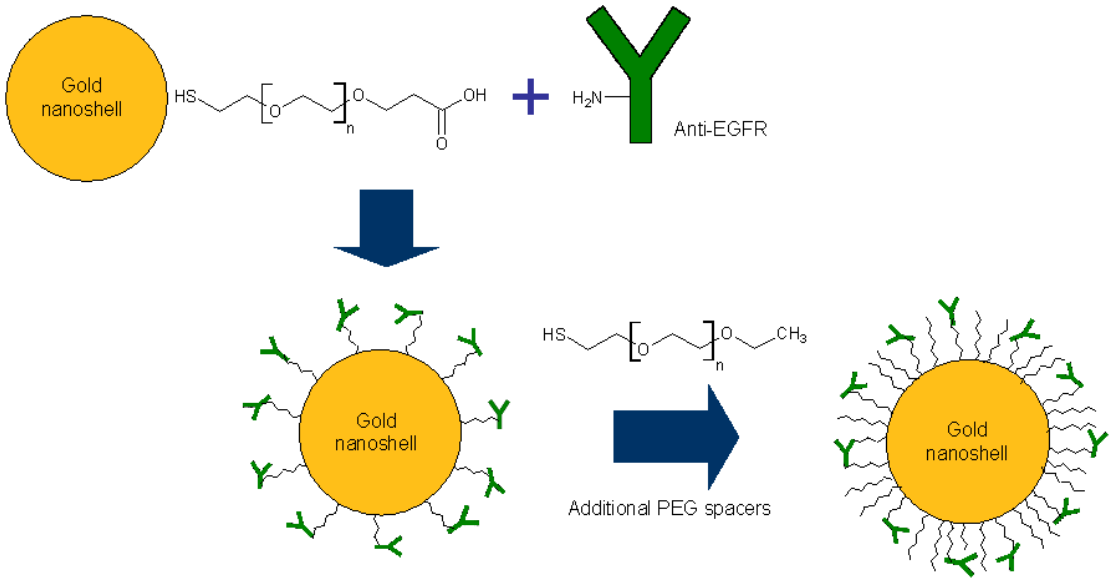

Figure 6.2. A schematic illustration of the protocol used to conjugate antibodies to the surface of the gold nanoshells using pegylated linkers. The use of pegylated linkers allows simultaneous pegylation of the gold nanoshells for great surface hydrophilicity and stability. Additional PEGs were also added as spacers in between the antibodies.

Both PEGs i.e. SH-PEG-COOH and mPEG-thiol were dissolved in water to give a concentration of 10 mg/ml each, before mixing them together in the ratio of 9 mPEG-thiol to 1 SH-PEG-COOH and adding the PEG mixture to the gold nanoshells. The mixture of both PEGs was attached to the gold nanoshells by incubating the gold nanoshells (5 x 10^9 particles per ml) with 1 ml of above mixture where the thiol group formed the Au-S bond at the gold surface within 30 minutes at room temperature.

After at least five washes in water to remove excess PEGs from the pegylated gold nanoshells, the anti-EGFR was then attached to the other end of the SH-PEG-COOH linker via carbodiimide chemistry, with the aid of 400 mM 1-ethyl-3-(3-dimethylaminopropyl)-carbo (EDC) (Sigma-Aldrich) and 100 mM of N-hydroxysuccinimide (NHS) (Sigma-Aldrich) as activators that converted the carboxylic group to a reactive succinimide group which then reacted with the amine group on the antibody to form a stable amide bond. The schematic of the above reaction is shown in Figure 6.3 below.

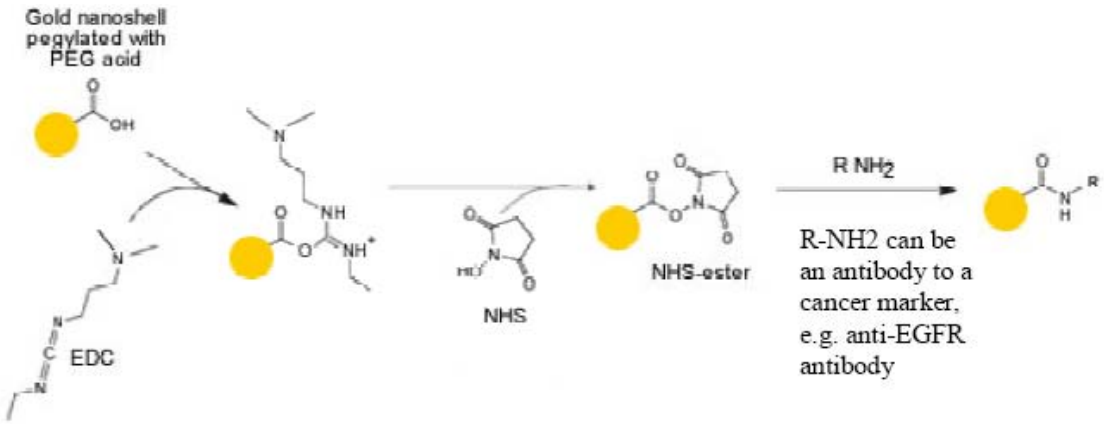

Figure 6.3. Chemical process of activation of PEG acid carboxyl end group by EDC and NHS.

Both 200 µl of EDAC and NHS were added to 1 ml of the pegylated gold nanoshells and incubated for about 20 min at room temperature, before the addition of 20 µl (i.e. 4 µg) of the anti-EGFR. The conjugation was completed within 1 h at room temperature. The anti-EGFR conjugated gold nanoshells were then washed for at least 5 times in water before redispersing them in 2 ml of 1X PBS (pH 7.4) and stored in 4 °C until further use. The successful pegylation as well as conjugation of the anti-EGFR on pegylated gold nanoshells was determined using X-ray photoelectron spectroscopy (XPS) by examining the changes in the sulphur (2p) and nitrogen (1s) spectra due to the presence of thiol group and amide bond formed with the antibodies respectively on the surface of the gold nanoshells.

6.2.3 Cell culture and EGFR expression analysis

The poorly-differentiated nasopharyngeal epithelium carcinoma CNE2 cell line and the normal human bronchial epithelium (NHBE) cell line were used as the diseased and normal control cells respectively. The CNE2 cells were grown in RPMI 1640 supplemented with 10% fetal bovine serum, 2 mM glutamine, sodium pyruvate, non-essential amino acids and 100 unit/ml penicillin/streptomycin while the normal cells were grown in Bronchial Epithelium Growth Medium (BEGM) (Cambrex Bio Science Walkersville, Inc). Both cell lines were grown on a coverslip placed in petri dish and maintained at 37^{o}C in humidified 5% CO_2 and 95% air atmosphere.

To validate the differential expression of EGFR between the normal and cancer cells, both the fluorescence activated cell sorting (FACS) and enzyme-linked immunosorbent assay (ELISA) analysis (Human EGFR ELISA Complete Kit, RayBiotech, Inc) were performed on the cell lines to ascertain a higher expression of

EGFR protein on the CNE2 cells compared to the NHBE cells. For FACS analysis, the primary mouse anti-EGFR conjugated to FITC (Santa Cruz Biotechnology, Inc) was used to stain the cells while the negative control staining was done with the normal mouse IgG2a conjugated to FITC (Santa Cruz Biotechnology, Inc). The cells were ran through a flow cytometer and sorted based on the fluorescence intensity of the FITC staining which corresponded to the EGFR expression on the cells.

6.2.4 Cellular imaging *in vitro*

Both the CNE2 and NHBE cells were incubated with anti-EGFR conjugated gold nanoshells for *in vitro* examination of the optical contrast of cancer cells over normal cells. Prior to imaging, both cell lines were washed in 1 X PBS and fixed in 4% paraformaldehyde, before incubating them with 100 μl of the anti-EGFR conjugated gold nanoshells in PBS i.e. 5 x 10^8 particles for 1 h at 37 °C. The CNE2 cells were also incubated with pegylated gold nanoshells in PBS without antibodies conjugated as a negative control to the antibody binding on cells. Following the incubation, the cells on the coverslip were then rinsed thrice with 1X PBS to wash away the excess and unbounded gold nanoshells. The coverslip with cells were then mounted on a microscope slide and sealed with nail varnish prior to imaging.

The cells were imaged under a laser scanning confocal microscope (Carl Zeiss LSM510 Meta) under differential interference contrast (DIC) and confocal reflectance mode with an Olympus 63x oil immersion objective. The confocal reflectance microscopy was performed under 633 nm excitation with a helium neon laser. Both the DIC and confocal reflectance images were taken at the mid-focal plane of the cells. To compare the performance of EGFR labeling on cells between staining with

gold nanoshells versus conventional immunofluorescence dye, the CNE2 cells were also labeled with primary mouse anti-EGFR conjugated to FITC (Santa Cruz Biotechnology, Inc) for 1 h at 37 °C and examined for immunofluorescence staining under confocal fluorescence microscopy at 488 nm excitation with an argon laser.

6.3 Results and discussion

6.3.1 Synthesis and characterization of gold nanoshells

Gold nanoshells with a silica core of radius 81 nm were synthesized. The gold hydroxide to seed solution volume ratio controls the amount of gold available for reduction onto the seed particles on the silica surface. Hence the growth of the gold shell depends on the amount of gold hydroxide solution used. With a volume ratio of 200:1, the amount of gold ions is barely sufficient to form a complete layer of gold shell with a thickness of about 12 nm around the silica core. This amount is consistent with that obtained from mass calculation needed to achieve the observed dimension. At higher volume ratio of 300:1, the shell thickens to about 23 nm.

The reduction of the gold hydroxide solution onto the silica results in a fast color change in the colloid: red, purple, blue or green corresponding to different degree of completeness of gold shell. Based on the results of the theoretically predicted backscattering cross section contour plot in Figure 2.9, gold nanoshells were synthesized with a silica core of radius 81 nm and a gold shell thickness of 23 nm such that this size configuration fit into the region having the largest backscattering cross section to provide an optimum backscattering response based on the theoretical prediction as described in Chapter 2.4.5 for subsequent experimental investigations.

The TEM image in Figure 6.4a shows the progressive growth of the gold shell around the silica core corresponding to the color change in the colloid as observed in Figure 6.4b. The gold nanoshells synthesized were spherical and generally monodispersed in size. The surface of the particles were also relatively smooth with an average surface roughness of 10 to 15 nm i.e. <10% of the particle radius from visual inspection.

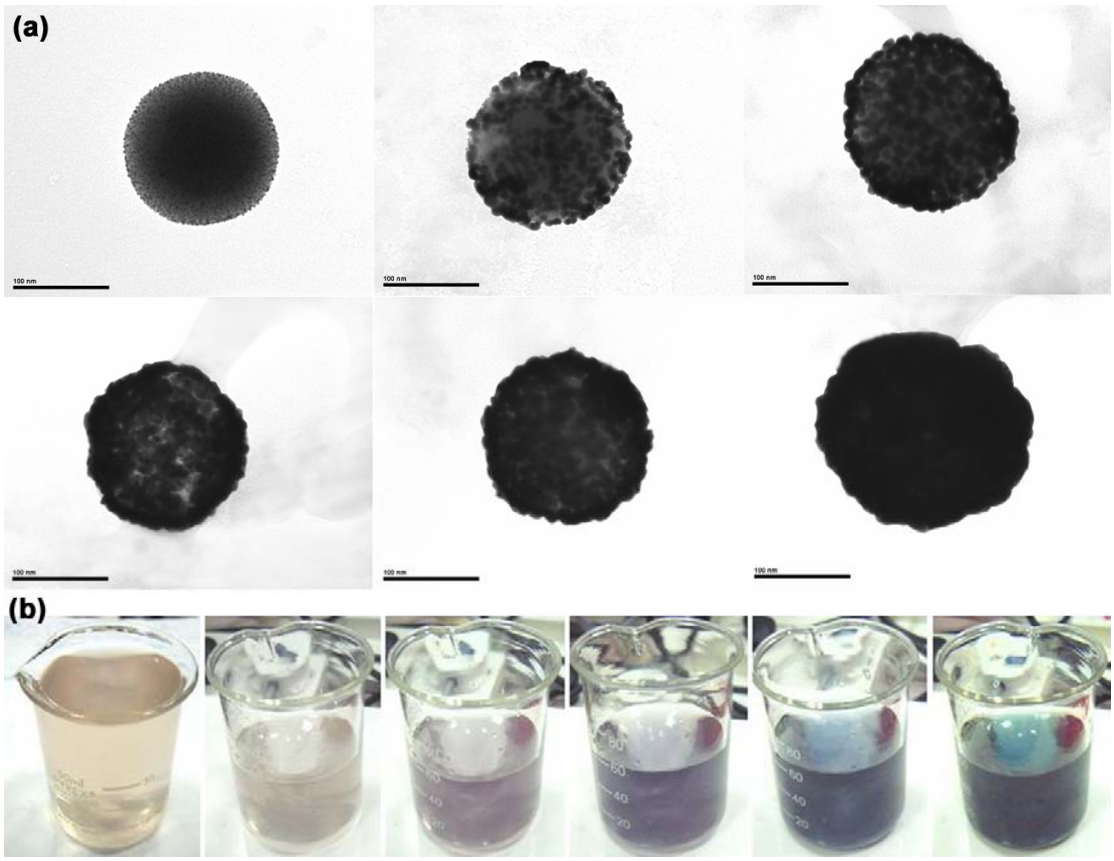

Figure 6.4. (a) TEM images of nanoshell growth on a 81 nm radius dielectric silica nanoparticle core showing the initial gold hydroxide nanoparticles deposited on the silica and gradual growth and coalescence of these nanoparticles on the silica surface until a complete growth of 23 nm thick gold shell is obtained. (b) Corresponding color changes in the colloid with the progressive growth of the gold shell demonstrating the changes in the optical properties as these gold nanoshells grow.

The measured UV-Vis extinction spectrum of the synthesized gold nanoshells in Figure 6.5 shows a double peak in its surface plasmon resonance for this size configuration with one peak at 840 nm and another peak at 650 nm. The peak at 840

nm matches the excitation wavelength of most OCT systems. Both the peaks observed can be attributed to the plasmon interaction taking place at the dielectric silica-to-gold interface and the gold-to-dielectric medium interface respectively.

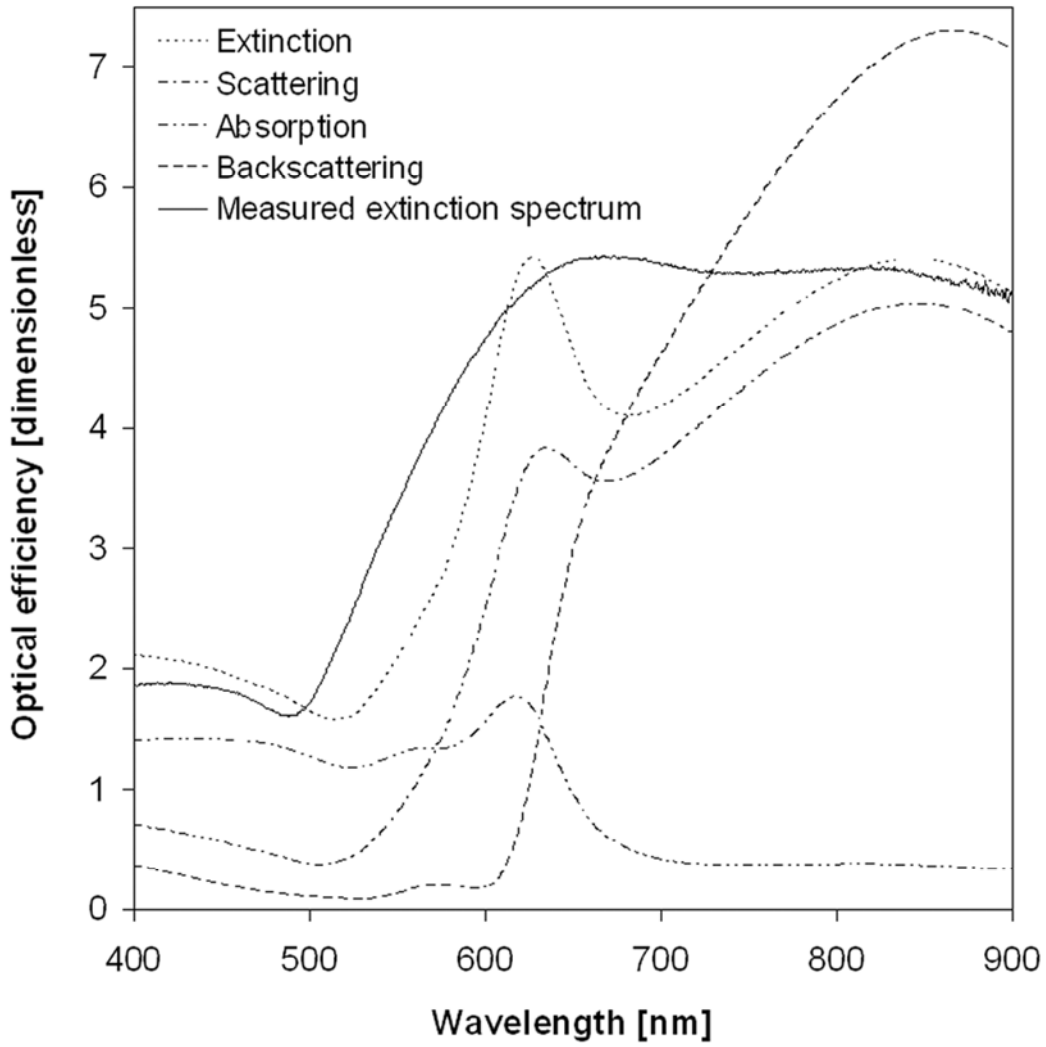

Figure 6.5. Measured UV-Vis extinction spectrum of the synthesized gold nanoshells with a silica core of 81 nm radius and a complete gold shell of 23 nm (solid line). The theoretically calculated extinction spectrum of gold nanoshells of the same dimension is shown for comparison (dotted line), together with the contributions from the constituent scattering (dash-dot) and absorption (dash-dot-dot) of gold shells with a silica core as derived from the Mie theory. The theoretically predicted backscattering spectrum (dash line) is also shown that predicts a strong backscattering response at around 800 nm coinciding with the operating wavelength of the OCT system used in this study.

When compared to the theoretical extinction spectrum based on Mie theory for a single gold nanoshell of the same size, the experimentally measured spectrum generally agrees well with the theoretical spectrum as shown in Figure 6.5, with the same two extinction peaks observed. The relatively intensity between the two peaks is also rather consistent between the two spectra. However, small differences due mainly to slight shifts in peak wavelength as well as broadening of the measured spectrum are also observed. These differences may be attributed to the heterogeneity within the population of gold nanoshells formed. Such heterogeneity is inevitable because of the size variation in the silica core (typically about 4% in the synthesis process [25]) as well as the small differences in shape, surface roughness and thickness of the shell formed. There is also the possibility that some of the gold nanoshells may form aggregates during the synthesis process which may add to the spectral broadening.

Using the same theoretical approach, the constituent scattering, absorption and backscattering spectrum as well as anisotropy factor of gold nanoshells can also be predicted (Figure 6.5). Since these optical spectra are usually difficult to determine experimentally, the agreement between the experimentally measured and theoretically predicted extinction spectrum based on Mie theory implies that the breakdown of the theoretical extinction spectrum into its constituent scattering and absorption spectrum can also predict the actual scattering and absorption spectrum of the synthesized gold nanoshells with good accuracy.

A closer examination of the theoretically predicted extinction spectrum and its constituent scattering and absorption spectrum shows that the extinction peak at around 800 nm is largely attributed to light scattering with minimal contribution (<

10%) from absorption. The prediction thus suggests that the synthesized gold nanoshells are predominantly scattering at the 800 nm wavelength with a particularly high backscattering efficiency appropriate for OCT applications. Although the extinction peak at around 650 nm is also scattering dominant, the contribution from light absorption is higher, accounting for up to one-third of its total extinction.

While the scattering-dominant peak at 800 nm renders the optical response of gold nanoshells favorable for OCT operating at around 800 nm, the other scattering-dominant peak at 650 nm also renders their optical response favorable to elicit a good reflectance signal for cellular imaging under confocal reflectance microscopy at 633 nm excitation. Since the light scattering in biological tissue within this NIR wavelength range is weak compared to the light scattering afforded by gold nanoshells [26], the presence of gold nanoshells in tissue may be discriminated from the surrounding tissue and made distinguishable based on their scattering intensity.

6.3.2 Pegylation and antibody conjugation of gold nanoshells

The optical characterization of the synthesized gold nanoshells encourages further evaluation of their actual optical response *in vitro* with the confocal reflectance microscope. Prior to these *in vitro* studies, surface functionalization was performed on the gold nanoshells in the form of pegylation and antibody conjugation to make them more stable in cell culture medium with high salt content and also more specific to the target to be imaged. Here, the anti-EGFR was used to confer the gold nanoshells specificity towards the EGFR target antigen located on the cell membrane. The results of the pegylation and conjugation were assessed by XPS as shown in Figure 6.6.

The XPS spectrum of both the pegylated and anti-EGFR conjugated gold nanoshells shows a peak at binding energy of ≈ 163 eV which correspond to the binding energy for sulphur (2p). This peak indicates the presence of thiol group on the surface of gold nanoshells arising from the successful pegylation of these two samples as such a peak is absent from the XPS spectrum of the naked gold nanoshells.

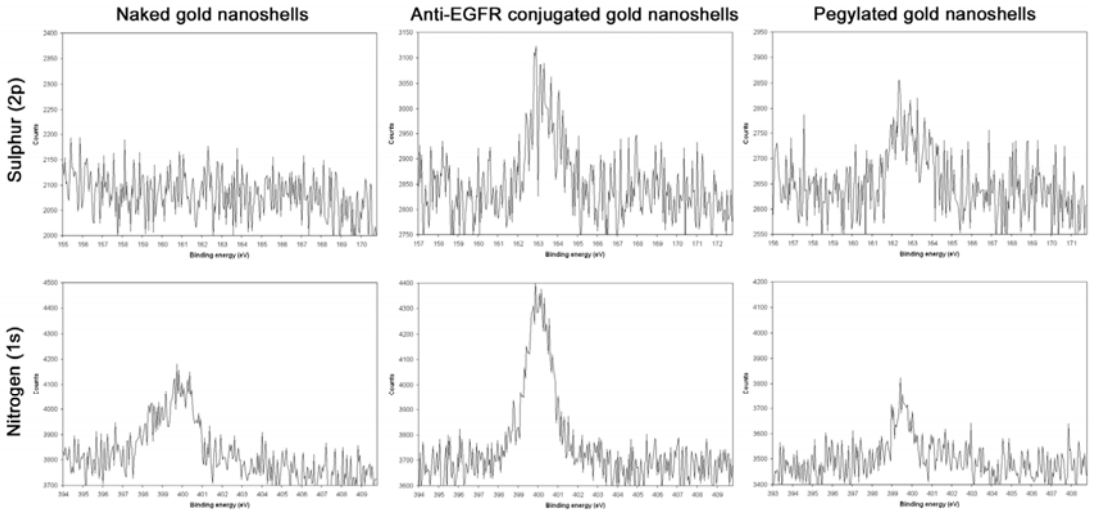

Figure 6.6. X-ray photoelectron spectroscopy (XPS) of naked gold nanoshells (left), anti-EGFR conjugated gold nanoshells (middle) and pegylated gold nanoshells (right) to detect the presence of sulphur (2p) at binding energy of 163 eV (top) and nitrogen (1s) at binding energy of 400 eV (bottom). The peak observed indicates the successful thiol bonding on the surface of gold due to pegylation and the successful formation of amide bond in the conjugation with antibody respectively.

The peak corresponding to nitrogen (1s) at ≈ 400 eV is observed in all three samples, including that of the naked gold nanoshells and pegylated gold nanoshells without antibodies conjugation. This may be due to the adsorption of ambient atmospheric nitrogen on the gold surface during the measurement. However, the nitrogen (1s) peak for anti-EGFR conjugated gold nanoshells is much stronger and distinct compared to the other two, thus indicating the presence of addition nitrogen found in the form of the amide bond that links the antibodies to the gold nanoshells. The successful

pegylation and conjugation of anti-EGFR onto the gold nanoshells based on the described scheme of reaction is thus ascertained from this XPS assessment.

6.3.3 Binding of anti-EGFR conjugated gold nanoshells to cells

The ability of anti-EGFR to retain their antigen binding affinity towards the cellular EGFR after conjugation was assessed by incubating the anti-EGFR conjugated gold nanoshells with CNE2 cells known to overexpress EGFR (see Figure 3.7). It is clear that the anti-EGFR conjugated gold nanoshells are able to bind to the cell surface just after 45 min of incubation to give the cells a greenish stain under the brightfield microscope due to the gold nanoshells as seen in Figure 6.7.

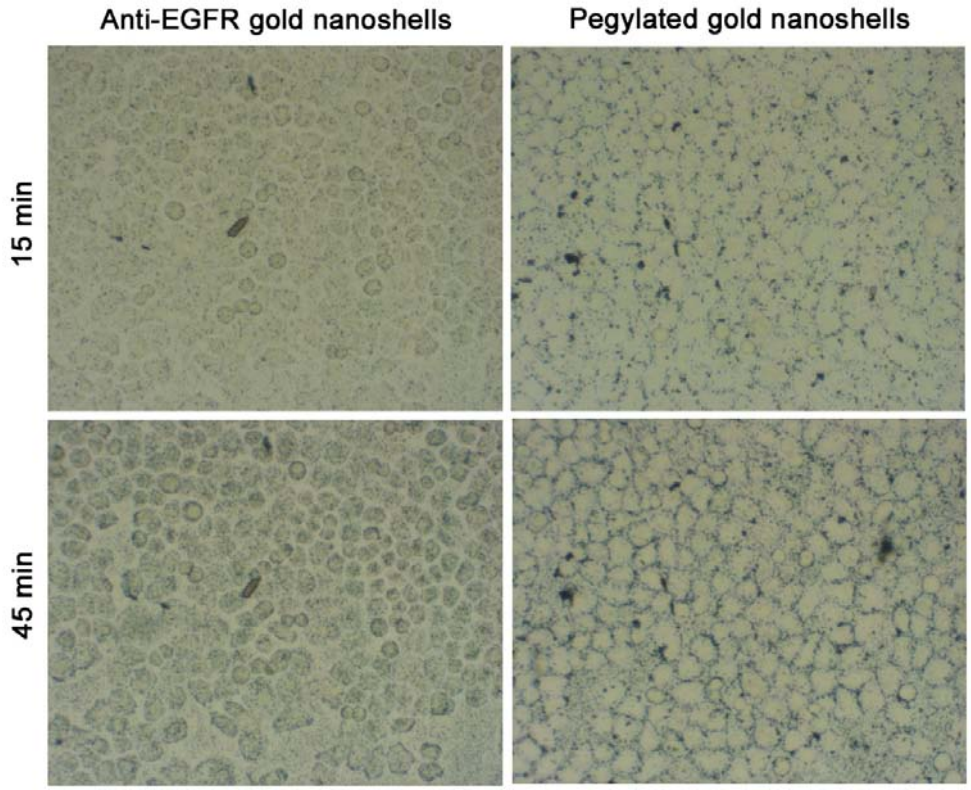

Figure 6.7. Brightfield microscopy of CNE2 cells incubated with pegylated gold nanoshells and antibody conjugated gold nanoshells after two different time points of 15 and 45 minutes. The images were taken prior to any washing of the cells after incubation and at a 20x magnification.

This implies that most of the anti-EGFR are linked to the gold surface via free amine groups located at their Fc region, leaving the Fab regions free for antigen binding. The pegylated gold nanoshells with no antibodies conjugated are unable to bind to the cell surface and thus settle down in the spaces between the cells. This shows that the anti-EGFR are still able to retain their antigen binding sites and bind to the extracellular domain of EGFR on the cellular membrane even after conjugation to gold nanoshells.

6.3.4 Increase in optical contrast in cells

The promising optical response computed based on the size of the synthesized gold nanoshells encourages further study on their application in reflectance-based imaging. To demonstrate the ability of anti-EGFR conjugated gold nanoshells to increase the optical reflectance properties of cells, the labeling of CNE2 cells by anti-EGFR conjugated gold nanoshells was imaged under DIC and confocal reflectance microscopy as shown in Figure 6.8. The labeling of CNE2 cells by pegylated gold nanoshells are also shown as control. As the anti-EGFR conjugated gold nanoshells attach themselves to the cell surface, the presence of gold nanoshells on the cells results in changes to their optical properties.

The confocal reflectance images show that the CNE2 cells by themselves are unable to produce any discernable signal against the background with their intrinsic reflectance. Although reflectance signal in biological cells is known to originate from refractive index variations in various cellular organelles and microstructures such as the nucleus or mitochondria [27], the microscope settings have been adjusted in this case such that the intrinsic reflectance of the cells is corrected for and any reflectance signal observed is due solely to an extrinsic optical contrast agent.

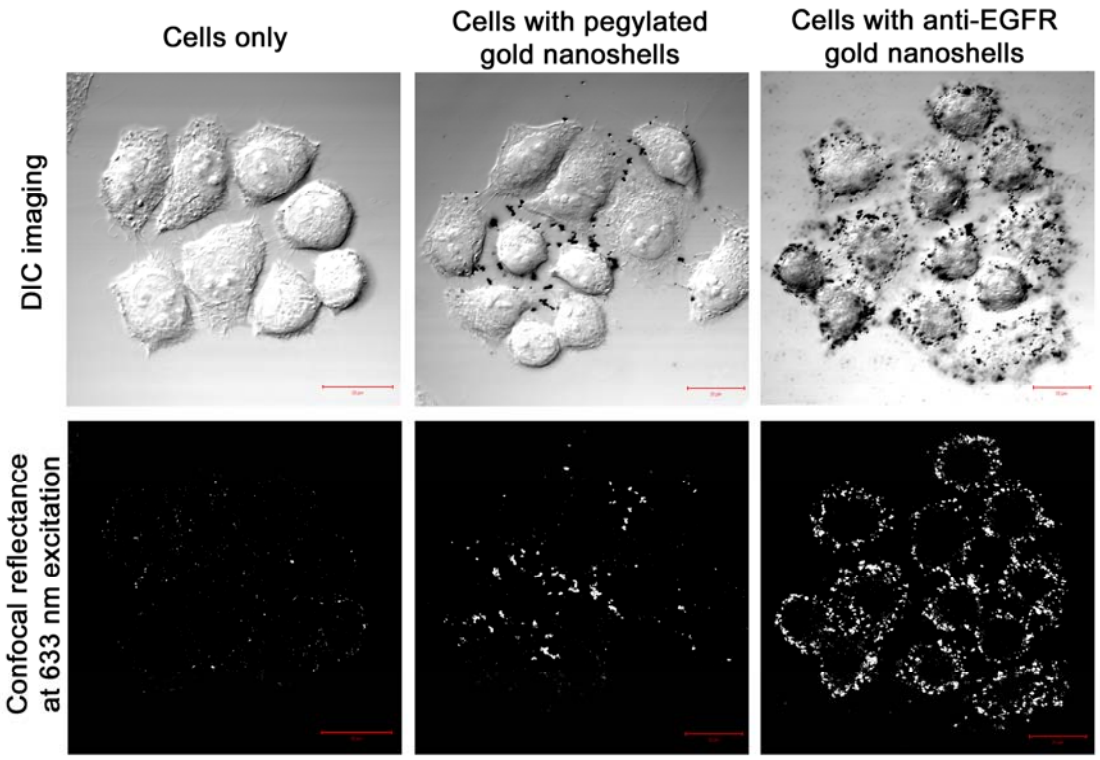

Figure 6.8. DIC (top) and confocal reflectance (bottom) images of CNE2 before labeling (left), after labeling with non-specific pegylated gold nanoshells (middle), and after labeling with anti-EGFR conjugated gold nanoshells (right). Images are cross-sectional slices of cells taken at the mid-focal plane at 63X magnification with an oil immersion lens. False-color reflectance images are obtained at excitation of 633 nm. Scale bar in all images is 20 μm.

Therefore, when the cells are incubated with anti-EGFR conjugated gold nanoshells, the presence of gold nanoshells on the cells give rise to strong reflectance signals that form a distinct bright reflective ring around the cells in the optically sectioned confocal image. The bright scattering ring around the cells can be attributed to the light scattering of the gold nanoshells. Furthermore, as the bright ring is continuous around the perimeter of the cells, this implies that the gold nanoshells may possibly be localized on the cell membrane where the EGFR antigens are located. Their localization on the cell membrane is ascertained and discussed in more detail below.

Such strong light scattering condition is known to be further enhanced when the gold nanoshells cluster close together on the cell membrane as they attach to their receptors and their surface plasmon interacts with each other [4, 18]. Hence, the mechanism of this optical contrast depends largely on the ability of anti-EGFR conjugated gold nanoshells to selectively bind to the extracellular domain of EGFR found overexpressed on cancer cells.

The addition of non-specific pegylated gold nanoshells also results in their attachment on cells being observed albeit to a smaller extent. The attachment of gold nanoshells gives rise to some reflectance signal in this case, although the signal is weak and the bright reflective spots appear random in the image. Such labeling are non-specific in nature and could arise from a small fraction of the gold nanoshells that were not adequately pegylated with their surface exposed for non-specific binding to the milieu of proteins found on the cells surface.

The quantification of this reflectance signal from the gold nanoshells is potentially possible with image analysis as with fluorescence dyes and such signal quantification could possibly provide a mean to correlate and hence quantify the protein or biomarker of interest being imaged. However, similar to non-specific labeling of conventional fluorescent dyes, the non-specific binding of the gold nanoshells can add to the noise level in the overall reflectance signal observed and may affect an accurate correlation between the reflectance signal observed and the protein of interest been measured in the case of signal quantification.

6.3.5 Discrimination of cancer from normal cells

The anti-EGFR conjugated gold nanoshells are not just able to increase the light scattering of cells to “illuminate” them for better reflectance contrast, but are also able to discriminate cancer from normal cells on the basis of their selective binding to different levels of EGFR expression on the cells surface. The labeling of anti-EGFR conjugated gold nanoshells on cancerous CNE2 cells as compared to normal NHBE cells under DIC and confocal reflectance microscopy is shown in Figure 6.9. The NHBE cells were used as healthy control and were exposed to anti-EGFR conjugated gold nanoshells in the same manner as the CNE2 cells. The DIC images on the top row were taken at the mid-focal place with their corresponding confocal reflectance images excited at 633 nm shown on the bottom row.

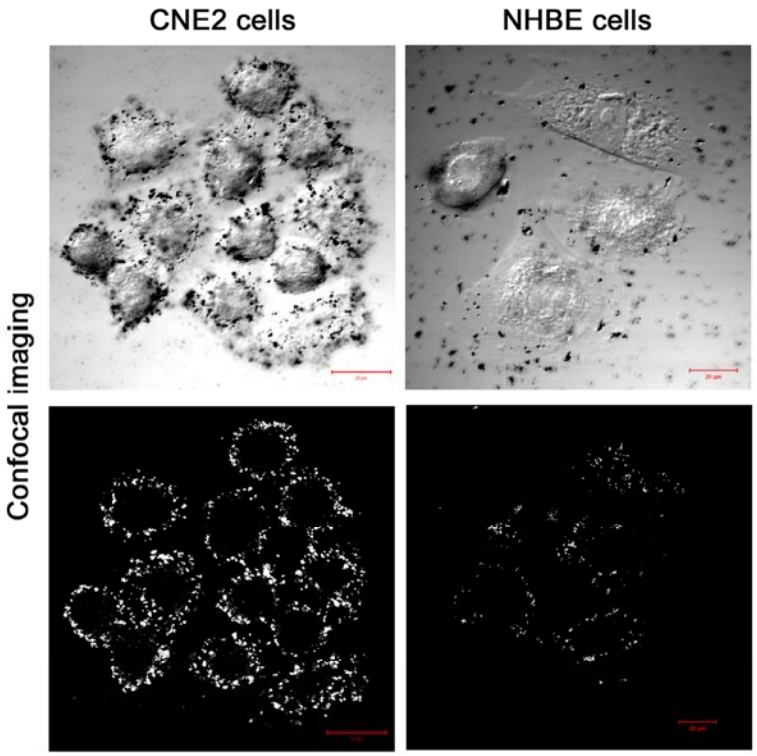

Figure 6.9. DIC (top) and confocal reflectance (bottom) images of both CNE2 and NHBE cells after labeling with anti-EGFR conjugated gold nanoshells.

The reflectance signal from the gold nanoshells on NHBE cells is significantly lower and can barely be resolved against the dark background. An analysis of the image histogram reveals that the reflectance intensity from the NHBE cells is about 30 times lower than that of the CNE2 cells. Such a difference in the reflectance intensity may be attributed to the different level of EGFR expression on both cell lines which directs the amount of anti-EGFR conjugated gold nanoshells bound to the cell surface.

The results of the FACS analysis for each cell line in Figure 6.10 below indeed show a 6-fold increase in the EGFR expression of CNE2 cells over NHBE cells. This is further confirmed by another independent observation based on ELISA analysis where the CNE2 cells contain 242 pg of EGFR per µg of cell lysate compared to 42 pg in NHBE cells.

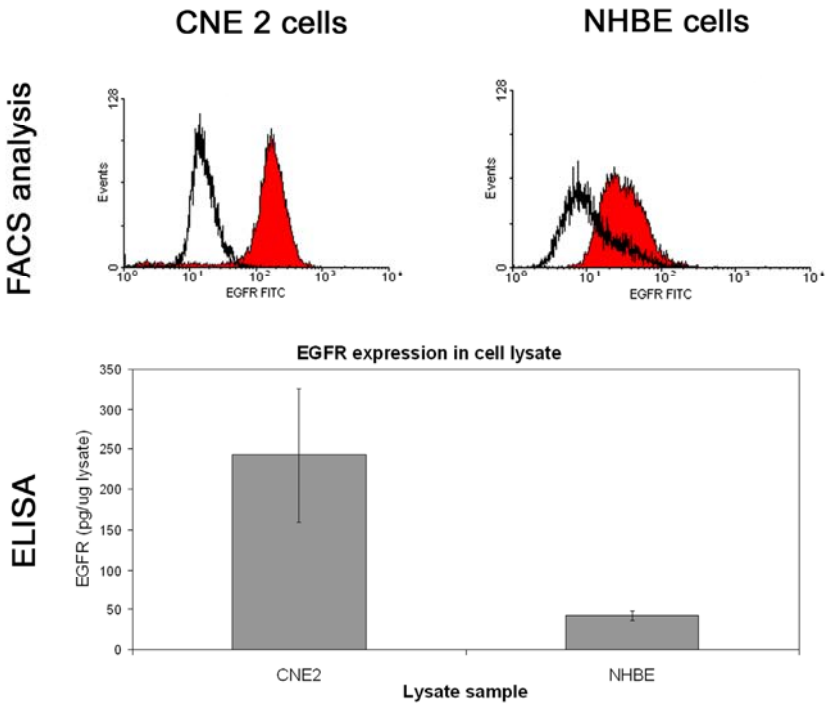

Figure 6.10. The reflectance signal observed from the gold nanoshells on the cells shown in Figure 6.9 provides an indication of their EGFR expression level which is assessed by FACS analysis (top) and ELISA (bottom) to show a six fold increase in EGFR expression in CNE2 cells over NHBE cells.

Since EGFR is differentially expressed in the two cell lines, this allows us to make use of their differential expression to regulate the amount of gold nanoshells being attached to the cells. As the NHBE cells are shown to have a lower expression of EGFR than CNE2 cells, they may give rise to fewer binding and localization of the anti-EGFR conjugated gold nanoshells on them, thus giving rise to a weaker reflectance signal. Such result thus shows that the anti-EGFR conjugated gold nanoshells are able to discriminate cancer cells from normal cells on the basis of their selective binding to different levels of EGFR expression on cells surface.

In practice, the EGFR expression in cells is detected at all stages of carcinogenesis, from normal-early hyperplasia, dysplasia to invasive carcinoma [28] and it is elevated during the progression from hyperplasia to dysplasia and increases during progression from dysplasia to invasive carcinoma [23], thus giving a spectrum of expression levels with disease progression. As the reflectance signal depends on the level of EGFR expression, its intensity may further provide indications to the progression of diseases at the molecular level in addition to simply discriminating diseased cells.

6.3.6 Molecular mapping of EGFR expression

The dependence of the reflectance intensity from gold labeling on EGFR expression provides an avenue where the anti-EGFR conjugated gold nanoshells can potentially be used as a probe for molecular imaging and quantification of cellular proteins. This can be investigated by first identifying the regions of high EGFR expression using conventional techniques with fluorescent dyes and subsequently mapping the corresponding reflectance signal from the gold nanoshells to the fluorescence signal to determine any correlation between these regions. The staining of EGFR by gold

nanoshells is compared to conventional immunofluorescence staining using FITC as shown in Figure 6.11 below.

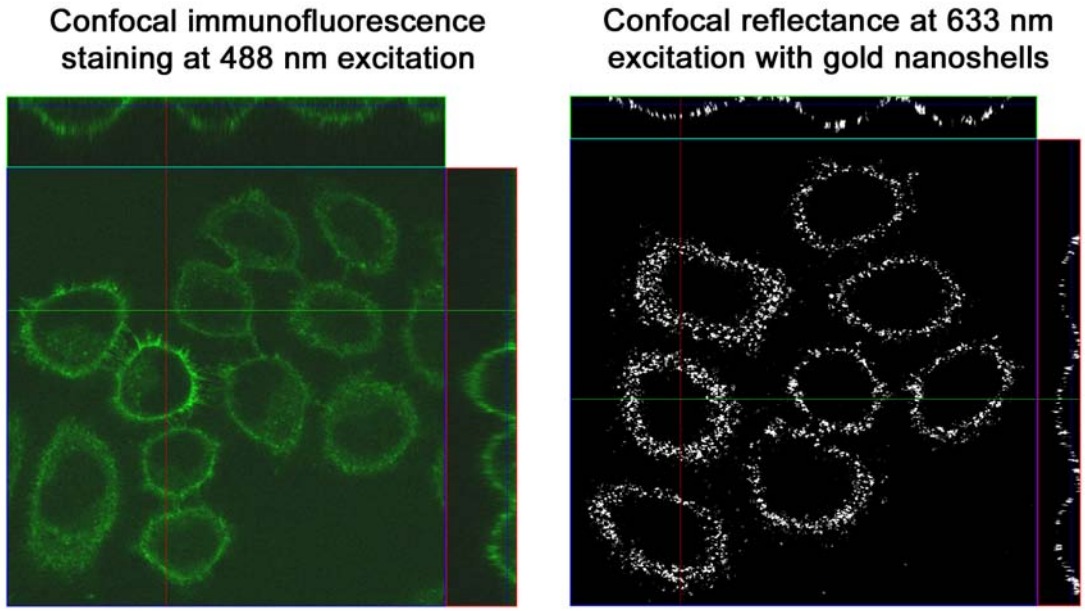

Figure 6.11. Comparison between the labeling of EGFR expression by gold nanoshells (right) and conventional immunofluorescence labeling using FITC (left) under the confocal reflectance microscopy at 633 nm excitation and confocal fluorescence microscopy at 488 nm excitation respectively. The reconstructed z-stacks of a series of confocal optical sectioning of CNE2 cells shown on the top and right side of the en face image show the staining on the cross section side profile of the cells. The top and right cross sectional image corresponds to the position of the horizontal (green) and vertical (red) line on the en face image respectively. The regions of strong reflectance signal that arises from the cell membrane are due to the presence of anti-EGFR gold nanoshells labeling the EGFR on the cell membrane.

As the anti-EGFR conjugated gold nanoshells are localized on the cell membrane to probe for EGFR, the transverse cross section labeling pattern of EGFR arising from the reflectance signal of gold nanoshells compares well with the fluorescence signal of FITC dye, thus indicating that the gold nanoshells are able to provide an accurate molecular mapping of EGFR expression under confocal reflectance microscopy. After acquiring a series of confocal optical sections, the reconstructed z-stacks showing the side profile of the CNE2 cells on the top and right side of the main image in Figure

6.11 also shows comparable staining pattern on the cell membrane by both methods of staining. The staining by gold nanoshells forms a distinct outline of the cells in the longitudinal cross sectional images and thus corroborates the postulation regarding the origin and localization of the bright reflective ring due to the gold nanoshells on the cell membrane.

Therefore, apart from simply increasing the reflectance signal and discriminating diseased from normal cells, the study has also shown the possibility of exploiting the light scattering properties of gold nanoshells to image the expression of EGFR in cells, similar to how the fluorescent properties of dyes are used to image such expression in conventional immunofluorescence imaging. The dependence of the reflectance signal on EGFR expression clearly demonstrates that the anti-EGFR conjugated gold nanoshells do not merely function as a generic non-specific contrast agent, but can also serve as a specific molecular probe for cancer biomarkers on cancer cells. The map of EGFR expression under reflectance-based images potentially holds several implications for cancer diagnosis particularly those of early detection based on molecular specific information.

6.4 Conclusion

Optical imaging in the non-fluorescent regime offers alternative perspectives in diagnosing diseased conditions despite being plague by poor contrast inherent to such techniques. Combining advances in these techniques with appropriate contrast agents may potentially offer even greater diagnostic value especially in the area of detecting early molecular changes. In this study, gold nanoshells are designed with a dimension

that would provide the optimum backscattering response appropriate for the two reflectance-based imaging modalities discussed in this thesis.

The cellular imaging results with gold nanoshells under the confocal reflectance microscopy suggest at least three areas where the imaging can be improved upon with the use of gold nanoshells: 1. The optical response of gold nanoshells are able to provide a general contrast enhancement. 2. This contrast enhancement can be made specific to discriminate disease from normal cells and 3. Molecular expression can be imaged and mapped when the gold nanoshells are conferred biomarker specificity with appropriate surface functionalization to provide a form of optical labeling based on light reflectance.

Although antibodies of murine origin are used in this study, potential clinical applications can involve the use of humanized antibodies currently in clinical trials which are much less immunogenic in humans. As molecular changes occurs before phenotypic changes of a disease becomes apparent, such a general trend of interest towards earlier cancer diagnosis of suspicious lesions at a stage before debilitating symptoms appear promises improved patient care in the near future.

The promising *in vitro* cellular microscopy results discussed in this chapter encourage further investigations on the optical properties of gold nanoshells in phantom models to optimize their optical contrast for subsequent imaging applications in OCT. Such a study on phantom models is discussed in the following Chapter 7.

6.5 References

1. Diao JJ, Chen GD. Electromagnetic cavity resonant absorption of the gold nanoshell. *Journal of Physics D: Applied Physics* 2001; 34(14): L79-L82.

2. Lim YT, Park OO, Jung H-T. Gold nanolayer-encapsulated silica particles synthesized by surface seeding and shell growing method: near infrared responsive materials. *Journal of Colloid and Interface Science* 2003; 263(2): 449-453.

3. Averitt RD, Sarkar D, Halas NJ. Plasmon Resonance Shifts of Au-Coated Au2S Nanoshells: Insight into Multicomponent Nanoparticle Growth. *Physical Review Letters* 1997; 78(22): 4217 LP - 4220.

4. Sokolov K, Follen M, Aaron J, Pavlova I, Malpica A, Lotan R, Richards-Kortum R. Real-time vital optical imaging of precancer using anti-epidermal growth factor receptor antibodies conjugated to gold nanoparticles. *Cancer Res* 2003; 63(9): 1999-2004.

5. Kah JC, Olivo MC, Lee CG, Sheppard CJ. Molecular contrast of EGFR expression using gold nanoparticles as a reflectance-based imaging probe. *Mol Cell Probes* 2008; 22(1): 14-23.

6. Kah JC, Kho KW, Lee CG, James C, Sheppard R, Shen ZX, Soo KC, Olivo MC. Early diagnosis of oral cancer based on the surface plasmon resonance of gold nanoparticles. *Int J Nanomedicine* 2007; 2(4): 785-798.

7. Alvarez-Puebla RA, Ross DJ, Nazri GA, Aroca RF. Surface-enhanced Raman scattering on nanoshells with tunable surface plasmon resonance. *Langmuir* 2005; 21(23): 10504-10508.

8. Loo C, Lin A, Hirsch L, Lee MH, Barton J, Halas N, West J, Drezek R. Nanoshell-enabled photonics-based imaging and therapy of cancer. *Technol Cancer Res Treat* 2004; 3(1): 33-40.

9. Hirsch LR, Gobin AM, Lowery AR, Tam F, Drezek RA, Halas NJ, West JL. Metal nanoshells. *Ann Biomed Eng* 2006; 34(1): 15-22.

10. West JL, Halas NJ. Engineered nanomaterials for biophotonics applications: improving sensing, imaging, and therapeutics. *Annu Rev Biomed Eng* 2003; 5: 285-292.

11. Wang Y, Xie X, Wang X, Ku G, Gill KL, O'Neal DP, Stoica G, Wang LV. Photoacoustic Tomography of a Nanoshell Contrast Agent in the in Vivo Rat Brain. *Nano Lett.* 2004; 4(9): 1689-1692.

12. Loo C, Hirsch L, Lee MH, Chang E, West J, Halas N, Drezek R. Gold nanoshell bioconjugates for molecular imaging in living cells. *Opt Lett* 2005; 30(9): 1012-1014.

13. Loo C, Lowery A, Halas N, West J, Drezek R. Immunotargeted nanoshells for integrated cancer imaging and therapy. *Nano Lett* 2005; 5(4): 709-711.

14. Oldenburg SJ, Westcott SL, Averitt RD, Halas NJ. Surface enhanced Raman scattering in the near infrared using metal nanoshell substrates. *The Journal of Chemical Physics* 1999; 111(10): 4729-4735.

15. Hirsch LR, Stafford RJ, Bankson JA, Sershen SR, Rivera B, Price RE, Hazle JD, Halas NJ, West JL. Nanoshell-mediated near-infrared thermal therapy of tumors under magnetic resonance guidance. *Proc Natl Acad Sci U S A* 2003; 100(23): 13549-13554.

16. Sun Y, Mayers B, Xia Y. Metal Nanostructures with Hollow Interiors. *Advanced Materials* 2003; 15(7-8): 641-646.

17. Oldenburg SJ, Averitt RD, Westcott SL, Halas NJ. Nanoengineering of optical resonances. *Chemical Physics Letters* 1998; 288(2-4): 243-247.

18. Khlebtsov BN, Khanadeyev VA, Ye J, Mackowski DW, Borghs G, Khlebtsov NG. Coupled plasmon resonances in monolayers of metal nanoparticles and nanoshells. *Physical Review B (Condensed Matter and Materials Physics)* 2008; 77(3): 035440-035414.

19. Abrams MJ, Murrer BA. Metal compounds in therapy and diagnosis. *Science* 1993; 261(5122): 725-730.

20. Connor EE, Mwamuka J, Gole A, Murphy CJ, Wyatt MD. Gold nanoparticles are taken up by human cells but do not cause acute cytotoxicity. *Small* 2005; 1(3): 325-327.

21. West JL, Halas NJ. Applications of nanotechnology to biotechnology commentary. *Curr Opin Biotechnol* 2000; 11(2): 215-217.

22. Huang X, El-Sayed IH, Qian W, El-Sayed MA. Cancer cell imaging and photothermal therapy in the near-infrared region by using gold nanorods. *J Am Chem Soc* 2006; 128(6): 2115-2120.

23. Shin DM, Ro JY, Hong WK, Hittelman WN. Dysregulation of epidermal growth factor receptor expression in premalignant lesions during head and neck tumorigenesis. *Cancer Res* 1994; 54(12): 3153-3159.

24. Ke LD, Adler-Storthz K, Clayman GL, Yung AW, Chen Z. Differential expression of epidermal growth factor receptor in human head and neck cancers. *Head Neck* 1998; 20(4): 320-327.

25. Kah JCY, Phonthammachai N, Wan RCY, Song J, White T, Ahmad I, Sheppard C, Olivo M. Synthesis of gold nanoshells based on the deposition-precipitation process. *Gold Bulletin* 2008; 41(1): 23-36.

26. Taroni P, Pifferi A, Torricelli A, Comelli D, Cubeddu R. In vivo absorption and scattering spectroscopy of biological tissues. *Photochem Photobiol Sci* 2003; 2(2): 124-129.

27. Rajadhyaksha M, Gonzalez S, Zavislan JM. Detectability of contrast agents for confocal reflectance imaging of skin and microcirculation. *J Biomed Opt* 2004; 9(2): 323-331.

28. Kannan S, Balaram P, Chandran GJ, Pillai MR, Mathew B, Nair MK. Co-expression of ras p21 and epidermal growth factor receptor during various stages of tumour progression in oral mucosa. *Tumour Biol* 1994; 15(2): 73-81.

CHAPTER SEVEN

PHANTOM STUDIES OF OPTICAL CONTRAST

Abstract

The study of different parameters of gold nanoshells in tissue phantom provides a realistic model to their contrast enhancement in tissue under OCT imaging. One such parameter is its concentration which is key to obtaining a good signal enhancement. The effective use of gold nanoshells as a contrast agent for OCT may be hampered by the delivery of a wrong dose to tissue that result in unwanted signal attenuation. In this chapter, gold nanoshells with a 81 nm radius silica core and 23 nm shell thickness are synthesized and their optical response is evaluated against phantom models under OCT. The effect of changes in scattering coefficient, μ_s due to concentration variations of gold nanoshells on the OCT image is also examined with the aim of defining a dosing range that would result in appropriate μ_s to maintain an acceptable signal attenuation level. The results show that gold nanoshells are able to elicit an increase in OCT signal near the imaging surface over 1% Intralipid commonly used to model intrinsic tissue scattering. Furthermore, an increase in sample μ_s not only enhances the OCT signal near the imaging surface but also attenuates the signal deeper into the sample. A gold nanoshells concentration range of $5.6 \times 10^9 < c < 2.3 \times 10^{10}$ particles/ml was found to provide an adequate signal enhancement near the surface without severely compromising the imaging depth due to signal attenuation. This concentration range was subsequently verified in *in vivo* studies with animal models. This work has been published in *Applied Optics 2009; 48: D96–D108.*

7.1 Introduction

The effectiveness of optical imaging is often improved with the aid of exogenous contrast agents such as bioluminescent and fluorescent dye that enhance the tissue contrast and highlight specific molecular events within the subject. Despite being widely used with incoherent light imaging systems such as confocal and multiphoton microscopy, these contrast agents rely on fluorescent process and are therefore not appropriate for use with coherent light imaging systems such as the Optical Coherence Tomography (OCT).

The previous chapter describes the use of gold nanoshells as a contrast agent to improve the optical signal in confocal reflectance microscopy. In this chapter, the *in vitro* confocal reflectance imaging results are extended to OCT which is another type of reflectance-based imaging modality that also form images based on incident light that are backscattered back from tissue sample. While the confocal reflectance microscope forms an image using mostly single backscattered light from a single optical plane of the sample, OCT forms its image based on both single and multiple backscattered coherent light from a continuous series of optical planes in the sample to give a depth profile.

OCT provides both real time and *in situ* imaging of tissue and is capable of producing <10 μm resolution cross-sectional images by detecting the optical echoes of coherent light backscattered from tissue [1]. The ability to obtain high resolution images has led to several promising applications in the diagnosis of cancers in real time without the need for tissue removal and sectioning [2-4]. Whilst the intrinsic optical contrast in OCT may arise from subcellular changes that alter light scattering such as increase

in nuclear size during carcinogenesis, the contrast between cancer and normal tissue, especially early stage lesions are often too modest to be of any significant value in clinical imaging. Furthermore, many other valuable molecular indicators of tissue abnormalities may not generate obvious intrinsic optical contrast. In these cases, the use of OCT would thus require a separate class of contrast agents that rely on elastic coherent light scattering.

The traditional way of improving the contrast in OCT images employs the use of osmotically active immersion liquids such as glycerol, propylene glycol, dextranes and concentrated glucose solution to cause a change in the tissue refractive index [5, 6]. This is improved with a new generation of contrast agents based on particle technologies due to their improved optical properties and ease of performing surface modifications. Several types of particulate contrast agents such as air-filled microbubbles, engineered microspheres and gold nanostructures have been developed to improve the OCT image by enhancing the intensity of backscattered light from the tissue [7, 8].

Amongst these, gold nanostructures of different types e.g. gold nanorods [9], gold nanocages [10] and gold nanoshells [11] have been the most widely studied. The choice of gold nanostructures as OCT contrast agents for is motivated by several factors: 1. the known biocompatibility of gold, 2. the small size of the nanoparticles that increases their portability in tissue, 3. the easy tunability of their optical properties, and 4. their high scattering efficiencies (>1) arising from the surface plasmon resonance of gold at the nanoscale compared to dielectrics such as polystyrene which must be micron-sized to achieve efficiencies near unity.

Amongst the different types of gold nanostructures, the optical efficiency of gold nanoshells as an exogenous contrast agent for optical imaging of cells and tissue phantoms is well documented [12, 13]. The optical and physico-chemical properties of gold nanoshells as well as an *in vitro* demonstration of their optical contrast under confocal reflectance microscopy have been described extensively in the preceding chapters. OCT imaging enhancement with gold nanoshells has been documented in literature although the results presented are mostly qualitative in nature [11, 13, 14]. The first effort to quantify the performance of nanoshells by Agrawal et al. [15] uses tissue phantom to examine the effect of different size configurations of gold nanoshells as well as the concentration dependence of gold nanoshells on the OCT signal intensity gain. However, a holistic characterization of the changes in OCT image due to addition of gold nanoshells to tissue demands more than just an understanding of the influence of size parameters and gold nanoshells concentration on the intensity gain.

In general, optical characterization of OCT has been studied by several groups and a few theoretical models have been established to relate the optical parameters of the sample being imaged to its corresponding depth-dependent A-scan signal profile [16-18]. It is known that the depth-dependent scattering in OCT has been modeled as a function of the scattering coefficient, μ_s of the medium [17, 19] and μ_s affects not only the intensity gain of the OCT signal, but also its attenuation with imaging depth. The available experimental data in literatures lack a detailed treatment of the influence of gold nanoshells concentration on the changes in the overall A-scan profile which is also significant in affecting the overall quality of the gold nanoshells-enhanced OCT images.

In this chapter, the optical enhancement by gold nanoshells under a benchtop OCT system is evaluated against tissue phantom models as well as other types of particle scatterers in a preliminary demonstration of their ability to improve the OCT signal when added to tissue. The influence of changes in tissue μ_s as modeled by varying concentration of Intralipid as well as the effect of changes in μ_s due to different concentrations of gold nanoshells added to tissue phantom on the OCT contrast enhancement is also examined on a commercial OCT system. An analysis algorithm is developed to extract the sample μ_s from the average OCT depth-dependent backscattering profiles i.e. A-scans.

The relationship between the gold nanoshells concentration and extracted μ_s implies that the extracted μ_s may be used to determine the unknown particle concentration in tissue from the OCT signal profile for concentration mapping. Since a tissue phantom with different concentrations of gold nanoshells is able to model the localization of gold nanoshells after various mode of nanoshells delivery in tissue, the results in this study could provide further insights on the changes in OCT image contrast for different delivery mode of nanoshells into tumor tissue of animal models.

7.2 Materials and methods

7.2.1 Synthesis and characterization of gold nanoshells

Gold nanoshells were synthesized and pegylated as described in preceding chapters. The pegylation provides steric stabilization to improve their stability in aqueous medium without adversely affecting their optical properties. The particle size was determined by transmission electron microscopy (TEM) (Jeol JEM-1010) operating at

100 kV. Their extinction spectrum was measured using a UV-Vis spectrophotometer (Shimadzu UV-2401 PC) in the wavelength range from 400 to 900 nm and compared to the theoretically predicted spectrum from Mie theory for a single nanoshell of the same size configuration.

The gold nanoshells were synthesized with a silica core diameter of 162 nm surrounded by a gold shell of 23 nm thick. The TEM image of synthesized gold nanoshells and its measured UV-Vis extinction spectrum is shown in Figure 7.1. This size configuration was selected based on an optimized backscattering cross section at 800 nm predicted from Mie theory as described in Chapter 2.4.5. Here, the 800 nm surface plasmon resonance peak of the synthesized gold nanoshells matches the 800 nm excitation wavelength of the OCT systems used in this study to generate a large optical extinction in the gold nanoshells when they are excited by the light source.

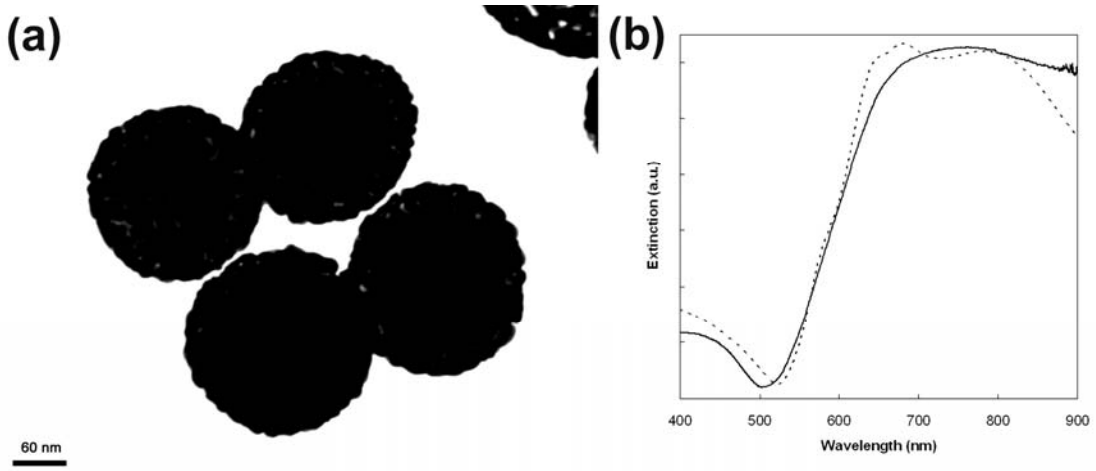

Figure 7.1. TEM image of the synthesized gold nanoshells with a 162 nm silica core surrounded by a 23 nm thick gold shell. (b) Comparison between the measured extinction spectrum (solid line) and theoretically predicted spectrum based on Mie theory for concentric spheres (dotted line).

The pegylated gold nanoshells were dispersed in phosphate buffer solution, pH 7.4 to a final concentration of 2.0 x 10^{13} particles/ml as determined by correlating its measured extinction spectroscopy data to the theoretical extinction cross-section data based on Mie theory for gold nanoshells having the same size configuration. In this case, the concentration can be obtained by dividing the extinction coefficient by the extinction cross section. The synthesized gold nanoshells were stored at 4 °C until further use.

7.2.2 Benchtop OCT system setup

Two OCT systems were employed in this phantom study: a benchtop setup used to compare the OCT signal of suspended gold nanoshells with tissue phantoms and other particle scatterers and a commercial system used to examine the concentration parameter of gold nanoshells. The benchtop setup was developed by Chow et al. from Nanyang Technological University. For the benchtop setup, a single-mode fiber based bench top Fourier-domain OCT system with operating wavelength centered at 800 nm was used with the schematic of system setup as shown in Figure 7.2. The light source used is a Ti:Sapphire laser (Integral OCT, Femtolaser Inc) operating at a centre wavelength of 800 nm with a bandwidth of 120 nm to give a power output of approximately 7 mW at the sample and a measured in-focus axial resolution of 4 μm. A low 0.3 NA, 10x microscope objective was used to provide a lateral resolution of 9 μm. Instead of having a reference arm in a typical time-domain OCT setup, a cover slip was placed at the sample arm to provide self-referencing.

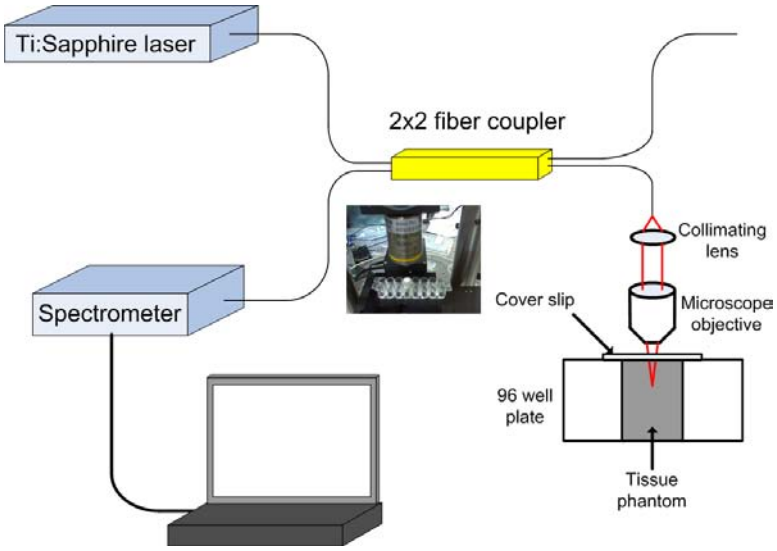

Figure 7.2. Schematic of the bench top Fourier-domain OCT system setup used for the phantom studies with a Ti:Sapphire laser source operating at 800 nm to give an axial resolution of 4 μm and lateral resolution of 9 μm. The scanning arrangement is shown as an insert in the figure.

Backscattered light from the samples was collected via the microscope objective and directed to a spectrometer (Ocean Optics HR4000) that was used as a detector to detect the interference fringes. The Fourier spectrum was then output to a computer for digital processing using a routine written in Labview 8.0 to obtain the OCT M-scan images.

7.2.3 Commercial OCT system setup

The commercial OCT system from Bioptigen, Inc. (Durham, NC) was used and the system schematic is shown in Figure 7.3. This portable system employs the Optical Spectral Domain Reflectometers (OSDR)^{TM} engine based on the Spectral Domain OCT (SDOCT) technology. The light source used is a superluminescence diode operating at a centre wavelength of 840 nm with a bandwidth of about 60 nm, giving an optical power output of 750 μW at the sample and an output SNR of 110 dB. This

broadband single-mode illumination gives a measured in-focus axial resolution of ≤ 6 μm in tissue and the lateral resolution is around 20 μm. The system is able to achieve an imaging speed of 20,000 lines (or A-scans) per second and an imaging depth of 1.5 to 2 mm. The OCT imaging scanner consists of a 0.6" x 5" 2-axes hand-held borescope probe with telecentric scanning optics that performs non-contact telecentric scan with a lateral scan range of 6 mm. Backscattered light from the samples was collected and directed to a spectrometer that was used as a detector to detect the interference fringes that provided the scattering profile of the samples.

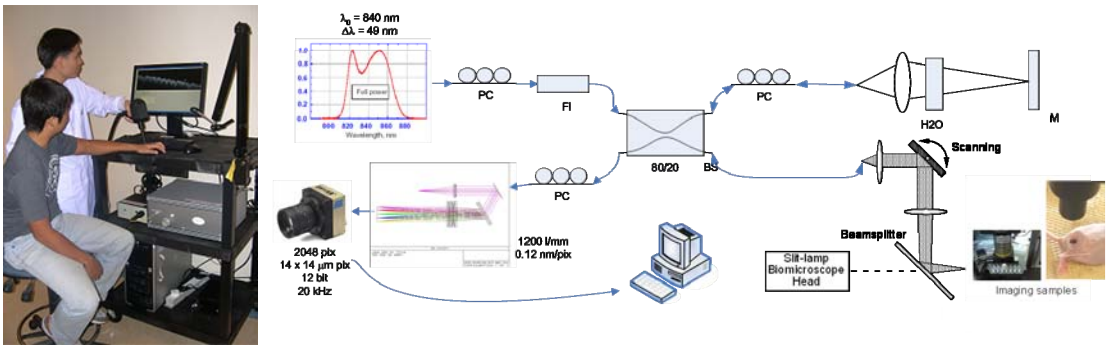

Figure 7.3. The schematic of the Spectral domain OCT imaging system used in this study. In the figure, the various components of the system are annotated as such: Polarization Controller (PC) which controls the polarization of light; Faraday Isolator (FI) that prevents back-reflection into the SLED; Beam Splitter (BS) which splits the beam into the reference and sample path; and mirror (M) which serves as the reference plane. The water (H2O) is used for dispersion compensation. Image courtesy of Bioptigen Inc. The phantom and small animal imaging setup are shown as insert in the figure.

The Fourier spectrum was then output to a computer for digital processing using the proprietary InVivoVue OCT software suite (Bioptigen Inc, Durham NC) to obtain the OCT individual A-scan and B-scan images. The two-dimensional B-scan images of 784 x 468 pixels were obtained by scanning the single-mode optical beam laterally over the sample. A custom routine was written in MATLAB to further process the

OCT image file offline to obtain the average A-scans for subsequent analysis and extraction of the μ_s of the imaged sample described in more details below.

7.2.4 OCT imaging for comparative studies of liquid phantoms

The OCT image of a colloidal solution of gold nanoshells (2×10^{11} particles/ml) was acquired together with that of a colloidal solution of naked silica core nanoparticles of the same size and concentration but without the gold shell as well as 1% Intralipid (Sigma-Aldrich) which is commonly used as a tissue phantom to mimic intrinsic tissue scattering over a wide range of wavelengths [20, 21]. At 1% Intralipid concentration, it has a known μ_s of 1.6 to 2.4 mm^{-1} (depending on the manufacturing batch) [22, 23] and an anisotropy factor, g of 0.68 in the 800 nm NIR region [22, 24]. OCT imaging was also performed on saline as a negative control, which is not known to give any signal with OCT as well as a sample of gold nanoshells added to 1% Intralipid to model the addition of gold nanoshells into tissue. The OCT images from all these five samples were compared in terms of image signal intensity.

These homogenous liquid samples were prepared in 7 mm circular wells of an immuno module (Nunc Maxisorp Immuno Module), filled to the brim with about 400 µl for imaging. Since the information of interest was the OCT signal as a function of depth, the surface of the liquid samples was placed at the same height with no tilt to reduce any error due to focusing. This was done by covering the top of the well with a coverslip to remove the meniscus of the liquid samples so that the transverse imaging location will not be affected by it (Figure 7.2 and 7.3). The coverslip also helps to reduce specular reflection at the air-liquid interface arising from the meniscus.

The samples were scanned using the benchtop OCT under M-mode imaging with 400 M-scans (scanning at a fixed spatial location with time) per image frame. Each colloidal suspension was agitated by micropipetting just prior to OCT imaging to ensure a homogeneous distribution of particles during scan. Due to the limited bandwidth of the spectrometer and limited dynamic range of the benchtop system, the imaging depth was limited to only 200 μm corresponding to 2000 axial points. The OCT images were analyzed using the ImageJ software (National Institutes of Health, USA) to determine the average histogram value of the M-scan images for comparison between their OCT signal.

7.2.5 OCT imaging for parametric studies of different sample μ_s

OCT B-mode imaging and its corresponding average A-scans were performed on two types of samples in the parametric studies using the commercial OCT system as described earlier. In the first sample imaging, the changes in OCT signal with varying μ_s were examined by using different concentrations of Intralipid. The 20% Intralipid stock solution were diluted with water to give 1, 2, 3, 4, 10 and 20% Intralipid tissue phantoms and OCT images of the individual concentration were acquired. In the second sample imaging, different concentrations of gold nanoshells in 1% Intralipid were imaged. The gold nanoshells stock solution was serially diluted in half to give a range of seven different concentrations: 1.4, 2.8, 5.6, 11.3, 22.5, 45.0 and 90.0 x 10^9 particles/ml. OCT B- and A-scans were also performed on water which is not known to give any signal with OCT, as a reference for any system gain correction.

The samples were prepared in the same manner as described above in 7 mm circular wells of an immuno module with the top covered by a coverslip. The samples were positioned and imaged with the top surface of the coverslip at 200 μm from the top of the OCT image screen for standardization. The scanning was done under B-mode with 1,000 axial A-scans to give an overall lateral scan range of 6 mm per B-scan image frame and the imaging depth was about 1.5 mm. All the 1,000 columns of axial A-scans from each B-scan were averaged to reduce random speckle fluctuations and obtain a reliable average A-scan profile for further analysis. All parameters including focus position and software constants remained the same throughout the entire study.

7.2.6 OCT theoretical curve fitting and μ_s extraction

In the analysis of OCT signal, the multiple scattering theoretical OCT model based on the extended Huygens-Fresnel (EHF) theory was used to fit the measured average A-scan profile to extract the μ_s of the sample under measurement [16]. This model accounts for both single and multiple scatterings in the sample and is thus able to fit well into the average A-scan profile for a wide range of μ_s including those used in this study. The detected signal intensity as a function of the optical axial depth, z in the theoretical OCT equation is given by:

$$i(z) = A\sqrt{\exp(-2\mu_s z) + \frac{2\exp(-\mu_s z)\left[1-\exp(-\mu_s z)\right]}{1+\left(\frac{w_S}{w_H}\right)^2} + \frac{\left[1-\exp(-\mu_s z)\right]^2}{\left(\frac{w_S}{w_H}\right)^2}} \qquad (7.1)$$

$$\left(\frac{w_s}{w_h}\right)^2 = 1+\left[\frac{2w_0}{\rho_0(z)}\right]^2, \text{ and } \rho_0 = \sqrt{\frac{3}{\mu_s z}}\frac{\lambda}{\pi\theta_{rms}}\left[\frac{nf}{z}\right], \qquad (7.2)$$

where A is a proportionality constant. w_H and w_s are the 1/e irradiance radii in the absence and presence of scattering. ρ_0 is the lateral coherence length and θ_{rms} is the root mean square scattering angle. The square root in Equation 7.1 accounts for the fact that OCT detects the electric field rather than the intensity of the sample. The curve fitting process utilized a non-linear least square fit of the data to Equation 7.1. For fitting of different concentrations of Intralipid and different concentrations of gold nanoshells in Intralipid, θ_{rms} was set to 0.8 for all cases. This is the θ_{rms} value for Intralipid [24] which is the dominant scatterer used in the study. The θ_{rms} value for gold nanoshells were not considered in the fitting as the volume fraction of gold nanoshells used in our study i.e. ranging from 0.00066 % to 0.0424 % is negligible to cause a substantial change in the overall scattering angle when added into tissue.

Since the system parameters such as the focal length, beam waist, source wavelength and sample refractive index of the sample are known *a priori*, the fitting process only involved μ_s, A and an additive factor i_0 representing the noise level. It is also known that the total sample extinction coefficient is the sum of the absorption and scattering coefficient i.e. $\mu_t = \mu_a + \mu_s$. For most samples being imaged in this study, the absorption is often assumed to be negligible i.e. $\mu_t \approx \mu_s$ since the absorption of Intralipid and gold nanoshells is known to be very small around the source wavelength. Hence, the OCT depth-dependent scattering has been modeled as a function of the scattering coefficient, μ_s of the medium instead of μ_t.

7.3 Results and discussion

7.3.1 Comparison of OCT signal with tissue phantom

The use of gold nanoshells to improve the OCT signal in simple tissue phantom is investigated by comparing the OCT M-scan images of gold nanoshells with other colloidal samples and the results are shown in Figure 7.4 below.

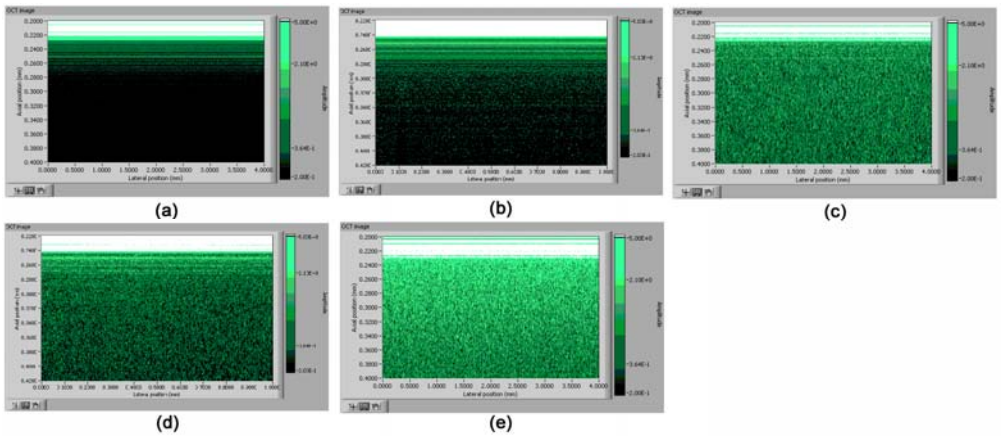

Figure 7.4. OCT M-scans of (a) saline as a negative control, (b) colloidal suspension of naked silica nanoparticles (162 nm, 2 x 10^{11} particles / ml) used as the core in the gold nanoshells, (c) colloidal suspension of synthesized gold nanoshells (2 x 10^{11} particles / ml) with a 162 nm silica core and 23 nm thick gold shell, (d) 1% Intralipid used to mimic intrinsic tissue scattering and (e) a mixture of gold nanoshells added to 1% Intralipid. These M-mode images were generated by performing repeated scans at a fixed spatial location in the phantom over an interval of time with the lateral axis represented by time. The range of scanning depth shown is 200 µm and the bright signal from the top reflective layer attributed to the reflective glass slide.

The mean histogram values and standard deviation of the 8-bit OCT M-scan images of the five samples are also shown in Table 7.1 for comparison. Apart from the saline used as a negative control, all of the samples that are evaluated for their OCT signal in this study are colloidal solution having different particulate nature. The results show that whilst the bare silica core nanoparticles of the same size and concentration as the gold nanoshells are able to elicit an observable OCT signal compared to the negative

saline control due to their inherent Mie scattering, the signal remains much weaker compared to signal from intrinsic tissue scattering as modeled by the 1% Intralipid. The mean histogram value of silica is slightly less than half that of the Intralipid.

The 1% Intralipid that is used in this study as a phantom model to mimic the intrinsic light scattering in tissue consisted of spherical shaped fat emulsion particles having a broad size distribution with a mean particle diameter of 1.01 μm and an anisotropy factor of around 0.8 in the NIR region [22, 25]. This makes the Intralipid particles forward light scatterers. In contrast, the silica core nanoparticles without the gold shell were smaller at 162 nm that their light scattering tends to be isotropic with an anisotropy factor of around 0.12 (based on theoretical Mie calculation). Although these silica core nanoparticles were able to generate an observable OCT signal, their smaller scattering cross section and more isotropic light scattering nature account for a weaker OCT signal with greater attenuation with depth compared to 1% Intralipid.

Table 7.1. The mean histogram value and standard deviation of the 8-bit OCT M-scan images of different samples examined in the phantom study.

Sample for OCT M-scan	**Mean histogram value (0 to 255)**	**Standard Deviation**
Saline	6.6	15.7
Naked core silica nanoparticles (2×10^{11} particles/ml)	18.4	23.9
Synthesized gold nanoshells (2×10^{11} particles/ml)	58.0	27.4
1% Intralipid	41.4	25.6
1% Intralipid with gold nanoshells (2×10^{11} particles/ml)	89.9	36.3

As the layer of gold shell is grown over the silica core, the geometric cross section of the particle is not only increased (diameter increased from 162 to 208 nm), the layer of gold shell also brought about an additional surface plasmon effect that increased the backscattering efficiency of the entire particle from 0.0029 to 6.1, based on theoretical Mie calculation. Such combination of an increase in backscattering efficiency coupled with an increase in geometric cross section resulted in a much larger backscattering cross section of the gold nanoshells to give a large positive offset in the OCT signal as discussed in Chapter 2.

The end result is that the surface plasmon resonance from the gold shell is able to increase the OCT signal to produce a correspondingly brighter OCT image compared to naked silica core nanoparticles of the same concentration as observed in Figure 7.4. This increase in the mean histogram value from 18.4 to 58.0 i.e. ≈ 3.2 times increase, is so distinct that the OCT signal from gold nanoshells alone is even stronger compared to the signal from 1% Intralipid tissue phantom within the 200 μm depth of imaging. In fact, the mean histogram value of the gold nanoshells scan is nearly 1.5 times that of the 1% Intralipid tissue phantom (58.0 vs. 41.4) despite having a geometric cross section about 23 times smaller compared to the Intralipid particles.

When the gold nanoshells are added to the 1% Intralipid to model the addition of the gold nanoshells into tissue, the final OCT image is brighter than any of its constituents and the mean histogram value of the 1% Intralipid increases from 41.4 to 89.9, which is slightly more than a twofold increase. This twofold increase in the mean histogram value shows that by adding appropriate amount of gold nanoshells

into tissue, the OCT image signal can potentially be increased by at least two orders since the visual observation from the image histogram value is in the log scale.

It is also interesting to note that the mean histogram value of the 1% Intralipid mixture with gold nanoshells is an approximate linear summation of the mean histogram values of its constituent 1% Intralipid and gold nanoshells i.e. $89.9 \approx 41.4 + 58.0$. Such observation assumes that the backscattering increase linearly with the concentration of the particles which is true only in the case of single scattering approximation at small depth of imaging. With the shallow scanning depth of 200 µm, the predominance of single scattering in sample validates such linear summation.

In the present discussion, it should also be noted that the depth of OCT imaging shown here using the benchtop setup is at most up to 200 µm. Such shallow depth of imaging does not permit any depth-dependent attenuation of the OCT signal deeper into the sample to be observed. Such depth-dependent attenuation affects the overall quality of the OCT images and can be examined with greater depth of imaging using the commercial OCT system. The effect of this depth-dependent attenuation is shown and discussed in the following section.

7.3.2 Changes in OCT signal with different μ_s

Intralipid of different concentrations were used to examine how changes in the tissue μ_s affect the OCT image and its corresponding average A-scan profile. The results in Figure 7.5 show at least two observable changes in the OCT images as the concentration of Intralipid increases. Firstly, the OCT signal attenuation with depth becomes more pronounce to result in a reduction in image brightness deeper into the

sample. This is accompanied by a corresponding increase in the OCT signal nearer to the sample surface, especially in the first 200 μm. The overall visual effect is a gradual “compression” of the OCT signal i.e. image brightness increases towards the superficial direction as μ_s increases to give two distinct regions: a bright but narrow band of about 200 μm from the sample surface atop a dark region arising from the attenuated OCT signal.

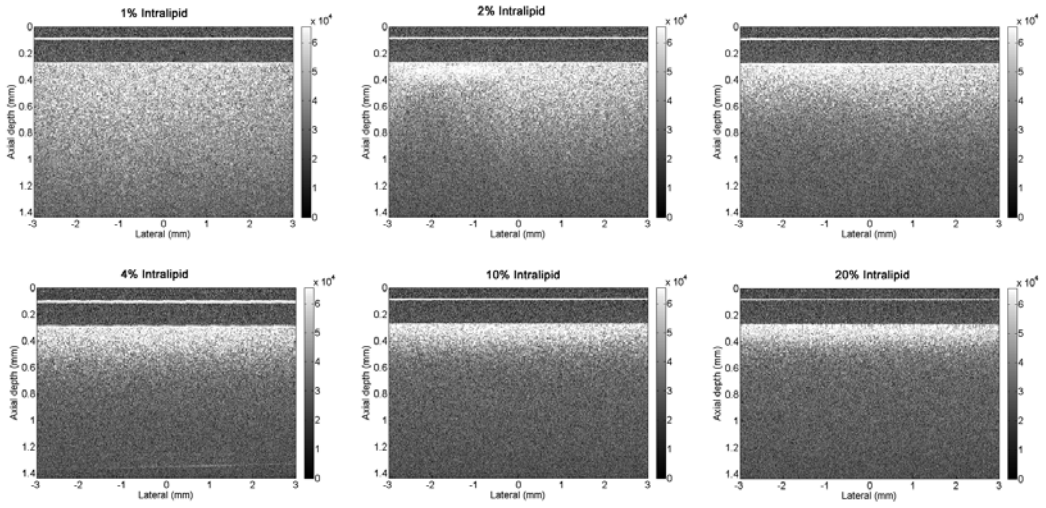

Figure 7.5. OCT imaging of tissue phantom samples based on Intralipid showing the changes observed in OCT image with increasing μ_s as given by an increasing Intralipid concentration.

The average A-scan profile shown in Figure 7.6 corresponding to each of the OCT image in Figure 7.5 characterizes the above mentioned changes with a gradual increase in the slope of the depth-dependent signal and the signal intensity at the sample surface as the μ_s increases. These observations imply that whilst the signal near the sample surface is strong, the effective imaging depth is compromised for highly scattering samples.

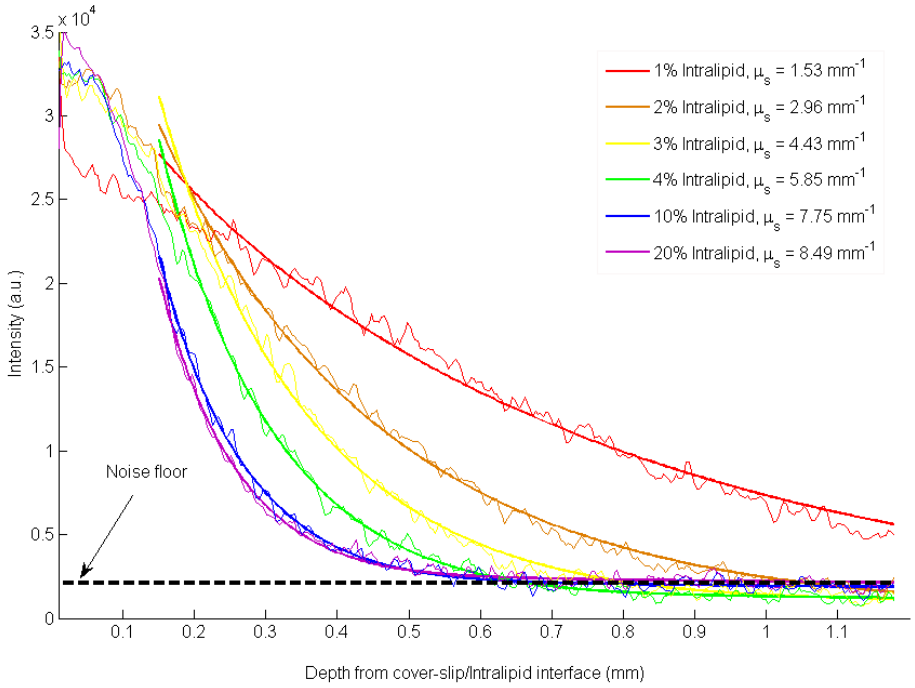

Figure 7.6. Changes in the average A-scan profile for different concentration of Intralipid corresponding to each of the OCT image in Figure 7.5. The fitted curve based on the theoretical multiple scattering OCT model is shown as an overlay onto the measured signal to extract the sample μ_s which is indicated in the figure. The noise floor is shown in dotted line.

Previous studies have shown that the negative gradient of the average A-scan profile is a function of μ_t [26, 27]. As μ_t increases, the slope of the depth attenuation profile also increases. Since Intralipid is known to be scattering dominant with negligible absorption i.e. $\mu_a \approx 0$, the extracted $\mu_t \approx \mu_s$. Therefore the slope of the average A-scan profile is determined by the μ_s of Intralipid. As μ_s increases with higher Intralipid concentration, the incident light source entering the sample experiences higher level of scattering near the surface which reduces its mean free paths.

This scattering is attributed to the presence of spherically shaped fat emulsion particles in Intralipid as described earlier. The amount of single backscattered light that collectively contribute to the overall backscattered light is also higher due to

higher concentration of the particles, thus presenting a strong OCT signal enhancement near the sample surface as observed in the results. With a significant amount of light backscattered out of the sample, the amount of light that reaches deeper into the sample is reduced, which explains the significant signal attenuation with depth as μ_s increases.

The plot of the μ_s extracted from the fitted model (see Figure 7.6) against different concentration of Intralipid is shown in Figure 7.7. The extracted μ_s of Intralipid based on the multiple scattering OCT model increases proportionately with lower concentrations of Intralipid. For higher concentrations of Intralipid, the μ_s does not scale linearly with concentration in the same way as for low concentration, but begins to deviate from linearity at 4% concentration. This nonlinear relationship between μ_s and Intralipid concentration was similarly observed by others [22, 24, 28] and occurs when the mean Intralipid particle spacing is small (typically less than 3-5 particle diameters [22]) at high concentrations to result in the shadowing effect of particles that effectively reduces the apparent Intralipid particle concentration and hence its μ_s.

As the Intralipid μ_s increases from 1.53 ± 0.16 mm^{-1} (1% Intralipid) to 8.49 ± 0.26 mm^{-1} (20% Intralipid), the depth at which the OCT signal attenuates to the noise floor decreases from >1.2 mm to about 500 μm. As the Intralipid is able to model the scattering behavior of tissue well, the same observation concerning the reduction in imaging depth with increasing Intralipid μ_s holds true for tissue with different μ_s.

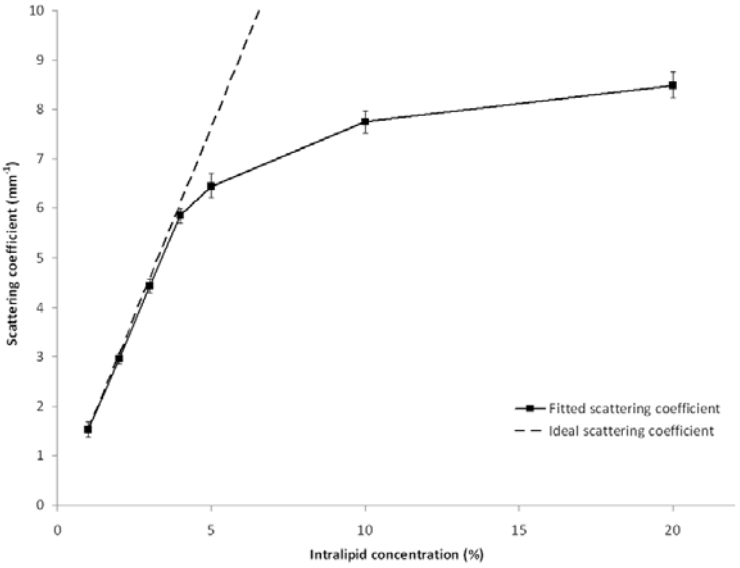

Figure 7.7. Plot of the extracted μ_s against different concentration of Intralipid. The predicted linear relationship between μ_s and concentration is shown in dotted line as a reference to show the nonlinearity occurring at high concentration of Intralipid.

This reduction in the depth of imaging suggests the importance of appropriate sample μ_s that would allow an acceptable imaging depth particularly for diseases such as cancer where the pathological changes may not be sufficiently superficial. Since most of the early phenotypic changes in tissue associated with diseases such as pre-cancers of the epithelium originates at about 300 - 600 µm beneath the tissue surface at the basal layer within the mucosa, the OCT signal level at 600 µm should be above the noise floor to be effective for cancer imaging.

The results in Figure 7.6 show that any sample μ_s less than 5.85 mm^{-1} would maintain the OCT signal above the noise floor at 600 µm to image any critical changes occurring at the mucosa. This criterion allows a wide range of human soft tissue to be imaged [29, 30]. It is noteworthy that the results obtained are specific to the commercial OCT system used in this study. Other OCT systems would give different outcomes depending on their SNR and dynamic range.

7.3.3 Change in OCT signal with different concentration of gold nanoshells

The effect of having different gold nanoshells concentration in Intralipid on the OCT image holds several implications on the delivery of these nanoparticle contrast agent into living systems as an imaging contrast agent since different delivery routes would result in different level of gold nanoshells localization at the targeted site of imaging. Different concentrations of gold nanoshells in 1% Intralipid were imaged to model the localization of their different amount in tissue and hence understand the effects on the image enhancement. The OCT image of a range of gold nanoshells concentration (1.4 x 10^9 to 9.0 x 10^{10} particles/ml) in 1% Intralipid is shown in Figure 7.8.

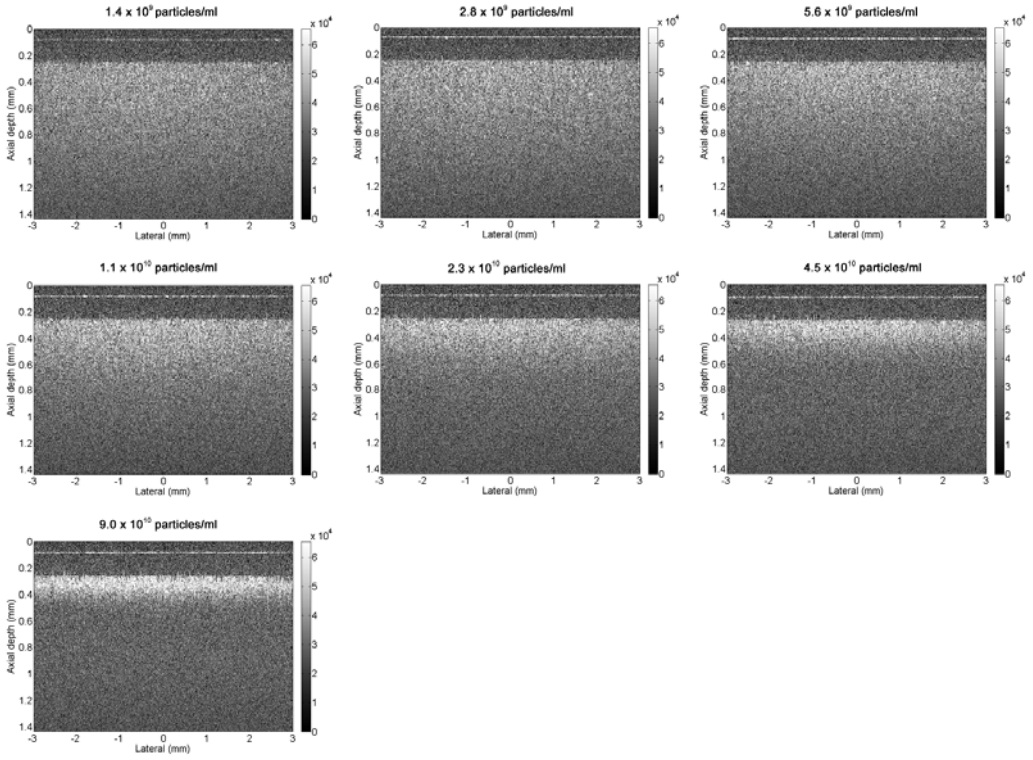

Figure 7.8. OCT imaging of phantom samples showing the changes observed in OCT image with increasing concentration of gold nanoshells in Intralipid.

At a low concentration of < 5.6 x 10^9 particles/ml, the change in OCT image is barely observable. The corresponding average A-scan profile of these concentrations in Figure 7.9 also remains largely unchanged except for slight increase in the slope of the signal attenuation with depth. The change in the image only becomes more apparent at 5.6 x 10^9 particles/ml where the signal intensity near the surface increases slightly and the OCT signal attenuation with depth becomes observable.

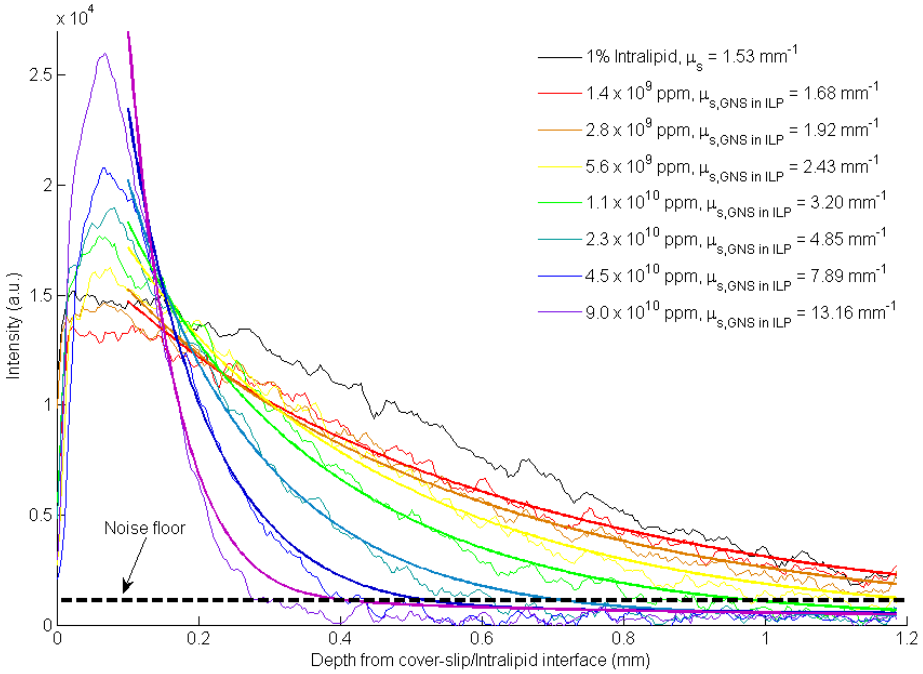

Figure 7.9. Changes in average A-scan profile for different concentration of gold nanoshells corresponding to each of the OCT image in Figure 7.8. The fitted curve based on the theoretical multiple scattering OCT model is shown as an overlay onto the measured signal to extract the sample μ_s which is indicated in the figure. The noise floor is shown in dotted line.

As the gold nanoshells concentration increases to 1.1 x 10^{10} particles/ml and beyond, the characteristic gradual "compression" of OCT image brightness towards the superficial direction as previously observed in Intralipid becomes increasingly pronounced. The average A-scan profile also show the gradual sharpening of the

signal attenuation with depth accompanied by an increasing signal intensity near the sample surface (< 200 μm) as observed previously.

The overall μ_s of different gold nanoshells concentration in 1% Intralipid (GNS in ILP) was extracted from their average A-scans in Figure 7.9. The μ_s contributed by gold nanoshells alone can be derived simply by subtracting the μ_s of Intralipid (i.e. 1.53 ± 0.16 mm^{-1} from the result the previous section 7.3.2) from $\mu_{s,GNS\ in\ ILP}$ [31] i.e.

$$\mu_{s,GNS} = \mu_{s,GNS\ in\ ILP} - \mu_{s,ILP} \tag{7.3}$$

The extracted $\mu_{s,GNS\ in\ ILP}$ and derived $\mu_{s,GNS}$ is plotted against different concentration of gold nanoshells as shown in Figure 7.10. The theoretical $\mu_{s,theoretical}$ based on Mie calculations for different gold nanoshells concentration is also shown as comparison.

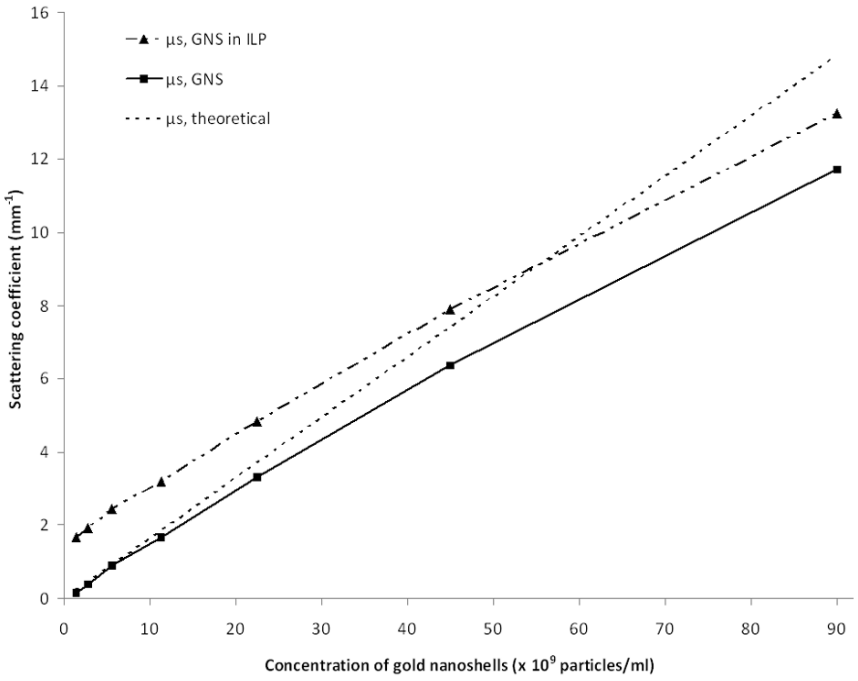

Figure 7.10. Plot of the calculated μ_s of gold nanoshells in Intralipid (solid line) derived from subtraction of $\mu_{s,\ ILP}$ from the extracted $\mu_{s,\ GNS\ in\ ILP}$ (dash-dot-dot) against different concentration of gold nanoshells in Intralipid. The theoretical linear relationship between μ_s and gold nanoshells concentration is shown in dotted line.

The μ_s of gold nanoshells derived from the measured OCT signal exhibit a positive linear relationship with concentration and agree well with that determined from theoretical calculation except for slight deviation towards higher concentration where the derived μ_s is lower than expected. To understand the link between the gold nanoshells concentration and extent of OCT signal enhancement or attenuation when different amount of gold nanoshells are delivered to tissue, the relationship between the μ_s and gold nanoshells concentration is examined by the following equation:

$$\mu_s = \rho A Q_{sca} \quad (7.4)$$

where ρ is the concentration in number of particles per unit volume, A is the geometric cross section and Q_{sca} is the scattering efficiency. With a constant gold nanoshells size configuration (81 nm core radius and 23 nm shell thickness) used throughout this study i.e. A = 3.40 x 10^{-14} m^2 and Q_{sca} at 840 nm = 4.58, μ_s scales linearly with concentration theoretically and can be further simplified to

$$\mu_s = 1.556 \rho \times 10^{-10} \text{ mm}^{-1} \quad (7.5)$$

where ρ is the concentration of the synthesized gold nanoshells in particles/ml. This linear relationship is seen in Figure 7.10, which is also observed at low Intralipid concentrations (Figure 7.7). Therefore, the changes observed in the OCT image for increasing gold nanoshells concentration is similar to that of increasing Intralipid concentration and can be explained in terms of the changes in μ_s as discussed earlier.

However, the nonlinearity observed at higher Intralipid concentrations is less apparent at higher gold nanoshells concentration where the measured μ_s of gold nanoshells appear to deviate only slightly from the theoretical linearity at high concentrations. The same argument used to account for the nonlinearity in Intralipid in terms of

interparticle effects also holds true in the case of gold nanoshells. However, this effect is less prominent in gold nanoshells probably due to their smaller sizes. This region of linearity allows for a good estimation of any unknown concentration of gold nanoshells in tissue given its extracted μ_s and a wide linearity region allows an accurate concentration to be mapped over a wide range.

By incorporating the extraction results into the average A-scan profiles in Figure 7.9, it is shown that a $\mu_{s,GNS\ in\ ILP}$ of 2.43 mm^{-1} (as given by 5.6 x 10^9 particles/ml) is just sufficient to elicit an increase in the signal intensity over that of 1% Intralipid within the first 200 µm. Although the signal intensity at the top 200 µm layer continues to increase with larger $\mu_{s,GNS\ in\ ILP}$ to give an even brighter image, the signal deeper into the sample gets rapidly attenuated. As the $\mu_{s,GNS\ in\ ILP}$ increases to 4.85 mm^{-1} (2.3 x 10^{10} particles/ml), the OCT signal is just above the noise floor at 600 µm depth, beyond which any higher concentration would render the contrast agent ineffective in maintaining an acceptable imaging depth. The results thus suggest an appropriate working range of 2.43 $mm^{-1} < \mu_{s,GNS\ in\ ILP} < 4.85\ mm^{-1}$. This working range falls within the earlier suggested range of $\mu_s < 5.85\ mm^{-1}$ in section 7.3.2 needed to maintain the OCT signal above the noise floor at 600 µm.

Using Equation 7.5, the above working range of μ_s translates to a gold nanoshells concentration window of 5.6 x $10^9 < c < 2.3$ x 10^{10} particles/ml that would be useful to provide signal enhancement and yet maintain an acceptable imaging depth of at least 600 µm for imaging tissue under the OCT. This concentration window lies within the linearity region in Figure 7.10 to suggest that the concentration can be accurately mapped from the extracted μ_s using the theoretical Equation 7.4.

The results above have demonstrated that an appropriate range of gold nanoshells concentration to be optimized for imaging exists. Although this concentration range is specific to the size of gold nanoshells and optical specifications of the OCT system used in this study, the approach to determine this range holds applicable for other OCT-gold nanoshells matching systems. The concentration window implies the need for an appropriate delivery protocol of gold nanoshells to achieve the desired amount in tissue. This is because different delivery protocol such as intratumoral or intravenous injection would deliver different amount of gold nanoshells to the target tissue and hence produce varying effect on the contrast enhancement as demonstrated in this phantom study.

7.4 Conclusion

The performance of OCT in achieving an acceptable imaging depth depends as much on the μ_s of the sample as its source power, dynamic range or SNR. This chapter has shown that an increase in the sample μ_s not only increase the OCT signal near the sample surface but also concurrently attenuates the signal further in depth. Such results hold several implications to the use of gold nanoshells as a contrast agent for OCT imaging since their addition into tissue affects the overall μ_s. For the gold nanoshells enhanced OCT investigated in this study, a concentration range of $5.6 \times 10^9 < c < 2.3 \times 10^{10}$ particles/ml in 1% Intralipid would achieve a good compromise between increasing the OCT signal near the sample surface while maintaining acceptable signal attenuation at the deeper region. This implies the need for an appropriate delivery protocol for subsequent *in vivo* studies that would result in this concentration to effectively enhance the tissue being imaged.

The phantom results have hitherto shown that the gold nanoshells have the optical response sufficient to function as a generic OCT contrast agent over intrinsic tissue scattering. With appropriate antibody functionalization as demonstrated in previous Chapter 6, these gold nanoshells can potentially be targeted to early lesions *in vivo* where only molecular changes occur. This will elicit an early molecular-based contrast under the OCT that facilitates earlier cancer diagnosis of suspicious lesions *in vivo* before phenotypic changes occur, while leaving surrounding normal tissue untouched, thus further adding value to its clinical significance. Such *in vivo* studies on the targeting, accumulation and image contrast of gold nanoshells in tumor tissue of mouse model will be described in more details in the following Chapter 8.

7.5 References

1. Huang D, Swanson EA, Lin CP, Schuman JS, Stinson WG, Chang W, Hee MR, Flotte T, Gregory K, Puliafito CA, et al. Optical coherence tomography. *Science* 1991; 254(5035): 1178-1181.

2. Brezinski ME, Tearney GJ, Bouma BE, Izatt JA, Hee MR, Swanson EA, Southern JF, Fujimoto JG. Optical coherence tomography for optical biopsy. Properties and demonstration of vascular pathology. *Circulation* 1996; 93(6): 1206-1213.

3. Sergeev A, Gelikonov V, Gelikonov G, Feldchtein F, Kuranov R, Gladkova N, Shakhova N, Snopova L, Shakhov A, Kuznetzova I, Denisenko A, Pochinko V, Chumakov Y, Streltzova O. In vivo endoscopic OCT imaging of precancer and cancer states of human mucosa. *Opt. Express* 1997; 1(13): 432-440.

4. Tearney GJ, Brezinski ME, Bouma BE, Boppart SA, Pitris C, Southern JF, Fujimoto JG. In vivo endoscopic optical biopsy with optical coherence tomography. *Science* 1997; 276(5321): 2037-2039.

5. Bashkatov AN, Genina EA, Sinichkin YP, Tuchin VV: The influence of glycerol on the transport of light in the skin *Proceedings of SPIE - The International Society for Optical Engineering* 2002; 4623:144-152.

6. Wang RK, Elder JB. Propylene glycol as a contrasting agent for optical coherence tomography to image gastrointestinal tissues. *Lasers in Surgery and Medicine* 2002; 30(3): 201-208.

7. Barton JK, Hoying JB, Sullivan CJ. Use of microbubbles as an optical coherence tomography contrast agent. *Acad Radiol* 2002; 9 Suppl 1: S52-55.

8. Lee TM, Oldenburg AL, Sitafalwalla S, Marks DL, Luo W, Toublan FJ, Suslick KS, Boppart SA. Engineered microsphere contrast agents for optical coherence tomography. *Opt Lett* 2003; 28(17): 1546-1548.

9. Troutman TS, Barton JK, Romanowski M. Optical coherence tomography with plasmon resonant nanorods of gold. *Opt Lett* 2007; 32(11): 1438-1440.

10. Chen J, Saeki F, Wiley BJ, Cang H, Cobb MJ, Li ZY, Au L, Zhang H, Kimmey MB, Li X, Xia Y. Gold nanocages: bioconjugation and their potential use as optical imaging contrast agents. *Nano Lett* 2005; 5(3): 473-477.

11. Loo C, Lin A, Hirsch L, Lee MH, Barton J, Halas N, West J, Drezek R. Nanoshell-enabled photonics-based imaging and therapy of cancer. *Technol Cancer Res Treat* 2004; 3(1): 33-40.

12. Loo C, Hirsch L, Lee MH, Chang E, West J, Halas N, Drezek R. Gold nanoshell bioconjugates for molecular imaging in living cells. *Opt Lett* 2005; 30(9): 1012-1014.

13. Zagaynova EV, Shirmanova MV, Orlova AG, Balalaeva IV, Kirillin MY, Kamensky VA, Bugrova ML, Sirotkina MA: Gold nanoshells for OCT imaging contrast: From model to in vivo study *Progress in Biomedical Optics and Imaging - Proceedings of SPIE* 2008; 6865.

14. Barton JK, Halas NJ, West JL, Drezek RA: Nanoshells as an optical coherence tomography contrast agent *Proceedings of SPIE - The International Society for Optical Engineering* 2004; 5316:99-106.

15. Agrawal A, Huang S, Wei Haw Lin A, Lee MH, Barton JK, Drezek RA, Pfefer TJ. Quantitative evaluation of optical coherence tomography signal enhancement with gold nanoshells. *J Biomed Opt* 2006; 11(4): 041121.

16. Thrane L, Yura HT, Andersen PE. Analysis of optical coherence tomography systems based on the extended Huygens-Fresnel principle. *J Opt Soc Am A Opt Image Sci Vis* 2000; 17(3): 484-490.

17. Kholodnykh AI, Petrova IY, Larin KV, Motamedi M, Esenaliev RO. Precision of Measurement of Tissue Optical Properties with Optical Coherence Tomography. *Appl. Opt.* 2003; 42(16): 3027-3037.

18. van Leeuwen TG, Faber DJ, Aalders MC. Measurement of the axial point spread function in scattering media using single-mode fiber-based optical coherence tomography. *Selected Topics in Quantum Electronics, IEEE Journal of* 2003; 9(2): 227-233.

19. Levitz D, Thrane L, Frosz M, Andersen P, Andersen C, Andersson-Engels S, Valanciunaite J, Swartling J, Hansen P. Determination of optical scattering properties of highly-scattering media in optical coherence tomography images. *Opt. Express* 2004; 12(2): 249-259.

20. Troy TL, Thennadil SN. Optical properties of human skin in the near infrared wavelength range of 1000 to 2200 nm. *J Biomed Opt* 2001; 6(2): 167-176.

21. Flock ST, Jacques SL, Wilson BC, Star WM, van Gemert MJ. Optical properties of Intralipid: a phantom medium for light propagation studies. *Lasers Surg Med* 1992; 12(5): 510-519.

22. van Staveren HJ, Moes CJM, van Marie J, Prahl SA, van Gemert MJC. Light scattering in Intralipid-10% in the wavelength range of 400?1100 nm. *Appl. Opt.* 1991; 30(31): 4507-4514.

23. Oldenburg AL, Hansen MN, Zweifel DA, Wei A, Boppart SA. Plasmon-resonant gold nanorods as low backscattering albedo contrast agents for optical coherence tomography. *Opt. Express* 2006; 14(15): 6724-6738.

24. Faber DJ, Aalders MCG, Van Leeuwen TG: Curve fitting for quantitative measurement of attenuation coefficients from OCT images *Progress in Biomedical Optics and Imaging - Proceedings of SPIE* 2005; 5690:325-333.

25. Moes CJM, van Gemert MJC, Star WM, Marijnissen JPA, Prahl SA. Measurements and calculations of the energy fluence rate in a scattering and absorbing phantom at 633 nm. *Appl. Opt.* 1989; 28(12): 2292-2296.

26. Izatt JA, Hee MR, Owen GM, Swanson EA, Fujimoto JG. Optical coherence microscopy in scattering media. *Opt. Lett.* 1994; 19(8): 590-592.

27. Faber D, van der Meer F, Aalders M, van Leeuwen T. Quantitative measurement of attenuation coefficients of weakly scattering media using optical coherence tomography. *Opt. Express* 2004; 12(19): 4353-4365.

28. Zaccanti G, Bianco SD, Martelli F. Measurements of Optical Properties of High-Density Media. *Appl. Opt.* 2003; 42(19): 4023-4030.

29. Marchesini R, Bertoni A, Andreola S, Melloni E, Sichirollo AE. Extinction and absorption coefficients and scattering phase functions of human tissues in vitro. *Appl. Opt.* 1989; 28(12): 2318-2324.

30. Cheong WF, Prahl SA, Welch AJ. A review of the optical properties of biological tissues. *Quantum Electronics, IEEE Journal of* 1990; 26(12): 2166-2185.

31. Lin AW, Lewinski NA, West JL, Halas NJ, Drezek RA. Optically tunable nanoparticle contrast agents for early cancer detection: model-based analysis of gold nanoshells. *J Biomed Opt* 2005; 10(6): 064035.

CHAPTER EIGHT

SMALL ANIMAL TUMOR IMAGING *IN VIVO*

Abstract

The results of the phantom study described in Chapter 7 implies that contrast enhancement can be controlled by the dosage administered to the tissue of interest, which is essential towards optimizing a contrast enhancement procedure in OCT. In this chapter, the *in vivo* control of optical contrast in a mouse tumor model is examined. Gold nanoshells were administered into mice via intratumoral or intravenous (i.v.) delivery. In the case of i.v., the injected dosage and particle surface parameters were further varied and the level of gold nanoshells localization in tumor under these variations were determined using the noninvasive theoretical OCT modeling technique described in Chapter 7. Compared to intratumoral delivery, i.v. delivery of pegylated gold nanoshells allows a moderate amount of gold nanoshells in tumor to achieve a good enhancement to OCT signal with minimal signal attenuation deeper into the tissue. Further increases in the i.v. dosage of gold nanoshells reveal a corresponding nonlinear increase in their tumor localization as well as a nonlinear reduction in the percentage of injected gold nanoshells that localizes in the tumor. Furthermore, this percentage is improved with the use of appropriate anti-EGFR surface functionalization, which not only facilitates a more specific active targeting to the cancer marker of interest, but also simultaneously reduces the time required for effective tumor delivery from 6 h to 2h. The work presented in this chapter has been accepted for publication in *Journal of Biomedical Optics 2009*.

8.1 Introduction

In biomedical imaging of tissue, it is often desirable to enhance the signal measured from specific structures. For most imaging modalities, the effectiveness of medical images has been enhanced with the aid of contrast agents. Contrast agents are often used to increase the diagnostic and analytical capabilities of imaging modalities by site-specific labeling of tissues of interest. They have been successfully utilized in almost every medical imaging techniques.

These agents selectively localize at specific organ sites or tissues of interest to produce specific image signatures. By targeting contrast agents to a specific tissue of interest, the imaging contrast between different cells and tissues can be increased over their inherent optical properties to provide a clear demarcation between normal and pathological tissues. Therefore, a selective optical agent would be useful to detect subtle changes in tissue morphology, better differentiate tissue types with similar scattering properties, and identify early cancerous changes in human tissues that are morphologically similar to surrounding normal tissues.

This above true for OCT, where the use of contrast agents offers the promise of enhanced diagnostic power to overcome the limitation of relying on inherent optical properties to discriminate pathology. Inasmuch as OCT detects scattering changes, this image contrast enhancement can be achieved by delivery of highly scattering contrast agents such as gold nanoshells into the tissue and allowing the agents to attach to specific regions of interest. Thus, the tissues with injected contrast agents scatter more light back from regions of interest and produce a stronger OCT signal, which is detected to form a contrast-enhanced OCT image. The efficiency of using

gold nanoshells in enhanced OCT imaging has been demonstrated in previous published studies [1-3].

O'Neal et al. reported on the use of polyethylene glycol coated gold nanoshells (≈ 130 nm in diameter) that localized in the tumor passively after i.v. injection [4] due to the enhanced permeability and retention (EPR) effect, by which nanoscale materials are preferentially deposited in tumors (as opposed to normal tissue) as they passively extravasate through the leaky and aberrant tumor vasculature [5, 6]. This nanoparticle localization within the tumor can be detected by its optical contrast under OCT.

However, gold nanoshells may also be tailored to adhere to specific molecules, cells, or tissue types, and thus provide additional selectivity that can further enhance *in vivo* delivery of gold nanoshells quantities that are suitable for imaging. This form of active targeting is effected through appropriate surface functionalization, for example by conjugation with antibody or proteins to facilitate extravasation from tumor blood vessels as well as extravascular transport through the interaction between tumor cell surface receptors and receptor ligands attached to gold nanoshells.

Despite the successful demonstration of gold nanoshells as an OCT contrast agent, there are at least three identified issues that should be addressed for a more effective imaging *in vivo*. Firstly, the available *in vivo* experimental data are insufficient for developing an appropriate contrasting procedure since detailed parametric studies such as dosage of gold nanoshells administered have not been performed to demonstrate control of optical contrast *in vivo*.

Secondly, while passive targeting of macromolecular anticancer drugs has been studied in detail, less is known about the dynamics of EPR for metal nanoparticles *in vivo* primarily due to the lack of techniques to monitor them in a tissue noninvasively. For example, the current standard method to measure gold nanoshells concentrations in tissue is neutron activation analysis (NAA) [7] which requires tissue excision, dehydration, and irradiation within a nuclear reactor. While extremely sensitive, this method is invasive, and thus, does not allow for longitudinal monitoring of metal nanoparticles distribution in living systems.

Thirdly, although improvement in optical contrast of tumor cells has been demonstrated *in vitro* using various shapes of immuno-gold nanoparticles, including spherical gold nanoshells [1], gold nanocages targeted to HER-2/*neu* receptors [8] and gold nanorods targeted to EGFR [9], active targeting of gold nanoshells capable of mediating a more specific improvement in optical contrast *in vivo* has not yet been reported to date.

In this chapter, the promising use of gold nanoshells as a contrast agent in OCT imaging is further examined in an *in vivo* model with the aim to address the issues described above. The control of optical contrast in tumors grown in a murine *in vivo* model is demonstrated through three approaches: 1. The use of different modes of gold nanoshells delivery into tumor tissue, 2. Variations in concentration of injected gold nanoshells via i.v. and 3. The use of active targeting with appropriate antibody surface functionalization compared to passive targeting. A noninvasive technique to determine the gold nanoshells concentration in tumor tissue of live mice based on the theoretical modeling of OCT backscattering signal profile is also developed and

described. Using this technique, the concentration of gold nanoshells in the tumor tissue for each of the delivery condition is estimated and cross-examined with the optical contrast in imaging to allow a better understanding of the dynamics of tumor delivery under different circumstances.

The studies described in this chapter builds on the results of the phantom model discussed in the previous chapter. The Intralipid tissue phantom with different concentrations of gold nanoshells added provides insights on the possible changes in OCT image contrast that may occur *in vivo* with different delivery modes and concentration variations of nanoshells since it accurately models the different levels of gold nanoshells localization. Two modes of gold nanoshells delivery into the tumor model *in vivo* are examined in this chapter, namely intratumoral and i.v. injection which delivers contrasting amounts of gold nanoshells to the tumor.

A covalent conjugation method was previously developed [10] to enable the synthesis of monoclonal antibody conjugated gold nanoshells with excellent colloidal stability. The selective targeting of epidermal growth factor receptor (EGFR) positive cancer cells *in vitro* using anti-EGFR monoclonal antibody has also been demonstrated in chapter 6 [11, 12]. EGFR is a transmembrane glycoprotein that is frequently overexpressed in a variety of solid tumors including cancers of the brain, breast, colon, head and neck, lung, ovary, and pancreas [13-15], and is used as a selected cancer marker for imaging in this study. The results showing a successful demonstration of the control of optical contrast and estimation of gold nanoshells concentration in tumors *in vivo* is briefly discussed.

8.2 Materials and methods

8.2.1 Preparation of anti-EGFR conjugated gold nanoshells

Gold nanoshells were synthesized and pegylated for passive targeting as described in preceding chapters and the antibody conjugation was performed on the synthesized gold nanoshells as described in Chapter 6.2.2. Both the pegylated and antibody conjugated gold nanoshells were then rinsed before being redispersed in 2 ml of phosphate buffer solution (1X PBS, pH 7.4) to a final concentration of 2.0 x 10^{13} particles/ml as determined by correlating its extinction spectroscopy data to the theoretical extinction cross section data of the gold nanoshells based on Mie theory. The synthesized gold nanoshells were stored at 4°C until further use.

Gold nanoshells with a 162 nm diameter silica core surrounded by a gold shell of 23 nm thickness were synthesized and used for subsequent study. The TEM image which shows the particle size in Figure 8.1a was obtained using a transmission electron microscopy (TEM) (Jeol JEM-1010) operating at 100 kV. This size configuration was selected based on an optimized backscattering cross-section at 840 nm as predicted from Mie theory described in Chapter 2. Their extinction spectrum in Figure 8.1b was measured using a UV-Vis spectrophotometer (Shimadzu UV-2401 PC) in the wavelength range from 400 nm to 900 nm. The measured spectrum shows a peak surface plasmon resonance at 765 nm which compares well to the theoretically predicted spectrum determined from a program written in MATLAB that calculates the theoretical optical spectra of core-shell structures based on Mie theory for a single gold nanoshell of the same size configuration [16]. This peak wavelength is also close to the operating wavelength of the OCT system to generate a large optical extinction in the gold nanoshells when excited by the light source.

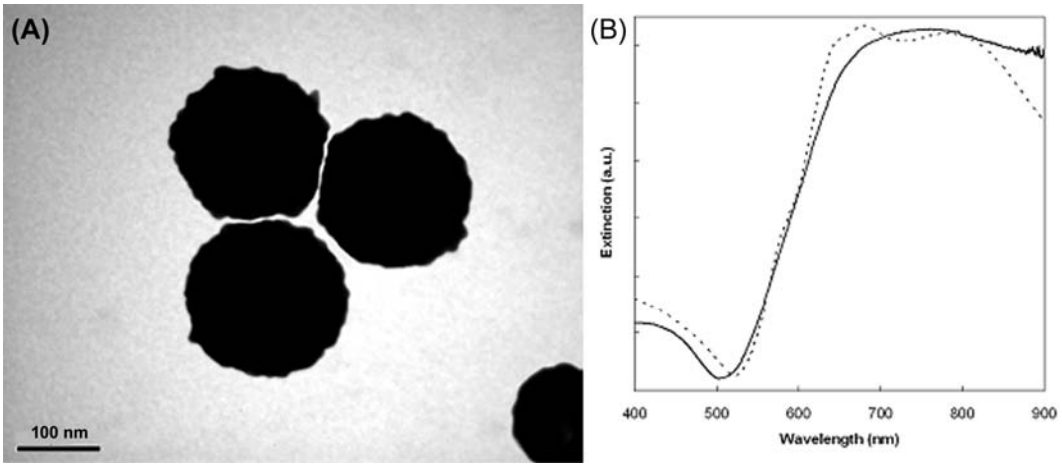

Figure 8.1. (a) Electron micrograph of synthesized gold nanoshells with an 81 nm radius dielectric silica nanoparticle core and 23 nm thick gold shell. (b) Measured UV-Vis extinction spectrum of the synthesized gold nanoshells (solid line). The theoretically calculated extinction spectrum of gold nanoshells of the same dimension as derived from Mie theory is shown for comparison (dotted line).

8.2.2 Mouse xenograft tumor model

The mouse xenograft tumor model used in this study was developed on male Balb/c nude mice obtained from the Animal Resource Centre (ARC, Western Australia). The mice were 6-8 weeks of age and weighed an average of 24-25 g. Approximately 5.0×10^6 human epidermoid carcinoma cell line, A-431 (ATCC) suspended in 150 µl of Hanks' balanced salt solution (HBSS) (Gibco, USA) were injected subcutaneously into the lower flanks of the mice to establish the xenograft tumor model. A-431 cells are widely known to overexpress EGFR, which is the selected cancer marker used in this study. The expression of EGFR in A-431 cells compared to other cancer cell types as well as normal cells is shown in Figure 1.4. The tumors were allowed to grow to 5–6 mm in diameter as measured using a vernier caliper approximately after 14 days of inoculation before OCT imaging was carried out. All handling procedures for mice were approved by the Institutional Animal Care and Use Committee (IACUC) at SingHealth, Singapore, in accordance with international standards.

8.2.3 Gold nanoshells delivery into mice

Prior to imaging, the pegylated gold nanoshells were suspended in HBSS to various concentrations and administered into the mice via intratumoral or i.v. injection. For the intratumoral injection, the mouse was first anaesthetized before 150 µl of the gold nanoshells (9.0×10^{10} particles/ml) was directly injected with care about 2 to 3 mm into the tumor. The injection was performed in at most two injection sites within the tumor to minimize leakage. For the i.v. delivery, 150 µl of the pegylated gold nanoshells of four different concentrations: 1.1×10^{10}, 2.3×10^{10}, 4.5×10^{10} and 9.0×10^{10} particles/ml were injected into the tail vein and allowed to circulate for 6 h for passive targeting to tumor before the mouse was anaesthetized for imaging. As a comparison between passive and active antibody targeting, 150 µl of anti-EGFR conjugated gold nanoshells with a concentration of 9.0×10^{10} particles/ml were also injected into the tail vein and allowed to circulate for 2 and 6 h prior to imaging to investigate and compare their longitudinal accumulation in tissue. For each of the test condition, the OCT measurements were performed in triplicates i.e. n = 3.

8.2.4 Mouse tumor imaging

The mouse tumor imaging was done with a commercial OCT system from Bioptigen, Inc. (Durham, NC) which is described in detail in Chapter 7.2.3. During the imaging procedure, the skin covering the tumor was removed to create an open tumor window as shown in Figure 8.1 that allowed the underlying tumor and the tumor-skin interface to be imaged. The normal skin adjacent to the tumor was also imaged as a reference. A coverslip was positioned on top of the exposed tumor to remove the uneven contour for imaging. The space in between was immerse with glycerol to provide index

matching to reduce specular reflective artifact at the tissue-glass interface. The OCT probe was placed directly on top of the coverslip and the tumors were vertically positioned and imaged with the top surface of the coverslip at 200 μm from the top of the OCT image screen for standardization.

Figure 8.2. OCT imaging of the tumor with the skin covering the tumor being removed to create an open tumor window that allows the underlying tumor and the tumor-skin interface to be imaged.

The scanning was done under B-mode imaging with 1,000 axial A-scans to give an overall lateral scan range of 6 mm per B-scan frame and the imaging depth was about 1.5 mm. All the 1,000 columns of axial A-scans from each B-scan were also averaged to obtain an average A-scan profile for further analysis. As each test condition were performed in triplicates i.e. n = 3, the A-scan profile for each of the mouse measurement was further averaged to obtain the mean A-scan profile of the triplicates for further analysis. All parameters including focus position and software constants remained the same throughout the entire study.

8.2.5 Tumor tissue examination for gold nanoshells

The imaged tumor tissues were examined for gold nanoshells using Hematoxylin and Eosin staining and confocal reflectance microscopy. Cryosections of 10 μm thickness

at the site of imaging were obtained using a microtome cryostat (Cryo-Star HM 560MV, Germany) and the tissue sections were mounted onto slides. Sections were then counterstained with a combination of Harris' hematoxylin and eosin, dehydrated in ascending grades of alcohol, mounted onto a coverslip with DePex as the mounting medium, and sealed with nail varnish prior to imaging.

Images from the slides were obtained using the Olympus CK40 microscope with a 20X objective and were captured in brightfield mode using the image processing software (Kontron KS400, version 3.0, Hallbergmoos, Germany). For confocal reflectance microscopy, the sectioned tissues were imaged using a laser scanning confocal microscope (Carl Zeiss LSM510 Meta) under confocal reflectance mode with an Olympus 20X objective. The confocal reflectance microscopy was performed under 633 nm excitation with a helium neon laser.

8.2.6 OCT theoretical curve fitting and analysis

In the analysis of OCT signal, the multiple scattering theoretical OCT model based on the extended Huygens-Fresnel (EHF) theory was used to fit the measured average A-scan profile to extract the μ_s of the sample under measurement [17]. This model accounts for both single and multiple scatterings in the sample and is thus able to fit well into the average A-scan profile for a wide range of μ_s including those used in this study. The detected signal intensity as a function of the optical axial depth in the theoretical OCT equation is given by Equation 7.1.

The curve fitting process utilized a non-linear least square fit of the data to Equation 7.1. For fitting of tumor tissue, the anisotropy factor of tumor tissue was set to 0.7 to

give a θ_{rms} of 0.77. The θ_{rms} value for gold nanoshells were not considered in the fitting as the volume fraction of gold nanoshells in the tumor is assumed to be negligible to cause any change in the overall scattering angle when added into tissue.

Since the system parameters such as the focal length, beam waist, source wavelength and refractive index of the sample are known *a priori*, the fitting process only involved μ_t. It is also known that the total tissue extinction coefficient is the sum of the absorption and scattering coefficient i.e. $\mu_t = \mu_a + \mu_s$. For most tissues, the absorption is often assumed to be negligible i.e. $\mu_t \approx \mu_s$ since the intrinsic tissue absorption is known to be very small around the source wavelength. Hence, the OCT depth-dependent scattering has been modeled as a function of the scattering coefficient, μ_s of the medium instead of μ_t.

8.3 Results and discussion

8.3.1 Changes in optical contrast with different delivery modes

The gold nanoshells concentration window deduced from the phantom model in Chapter 7 suggests a relatively tight range of concentration that would require an appropriate delivery mode to deliver the right amount of gold nanoshells for effective tumor contrast enhancement *in vivo*. The significance of such an appropriate delivery is demonstrated by delivering gold nanoshells via two different modes into the tumor: intratumoral and i.v. These two delivery modes deliver different amount of gold nanoshells to the target tumor, resulting in different levels of gold nanoshells localization in tumors.

The OCT images in Figure 8.3 were acquired at the interface between the tumor and surrounding normal skin tissue. Compared to tumor tissue without the presence of gold nanoshells, a large amount of gold nanoshells delivered to the tumor via intratumoral injection shows at least two distinct changes in the OCT images. Firstly, the OCT signal attenuates rapidly with depth to result in a loss of image brightness deeper into the tissue. This is accompanied by a signal intensity enhancement at the tissue surface. The overall visual effect is a bright but narrow signal band at the sample surface atop a dark region arising from the highly attenuated OCT signal. This characteristic bright surface enhancement on top of a highly attenuated signal region is similar to that observed in the earlier phantom study with a high gold nanoshells concentration of 9.0 x 10^{10} particles/ml in Intralipid (Figure 7.8).

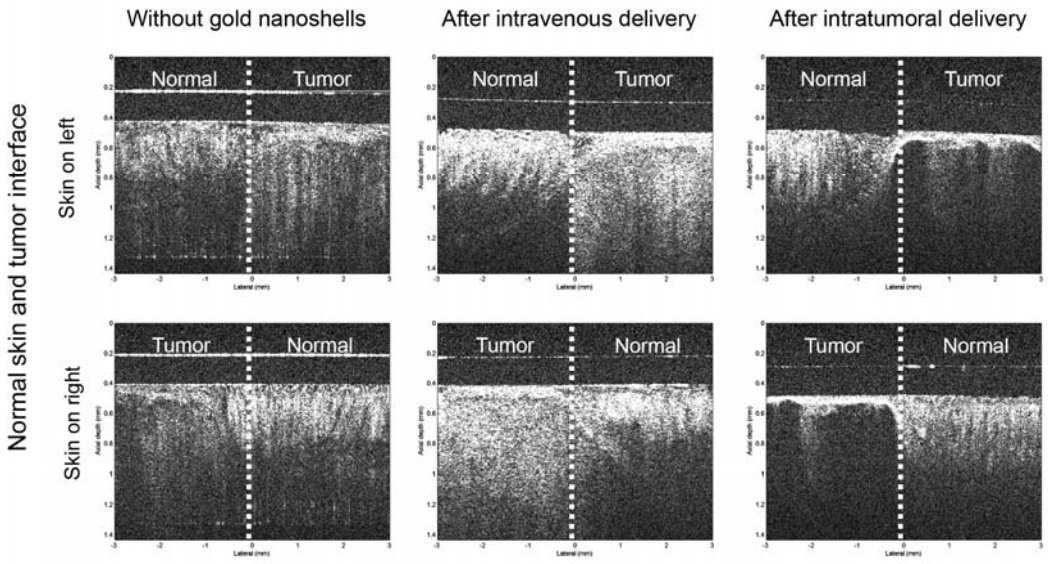

Figure 8.3. OCT images of the interface between normal peripheral skin and tumor tissue of mouse model prior to and after i.v. and intratumoral gold nanoshells delivery. The horizontal reflective surface shown on top of the tissue arises from the coverslip used to remove the uneven tissue contour for imaging. The top row of images show the skin on the left of the interface while the bottom row of images show the skin on the right of the interface.

With a large amount of gold nanoshells delivered to the tumor via intratumoral injection, the incident light entering the tumor experiences a high level of scattering near the surface due to the presence of gold nanoshells scatterers, which reduces its mean free path. The amount of single backscattered light that collectively contribute to the overall backscattered light is also higher due to a higher concentration of particle scatterers, thus accounting for the strong OCT signal enhancement near the tissue surface as observed in Figure 8.3. With a significant amount of light backscattered out of the tissue, the amount of light that reaches deeper into the tissue is reduced, which explains the significant signal attenuation with depth.

However, for a moderately small amount of gold nanoshells localized in the tumor after i.v. delivery, the OCT signal intensity from the tumor is generally increased more uniformly with depth with slower signal attenuation with depth into the tissue. This change is similar to that observed in the phantom model with a moderate 5.6 x 10^9 particles/ml of gold nanoshells in Intralipid (Figure 7.8). In this case, the incident light entering the tumor experiences a longer mean free path that allows them to reach deeper into the tissue, thus reducing the signal attenuation with depth. Consequently, the amount of single backscattered light near the tissue surface is reduced, thus giving a weaker signal enhancement there compared to intratumoral delivery.

The differences in OCT images between i.v. and intratumoral delivery of gold nanoshells implies the need for an appropriate delivery mode to deliver the desired amount in tissue. This is because different delivery modes would deliver different amount of gold nanoshells to the target tissue and hence produce varying effect on the contrast enhancement as demonstrated in the two cases earlier. Both of the delivery

modes used in this study are commonly used to deliver therapeutic compounds to the target site of interest, which is the tumor in this case.

In intratumoral delivery, the bolus injection of a 9.0 x 10^{10} particles/ml dosage of gold nanoshells directly into the tumor causes a high concentration to localize there. On the other hand, the delivery of the same dose by i.v. results in a much lower amount of gold nanoshells passively reaching the tumor site via the Enhanced Permeation and Retention (EPR) effect. The exact concentration of gold nanoshells in the tumor for both cases is determined and discussed further in Section 8.3.4.

The reason for a much lower tumor localization after i.v. delivery is because a significant amount of injected gold nanoshells is either lost from the bloodstream during the circulation due to renal excretion or removal by the reticulo-endothelial system (RES) such as the liver. In this case, the liver of the mice before and after 6 h of gold nanoshells circulation is shown in Figure 8.4 below.

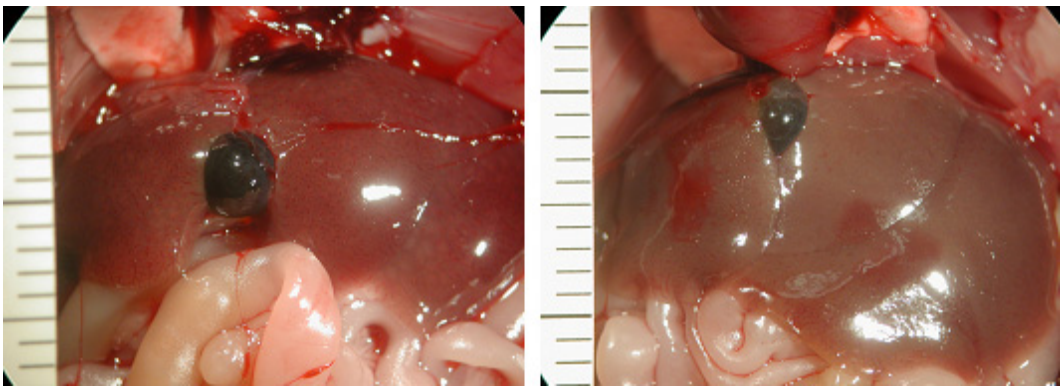

Figure 8.4. Liver of male balb/c nude mice before (left) and after (right) i.v. delivery of 150 µl of gold nanoshells (9.0 x 10^{10} particles/ml) with 6 h of vascular circulation.

The RES removal of gold nanoshells by the liver causes the gold nanoshells to accumulate and result in a dull brown coloration in the liver. The removal of gold nanoshells by RES is inevitable despite their pegylation since pegylation only serves to minimize the RES uptake as discussed in Chapter 5. The instability of the gold-monothiol interaction between the gold surface and mPEG-thiol tether after prolonged circulation in the biological environment such that the PEGs are easily detached from the gold nanoshells may have contributed significantly towards the RES uptake.

In terms of its efficacy in improving the tumor contrast with the surrounding normal tissue, Figure 8.3 shows that i.v. delivery of gold nanoshells seems to improve the visibility of tumor compared to intratumoral delivery. In addition to improvement in tumor visibility, the OCT images also show that the tumor margin between the tumor and adjacent normal skin tissue is also more clearly demarcated.

In both delivery modes, the amount of gold nanoshells that localizes in the surrounding normal skin tissue is insignificant to warrant any observable change in the OCT signal intensity compared to the tumor. This is because the gold nanoshells injected directly into the tumor via intratumoral delivery are unable to diffuse out of the tumor to the surrounding skin tissue sufficiently via the interstitial space or the capillary circulation within the 6 h of circulation. Furthermore, the blood vessels supplying gold nanoshells to the non-cancerous normal tissue are also not sufficiently porous to facilitate the migration of gold nanoshells out of the bloodstream and into the skin tissue after i.v. delivery. Because of their preferential localization in the tumor, the gold nanoshells are therefore able to elicit an optical contrast to discriminate the tumor from surrounding normal tissue.

8.3.2 Changes in average A-scan profile

The changes in the OCT images with different modes of gold nanoshells delivery described above can be characterized by changes to the scattering coefficient, μ_s of the tumor tissue, which in turn, can be extracted from the average OCT A-scans of the tissue. This will be discussed in more detail in the following section 8.3.3. The average A-scan profile of the tumors prior to and after i.v. and intratumoral delivery of gold nanoshells is shown in Figure 8.5.

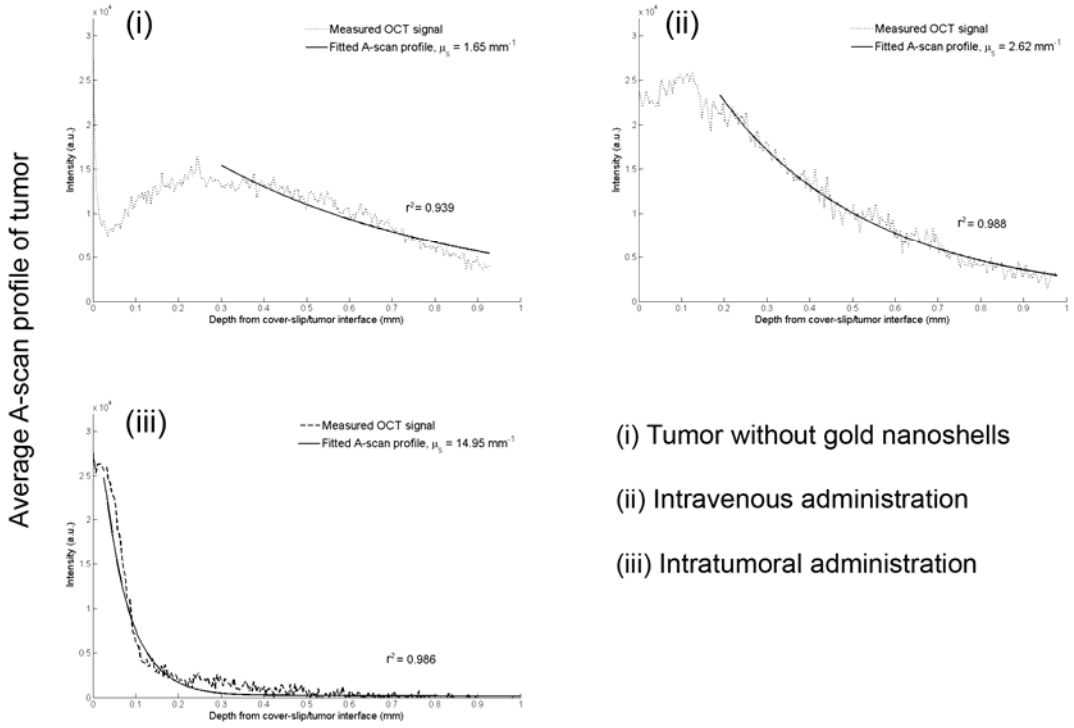

Figure 8.5. Average A-scan profiles of the mouse tumor tissue (i) prior to gold nanoshells delivery i.e. tumor without gold nanoshells and after (ii) i.v. and (iii) intratumoral delivery of 150 µl pegylated gold nanoshells (9.0 x 10^{10} particles/ml) colloid. The measured OCT signal is shown in dotted line while the non-linear least square fit of the data based on the multiple scattering EHF theory is shown in solid line superimposed, giving an extracted μ_s of the composite gold nanoshells in tumor tissue of (i) 1.65 mm^{-1}, (ii) 2.62 mm^{-1} and (iii) 14.95 mm^{-1}. In all three fittings, the coefficient of determination, $r^2 > 0.90$.

Compared to the average A-scan profile of tumor tissue without gold nanoshells, the inclusion of gold nanoshells in tumor after i.v. delivery causes an increase in the OCT signal intensity mainly at the top 200 μm of tissue while the signal attenuation with depth as given by the slope of the depth-dependent OCT signal becomes slightly more pronounced. This depth related attenuation is relatively small compared to that by intratumoral delivery where the large amount of gold nanoshells delivered to the tumor causes the signal in the average A-scan to attenuate rapidly with depth.

The OCT images and histological tissue sections corresponding to the A-scan profiles acquired from the same scanned site are shown in Figure 8.6 below. The OCT images of adjacent normal skin tissue are also shown as a reference. The changes in the average A-scan profile with different modes of gold nanoshells delivery are well reflected in the corresponding OCT images (Figure 8.6a) and have been described earlier. The corresponding histological tissue sections after H & E staining in Figure 8.6b show the localization of the gold nanoshells in the tumor tissue. Despite their nanoscale sizes smaller than the resolution limit of conventional light microscope, the sudden intratumoral bolus injection of gold nanoshells forces them to be highly concentrated in the tumor tissue to the point of aggregation where these nanoparticle aggregates become observable under the light microscope.

With a slower delivery of gold nanoshells to the tumor via i.v., the quantity of gold nanoshells that localizes in the tissue is smaller and the gold nanoshells are more uniformly scattered with a much reduced aggregation within the tumor tissue. In fact, their presence in tumor can hardly be discerned visually from the tissue section since the sizes of these nanoparticles are beyond the resolution limit of the light microscope

used, except in isolated instances of aggregation. In both cases, the gold nanoshells seem to be distributed evenly throughout the tumor tissue with no preferential localization in any part of the tissue.

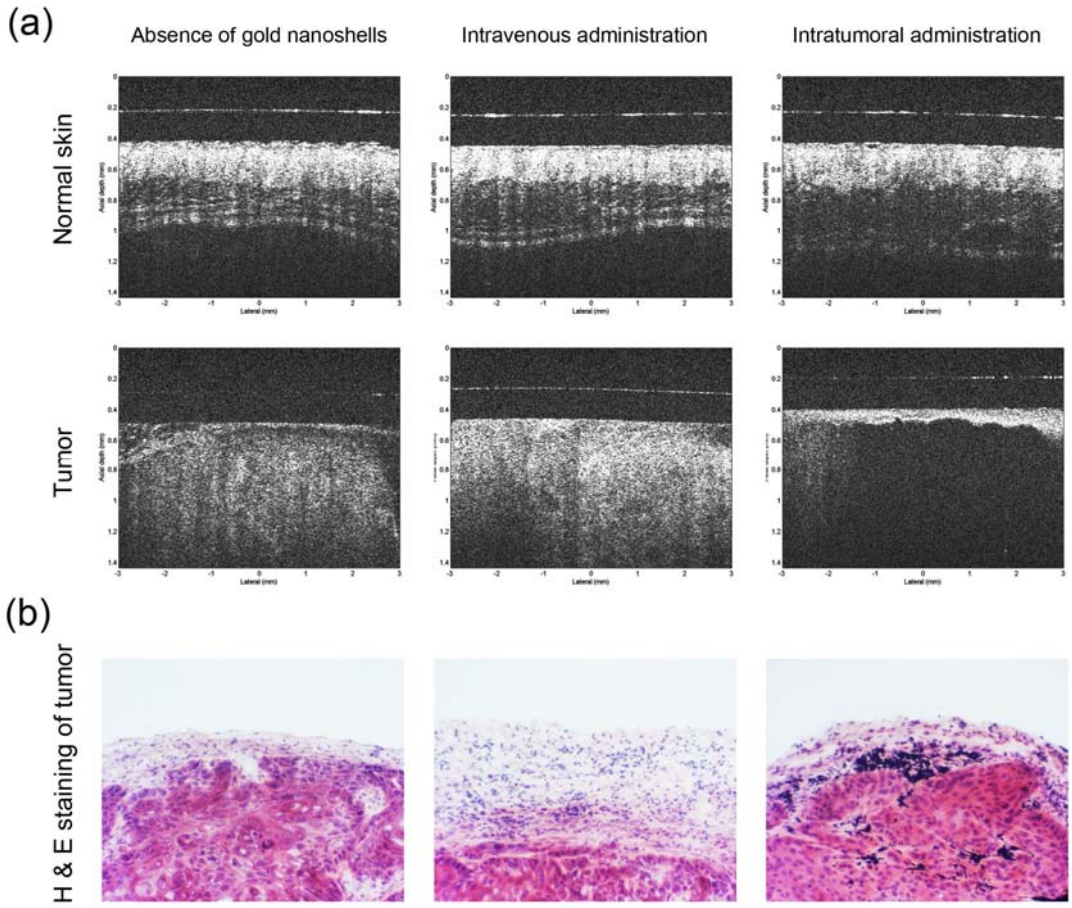

Figure 8.6. (a) OCT images of normal skin (top row) and tumor tissue (bottom row) of mouse model prior to gold nanoshells delivery i.e. tumor without gold nanoshells and after i.v. and intratumoral gold nanoshells delivery. The horizontal reflective surface shown on top of the tissue arises from the coverslip used to remove the uneven tissue contour for imaging. (b) Histological tissue sections of the tumor after H & E staining for tumor without gold nanoshells (left) and tumor post i.v. (middle) and intratumoral (right) gold nanoshells delivery. The H & E stained tissue sections show the localization of the gold nanoshells in the tumor tissue. Images were acquired with a 20X objective.

8.3.3 Determination of tissue μ_s

The average A-scan profiles allow the extraction of overall $\mu_{s,GNS\ in\ tumor}$ of the tumor with embedded gold nanoshells (GNS in tumor) by means of a non-linear least square curve fitting of the theoretical OCT model [17]. In general, the theoretical optical characterization of OCT has been studied by several groups and a few theoretical models have been established to relate the sample optical parameters to its corresponding A-scan profile [17-19] with the aim to extract out the parameters for diagnostic purposes such as diabetic glucose sensing [20].

Previous studies have shown that the negative gradient of the average A-scan profile is a function of sample μ_t [21, 22]. In this case, the μ_t refers to $\mu_{t,GNS\ in\ tumor}$. As μ_t increases, the slope of the depth attenuation profile also increases. Since biological tissues as well as gold nanoshells are known to be scattering dominant with negligible absorption i.e. $\mu_{a,GNS\ in\ tumor} \approx 0$, the extracted $\mu_{t,GNS\ in\ tumor} \approx \mu_{s,GNS\ in\ tumor}$ of tissue. Therefore, the slope of the average A-scan profile determines the $\mu_{s,GNS\ of\ tumor}$ of the tissue being examined.

The $\mu_{s,GNS}$ contributed by gold nanoshells alone in the tumor can then be derived simply by subtracting the $\mu_{s,tumor}$ of tumor tissue from $\mu_{s,GNS\ in\ tumor}$ [23] according to the following equation:

$$\mu_{s,GNS} = \mu_{s,GNS\ in\ tumor} - \mu_{s,tumor} \tag{8.1}$$

The results of the curve fitting on the average A-scan profiles in Figure 8.5 shows that the extracted $\mu_{s,tumor}$ of mouse tumor tissue without gold nanoshells is 1.65 ± 0.73 mm^{-1}, while the extracted overall μ_s of tumor after i.v. and intratumoral delivery of

gold nanoshells i.e. $\mu_{s,GNS\ in\ tumor}$ are 2.62 ± 0.23 mm^{-1} and 14.95 ± 0.65 mm^{-1} respectively. The post-subtraction $\mu_{s,GNS}$ contributed by gold nanoshells alone in tumor after i.v. and intratumoral delivery is then calculated to be 0.97 and 13.30 mm^{-1} respectively. It would be of worth to note here that the 1% Intralipid (extracted μ_s = 1.53 ± 0.16 mm^{-1}) used as a phantom model in Chapter 7 indeed models the mouse tumor tissue well, hence verifying that the phantoms can be used to model the actual small animal tissue accurately.

In the extraction of μ_s from the average A-scan profile, the importance of tissue homogeneity should not be understated. This is because the theoretical OCT model used to fit the A-scan profile was developed based on an optically homogenous sample whose entire signal profile can be fitted by a single equation. Heterogeneous samples with multiple layers or regions of different μ_s would require multiple equations to fit different layers individually thus rendering the single equation fitting inappropriate. For this reason, the average A-scan profile of normal skin with multiple stromal layers of different μ_s was not fitted to extract the "mean" μ_s of skin.

The tumor tissue, on the other hand, is often assumed to have homogenous optical properties [24]. Therefore, the μ_s of the tumor tissue can be extracted with a good degree of fit, having a coefficient of determination, r^2 = 0.94. In fact, the rest of the average A-scans in the small animal imaging were also well fitted with $r^2 > 0.97$ to provide an accurate extraction of μ_s. To enable the current technique to be more robust for multilayer tissue, further studies are needed to develop an analysis algorithm that would accurately extract out the μ_s of individual layers.

8.3.4 Determination of gold nanoshells concentration

The extracted μ_s contributed by gold nanoshells alone in tumor tissue allows its concentration in the tumor to be deduced through the following theoretical relationship:

$$\mu_s = \rho A Q_{sca} \quad (8.2)$$

where ρ is the concentration of the synthesized gold nanoshells in particles/ml, A is its geometric cross section and Q_{sca} is the scattering efficiency.

With a constant gold nanoshells size configuration (81 nm core radius and 23 nm shell thickness) of $A = 3.40 \times 10^{-14}$ m^2 used in this study and a Q_{sca} of 4.58 at 840 nm based on theoretical calculations, μ_s scales linearly with concentration and the relationship can be further simplified to:

$$\mu_s = 1.556 \rho \times 10^{-10} \text{ mm}^{-1} \quad (8.3)$$

This linear relationship allows for a good estimation of any unknown concentration of gold nanoshells in tissue given its extracted μ_s. In both cases described above, the gold nanoshells concentration in the tumor after i.v. and intratumoral delivery is approximately 6.2×10^9 and 8.5×10^{10} particles/ml respectively. This estimated concentration suggests that 94.4 % of the intratumoral dose administered reaches the tumor while only about 6.9 % of the injected gold nanoshells eventually reached the tumor after i.v. delivery, which agrees well with other delivery studies [7].

Here, it is of worth to note that accuracy of the estimated concentration using this technique assumes that the absorption in gold nanoshells is small such that the extracted μ_t of gold nanoshells approximates its μ_s as in the case of the biological tissue. This is true given that the gold nanoshells of this size configuration are predominantly scattering as determined from Mie theory in Chapter 2.

In the subtraction of $\mu_{s,GNS\ in\ tumor}$ to obtain the $\mu_{s,GNS}$ in tissue, the scattering coefficient of tumor, $\mu_{s,tumor}$ is assumed to be 1.65 mm^{-1} (Figure 8.5) and this is used in all the analysis across different mice in this study. This value concurs with those reported in literature [25, 26] and is used although there may be some small variations in the scattering coefficients of tumor tissue which may affect the computation of the gold nanoshells concentration.

The use of Equations 8.2 and 8.3 also assumes the monodispersity of gold nanoshells in the tissue to give a narrow size profile centered around the experimental size configuration. In practice, the gold nanoshells do not remain in a monodisperse state in tissue since there is a tendency for them to aggregate to different degree as observed in the histological tissue sections in Figure 8.6. This aggregation occurs despite prior successful pegylation [27] *in vitro* and could possibly be attributed to the instability of the gold-monothiol interaction between the gold surface and mPEG-thiol tether in the tissue interstitial environment such that the PEGs are easily detached from the gold nanoshells. The aggregation of gold nanoshells results in changes to their optical properties. Such hypothesis is also discussed earlier to account for the high RES uptake of gold nanoshells.

Furthermore, the linear relationship between μ_s and particle concentration is limited; as studies with other particle scatterers such as Intralipid have shown that the relationship turns nonlinear at high particle concentrations due to the interparticle shadowing effects [28]. Nonetheless, the previous studies on Intralipid phantom models in Chapter 7 have shown that the measured μ_s of gold nanoshells appear to deviate only slightly from the theoretical linearity even at high concentrations. This linear region is thus sufficiently wide to allow an accurate gold nanoshell concentration to be determined over a wide range which includes that used in this study. Therefore, the deduced concentration from the μ_s is only an approximation that is highly subjected to the various physical properties of gold nanoshells e.g. size configuration, state of aggregation and concentration in tissue as discussed.

Despite the approximation, such a technique in determining the concentration of gold nanoshells in tissue from the OCT average A-scan profile holds possible applications in biodistribution studies and may allow concentration mapping of gold nanoshells for quantitative molecular imaging of certain crucial biomarkers associated with cancer, especially if the gold nanoshells are functionalized for specific antibody targeting to that identified biomarker as shown in this study.

8.3.5 Changes in optical contrast with concentration variations

The previous results suggest that i.v. delivery of gold nanoshells is effective for tumor contrast enhancement, having minimal signal attenuation with tissue depth compared to intratumoral delivery. The study on i.v. delivery is extended further to demonstrate that intravenous control of optical contrast in tumors is possible by varying the concentration of gold nanoshells injected. The mice were injected with a range of gold

nanoshells concentrations via i.v. (1.1 x 10^{10} to 9.0 x 10^{10} particles/ml) for passive targeting to tumor and the OCT images of the tumor after 6 h of vascular circulation is acquired.

The OCT images in Figure 8.7 show a gradual increase in the signal intensity especially from the top 300 μm region as the concentration of gold nanoshells injected increases. The signal attenuation with depth also becomes more slightly pronounced with increasing concentration.

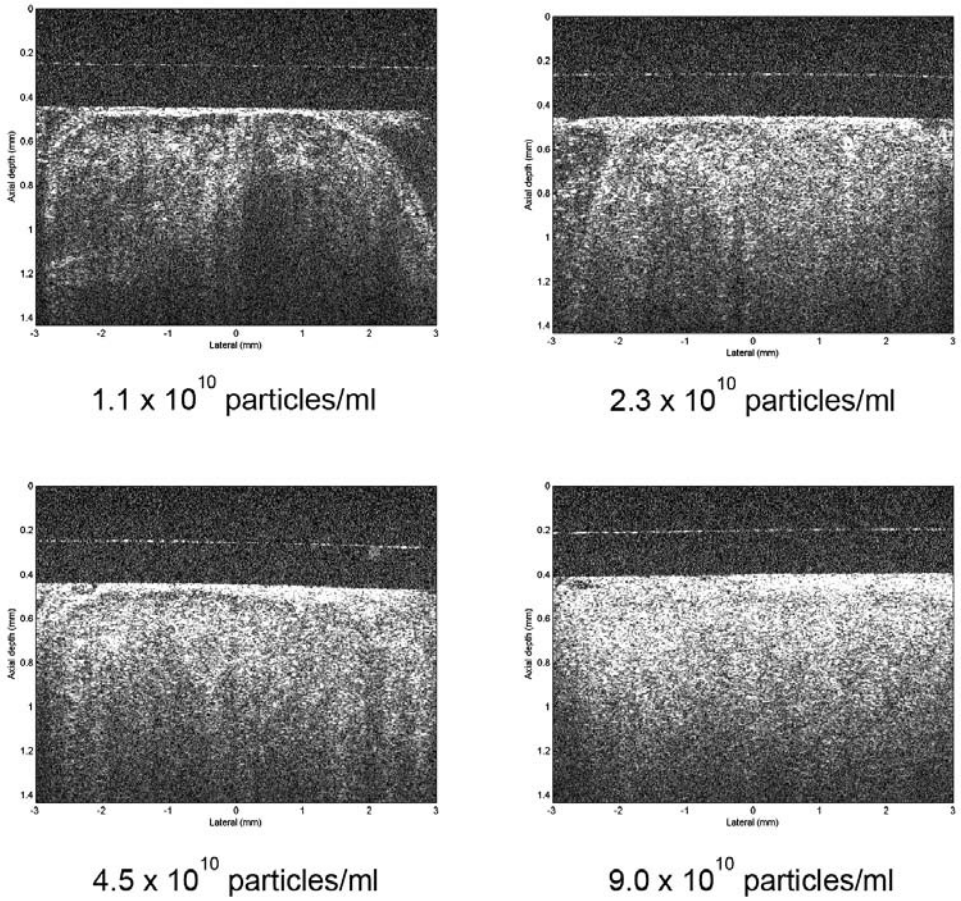

Figure 8.7. Changes in the OCT image after 6 h of vascular circulation for a range of gold nanoshells concentration (1.1 x 10^{10} to 9.0 x 10^{10} particles/ml) injected intravenously.

These changes are similarly observed in the corresponding average A-scan profiles after 6 h of vascular circulation as shown in Figure 8.8 where the negative slope of the depth-dependent A-scan curve increases together with an increase in the OCT signal intensity at the more superficial region as more gold nanoshells were being administered.

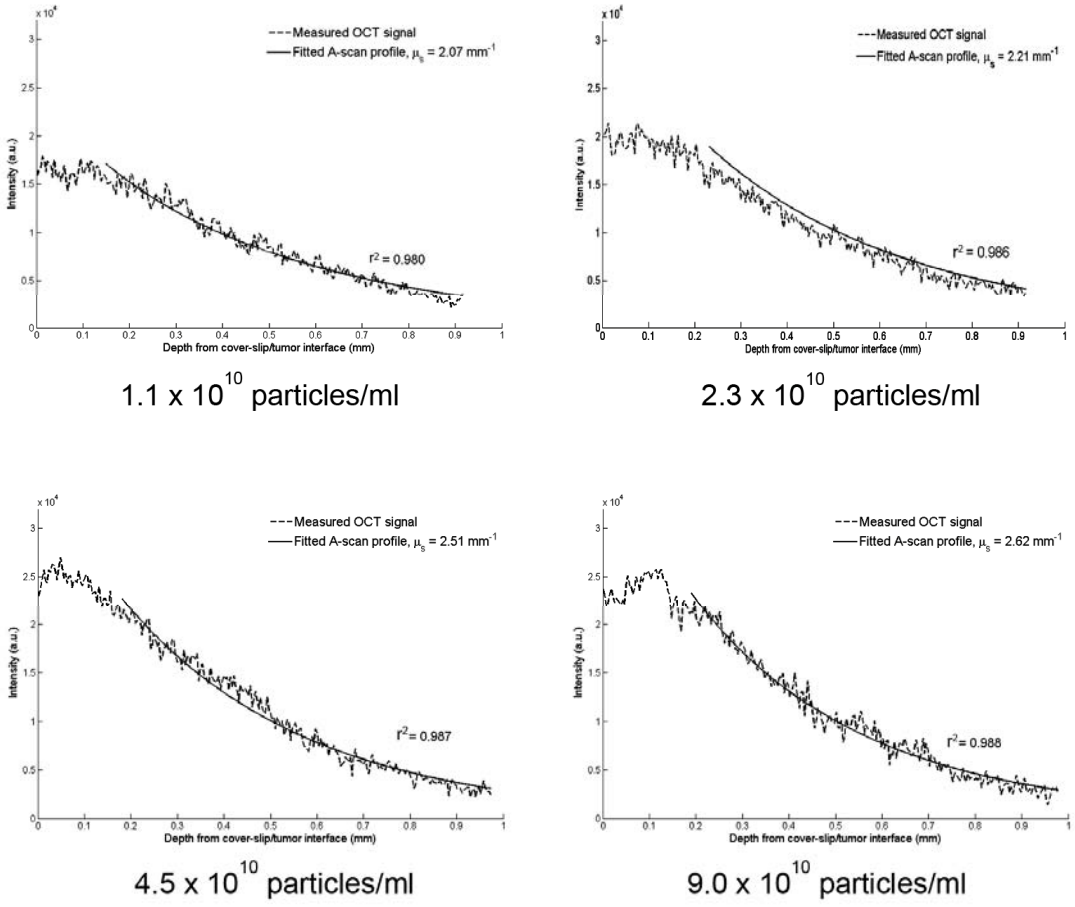

Figure 8.8. Changes in the average A-scan profile of mouse tumor tissue after 6 h of vascular circulation for a range of gold nanoshells concentration (1.1 x 10^{10} to 9.0 x 10^{10} particles/ml) injected intravenously. The measured OCT signal is shown in dotted line while the non-linear least square fit of the data is shown in solid line superimposed with the extracted μ_s.

The corresponding confocal reflectance images of the tissue sections acquired at the same imaging site as shown in Figure 8.9 further verify the increasing localization of gold nanoshells in the tumor tissue with an increasing dosage administered. Here, the reflectance signal arising from the gold nanoshells are pseudo-colored red. The confocal images show that the gold nanoshells localize in the tumor tissue to form random bright specks that are scattered with increasing amount in the tissue as the injected concentration increases. These visible bright specks are possibly due to the aggregation of the gold nanoshells in the tissue environment although the presence of noise from the tissue reflectance cannot be ruled out.

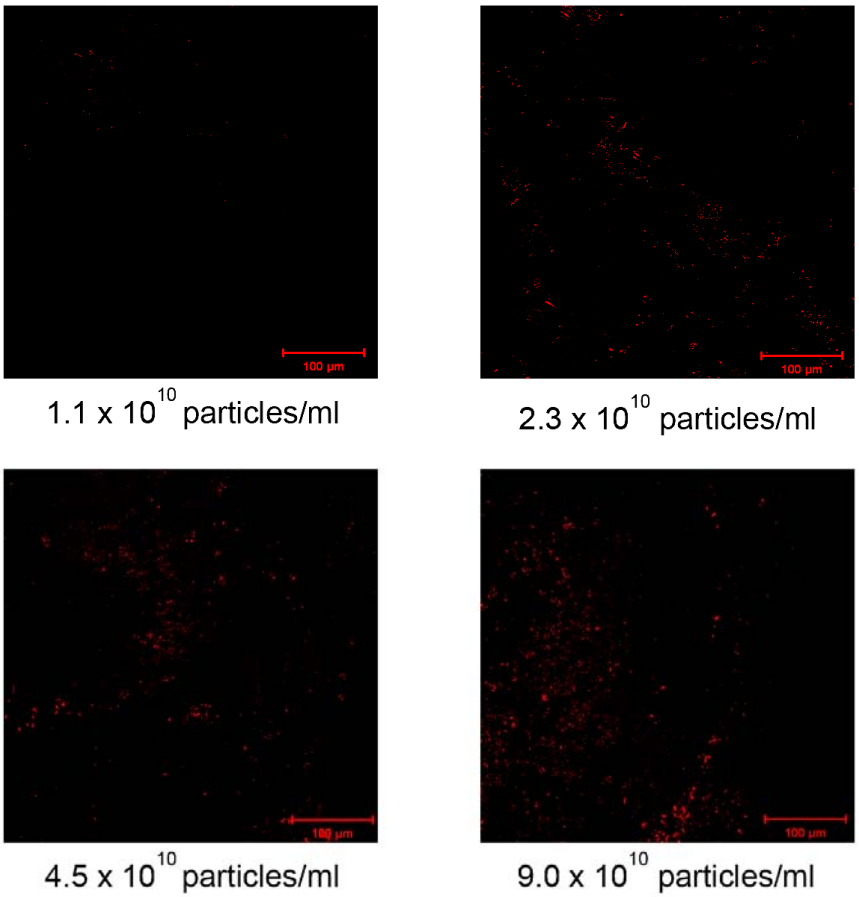

Figure 8.9. Changes in the confocal reflectance image of mouse tumor tissue taken from the OCT imaging site after 6 h of vascular circulation for a range of gold nanoshells concentration (1.1×10^{10} to 9.0×10^{10} particles/ml) injected intravenously. The confocal images were acquired under a 20X objective and the confocal reflectance microscopy was performed under 633 nm excitation.

The extracted μ_s of gold nanoshells laden tumor as determined from the theoretical curve fitting of the average A-scan profile for different gold nanoshells concentrations i.e. $\mu_{s,GNS\ in\ tumor}$ is indicated in Figure 8.8 and summarized in Table 8.1 below. The post-subtraction $\mu_{s,GNS}$ contributed by gold nanoshells alone in tumor shows that the scattering coefficient attributed to gold nanoshells and its estimated tumor concentration exhibit a positive correlation with the injected concentration although the relationship does not scale linearly with the amount of gold nanoshells injected as shown in Figure 8.10.

Table 8.1. Summary of extracted $\mu_{s,GNS\ in\ tumor}$ of gold nanoshells laden tumor as determined from the theoretical curve fit of average A-scan profile as well as the estimated gold nanoshells concentration in tumor for different concentration of gold nanoshells injected intravenously. In all cases, the tumor tissue μ_s of 1.65 mm^{-1} is subtracted from $\mu_{s,GNS\ in\ tumor}$ to obtain the $\mu_{s,GNS}$ due to gold nanoshells alone.

Concentration of gold nanoshells injected (particles/ml)	Extracted $\mu_{s,GNS\ in\ tumor}$ (mm^{-1})	Post-subtraction $\mu_{s,GNS}$ (mm^{-1})	Estimated gold nanoshells concentration in tumor (particles/ml)	Percentage of injected gold nanoshells that localize in tumor
1.1×10^{10}	2.07 ± 0.30	0.42 ± 0.30	$2.7 \pm 1.9 \times 10^{9}$	24.0 %
2.3×10^{10}	2.21 ± 0.31	0.56 ± 0.31	$3.6 \pm 2.0 \times 10^{9}$	16.0 %
4.5×10^{10}	2.51 ± 0.25	0.86 ± 0.25	$5.5 \pm 1.6 \times 10^{9}$	12.3 %
9.0×10^{10}	2.62 ± 0.34	0.97 ± 0.34	$6.2 \pm 2.2 \times 10^{9}$	6.9 %

However, when the estimated gold nanoshells concentration in the tumor is expressed as a fraction of the injected concentration, we observe that this fractional concentration actually decreases with increasing injected concentration to show a negative correlation. Likewise, this negative correlation does not scale linearly to the injected concentration. As the injected concentration increases eight-fold from 1.1×10^{10} to 9.0×10^{10} particles/ml, the fractional concentration of injected gold nanoshells that localizes in the tumor merely decreases about four-fold from 24.0 % to 6.9 %.

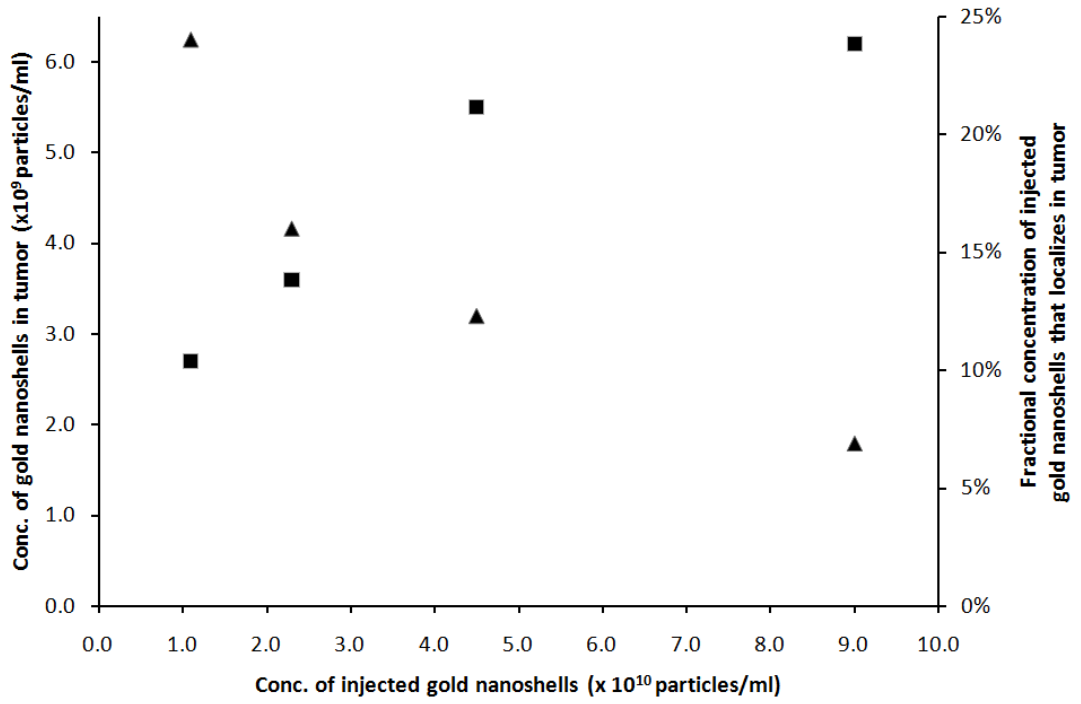

Figure 8.10. Nonlinear relationship between the concentration of gold nanoshells localized in tumor and the injected gold nanoshells concentration (-■-). The tumor concentration of gold nanoshells expressed as a fractional concentration of the injected gold nanoshells concentration (-▲-) is also plotted.

One clear observation that emerges from the trend observed above is a less responsive tumor localization at higher gold nanoshells dosage. The data could suggest a limiting concentration of gold nanoshells in the tumor at the 6 h time point based on a limiting rate of passive localization. This result shows that a higher dosing may not necessarily be more efficient in delivering the gold nanoshells to the tumor site despite being able to deliver a larger amount. An even larger percentage of gold nanoshells are wasted at higher injection dose.

The changes in OCT images and average A-scan profiles for increasing gold nanoshells content in the tumor agree well with the phantom model shown in Figure 7.8. The effect of different concentration of gold nanoshells in tumor on the OCT image holds several implications on the dosing of these nanoparticulate contrast agent

in living systems to control the OCT image enhancement. Therefore, it is imperative that the gold nanoshells dosage administered to the mouse can be controlled to establish an appropriate dosing regime so as to achieve a good compromise between OCT signal enhancement at the surface region and minimal signal attenuation deeper into the tissue. This control can be achieved based on the nonlinear relationship between the injected and localized amount arising from passive targeting as described earlier, which has not been reported to date and may be useful to further understand the dynamics of gold nanoshells passive localization in tumors.

8.3.6 Comparison between passive and active targeting

The percentage of injected gold nanoshells delivered to the tumor can be increased with appropriate antibody surface functionalization on the gold nanoshells to allow specific targeting to cancer markers of interest. By altering the dynamics of gold nanoshells tumor localization this way, active antibody targeting facilitates the control of optical contrast in tumors. The anti-EGFR conjugated gold nanoshells were injected i.v. into the mice at a concentration of 9.0×10^{10} particles/ml and allowed to circulate in the blood before OCT images of tumor were acquired after 2 and 6 h. The pegylated gold nanoshells without antibody functionalization were also injected with the same dosage in separate mice and monitored as a control for comparison.

The OCT images in Figure 8.11 show that the signal intensity at both 2 and 6 h for tumor targeted with anti-EGFR gold nanoshells is generally higher especially at regions nearer to the tissue surface compared to tumor targeted with pegylated gold nanoshells and the difference is more significant at 2 h time point. The signal

attenuation with depth is also slightly more pronounced with the anti-EGFR gold nanoshells compared to their non-antibody counterparts at both time points.

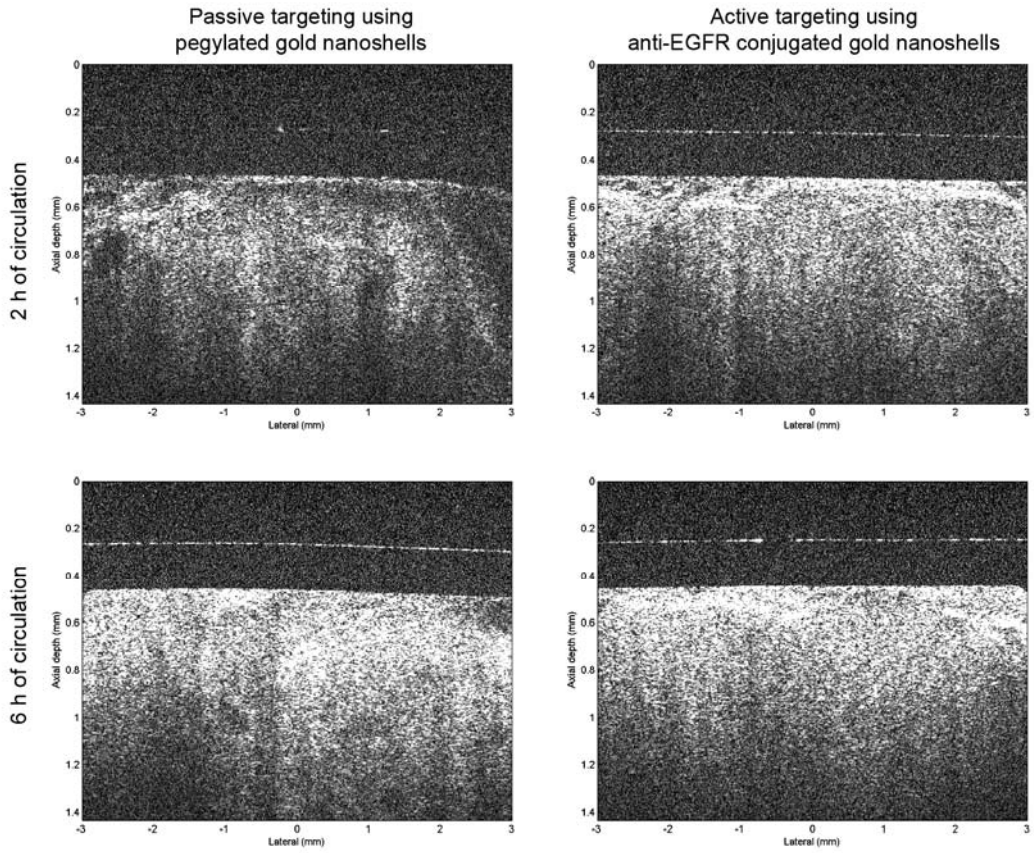

Figure 8.11. Comparison of the gold nanoshells localization in tumor tissue between passive targeting using pegylated gold nanoshells (left column) and active targeting using anti-EGFR conjugated gold nanoshells (right column) showing the changes in OCT images after 2 h (top) and 6 h (bottom) of gold nanoshells (9.0×10^{10} particles/ml) i.v. delivery.

Furthermore, the change in optical contrast of tumor from 2 to 6 h due to gold nanoshells localization is observable for both types of gold nanoshells, although the longitudinal signal change seems more apparent for the passively targeted pegylated gold nanoshells compared to the anti-EGFR targeted gold nanoshells. In the case of pegylated gold nanoshells, the increase in optical contrast over the tumor baseline i.e.

tumor without gold nanoshells is hardly observable at 2 h and would require another 4 h of circulation before the optical effect of gold nanoshells can be observed clearly. This is unlike the case of anti-EGFR gold nanoshells where the increase in optical contrast is already observable after 2 h and it continues to increase, albeit more slowly, during the next 4 h.

The average A-scans shown in Figure 8.12 below correspond to the OCT images in Figure 8.11. It shows the non-linear least square fit of the theoretical curve over the tumor data and the extracted $\mu_{s,GNS \text{ in tumor}}$ for all the four instances in Figure 8.11. From the post-subtraction $\mu_{s,GNS}$, the gold nanoshells concentration in tumor is derived as shown in Table 8.2. The results show that the concentration of pegylated gold nanoshells is estimated to increase from 2.6×10^8 particles/ml at 2 h to 6.2×10^9 particles/ml at 6 h. This represents a 24-fold increase from 0.29 % to 6.9 % of injected gold nanoshells that reaches the tumor over the two time points.

In comparison, the estimated concentration of anti-EGFR conjugated gold nanoshells in tumor is higher at both time points and it increases from 4.9×10^9 particles/ml at 2 h to 7.4×10^9 particles/ml at 6 h. Despite having a higher concentration of gold nanoshells in tumor at both time points, the percentage of injected anti-EGFR gold nanoshells that reaches the tumor over the 4 h interval increases by only 1.5 times from 5.5 % at 2 h to 8.2 % at 6 h of circulation.

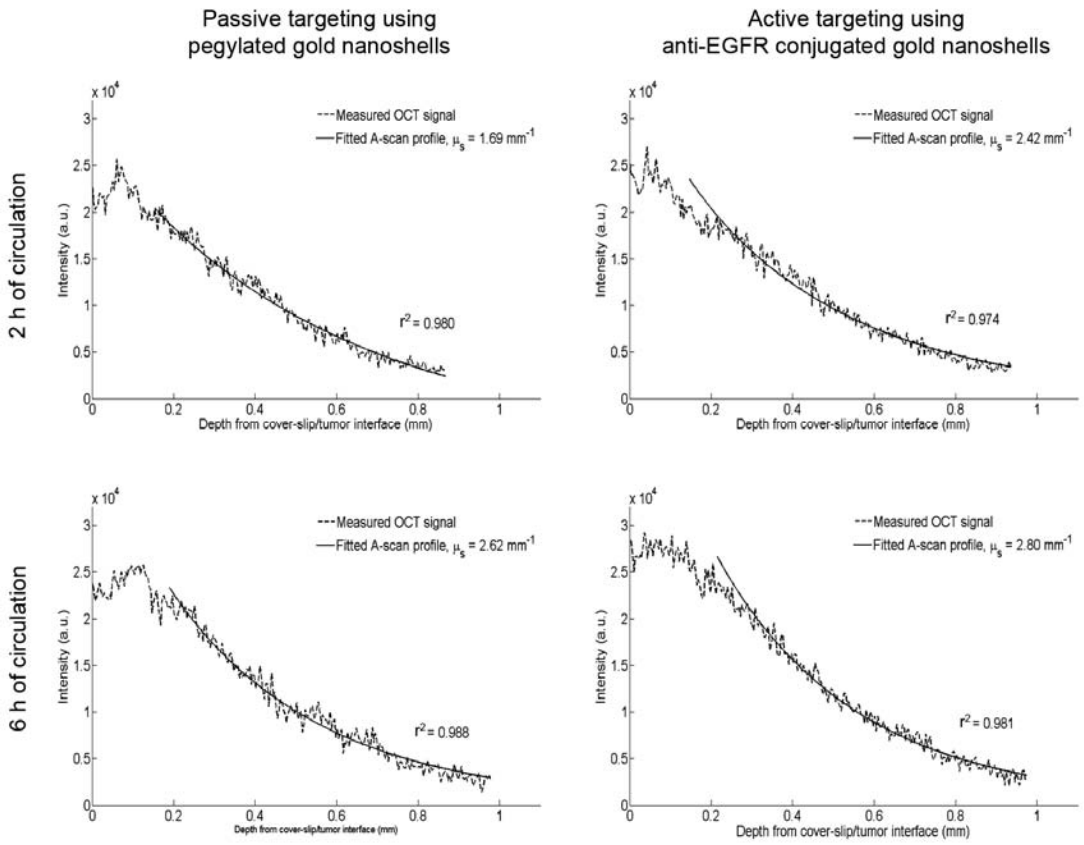

Figure 8.12. Comparison of the gold nanoshells localization in tumor tissue between passive targeting using pegylated gold nanoshells (left column) and active targeting using anti-EGFR conjugated gold nanoshells (right column) showing the changes in the average A-scan profile after 2 h (top) and 6 h (bottom) of gold nanoshells (9.0 x 10^{10} particles/ml) i.v. delivery. The measured OCT signal is shown in dotted line while the non-linear least square fit of the data is shown in solid line superimposed with the extracted μ_s shown in the figure.

The results from this study have also shown that antibody targeting with the use of appropriate antibody surface functionalization is one strategy that can improve the speed and efficiency of gold nanoshells tumor localization. In this study, the overexpression of EGFR is used as an appropriate cancer marker and the anti-EGFR antibody is used to guide the gold nanoshells to the mouse tumor based on this marker. This form of antibody guidance is specific to the tumor due to the overexpression of the EGFR receptor on the surface of tumor forming cancer cells.

Table 8.2. Summary of extracted $\mu_{s,GNS\ in\ tumor}$ of tumor with gold nanoshells as determined from the theoretical curve fit of average A-scan profile as well as the estimated gold nanoshells concentration in tumor after 2 h and 6 h of vascular circulation with non-specific pegylated and anti-EGFR conjugated gold nanoshells. The $\mu_{s,GNS}$ of gold nanoshells alone in tumor is obtained from the subtraction of μ_s of tumor tissue i.e. 1.65 mm^{-1} from $\mu_{s,GNS\ in\ tumor}$.

Type of gold nanoshells injected	Blood circulation period	Extracted $\mu_{s,GNS\ in\ tumor}$ ($mm^{-1)}$	Post-subtraction $\mu_{s,GNS}$ (mm^{-1})	Estimated gold nanoshells concentration in tumor (particles/ml)	Percentage of injected gold nanoshells that localize in tumor
Pegylated gold nanoshells	2 h	1.69 ± 0.27	0.04 ± 0.27	$2.6 \pm 1.7 \times 10^8$	0.29 %
	6 h	2.62 ± 0.34	0.97 ± 0.34	$6.2 \pm 2.2 \times 10^9$	6.9 %
Anti-EGFR conjugated gold nanoshells	2 h	2.42 ± 0.23	0.77 ± 0.23	$4.9 \pm 1.5 \times 10^9$	5.5 %
	6 h	2.80 ± 0.25	1.15 ± 0.25	$7.4 \pm 1.6 \times 10^9$	8.2 %

The A-431 cells that were inoculated to form the xenograft tumor in mice are known to have a high expression of EGFR, several times higher than normal cells. This high expression of EGFR, together with a relatively porous tumor vasculature, facilitates a greater amount of receptor-ligand interaction that results in larger quantity of gold nanoshells targeting and binding to the cancer cells. On the other hand, the nominal EGFR expression found in normal cells coupled with the non-porosity of the normal vasculature does not encourage much receptor -anti-EGFR interaction and thereby resulting in minimal tumor localization.

While passive targeting using pegylated gold nanoshells relies solely on vascular porosity to confer a moderate level of tumor specificity, antibody targeting offers a higher level of tumor specificity that is based on differences in cancer marker

expression in addition to vascular porosity. For this reason, active targeting with anti-EGFR gold nanoshells offers greater control of gold nanoshells delivery to the tumor site to enable a larger amount of gold nanoshells to be delivered to the tumor within a shorter period of time. This explains the increase in absolute amount as well as percentage increase of injected gold nanoshells that localizes in the tumor at both time points compared to passive targeting.

Apart from a greater amount of tumor localization, active targeting using anti-EGFR also tends to accelerate the rate gold nanoshells tumor localization, which explains the significant difference in the OCT image intensity between active and passive targeting at 2 h. This comes about because the EPR effect of passive targeting is an inefficient biological process of transporting gold nanoshells out of the blood circulation into the tumor and would thus require prolong period of vascular circulation i.e. 6 h before a sufficient amount of gold nanoshells are localized to cause an observable change in the OCT image.

The antibody receptor binding in active targeting eliminates this problem through promoting a strong interaction between the nanoparticles and the biological environment, thus allowing sufficient amount of gold nanoshells to localize within a shorter time of 2 h. However, given more time for the pegylated gold nanoshells to localize passively in the tumor, the difference in the OCT image intensity between passive and active targeting at 6 h is reduced. This occurs as the pegylated gold nanoshells continue to accumulate consistently in the tumor while the rate of anti-EGFR gold nanoshells delivery to tumor becomes slower when the EGFR receptors

available for binding is reduced as increasingly more and more receptors are being bounded to the anti-EGFR gold nanoshells.

For the same reason as discussed above, the longitudinal change in the OCT image and average A-scan profile between 2 and 6 h is more apparent with passively targeted gold nanoshells compared to antibody targeted gold nanoshells since the pegylated gold nanoshells would require a longer period of 6 h before they localizes to produce an observable contrast while the anti-EGFR conjugated gold nanoshells localizes sufficiently fast within 2 h to produce the same observable contrast. Such delivery dynamics hold considerable implications towards developing a contrasting regime where time is crucial to the subject being studied.

8.4 Conclusion

In this chapter, the *in vivo* control of optical contrast in a mouse xenograft tumor model using gold nanoshells as a contrast agent in OCT is demonstrated. This is achieved via three approaches: 1. Employing different gold nanoshells delivery modes such as intratumoral or i.v., 2. Varying the concentration of injected dosing and 3. Enabling active targeting with appropriate antibody surface functionalization on gold nanoshells. The estimation of gold nanoshells concentration in tumor tissue of live mice derived from the extraction of μ_s presents a novel technique that could be used to noninvasively determine gold nanoshells concentration in tissue in real time. When used to examine the dynamics of gold nanoshells localization in tumor with variations in i.v. dosage and presence of surface functionalization and the results reveal a non-linear response of gold nanoshells tumor localization with increasing dosage.

Furthermore, the use of antibody active targeting serves not just to improve the tumor localization of gold nanoshells but also hasten their delivery over passive targeting. Such insights aid in better understanding of the dynamics of gold nanoshells tumor delivery and thereby hold several implications towards developing an optimized contrast protocol to add further value to the clinical significance of OCT. Being able to target the tumor cells overexpressing EGFR, the findings also highlight the versatility of gold nanoshells not just as a generic contrast agent but one which can potentially be associated with disease markers to further elucidate the molecular mechanism of diseases under the OCT, thus further adding value to its clinical significance.

8.5 References

1. Loo C, Lowery A, Halas N, West J, Drezek R. Immunotargeted nanoshells for integrated cancer imaging and therapy. *Nano Lett* 2005; 5(4): 709-711.

2. Gobin AM, Lee MH, Halas NJ, James WD, Drezek RA, West JL. Near-infrared resonant nanoshells for combined optical imaging and photothermal cancer therapy. *Nano Lett* 2007; 7(7): 1929-1934.

3. Loo C, Lin A, Hirsch L, Lee MH, Barton J, Halas N, West J, Drezek R. Nanoshell-enabled photonics-based imaging and therapy of cancer. *Technol Cancer Res Treat* 2004; 3(1): 33-40.

4. O'Neal DP, Hirsch LR, Halas NJ, Payne JD, West JL. Photo-thermal tumor ablation in mice using near infrared-absorbing nanoparticles. *Cancer Lett* 2004; 209(2): 171-176.

5. Matsumura Y, Maeda H. A new concept for macromolecular therapeutics in cancer chemotherapy: mechanism of tumoritropic accumulation of proteins and the antitumor agent smancs. *Cancer Res* 1986; 46(12 Pt 1): 6387-6392.

6. Maeda H, Fang J, Inutsuka T, Kitamoto Y. Vascular permeability enhancement in solid tumor: various factors, mechanisms involved and its implications. *Int Immunopharmacol* 2003; 3(3): 319-328.

7. James WD, Hirsch LR, West JL, O'Neal PD, Payne JD. Application of INAA to the build-up and clearance of gold nanoshells in clinical studies in mice. *J Radioanal Nucl Ch* 2007; 271: 455-459.

8. Chen J, Saeki F, Wiley BJ, Cang H, Cobb MJ, Li ZY, Au L, Zhang H, Kimmey MB, Li X, Xia Y. Gold nanocages: bioconjugation and their potential use as optical imaging contrast agents. *Nano Lett* 2005; 5(3): 473-477.

9. Huang X, El-Sayed IH, Qian W, El-Sayed MA. Cancer cell imaging and photothermal therapy in the near-infrared region by using gold nanorods. *J Am Chem Soc* 2006; 128(6): 2115-2120.

10. Kah JC, Wan RC, Wong KY, Mhaisalkar S, Sheppard CJ, Olivo M. Combinatorial treatment of photothermal therapy using gold nanoshells with conventional photodynamic therapy to improve treatment efficacy: an in vitro study. *Lasers Surg Med* 2008; 40(8): 584-589.

11. Kah JC, Kho KW, Lee CG, James C, Sheppard R, Shen ZX, Soo KC, Olivo MC. Early diagnosis of oral cancer based on the surface plasmon resonance of gold nanoparticles. *Int J Nanomedicine* 2007; 2(4): 785-798.

12. Kah JC, Olivo MC, Lee CG, Sheppard CJ. Molecular contrast of EGFR expression using gold nanoparticles as a reflectance-based imaging probe. *Mol Cell Probes* 2008; 22(1): 14-23.

13. Yasui W, Sumiyoshi H, Hata J, Kameda T, Ochiai A, Ito H, Tahara E. Expression of epidermal growth factor receptor in human gastric and colonic carcinomas. *Cancer Res* 1988; 48(1): 137-141.

14. Costa S, Stamm H, Almendral A, Ludwig H, Wyss R, Fabbro D, Ernst A, Takahashi A, Eppenberger U. Predictive value of EGF receptor in breast cancer. *Lancet* 1988; 2(8622): 1258.

15. Ang KK, Berkey BA, Tu X, Zhang HZ, Katz R, Hammond EH, Fu KK, Milas L. Impact of epidermal growth factor receptor expression on survival and pattern of relapse in patients with advanced head and neck carcinoma. *Cancer Res* 2002; 62(24): 7350-7356.

16. Bohren CF, Huffman DR. Absorption and Scattering of Light by Small Particles. New York, NY: Wiley-Interscience, 1998.

17. Thrane L, Yura HT, Andersen PE. Analysis of optical coherence tomography systems based on the extended Huygens-Fresnel principle. *J Opt Soc Am A Opt Image Sci Vis* 2000; 17(3): 484-490.

18. Kholodnykh AI, Petrova IY, Larin KV, Motamedi M, Esenaliev RO. Precision of measurement of tissue optical properties with optical coherence tomography. *Appl Opt* 2003; 42(16): 3027-3037.

19. van Leeuwen TG, Faber DJ, Aalders MC. Measurement of the axial point spread function in scattering media using single-mode fiber-based optical coherence tomography. *Selected Topics in Quantum Electronics, IEEE Journal of* 2003; 9(2): 227-233.

20. Esenaliev RO, Larin KV, Larina IV, Motamedi M. Noninvasive monitoring of glucose concentration with optical coherence tomography. *Opt Lett* 2001; 26(13): 992-994.

21. Izatt JA, Hee MR, Owen GM, Swanson EA, Fujimoto JG. Optical coherence microscopy in scattering media. *Opt Lett* 1994; 19(8): 590-592.

22. Faber D, van der Meer F, Aalders M, van Leeuwen T. Quantitative measurement of attenuation coefficients of weakly scattering media using optical coherence tomography. *Opt Exp* 2004; 12(19): 4353-4365.

23. Lin AW, Lewinski NA, West JL, Halas NJ, Drezek RA. Optically tunable nanoparticle contrast agents for early cancer detection: model-based analysis of gold nanoshells. *J Biomed Opt* 2005; 10(6): 064035.

24. Zaman RT, Diagaradjane P, Wang JC, Schwartz J, Rajaram N, Gill-Sharp KL, Cho SH, Rylander HG, Payne JD, Krishnan S, Tunnell JW. In vivo detection of gold nanoshells in tumors using diffuse optical spectroscopy.

25. Clark AL, Gillenwater A, Alizadeh-Naderi R, El-Naggar AK, Richards-Kortum R. Detection and diagnosis of oral neoplasia with an optical coherence microscope. *J Biomed Opt* 2004; 9(6): 1271-1280.

26. Garofalakis A, Zacharakis G, Filippidis G, Sanidas E, Tsiftsis DD, Stathopoulos E, Kafousi M, Ripoll J, Papazoglou TG. Optical characterization of thin female breast biopsies based on the reduced scattering coefficient. *Phys Med Biol* 2005; 50(11): 2583-2596.

27. Kah JC, Wong KY, Neoh KG, Song JH, Fu JW, Mhaisalkar S, Olivo M, Sheppard CJ. Critical parameters in the pegylation of gold nanoshells for biomedical applications: An in vitro macrophage study. *J Drug Target* 2008: 1.

28. van Staveren HJ, Moes CJM, van Marie J, Prahl SA, van Gemert MJC. Light scattering in Intralipid-10% in the wavelength range of 400-1100 nm. *Appl Opt* 1991; 30(31): 4507-4514.

CHAPTER NINE

PHOTOTHERMAL CANCER THERAPY

Abstract

Besides imaging applications, the optical properties of gold nanoshells can also be exploited for cancer therapy as in the case of photothermal cancer therapy (PTT). Similar to photodynamic therapy (PDT), both treatments have proven to be effective treatment strategies for cancer, but the approach of combining them into a single treatment modality may offer better treatment efficacy. In this chapter, the combinational treatment of PTT using gold nanoshells with conventional PDT to improve treatment efficacy is described in an *in vitro* study. The treatment efficacy of such combined treatment is compared with that of the individual treatment. The individual PDT, PTT and combined treatment were performed under selected *in vitro* condition with a low light dose of 1.44 J/cm^2 and their cell viability were compared using crystal fast violet assay. Compared to PDT and PTT alone which can reduce cell viability to 30.9% and 44.0% respectively, the combined treatment under a single irradiation can further reduce the cell viability to 17.5%. A combined PDT and PTT treatment appears to be a more effective treatment strategy compared to conventional PDT or emerging PTT treatment. The work presented in this chapter has been published in *Lasers in Surgery and Medicine 2008; 40: 584-589.*

9.1 Introduction

Photodynamic therapy (PDT) has emerged as a promising treatment modality in cancer. It involves a combined effect of a photosensitizer administered either topically or intravenously and a non-thermal light dose with appropriate fluence and wavelength that matches the excitation of photosensitizer to initiate an irreversible photochemical destruction to cells. Whilst PDT has achieved much success in the clinical settings [1-3], it is without its own limitations. Apart from its known side effects of phototoxicity, most of the photosensitizers require the activation by light of wavelengths that limits its penetration into tissue, thus confining the treatment area to superficial regions. These photosensitizers also suffer from modest specificity and thus have a tendency to also localize in non-pathological region of tissue [4].

The destruction of tumors using hyperthermia has been under investigation for some time but photothermal therapy (PTT) only emerge as a promising treatment modality after the advent of exogenous absorption agents such as indocyanine green [5, 6]. This is because these agents can interact with deep penetrating near infrared (NIR) lasers and allow the lethal dose of heat formed to be localized deep in target site with little damage to the intervening and surrounding healthy tissue as the activating NIR light propagates through the tissue with minimum absorption and maximum transmission to reach the underlying tumor.

Gold nanoshells have also recently shown efficacy in PTT both *in vitro* [7, 8] and *in vivo* [9, 10] due to their tunable surface plasmon resonance coupled with a large absorption cross section (exceeding indocyanine green by several orders of magnitude) which allows them to strongly absorb light in the NIR wavelength with

maximum tissue penetration. The mechanism of cell kill that has been reported by others [11] is shown in Figure 9.1 below. Gold nanoshells are also photostable, biocompatible [12, 13] and can be easily conjugated to targeting moieties such as antibodies and oncoproteins to confer greater specificity for targeted PTT [14]. These benefits associated with nanoshell-mediated photothermal therapy seem to have the potential to address the limitations of PDT.

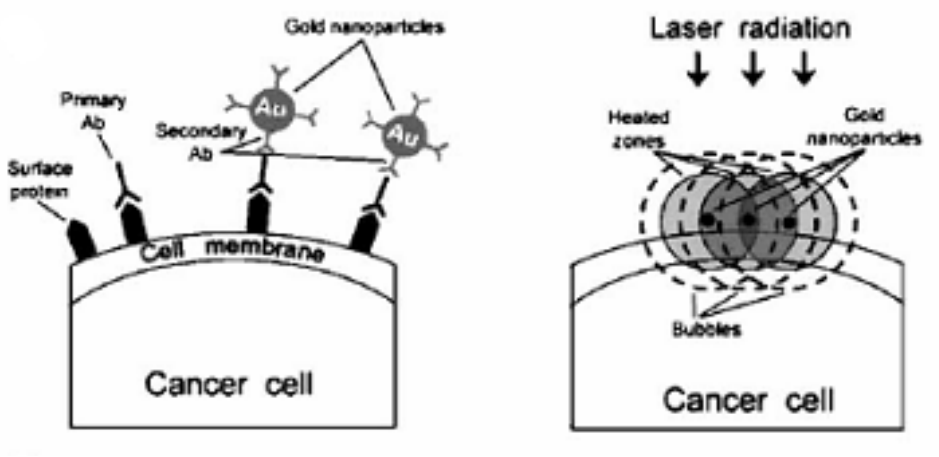

Figure 9.1. The principle of selective nanophotothermolysis with self-assembling gold nanoclusters. Based on the study by Zharov et al. [11], the human breast adenocarcinoma cell (MDA-MB-231) targeted with primary antibody IgG (F19), which is selectively attached to surface proteins (seprase), and secondary goat anti-mouse IgG conjugated with 40 nm gold nanoparticles, which is selectively attached to the primary antibodies. The schematics of laser-induced overlapping heated zones and bubbles from closely located nanoparticles.

The present study described in this chapter aim to determine if the combination of PDT and PTT administered with a single irradiation will result in a better treatment efficacy compared to their individual treatment in terms of lower cell viability. The approach of combining both treatment modalities has not been reported and may potentially offer greater therapeutic efficacy. The PDT performed in this study is based a previously published *in vitro* treatment regime using a low light dose with hypericin as the photosensitizer [15] while the *in vitro* PTT involves the same light

dose with gold nanoshells that are conjugated to anti-epidermal growth factor receptor (EGFR) as the photothermal agent.

As there are currently no report on PTT using a low light dose to date, two factors will first be examined, namely the irradiation time and concentration of gold nanoshells and quantified for their photothermal treatment efficacy in order to select a suitable treatment condition to yield maximum cell kill based on the low light dose prior to evaluating the combination treatment. The results demonstrate that upon combining both PDT and PTT together under a single irradiation, a synergistic effect that leads to a further reduction in cell viability is observed and this will be discussed briefly.

9.2 Materials and methods

9.2.1 Preparation of antibody conjugated gold nanoshells

Gold nanoshells with a silica core radius of 81 nm and gold shell thickness of 23 nm were synthesized in a four-step process which is described in more detail in Chapter 4. The gold nanoshells were imaged under the TEM (Jeol JEM-1010) and their extinction spectrum was characterized using a UV-Vis spectrophotometer (Shimadzu UV-2401 PC) The monoclonal anti-EGFR (Santa Cruz Biotechnology Inc.) was conjugated to gold nanoshells using the heterobifunctional poly(ethylene)glycol (PEG) SH-PEG-COOH (MW = 3000 g/mol, Celares GmbH) as the linker where the thiol end was attached to the gold surface of the nanoshells and the carboxylic end reacted with amine groups on the anti-EGFR via carbodiimide chemistry to form an amide bond. The details of the antibody conjugation are documented in Chapter 6.

9.2.2 Light source for treatment

The irradiation were performed using a 100 x 50 cm light diffusing surface illuminated by a bank of 14 fluorescent tubes (Philips type OSRAM L30W11-860, 30W), filtered with red acetate filters (No. 17; Roscolux, Rosco, CA, USA) to give to a wide band illumination above 585 nm. The energy fluence rate was 4 mW/cm^2 at 800 nm as measured using a power meter (Laser check; Coherent, USA). The cells were irradiated for a range of time to give light fluence of 0.48 to 2.88 J/cm^2.

9.2.3 Photodynamic therapy *in vitro*

The photosensitizer hypericin with a peak absorbance at 595 nm was obtained from Molecular Probes. For PDT treatment, the poorly differentiated CNE2 cells were plated in 96-well plates at 2 x 10^4 cells per well and allowed to attach overnight. Medium was then removed and replaced with 200 µl of fresh medium containing 1.25 µM of Hypericin for 6 h. After 6 h of hypericin incubation, the hypericin-containing medium was then replaced with fresh growth medium, and the cells were irradiated for 6 minutes and incubated again in the dark for 18 h. After 18 h of incubation, the irradiated cells were evaluated for cell kill using the crystal fast violet assay. The use of crystal fast violet assay to quantify cell viability in *in vitro* assays is well documented [15]. It detects cell viability by binding to DNA of viable cells. Incubation of live cells in a mixture of crystal violet causes cells to lyse and the released nuclei to be stained purple. Cells exposed to the light alone without any drug and cells receiving drug alone without any light were used as controls.

9.2.4 Photothermal therapy *in vitro*

For the PTT study, the following factors were investigated to select a suitable treatment condition: irradiation exposure and concentration of gold nanoshells. The protocol used for PTT is the same as that for PDT, except that instead of hypericin, the cells were incubated with medium containing a range of concentration of anti-EGFR conjugated gold nanoshells (3.0×10^9 to 6.0×10^{11} particles/ml) for 45 minutes. The 45 minutes of incubation period is the typical time known to be sufficient for antibodies binding to their antigens. The cells were then irradiated for a range of exposure time. The controls were the same as that of PDT. The study was performed in triplicates and the unpaired 2-sided Student's *t*-test was performed to determine any statistical difference in the treatment efficacy between each condition and its respective controls. The temperature rise in the culture medium after irradiation was measured by a thermocouple (type K) that is able to exhibit instantaneous response to real-time temperature changes with an accuracy range of ±[0.05% + 0.3°C] (Fluke 52 II Thermometers, USA).

9.2.5 Combinational treatment of PDT and PTT

The protocol is the same as above. The CNE2 cells were incubated with fresh medium containing 1.25 μM of hypericin for 6 h and anti-EGFR conjugated gold nanoshells (6.0×10^{10} particles/ml) were added to the hypericin-containing medium 45 minutes before the 6 h incubation lapsed so as to allow 45 minutes of incubation of cells with gold nanoshells. After incubation, the medium was replaced with fresh medium and cells were irradiated for 6 minutes. The controls were the same as that of PDT and the study was performed in triplicates. The one-way ANOVA test with one-way analysis

of variance was performed to determine any statistical difference in the treatment efficacy between the combined treatment and the individual PDT or PTT treatment as well as their respective controls with either drug or light alone.

9.3 Results and discussion

9.3.1 Synthesis and characterization of gold nanoshells

The TEM image of the gold nanoshells and its UV-Vis absorption spectrum is shown in Figure 9.2. The emission spectrum of the light source used for the irradiation is also shown as a comparison. The gold nanoshells synthesized were generally spherical and monodispersed. Their absorption spectrum shows a rather broad extinction band of wavelength > 580 nm with two discernable peaks at around 650 nm and 800 nm. This absorption spectrum matches the emission spectrum of the light source well and thus allows an efficient transfer of optical energy from the light source to the gold nanoshells for photothermal conversion.

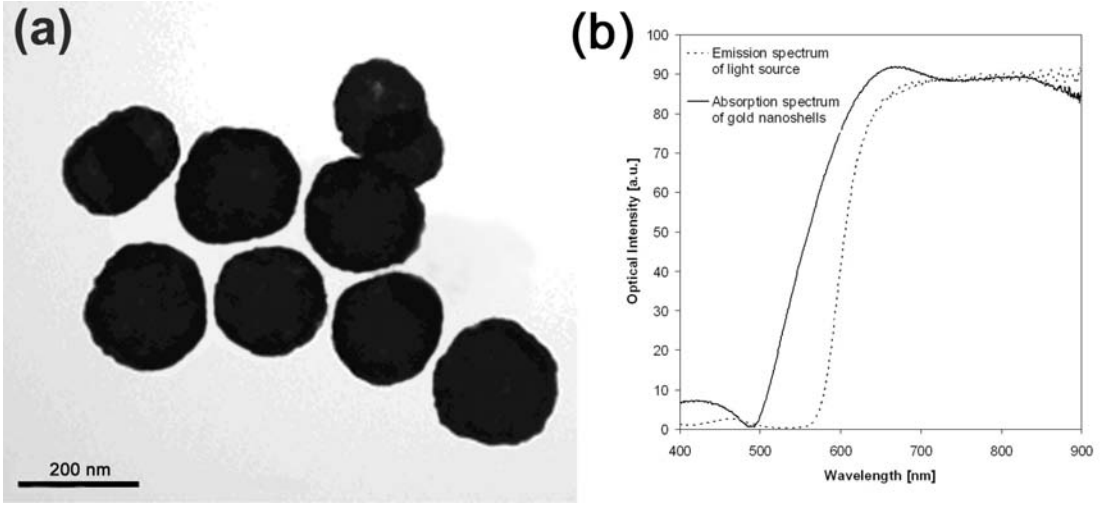

Figure 9.2. (a) TEM image of the synthesized gold nanoshells with a 162 nm silica core and a 23 nm gold shell, and (b) their absorption spectrum (solid curve) compared to the emission spectrum (dotted curve) of the light source used in this study.

9.3.2 Optimization of irradiation dose for PTT

The CNE2 cell lines were incubated with these gold nanoshells conjugated to anti-EGFR (6.0 x 10^9 particles/ml) and irradiated under various exposure times to investigate the effect of different irradiation dose on cell viability. The cell viability and temperature in cell medium after exposing them to light from 2 to 12 minutes is shown in Figure 9.3. As the cells were irradiated, the temperature of the medium increased rapidly from 33.0 °C after 2 minutes of irradiation to 40.1 °C after 6 minutes of irradiation. Thereafter, the temperature rise in the medium becomes more gradual beyond 6 minutes of irradiation, eventually reaching a plateau of around 43 °C. This temperature rise is the result of the light absorption of gold nanoshells attached to the surface of cells via the EGFR receptors and their subsequent photothermal conversion to heat up the cells, thereby causing the temperature rise.

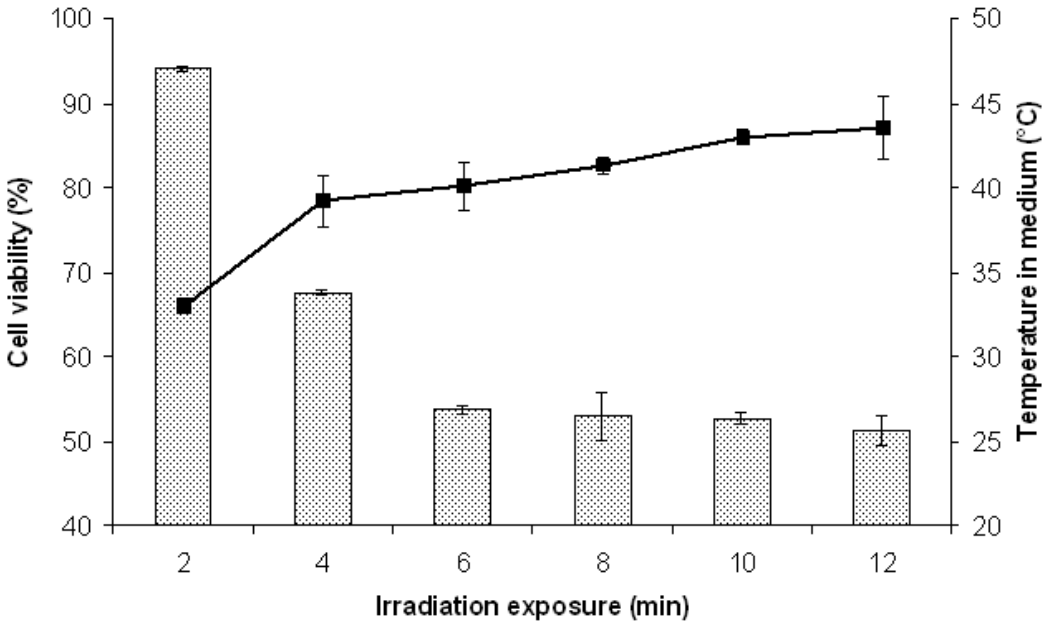

Figure 9.3. Cell viability and temperature of cell medium after incubating the CNE2 cells with gold nanoshells (6.0 x 10^9 particles/ml) for 45 minutes and subsequently exposing them to light for a range of irradiation exposure to give a PTT light dose of 0.48 to 2.88 J/cm^2.

This thermal effect on the cells also resulted in their destruction as the corresponding cell viability decreased from 94.0% after 2 minutes of irradiation to just 53.6% after 6 minutes of irradiation. The cell viability remained relatively constant at around 52% beyond 6 minutes of irradiation. The results for each irradiation exposure time were significantly different when compared to their respective control of irradiation without gold nanoshells using an unpaired Student's *t*-test with a p-value of <0.05. Therefore, there seems to be a negative correlation between the cell viability and the temperature of the medium as controlled by the irradiation exposure.

An exposure time of 6 minutes would be sufficient to optimize the cell kill with a low light dose of 1.44 J/cm^2 as any further irradiation have little or no impact on the cell viability. The published data on PTT *in vitro* have so far demonstrated cell kill qualitatively with cell viability staining immediately after irradiation under a high light dose with a fluence rate of >10W/cm^2 [16, 17]. While a high light dose is known to induce immediate necrotic cell death with severe heating, PTT with a low light dose may induce cell death via a slower mechanism with its gentler thermal effect.

As the temperature in the medium rise beyond 40 °C due to the photothermal conversion between the matching source spectrum and the absorption spectrum of the gold nanoshells, the cell viability drops by nearly half. Although this temperature is only slightly higher than normal physiological temperature, it would be worth noting that the actual temperature experienced by the cells with the presence of gold nanoshells heating on their surface will be higher than the measured temperature in the medium. Whilst the actual difference could not be determined experimentally with the current setup, it could be significant enough to induce cell mortality. This is

especially true for cancer cells which are known to be more sensitive to increase in temperature in terms of their biochemical changes compared to normal cells [18, 19]. Previous studies have shown that these cells are susceptible to destruction at temperature of 43 °C as effects due to DNA damage, glucose deprivation etc. during hyperthermia prove to be strongly accelerated to result in a lethal lack of cellular energy and subsequent cell death [20-22].

As the irradiation exposure increases, the gold nanoshells continue to absorb more photons and convert them to thermal energy to heat its surroundings until a point where the temperature in the medium reaches a steady state of around 43 °C after 6 minutes of irradiation and any further temperature rise is limited by the fluence rate of the light source. Such a steady state in the temperature thus results in a corresponding plateau in the cell mortality where no further lowering of cell viability is observed upon further irradiation.

9.3.3 Optimization of gold nanoshells concentration for PTT

The same correlation between the cell viability and temperature of medium was observed when the concentration of gold nanoshells added to the cells was varied as shown in Figure 9.4. The temperature of the medium increased gradually from 38.0 °C with 3.0×10^9 particles/ml to 45.4 °C with 6.0×10^{10} particles/ml and remained rather constant thereafter at temperature of around 46 °C even with further addition of gold nanoshells to the cells. With an increasing temperature heating the cells, the corresponding cell viability decreased from 63.0% with 3.0×10^9 particles/ml to 44.0% with 6.0×10^{10} particles/ml and likewise remained constant with a cell viability of around 43%, independent of any further addition of gold nanoshells.

The results for each concentration were significantly different when compared to their respective control without irradiation using an unpaired Student's *t*-test with a p-value of < 0.05. This result suggests that a concentration of 6.0×10^{10} particles/ml would be sufficiently suitable to maximize cell kill with the low light dose treatment condition without the addition of more than necessary amount of gold nanoshells to the cells.

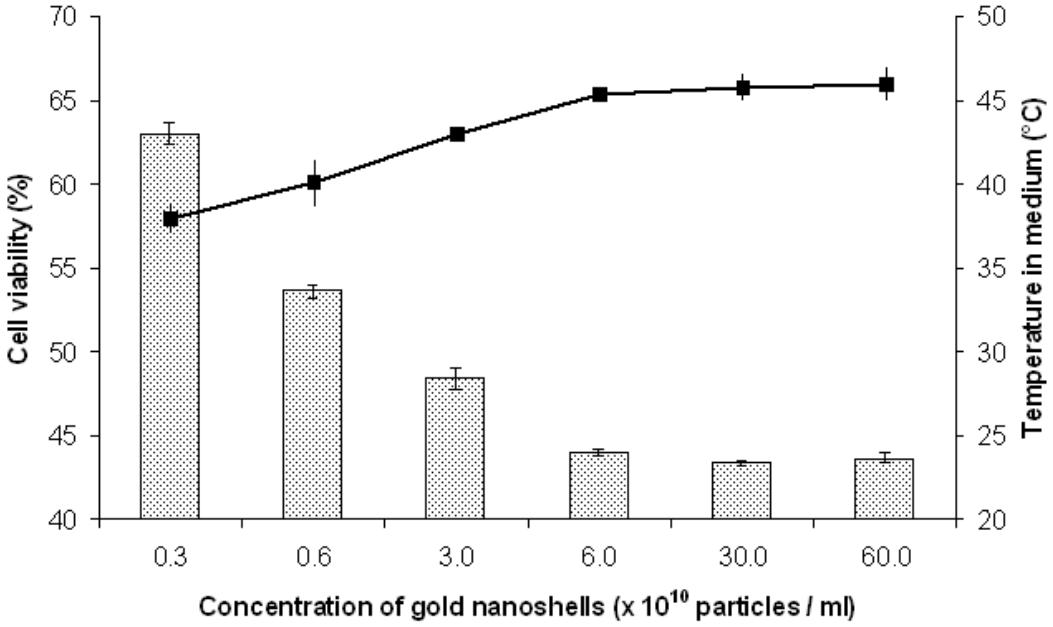

Figure 9.4. Cell viability and temperature of cell medium after incubating the CNE2 cells with a range of gold nanoshells concentration from 3.0×10^9 to 6.0×10^{11} particles/ml for 45 minutes and subsequently exposing them to light for 6 minutes to give a PTT light dose of 1.44 J/cm^2.

The temperature in the medium and hence the cell viability is therefore affected by the concentration of the gold nanoshells added to the cells. This concentration determines the amount of anti-EGFR conjugated gold nanoshells available to bind to the EGFR receptors on the CNE2 cells. As the cells were incubated with an increasing concentration of gold nanoshells from 3.0×10^9 to 6.0×10^{11} particles/ml, more of the nanoshells were bound to the cells which resulted in a higher temperature rise with

more photothermal centre and consequently lower cell viability when the cells were subsequently irradiated for 6 minutes.

The EGFR signaling pathway is one of the most important pathways that regulate proliferation in mammalian cells and an abnormal expression of EGFR is often associated with increased cell proliferation and decreased apoptosis leading to carcinogenesis. The EGFR is highly expressed in a variety of human cancer of epithelial origin. Based on a separate ELISA analysis as described in Chapter 6, the CNE2 cells express about 180.9 pg of EGFR per 1000 cells which is about 6×10^5 EGFR receptors on each cell. This represents an approximate 6 times higher expression compared to normal cells with typical expression level of 9×10^4 EGFR per cell. This difference in expression level allows the PTT treatment with anti-EGFR gold nanoshells to be targeted more specifically to cancer cells.

As the concentration of gold nanoshells added to the cells increases, more of the EGFR receptors on the cells will be bound to the anti-EGFR gold nanoshells and subsequent irradiation raises the temperature due to a larger amount of gold nanoshells present to heat the cells. This ligand-receptor binding continues until all the EGFR binding sites on cells are saturated. This saturation concentration roughly corresponds to 6.0×10^{10} particles/ml where about 1.2×10^{10} anti-EGFR gold nanoshells were added to fully bind to all the receptors on the 2×10^4 CNE2 cells in each well. Any further addition of gold nanoshells that exceeds this saturation concentration will form unbound excesses in medium which will be removed by washing and will have no impact on further increasing the photothermal effect and reducing the cell viability.

9.3.4 Combinational treatment of PDT and PTT

A quantitative analysis of the cell viability under low light dose has not been reported to date and the results from previous section show that a light dose of 1.44 J/cm^2 from 6 minutes of irradiation on CNE2 cells incubated with 6.0 x 10^{10} particles/ml of gold nanoshells is sufficient to reduce the cell viability to 44.0% and any further increase in the light dose or concentration of gold nanoshells does not affect the cell viability much. Once the suitable treatment condition to maximize cell kill for PTT was established based on this condition, the treatment efficacy when both PDT and PTT were combined under a single irradiation of 6 minutes was evaluated.

The results in Figure 9.5 show that both PDT and PTT alone resulted in a cell viability of 30.9% and 44.0% respectively. For the *in vitro* PDT treatment, the cell viability of 30.9% achieved is consistent with previously published results using the same PDT treatment regime [23]. When the treatment was combined under a single irradiation, the cell viability was reduced to just 17.5%, which is lower than either of the individual treatment. These three treatment results were significantly different ($p < 0.05$) compared to their respective controls with either the drug or light alone which maintained a high cell viability of > 94.5% for all control cases (Figure 9.5). Furthermore, the improvement from combined treatment in terms of lowering the cell viability was also statistically significant compared to the respective individual PDT or PTT treatment ($p < 0.05$).

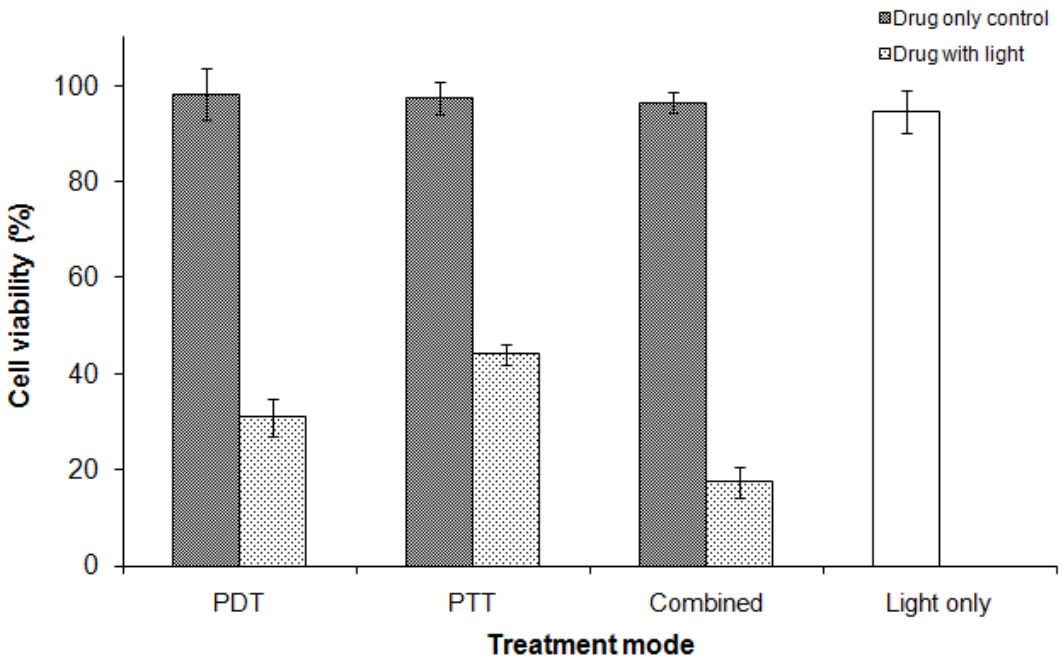

Figure 9.5. Cell viability after the individual PDT and PTT as well as the combined treatment. The conditions for *in vitro* PDT follows a previously published treatment protocol [15] while the condition for *in vitro* PTT follows that which is established in this study i.e. incubation of cells with 6 x 10^{10} particles/ml of gold nanoshells for 45 minutes followed by light irradiation of 6 minutes to give a light dose of 1.44 J/cm^2. The cell viability of their respective controls with either the drug or light alone is also shown for comparison.

Although both PDT and PTT have the same basic treatment principle that involves a synergistic interaction between a light source and a drug of interest, their mechanism for eliciting cell kill is different. While the cell kill for PTT is attributed to the photothermal heating of the cancer cells due to the light absorption of gold nanoshells, the cell death induced by PDT is due to the generation of toxic singlet oxygen species by the activation of photosensitizer in the presence of light and ambient oxygen. As in the case of PDT, PTT may also induce cell death via necrosis or apoptosis depending on the light dose administered.

Previous results with PDT have shown that necrotic cell death tends to occur with high light dose from a high fluence rate coupled with a long exposure time while a low light dose PDT tends to trigger a slower apoptotic cell death that promotes subsequent tissue healing with lesser inflammatory response [24]. The low light dose used in the PTT treatment in this study may induce cell death via apoptosis since the temperature rise is gentler and may not be sufficient to “cook” the cells but yet sufficient to raise their temperature to the apoptotic window to trigger the slower programmed cell death [25]. With this in mind, the irradiated cells were evaluated for cell kill only after 18 h of further incubation in fresh medium instead of immediate staining with tryphan blue after irradiation.

It is also clear from the cell viability results of the individual treatment that a full eradication of the cancer cells was not achieved with the treatment protocol based on the low light dose. However, when both treatments are combined under a single 6 minutes irradiation, the combined treatment is able to achieve about 15 to 30% more cell kill compared to the individual treatment to further reduce the cell viability to 17.5%. Full eradication of the cancer cells may be possible with the combined treatment under a low light dose if the combined drug conditions are further optimized. Such improvements with a combined treatment have also been observed in other forms of treatment when combined with hyperthermia such as chemotherapy [26, 27] and radiotherapy [27-29].

The improvement in treatment efficacy observed in this study may be due to a variety of possible synergistic effect. One such possibility is when either treatment alone may damage the cells but not sufficient to induce cell death. In this case, the presence of

another treatment may further augment the damage and trigger the actual cell death. The thermal energy generated by the gold nanoshells may also accelerate the generation of the singlet oxygen species. It would also be of worth to note that the results observed could also be specific to the particular response assay used, which is the crystal fast violet assay in this case. A different assay such as a clonogenic assay may produce a qualitatively different result. An elucidation of the actual mechanism that improves the treatment efficacy and the type of cell death induced would warrant further studies.

9.4 Conclusion

This study presents a preliminary *in vitro* evaluation on the treatment efficacy of a combined PDT and PTT treatment regime under low light dose condition compared to their individual treatment response. Compared to PDT and PTT alone which can reduce cell viability to 30.9% and 44.0% respectively, a combined treatment regime under a single irradiation can further reduce the cell viability to 17.5%. In essence, the current finding shows the versatility of gold nanoshells not just as an optical contrast agent for reflectance-based imaging, but also its potential is improving current cancer therapeutics. The combined PDT and PTT treatment modality as demonstrated in this chapter promises to be a more effective treatment strategy compared to conventional PDT or emerging PTT treatment method. Such combined treatment may impact current clinical practice by potentially yielding better treatment efficacy in terms of higher cell kill and greater tumor specificity conferred by the antibody targeting to make the treatment process more cost effective.

9.5 References

1. Pinthus JH, Bogaards A, Weersink R, Wilson BC, Trachtenberg J. Photodynamic therapy for urological malignancies: past to current approaches. *J Urol* 2006; 175(4): 1201-1207.

2. Thong PS, Ong KW, Goh NS, Kho KW, Manivasager V, Bhuvaneswari R, Olivo M, Soo KC. Photodynamic-therapy-activated immune response against distant untreated tumours in recurrent angiosarcoma. *Lancet Oncol* 2007; 8(10): 950-952.

3. Wang JB, Liu LX. Use of photodynamic therapy in malignant lesions of stomach, bile duct, pancreas, colon and rectum. *Hepatogastroenterology* 2007; 54: 718-724.

4. Jichlinski P, Forrer M, Mizeret J, Glanzmann T, Braichotte D, Wagnieres G, Zimmer G, Guillou L, Schmidlin F, Graber P, van den Bergh H, Leisinger HJ. Clinical evaluation of a method for detecting superficial surgical transitional cell carcinoma of the bladder by light-induced fluorescence of protoporphyrin IX following the topical application of 5-aminolevulinic acid: preliminary results. *Lasers Surd Med* 1997; 20(4): 402-408.

5. Sawa M, Awazu K, Takahashi T, Sakaguchi H, Horiike H, Ohji M, Tano Y. Application of femtosecond ultrashort pulse laser to photodynamic therapy mediated by indocyanine green. *Br J Ophthalmol* 2004; 88(6): 826-831.

6. Urbanska K, Romanowska-Dixon B, Matuszak Z, Oszajca J, Nowak-Sliwinsk P, Stochel G. Indocyanine green as a prospective sensitizer for photodynamic therapy of melanomas. *Acta Biochim Pol* 2002; 49(387-391).

7. Loo C, Lowery A, Halas N, West J, Drezek R. Immunotargeted nanoshells for integrated cancer imaging and therapy. *Nano Lett* 2005; 5(4): 709-711.

8. Lowery AR, Gobin AM, Day ES, Halas NJ, West JL. Immunonanoshells for targeted photothermal ablation of tumor cells. *Int J Nanomedicine* 2006; 1(2): 149-154.

9. O'Neal DP, Hirsch LR, Halas NJ, Payne JD, West JL. Photo-thermal tumor ablation in mice using near infrared-absorbing nanoparticles. *Cancer Lett* 2004; 209(2): 171-176.

10. Gobin AM, Lee MH, Halas NJ, James WD, Drezek RA, West JL. Near-infrared resonant nanoshells for combined optical imaging and photothermal cancer therapy. *Nano Lett* 2007; 7(7): 1929-1934.

11. Zharov VP, Kim J-W, Curiel DT, Everts M. Self-assembling nanoclusters in living systems: application for integrated photothermal nanodiagnostics and nanotherapy. *Nanomedicine: Nanotechnology, Biology and Medicine* 2005; 1(4): 326-345.

12. West JL, Halas NJ. Applications of nanotechnology to biotechnology commentary. *Curr Opin Biotechnol* 2000; 11(2): 215-217.

13. Connor EE, Mwamuka J, Gole A, Murphy CJ, Wyatt MD. Gold nanoparticles are taken up by human cells but do not cause acute cytotoxicity. *Small* 2005; 1(3): 325-327.

14. Loo C, Lin A, Hirsch L, Lee MH, Barton J, Halas N, West J, Drezek R. Nanoshell-enabled photonics-based imaging and therapy of cancer. *Technol Cancer Res Treat* 2004; 3(1): 33-40.

15. Ali SM, Chee SK, Yuen GY, Olivo M. Hypericin and hypocrellin induced apoptosis in human mucosal carcinoma cells. *J Photochem Photobiol B* 2001; 65(1): 59-73.

16. Huang X, El-Sayed IH, Qian W, El-Sayed MA. Cancer cell imaging and photothermal therapy in the near-infrared region by using gold nanorods. *J Am Chem Soc* 2006; 128(6): 2115-2120.

17. Hirsch LR, Stafford RJ, Bankson JA, Sershen SR, Rivera B, Price RE, Hazle JD, Halas NJ, West JL. Nanoshell-mediated near-infrared thermal therapy of tumors under magnetic resonance guidance. *Proc Natl Acad Sci U S A* 2003; 100(23): 13549-13554.

18. Dickson JA, Oswald BE. The sensitivity of a malignant cell line to hyperthermia (42 degrees C) at low intracellular pH. *Br J Cancer* 1976; 34(3): 262-271.

19. Hofer KG, Mivechi NF. Tumor cell sensitivity to hyperthermia as a function of extracellular and intracellular pH. *J Natl Cancer Inst* 1980; 65: 621-625.

20. Haveman J, Hahn GM. The role of energy in hyperthermia-induced mammalian cell inactivation: a study of the effects of glucose starvation and an uncoupler of oxidative phosphorylation. *J Cell Physiol* 1981; 107(2): 237-241.

21. Ishiguro K, Hatcho M, Miyoshi N, Fukuda M, Ueda K. Microfluorocytometric detection of nuclear DNA damage to cancer cells in squamous cell carcinoma after hyperthermia. *J Dermatol* 1994; 21(2): 92-97.

22. Fujimoto S, Takahashi M, Kiuchi S, Kobayashi K, Mutou T, Masaoka H, Shimanskaya RB, Ohkubo H. Hyperthermia-induced antitumor activity in human gastric cancer cells serially transplanted into nude mice. *Anticancer Res* 1994; 14(1A): 67-71.

23. Ali SM, Olivo M. Bio-distribution and subcellular localization of Hypericin and its role in PDT induced apoptosis in cancer cells. *Int J Oncol* 2002; 21(3): 531-540.

24. Thong PS, Watt F, Ren MQ, Tan PH, Soo KC, Olivo M. Hypericin-photodynamic therapy (PDT) using an alternative treatment regime suitable for multi-fraction PDT. *J Photochem Photobiol B* 2006; 82(1): 1-8.

25. Shellman YG, Howe WR, Miller LA, Goldstein NB, Pacheco TR, Mahajan RL, LaRue SM, Norris DA. Hyperthermia induces endoplasmic reticulum-mediated apoptosis in melanoma and non-melanoma skin cancer cells. *J Invest Dermatol* 2008; 128(4): 949-956.

26. Yoo J, Lee YJ. Effect of hyperthermia and chemotherapeutic agents on TRAIL-induced cell death in human colon cancer cells. *J Cell Biochem* 2008; 103(1): 98-109.

27. Nakajima K, Hisazumi H. Enhanced radioinduced cytotoxicity of cultured human bladder cancer cells using 43 degrees C hyperthermia or anticancer drugs. *Urol Res* 1987; 15(5): 255-260.

28. Sakurai H, Mitsuhashi N, Kitamoto Y, Nonaka T, Harashima K, Higuchi K, Muramatsu H, Ebara T, Ishikawa H, Niibe H. Cytotoxic enhancement of low dose-rate irradiation in human lung cancer cells by mild hyperthermia. *Anticancer Res* 1998; 18(4A): 2525-2528.

29. Tur GE, Sato Y, Fukuoka T, Andoh H, Kotanagi H, Koyama K. Effect of the combination of hyperthermia and irradiation on human colon cancer cells. *J Surg Oncol* 1994; 56(2): 128-131.

CHAPTER TEN

FINAL CONCLUSION

This thesis discusses the use of gold nanostructures, in particular, gold nanoshells as an optical contrast agent in reflectance-based imaging with the potential of performing molecular contrast of relevant cancer markers. Two of such imaging technique is described in this work, namely, the confocal reflectance microscope and the OCT. Preliminary studies were done using simple spherical gold nanoparticles where they have shown to provide an optical contrast to discriminate cancer from normal cells as well as to map the expression of EGFR cancer marker under a suitably matching wavelength to their surface plasmon resonance at 520 nm. However, most of the clinical optical imaging system that operates in NIR would require nanoparticles with matching optical response in the NIR and the tunability of gold nanoshells facilitates further study which forms the main focus of this thesis.

The use of gold nanoshells would require their size configuration to provide an optimized backscattering response which can be predicted by Mie theory based on a concentric shell configuration. The synthesis of gold nanoshells using the DP process of seeding has shown to be a time and cost efficient technique compared to conventional synthesis techniques. Pegylation of gold nanoshells with mPEG-thiol provides an effective means to increase their stability in solution and reduce macrophageal clearance and the PEG surface density is a critical end parameter that determines such clearance. This surface density is not just affected by the amount of PEG added, but also on its molecular weight and the size of gold nanoshells.

The optical response of gold nanoshells is able to provide a contrast enhancement under *in vitro* confocal reflectance in NIR and antibody conjugation to gold nanoshells confers specificity to this contrast enhancement to discriminate cancer from normal cells based on differential molecular expression, which can coincidently be imaged and mapped with gold nanoshells. Further phantom studies have confirmed the improvement in OCT signal with gold nanoshells and have shown a concentration window of gold nanoshells in tissue that achieves a good compromise between signal enhancement near sample surface and signal attenuation deeper into sample.

The results from the phantoms model the actual optical response in an *in vivo* mouse xenograft tumor model well. The contrast enhancement in tumor tissue can be controlled by varying the dosage administered to the tissue of interest and the gold nanoshells concentration in tumor can be reliably estimated from the OCT signal profile. The use of antibody conjugated gold nanoshells results in stronger signal enhancement in tumor within a shorter circulation time in mice. Besides promising *in vivo* imaging results, gold nanoshells also show potential as a cancer therapeutic *in vitro* when combined with conventional PDT to further improve treatment efficacy, thus showing promise of an integrated cancer imaging and therapeutic agent.

10.1 Future directions

The final conclusion would not be complete without the mention of possible future directions that would bring the use of gold nanoshells closer to the clinic. The present *in vivo* study discussed in this thesis can be further developed in at least three different aspects. The first aspect addresses the limitations of the current analytical technique to deduce the concentration of gold nanoshells in multilayer tissue. The

present OCT theoretical models used to extract the μ_s of the sample is only applicable for homogenous sample whereas most tissues are present with multiple stromal layers. To enable the current technique to be more robust for multilayer tissue, the analysis algorithm has to be further develop to accurately extract out the μ_s of the individual layers. An evaluation of the accuracy of this technique in determining the gold nanoshells concentration in tissue is also necessary and would warrant further study to compare against the concentration obtained from another independent technique such as inductively coupled plasma mass spectroscopy (ICP-MS).

The second aspect addresses the experimentation needed to further understand the dynamics of gold nanoshells passive localization in tumor *in vivo*. The current nonlinear logarithmic relationship between the injected and localized gold nanoshells amount arising from passive targeting is deduced from a single 6 h time point based on a narrow concentration range. The results can be made more conclusive following further studies involving a wider dosing range over more time points to facilitate a proper interpretation of the results. The same can be applied to antibody functionalized gold nanoshells to further understand the dynamic of gold nanoshells active targeting to tumors.

The third aspect lies with possible improvements to the *in vivo* tumor model to more accurately represent the disease progression in cancer. Whilst the current *in vivo* results demonstrate the control of contrast enhancement by varying the gold nanoshells delivery, the use of xenograft tumor models with a gradient expression of EGFR arising from well calibrated cell lines will serve well to correlate the contrast enhancement with EGFR expression for quantitative molecular imaging. The use of

orthotropic tumor model such as the hamster's cheek pouch model with well defined tumor progression parameters can also serve to evaluate the effectiveness of optical contrast from targeted gold nanoshells to monitor cancer progression.

In addition, the promising integrated imaging and therapeutic feature of gold nanoshells can also be further evaluated on its efficacy in performing simultaneous imaging and photothermal therapy. Besides their performance evaluation, the biodistribution and long term clearance of gold nanoshells would also deserve further studies to ascertain minimal health risk prior to potential clinical applications.

The successful implementation of anti-EGFR conjugated gold nanoshells as a molecular specific contrast agent in OCT have the potential to significantly impact current clinical practice in the following ways. Firstly, it will provide a noninvasive alternative to tissue biopsy and allows clinicians to have an accurate real time diagnosis that minimizes waiting time. Secondly, the combination of phenotypic markers and molecular expression profiling will allow earlier detection and improved diagnosis of suspicious premalignant lesion, thus enhancing its diagnostic capability which is currently limited to detecting phenotypic abnormalities. Thirdly, expression profiling will also provide critical information for rational selection of therapy.

The combination of detailed anatomical resolution given by OCT together with molecular information generated by optical contrast from the antibody conjugated gold nanoshells will enhance the sensitivity and specificity of early epithelial cancer diagnosis *in vivo*. Early detection of curable precancers can dramatically reduce the incidence and mortality of cancer in high-risk individuals.